



TECHNISCHE
UNIVERSITÄT
WIEN

Vienna University of Technology

Diplomarbeit

Recrystallization in a Dispersoid-Free Al-Mg-Si Model Alloy

Ausgeführt zum Zwecke der Erlangung des akademischen Grades eines
Diplom-Ingenieurs unter der Leitung von

Univ.Prof. Dipl.-Ing. Dr.techn. Ernst Kozeschnik,

Univ.Ass. Dipl.-Ing. Dr.techn. Ahmad Falahati

und

Univ.Lektor Dipl.-Ing. Thomas Weisz, BSc

E308 - Institut für Werkstoffwissenschaft und Werkstofftechnologie

Eingereicht an der Technischen Universität Wien
Fakultät für Maschinenwesen und Betriebswissenschaften

von

David Lukavsky, BSc

0825908

Lieleggweg 1

1210 Wien

Wien, im Oktober 2016

David Lukavsky



TECHNISCHE
UNIVERSITÄT
WIEN
Vienna University of Technology

Ich habe zur Kenntnis genommen, dass ich zur Drucklegung meiner Arbeit unter der Bezeichnung

Diplomarbeit

nur mit Bewilligung der Prüfungskommission berechtigt bin.

Ich erkläre weiters Eides statt, dass ich meine Diplomarbeit nach den anerkannten Grundsätzen für wissenschaftliche Abhandlungen selbstständig ausgeführt habe und alle verwendeten Hilfsmittel, insbesondere die zugrunde gelegte Literatur, genannt habe.

Weiters erkläre ich, dass ich dieses Diplomarbeitsthema bisher weder im In- noch Ausland (einer Beurteilerin/einem Beurteiler zur Begutachtung) in irgendeiner Form als Prüfungsarbeit vorgelegt habe und dass diese Arbeit mit der vom Begutachter beurteilten Arbeit übereinstimmt.

Wien, im Oktober 2016

David Lukavsky

Kurzfassung

Dispersoide in Aluminiumlegierungen der 6xxx-Reihe sind intermetallische Phasen bestehend aus Al, Fe, Cr, Mn und Si mit einer Größe von $\sim 0,02-0,5\mu\text{m}$. Sie entstehen bei hohen Temperaturen und spielen eine wichtige Rolle in der thermomechanischen Verarbeitung. Die Dispersoide behindern die Versetzungsbewegungen und reduzieren dadurch Erholung, Rekristallisation und Kornwachstum. Dieser Effekt, genannt Zener Drag, hat direkten Einfluss auf die resultierende Festigkeit und Duktilität des verarbeiteten Materials.

Im Zuge dieser Diplomarbeit wurde im Speziellen das Rekristallisationsverhalten einer dispersoidfreien Aluminiumlegierung während der Warmumformung untersucht. Für diesen Zweck wurde eine Modelllegierung gesucht, in der keine Dispersoidbildung möglich ist und die im Weiteren als Referenz im Vergleich mit regulärem 6061 dient.

Als Modelllegierung wurde ein Al-Mg-Si-Barren mit einem möglichst geringen Gehalt an dispersoidbildenden Elementen wie Fe, Cr und Mn hergestellt. Dieser wurde im Labor einer Wärmebehandlung unterzogen und daraufhin auf Dispersoidbildung untersucht. Mit Hilfe von Transmissionselektronenmikroskopie konnte nachgewiesen werden, dass die Dispersoidbildung erfolgreich unterdrückt werden konnte.

Im nächsten Schritt wurden Proben des Materials in einem Dilatometer auf 550°C erhitzt, homogenisiert, verformt und danach abgeschreckt. Dabei wurden der Verformungsgrad, die Verformungsgeschwindigkeit und die Haltezeit nach der Verformung schrittweise variiert. Anschließend wurde die Mikrostruktur der verformten Proben mittels 'electron backscatter diffraction' untersucht. Daraus ergaben sich Kristallorientierungen, woraus wiederum direkt auf die Korngröße und den Rekristallisationsgrad geschlossen werden konnte.

Die Ergebnisse zeigten wie erwartet, dass mit größerem Verformungsgrad, höherer Verformungsgeschwindigkeit und längerer Haltezeit der Rekristallisationsgrad zunimmt. In nur wenigen Sekunden war die Rekristallisation im dispersoidfreiem Material vollständig abgeschlossen. Bei vergleichbaren Parametern in Anwesenheit von Dispersoiden benötigt die Rekristallisation ein Vielfaches der Zeit.

Dank der neuen dispersoidfreien Legierung kann nun in weiteren Versuchsreihen der Beitrag des Zener Drags zur Rekristallisationskinetik in den verschiedenen Parametervariationen ermittelt werden.

Abstract

Dispersoids in 6xxx-series aluminium alloys are intermetallic phases consisting of Al, Fe, Cr, Mn, and Si with a size of $\sim 0.02\text{-}0.5\mu\text{m}$. They form during high temperature heat treatments and play a significant role in thermomechanical processing. Dispersoids pin dislocations and therefore retard recovery, recrystallization, and grain growth. This effect, referred to as Zener drag, directly influences the resulting strength and ductility of the processed material.

Special focus of this master's thesis lies on recrystallization in a dispersoid-free aluminium alloy during hot deformation. To gain further insight on the effect of dispersoids, it was necessary to develop a model alloy entirely free of dispersoid formation. This model alloy will serve as a reference for a comparison to regular 6061.

In an attempt to avoid the formation of dispersoids, an Al-Mg-Si ingot was cast where the contents of Fe, Cr, and Mn were reduced to a minimum. Samples of the ingot underwent an industrial homogenization heat treatment and were then examined thoroughly with transmission electron microscopy. It was possible to confirm that dispersoid formation was successfully suppressed.

As a next step, samples of the model alloy were placed in a dilatometer, heated to 550°C , homogenized, deformed, and finally quenched. The degree of deformation, the rate of deformation, and the holding time after deformation were varied incrementally in a series of tests. The microstructure of the deformed samples was subsequently examined with electron backscatter diffraction. The resulting diffraction patterns translated into crystal orientations from which grain size and degree of recrystallization could be determined.

As expected, the degree of recrystallization increased with larger degrees of deformation, higher rates of deformation, and longer holding times. It took only a few seconds for the samples of the dispersoid-free model alloy to fully recrystallize. Similar experiments with comparable parameters under the presence of dispersoids showed significantly slower recrystallization rates.

With the help of the new dispersoid-free aluminium alloy it is now possible to accurately assess the impact of the Zener drag on the rate of recrystallization at different sets of parameters.

Acknowledgements

I hereby would like to thank everybody from the 'Vienna University of Technology' and the 'Austria Metall AG' (AMAG) who was involved in the course of this thesis, as well as my family and friends who helped me to fulfil my goal.

First of all, special thanks to my supervisor Thomas Weisz for guiding and supporting me throughout my thesis. Thank you to Prof. Ernst Kozeschnik and Dr. Ahmad Falahati for giving me the opportunity to conduct my research in this field.

I would like to thank 'Austria Metall AG' (AMAG) for the financial support and for providing the material used in the experimental procedures. Thank you to Thomas Ebner for the successful cooperation and Anna Kaiß for sharing her expertise on casting. In this context I am particularly grateful to the colleagues from the casting division who supported Thomas Weisz and me during alloying and casting of the ingots.

My special thanks go to Edith Asiemo and Christian Zaruba from the metallurgical laboratory. Without their patient assistance and experience I would not have been able to prepare and examine my metallurgical samples. Furthermore, thank you to Daniel Sparben for his advice on preparation techniques as he was confronted with similar obstacles while working on his own thesis.

I greatly appreciate the work of the 'drei Ofenburschen' for setting up and calibrating the furnace. I would like to say thank you to Kurt Caloun for helping me to assemble a durable thermocouple that was used in my heat treating experiments. I would also like to express my gratitude to Heinz Kaminski and Stefan Zellhofer who briefed me on working with the dilatometer and supplied me with the equipment needed for my compression tests.

Further, I would like to express my gratitude to the colleagues from the 'University Centre for Transmission Electron Microscopy' (USTEM), to Jakob Gruber for showing me how to prepare TEM samples, to Sabine Schwarz for helping me with the electrolysis and the conduction of the TEM analysis, and to Johannes Bernardi for stepping in when problems arose. At this point, I also want to thank Thomasz Wojcik for his support during my TEM examinations.

Finally, I wish to thank friends and family for proofreading my thesis, for their insightful feedback, and for supporting me beyond the work on my thesis.

Table of Contents

1	Introduction.....	1
2	Objectives.....	2
3	State of the Art.....	3
3.1	Alloying Elements	3
3.1.1	Classification of Aluminium Alloys.....	3
3.1.2	The 6xxx Series and 6061.....	4
3.1.3	Solubility of Alloying Elements in Aluminium.....	5
3.1.4	Phases in 6061.....	7
3.1.4.1	β -Mg ₂ Si.....	9
3.1.4.2	Q-Phase.....	12
3.1.4.3	Fe-Containing Primary Phases	13
3.1.4.4	Dispersoids.....	14
3.2	The Deformed State.....	16
3.3	Annealing after Deformation	17
3.3.1	Recovery.....	19
3.3.2	Recrystallization.....	20
3.3.3	Grain Growth.....	23
3.3.4	Effects of Alloying Elements on Annealing.....	24
3.3.4.1	Effects of Solutes.....	24
3.3.4.2	Effects of Dispersoids on Grain Boundary Mobility	25
3.3.4.3	Particle-Limited Grain Size	26
3.3.4.4	Particle Stimulated Nucleation.....	28
3.4	Dynamic Restoration	29
3.4.1	Dynamic Recovery	29
3.4.2	Dynamic Recrystallization.....	31
3.5	Measuring Recrystallization.....	32
4	Experimental.....	35
4.1	Casting.....	35
4.2	Heat Treatment.....	37

Table of Contents

4.3	Optical Microscopy and Scanning Electron Microscopy	40
4.4	Grain Size Analysis	41
4.5	Transmission Electron Microscopy	41
4.6	Compression Tests	42
4.7	Electron Backscatter Diffraction	45
5	Results	47
5.1	Casting	47
5.2	Homogenization	49
5.2.1	Optical Microscopy and Scanning Electron Microscopy	49
5.2.2	Transmission Electron Microscopy	54
5.2.3	Grain Size Analysis	57
5.3	Shortened Homogenization.....	60
5.4	Compression Tests	63
6	Discussion	73
6.1	Alloy Composition and Casting.....	73
6.2	Microstructure	74
6.3	Heat Treatment.....	75
6.4	Recrystallization	76
7	Summary and Conclusion.....	78
8	Symbols and Abbreviations.....	79
9	Bibliography.....	80
10	List of Figures	84
11	List of Tables	88
12	Appendix.....	i
12.1	Evaluation of Cast Samples	i
12.2	Evaluation of Heat-Treated Samples (Group A)	xii
12.3	Deformation Profiles.....	xxvi
12.4	Evaluation of Deformed Samples (Group B)	xxviii
12.5	Evaluation of Deformed Samples (Group C).....	xl

1 Introduction

The processing of aluminium is a complex task and numerous variables have to be considered to optimize the properties of the final material. The following thesis will focus on the microstructural alterations occurring in the course of hot deformation in Al-Mg-Si aluminium alloys.

The most important factors influencing the alloy during hot deformation are the alloy composition, the applied temperature profile, the deformation rate, and the degree of deformation. A vast amount of effects interact during processing and influence the mechanical properties of the alloy. Controlling recrystallization during and after deformation is especially important in this context. By adjusting the rate and fraction of recrystallization it is possible to tailor the strength and ductility according to specific requirements. When recrystallization advances too far, it results in a loss of strength. If recrystallization is suppressed entirely, the material becomes brittle. Instruments to regulate recrystallization are for example dispersoids.

Dispersoids are finely distributed particles consisting of alloying elements such as Fe, Cr, and Mn in the case of 6xxx series aluminium alloys. These particles influence the microstructure by pinning grain boundaries and dislocations. This effect is known as Zener drag. The result is a retarding force on recovery, recrystallization, and grain growth. [1], [2]

To produce high-quality aluminium parts through forming processes economically, it is vital to predict and calculate the extent of the Zener drag precisely. This is particularly important for recycled aluminium. Aluminium can be recycled repeatedly. However, unwanted elements can accumulate in the remelted material. Alloying elements such as Cu, Fe, Zn, or Si cannot be extracted economically [3]. Their contents can only be varied by systematically blending the melt with other scrap or fresh primary aluminium. Estimating the impact of the impurities accurately allows to minimize the usage of expensive primary material and guarantees the quality. Reducing the need for primary aluminium has the additional advantage of avoiding toxic waste and saving energy. The energy expenditure of 168,000MJ and the amount of two tonnes of hazardous red mud accruing for each tonne of primary aluminium can be reduced this way [3].

Considering the numerous applications of aluminium in the transport industry, the consumer industry, and in the construction industry, this research is of high significance.

2 Objectives

The objective of this thesis is to gain further understanding of recrystallization and the influence of the Zener drag in Al-Mg-Si alloys.

As a first step, a pure Al-Mg-Si model alloy based on 6061 has to be produced that is entirely devoid of any dispersoid formation during annealing. This model alloy will therefore be free of any effects caused by the Zener drag and will act as a reference material. All other characteristics of this model alloy and regular 6061 have to remain as similar as possible to minimize the influences of other factors.

In the following compression tests, the recrystallization will be asserted depending on the degree of deformation, the deformation rate, and the holding time at elevated temperatures after deformation. When comparing the recrystallization behaviour of the model alloy and regular 6061, the pinning pressure caused by the Zener drag can then be determined.

For the measurement of the recrystallization, a suitable method has to be selected and, if necessary, adapted to the characteristics of the model alloy.

3 State of the Art

The alloying elements and the thermo-mechanical treatment are crucial for the production of aluminium parts. The type of alloying elements, their amount, the applied forces during processing, and the heat treatments define the strength and quality of the final product. Therefore, it is necessary to understand the effects caused by the different factors and to identify interdependencies. To this day, various effects remain to be discovered and investigated further.

The first part of this chapter deals with alloying elements in the 6xxx series, their influence on the microstructure of the alloy, and their appearance in micrographs. The second part describes the effects of deformation and heat treatments on aluminium alloys with focus on recrystallization and its measurement.

3.1 Alloying Elements

Intentional alloying and impurities can alter the characteristics of metals significantly. Even minimal traces of alloying elements can have an impact. To tailor the properties of aluminium alloys according to specific needs, various alloying elements can be added. Widely in use are Cu, Mg, Mn, Si, and Zn. In special cases Ni, Ag, V, Zr, Sn, Pb, Bi, Co, and Li can be part of the alloys, too. Fe, Cr, and Ti often occur in aluminium alloys in small amounts as impurities or can be deliberately added. Ti, for instance, can aid grain refinement and is used to adjust the grain growth in the cast. [4], [5]

3.1.1 Classification of Aluminium Alloys

Aluminium alloys can be classified as wrought alloy or cast alloy depending on the intended application. Wrought alloys usually contain 1-2% of alloying elements and are characterized by their excellent workability. The properties of cast alloys are focused on castability, mould filling properties, melting temperature, and fluidity. These alloys have a significantly higher content of alloying elements in comparison to wrought alloys with about 10-12%. [5]

The next classification criteria are the used alloying elements. Aluminium with a purity of more than 99% forms the 1xxx series. Series 2xxx, for example, is a combination with

Cu and in some cases Mg. The complete alloy designation system for wrought alloys is summarized in Table 1.

Table 1: Alloy designation system for wrought alloys [6], [7]

Series	Major alloying elements	Heat-treatable
1xxx	Al \geq 99%	No
2xxx	Al-Cu-(Mg)	Yes
3xxx	Al-Mn	No
4xxx	Al-Si	No/Yes (e.g. 4032 is heat-treatable)
5xxx	Al-Mg	No
6xxx	Al-Mg-Si	Yes
7xxx	Al-Zn-(Mg)-(Cu)	Yes
8xxx	Al-(other elements)	No/Yes (e.g. 8090 is heat-treatable)

The alloying elements lead to solid solution strengthening and influence the properties of the material in several other ways. Heat-treatable alloys can be further hardened by precipitation hardening. Likewise, the same heat treatment can lead to a decrease in strength if the alloy is not heat-treatable. An additional strengthening by work-hardening is possible in both cases.

3.1.2 The 6xxx Series and 6061

The 6xxx series is the subject of this thesis with special focus on 6061. The main alloying elements of the 6xxx series are Si (up to 1.6wt%) and Mg (up to 1.5wt%). The exact composition of 6061 including further alloying elements according to the engineering standard “*ÖNORM EN 573-3:2013-12-01*” by the ‘Austrian Standards Institute’ is displayed in Table 2.

Due to its versatile properties and relatively low production costs, the 6xxx series is the most commonly used aluminium series and contributes to more than 50% of the global aluminium production. Among other applications, it is used for sheets and structural parts in the automotive industry and in architecture. Al-Mg-Si alloys can be hardened by artificial ageing and reach strengths of up to 310MPa. Further advantages of the 6xxx series is its good processibility and great corrosion resistance. [8]

Table 2: Composition of 6061 [9]

Alloying element	Percentage by weight
Silicon (Si)	0.4%-0.8%
Iron (Fe)	up to 0.7%
Copper (Cu)	0.15%-0.4%
Manganese (Mn)	up to 0.15%
Magnesium (Mg)	0.8%-1.2%
Chromium (Cr)	0.04%-0.35%
Zinc (Zn)	up to 0.25%
Titanium (Ti)	up to 0.15%
Other elements	no more than 0.05% each no more than 0.15% in total
Remainder Aluminium	95.85%-98.56

3.1.3 Solubility of Alloying Elements in Aluminium

None of the previously mentioned alloying elements are unrestrictedly soluble in aluminium in its solid state. Zn shows the highest solubility in Table 3 with more than 30wt%. Mg places second with up to 17.4wt% at 450°C. The solubility of Fe, Cr, Mn, and Ti is very limited and at low temperatures almost non-existent. The relevant elements for the 6xxx series are highlighted in Table 3 in contrast to several other elements occurring in different aluminium alloys.

When the host material forms a single homogenous phase with the impurities after solidification, it is called a solid solution. In the solid solution, solutes either act as substitutional or interstitial atoms as visualized in Figure 1.

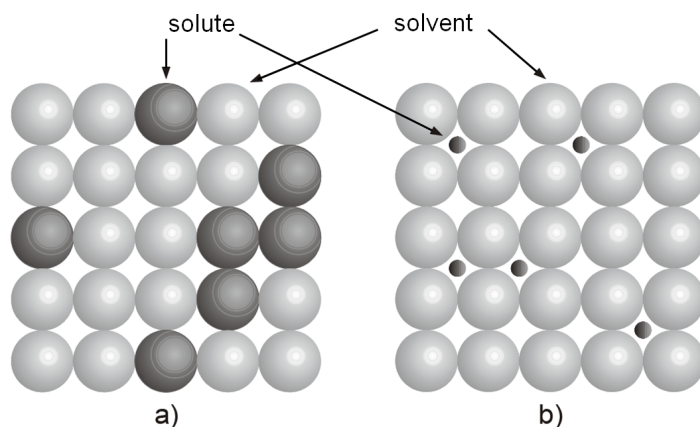


Figure 1: Schematic illustration of substitutional (a) and interstitial (b) alloying atoms [10]

Table 3: Solubility of alloying elements in aluminium solid solution [5]

Alloying Element	Temperature of the eutectic (T_e), peritectic (T_p), or monotectic (T_m)	Solubility (% by weight) at				
		T_e , T_p , or T_m	500°C	400°C	300°C	200°C
Be	645°C (T_e)	0.08	0.01	0.005		
Bi	657°C (T_m)	~0.05				
Cd	649°C (T_m)	~0.4	0.15	0.08	0.04	
Co	657°C (T_e)	<0.02				
Cr	661°C (T_p)	~0.8	0.4	0.35	0.1	
Cu	547°C (T_e)	5.7	4.4	1.6	0.6	0.2
Fe	655°C (T_e)	~0.04	0.005	<0.001		
Li	602°C (T_e)	4.7	2.8	2.0	1.5	1.0
Mg	450°C (T_e)	17.4	~12.0	12.2	6.6	3.5
Mn	657°C (T_e)	1.82	0.36	0.17	0.02	
Ni	640°C (T_e)	0.04	0.006			
Pb	658°C (T_m)	~0.17				
Sb	658°C (T_e)	<0.1				
Si	577°C (T_e)	1.65	0.8	0.3	0.07	0.01
Sn	228°C (T_e)	~0.06	~0.08			
Ti	665°C (T_p)	1.3	0.2			
V	661°C (T_p)	~0.37	<0.2			
Zn	275°C	31.6				14.5
Zr	661°C (T_p)	0.28		0.05		
Mg₂Si	595°C (T_e)	1.85	1.10	0.52	0.30	0.20

For solutes to be substitutional atoms, they have to meet the criteria according to the rules of Hume-Rothery [4]:

- The difference between the atomic radii $\Delta = (r_{solvent} - r_{solute})/r_{solvent}$ must be less than $\pm 15\%$.
- The crystal structure and electronegativity must be very similar.
- A metal has a tendency to dissolve another metal of a higher valency better than one of a lower valency. If the difference of the valencies is too high the solubility is limited.

For the solutes to be interstitial atoms, their size has to be significantly smaller than the host atoms' and the electronegativity of both needs to be similar. Interstitial atoms in

aluminium alloys do not play a major role considering that aluminium atoms already are very small in comparison to other metals. If the criteria for substitutional or interstitial alloying elements are not met, new phases are formed or the impurities and the host material form intermetallic compounds.

The solute atoms act as point defects and impose tensile ($r_{\text{solvent}} > r_{\text{solute}}$) or compressive ($r_{\text{solvent}} < r_{\text{solute}}$) strain on the surrounding lattice. Additionally, the solute atoms tend to accumulate around dislocations forming 'Cottrell Atmospheres' [10]. This restricts the movement of dislocations and thereby leads to a decrease in ductility and an increase in strength. This hardening mechanism is called solid solution strengthening and the contribution of the solutes to the overall strength can be calculated with the formula

$$\sigma_{ss} = \sum_j k_j C_j^{2/3} \quad (1)$$

where C_j is the concentration of the solute atoms, k_j the corresponding scaling factor, and j the number of different alloying elements [11], [12].

3.1.4 Phases in 6061

Since the solubility of the alloying elements at ambient temperature is very low, various phases can form during solidification, cooling, and heat treatment of the alloy. Phases formed immediately after solidification are called primary phases. Besides the solid solution α -Al, the commonly occurring primary phases are β -Mg₂Si, the Cu-containing Q-phase, and several Fe-containing ones including α -AlCrFeMnSi or β -AlFeSi. Secondary phases form during a subsequent heat treatment.

The temperature profile over time of a typical industrial process of hot-deformed aluminium is outlined in Figure 2. This thesis focuses on the first three steps: casting, homogenization, and deformation.

From its initial melted state, the alloy solidifies at the solidification temperature and is cooled down to room temperature. During solidification and cooling, primary phases form and grow. The as-cast state is still unfavourable for deformation and therefore a homogenization is added before hot deformation. The alloy is gradually heated up to the solution temperature over the course of several hours. In this time, microsegregations are reduced, β -Mg₂Si and Q dissolve, dispersoids form, and the brittle β -AlFeSi is transformed into favourable α -AlCrFeMnSi.

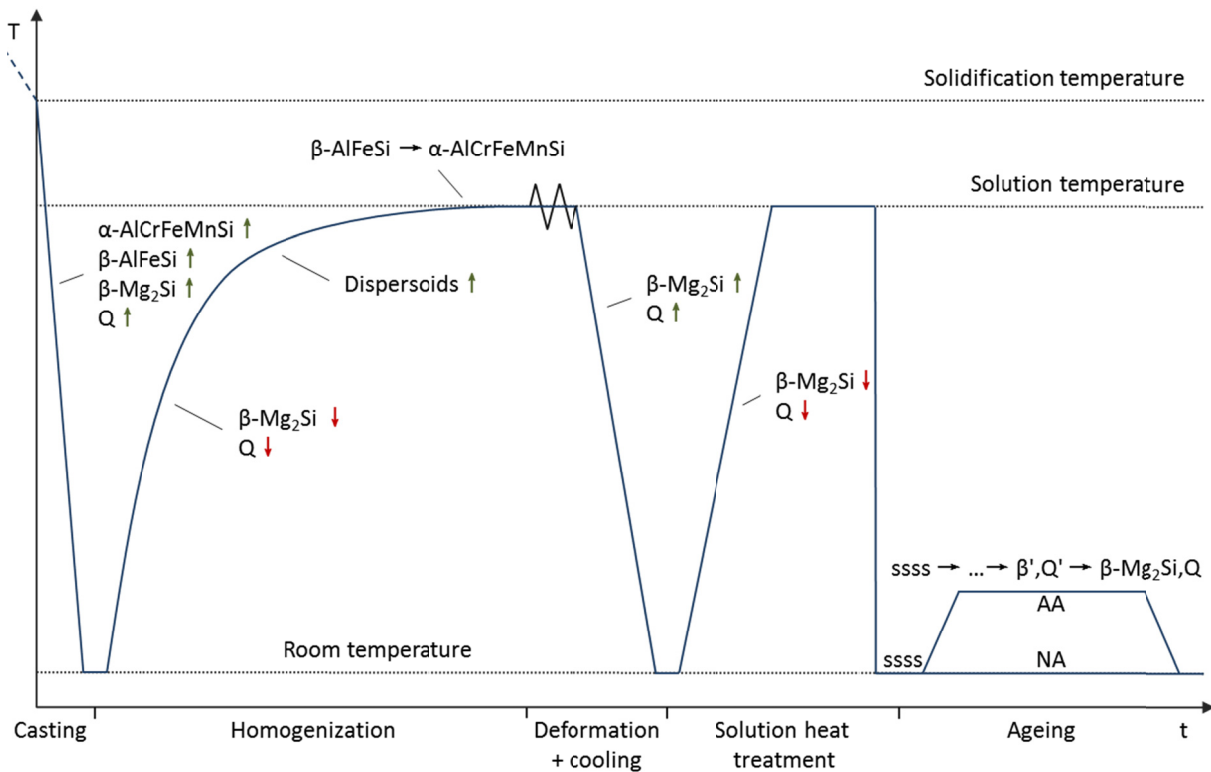


Figure 2: Temperature profile of industrial process for hot forming aluminium

The heat introduced during homogenization is directly used for hot deformation through which the material is deformed into the desired thickness. The temperature is then reduced to room temperature and several phases, such as $\beta\text{-Mg}_2\text{Si}$ and Q , precipitate again. At this point, the form shaping process is completed. However, the strength of 6061 and other age-hardenable alloys can be increased with a further heat treatment.

The process of age hardening is also known as precipitation hardening and consists of two steps: the solution heat treatment and ageing. The material is solutionized at around 550°C for approximately 30min to form a solid solution $\alpha\text{-Al}$. When quenching $\alpha\text{-Al}$ rapidly, all diffusion processes are suppressed and the equilibrium state of the material cannot be established. Instead, a supersaturated solid solution (ssss) with excess vacancies is formed. By quenching the material right after deformation, the solution heat treatment can be skipped. In practice, however, the two heat treatments are often performed separately.

The second part of the heat treatment usually takes place at approximately $100\text{-}200^\circ\text{C}$ for several hours. At this temperature level, the diffusion rate in the ssss increases and

the solutes start to precipitate as finely dispersed particles. These particles impede the movement of dislocations through the α -Al matrix and thus lead to a hardening of the material. The process of this second heat treatment is also referred to as artificial ageing (AA). Depending on alloy composition, ageing can already occur at room temperature. This effect is known as natural ageing (NA).

The precipitation sequences of β -Mg₂Si and Q are described in detail in the following chapters.

3.1.4.1 β -Mg₂Si

With a balanced Mg:Si mass ratio of 1.73:1 (equivalent to a molar ratio of 2:1), pure Al-Mg-Si acts as a binary alloying system with aluminium and Mg₂Si as components. Many industrial alloys have an excess of Si with a ratio of <1.73. The aluminium rich corner of this quasi-binary phase diagram is shown in Figure 3.

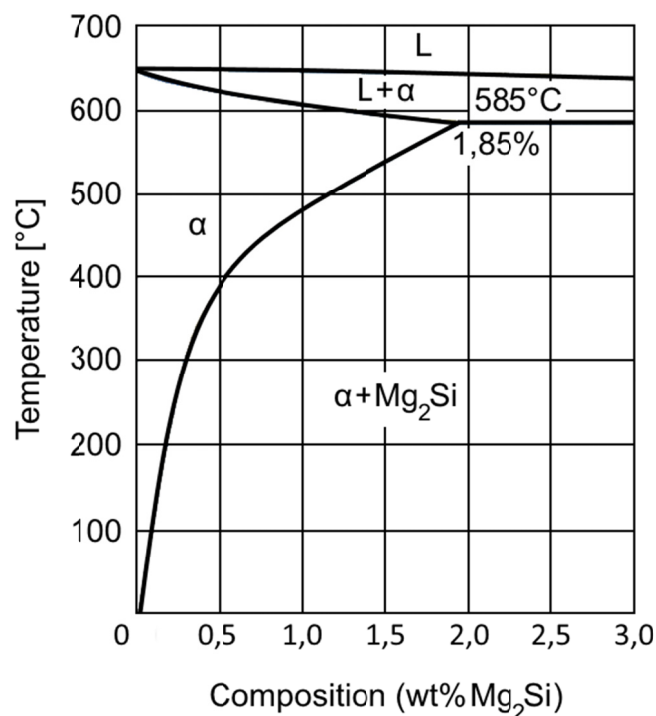
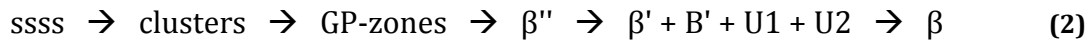


Figure 3: Al-Mg₂Si phase diagram [5]

In liquid state above 660°C, the alloy is fully soluble. Below the liquidus line, α -Al starts to crystallize and completely solidifies at the solidus line. With decreasing temperature,

β -Mg₂Si precipitates due to its limited solubility. The precipitation of Mg-Si is the main hardening mechanism of 6xxx series alloys, also known as age hardening.

The precipitation of β -Mg₂Si does not happen spontaneously, but is a complex and still controversial process. The widely accepted model for the precipitation sequence of β -Mg₂Si [13], [14] from a ssss is considered



After quenching from the solution temperature, the ssss is formed. When increasing the temperature for the ageing process, cluster of the alloying elements assemble out of the ssss. Initially, the clusters will be rich in Si as a result of the lower solubility of Si in α -Al (compare to Table 3). Over time, the Mg:Si ratio will increase and Mg-Si co-clusters will form. Subsequently, the clusters will transform into fully coherent GP-zones (GP-I) with varying Mg-Si contents depending on the initial alloying ratio. At the next stage, β'' (GP-II) forms fine semi-coherent needles with the dimension of $\sim 4 \times 4 \times 50 \text{ nm}$ along the directions of $\langle 100 \rangle_{\text{Al}}$. At this point, the hardness reaches its maximum. With the formation of the larger β' and B' with sizes of up to $1 \mu\text{m}$, the hardness diminishes [17]. Parallel to the hexagonal structures (β' , B') also trigonal and orthorhombic phases named U1 and U2 were described in the literature. If ageing is continued, the equilibrium phase β is formed out of the previous energetically unfavourable phases.

The nomenclature of the different phases varies throughout the literature. Matsuda et al. refer to the parallel phases of β' as type A (U1), type B (U2), and type C (B') [15]. Instead of GP-zones van Huis uses the terms initial- β'' and pre- β'' [16].

An overview of the composition, crystal structure, and morphology of the different steps of the precipitation sequence is given in Table 4.

The evolution from GP-Zones to B' phase during ageing is depicted in Figure 4. After 10min at 175°C rather fine precipitates are visible and first indications for β'' (arrowed) appear in b.) in the underaged microstructure. After 30min, more β'' manifests and grows until the maximum hardness is reached after 4h. Images e.) and f.) represent an already overaged microstructure. Especially with the occurrence of B' (arrowed) after 20h at 200°C, the reduction in hardness is significant.

Table 4: Phases observed during precipitation hardening of Al-Mg-Si alloys [13]

Phase	Composition	Crystal structure	Morphology*
GP (GP-I)	$Mg_xAl_{5-x}Si_6$	Primarily monoclinic	Ranging from 1 to 3nm spherical particles to needles of $\sim 2 \times 2 \times 20$ nm
β'' (GP-II)	Mg_5Si_6	Monoclinic	Needles of $\sim 4 \times 4 \times 50$ nm
β'	$Mg_{1.8}Si$	Hexagonal	Rods several hundred nanometres long, with ~ 10 nm diameter
U1 (type A)	$MgAl_2Si_2$	Trigonal	Needles several hundred nanometres long, with ~ 15 nm diameter
U2 (type B)	$MgAlSi$	Orthorhombic	Needles several hundred nanometres long, with ~ 15 nm diameter
B' (type C)	$MgSi_{>1}$	Hexagonal	Ribbons up to $1\mu m$ long
β	Mg_2Si	FCC (CaF ₂ type)	Plates or cubes, up to $10\text{--}20\mu m$ across

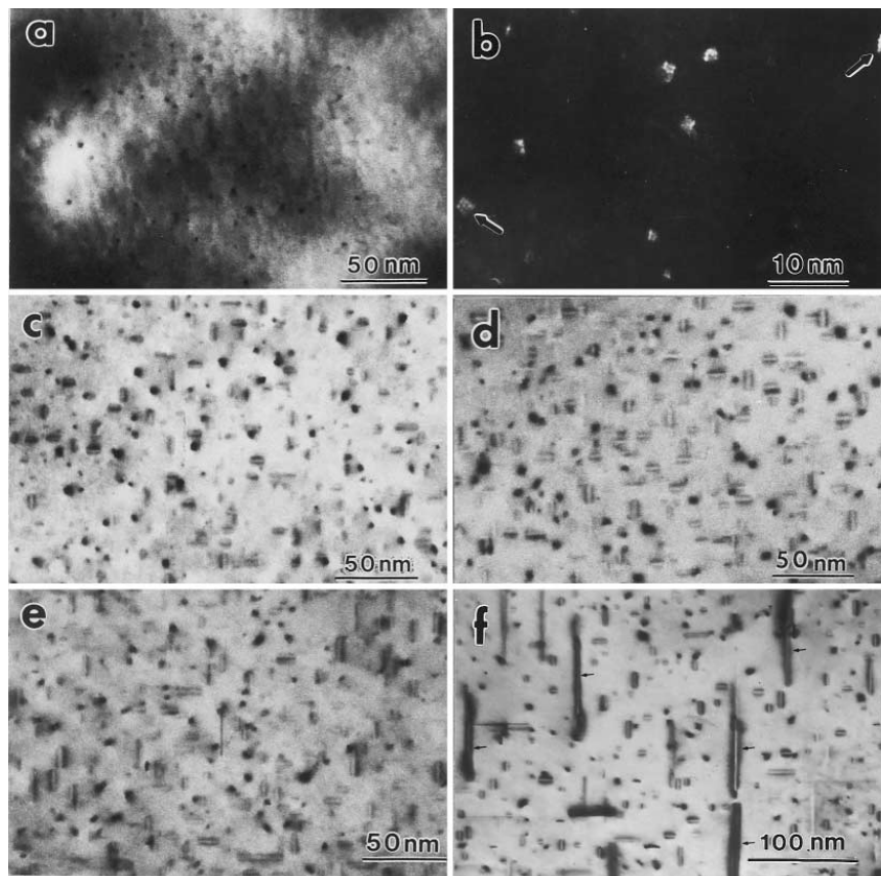


Figure 4: TEM micrographs of precipitate dispersions at different stages of artificial ageing. (a) and (b) 10mins at 175°C, (c) 0.5h at 175°C, (d) 4h at 175°C, (e) 72h at 175°C, (f) 20h at 200°C [17]

* The dimensions given are only a rough indication; the actual values will depend strongly on the composition of the starting alloy and the heat treatment applied.

3.1.4.2 Q-Phase

6061 can contain up to 0.4wt% of Cu and it is added to improve the ageing behaviour of the alloy. Already 0.24wt% Cu suffice to increase the strength level and reduce the rate of natural ageing by stabilizing the Mg-Si GP-zones and suppressing coarsening [18].

The Cu-containing equilibrium phase of the quaternary Al-Mg-Si-Cu system is known as Q-phase. The proposed crystal structure is a hexagonal lattice with the parameters $a=1.04\text{nm}$ and $c=0.405\text{nm}$ [19] and its morphology is needle shaped. The exact chemical composition remains uncertain. $\text{Al}_5\text{Cu}_2\text{Mg}_8\text{Si}_6$, $\text{Al}_4\text{Cu}_2\text{Mg}_8\text{Si}_7$, $\text{Al}_4\text{CuMg}_5\text{Si}_4$, and $\text{Al}_3\text{Cu}_2\text{Mg}_9\text{Si}_7$ are among those that have been reported so far [20]–[22]. The precipitation sequence in Al-Mg-Si-Cu is given by Zanderbergen et al. [23] as



β'' , β' , and β occur in the ternary Al-Mg-Si system as well and have been described previously (Chapter 3.1.4.1). Q' has a similar structure and chemical composition as Q. The precursors of Q' (S, L, C, QP, QC) are not fully investigated at this point and uncertainties about their properties prevail [23].

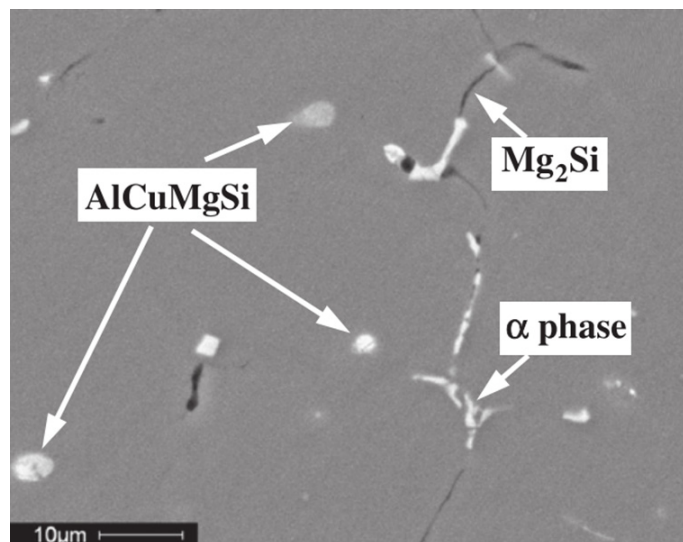


Figure 5: SEM micrograph of alloy with 0.74wt% Mg, 0.96wt% Si, 0.50wt% Cu, and 0.22wt% Fe [24]

Experiments performed by Miao and Laughlin [25] showed that the Cu content must reach a specific threshold before the Q-phase can form. At 0.07wt% Cu the equilibrium

phase only consists of β while at 0.91wt% Cu the Q-phase is detectable. With SEM and LOM, the Q-phase is visible as light circular structures as in Figure 5. The alloy in this micrograph has a Cu content of 0.5wt%. The dark objects were identified as Mg_2Si and the light, plate-like phase as α -AlCrFeMnSi.

3.1.4.3 Fe-Containing Primary Phases

Industrial-grade Al-Mg-Si alloys always contain traces of Fe and since the solubility of Fe in the Al-matrix is extremely low, Fe-containing phases are inevitable. In pure Al-Fe binary systems, the elements form Al_3Fe needles [5]. In 6061, Fe forms phases with Al, Cr, Mn, and Si. The role of Mg is negligible in this context for it is bound in Mg_2Si or in solid solution with α -Al. On the other hand, there is usually a surplus of Si in 6061 alloys and Si has a 35 times lower solubility in Al than Mg. For this reason, there is lots of free Si to interact with Al-Fe.

The predominant Fe-containing phases are β - Al_5FeSi (in some cases reported as β - $Al_9Fe_2Si_2$) and α - $Al_{12}Fe_3Si$ [26]. Depending on the alloying ratio, the Fe in the α -phase can be substituted with Mn or Cr forming a variation of α - $Al_{12-15}(Fe,Cr,Mn)_3Si_{1-2}$. β - $Al_9Fe_2Si_2$ has a monoclinic lattice, a plate-like appearance, and dimensions of up to $20 \times 1 \mu m$ [27]. In Figure 6, it is visible as light grey structures. The cubic α - $Al_{12}Fe_3Si$ has a noticeable 'Chinese script-like' morphology and appears a bit darker than the β -phase.

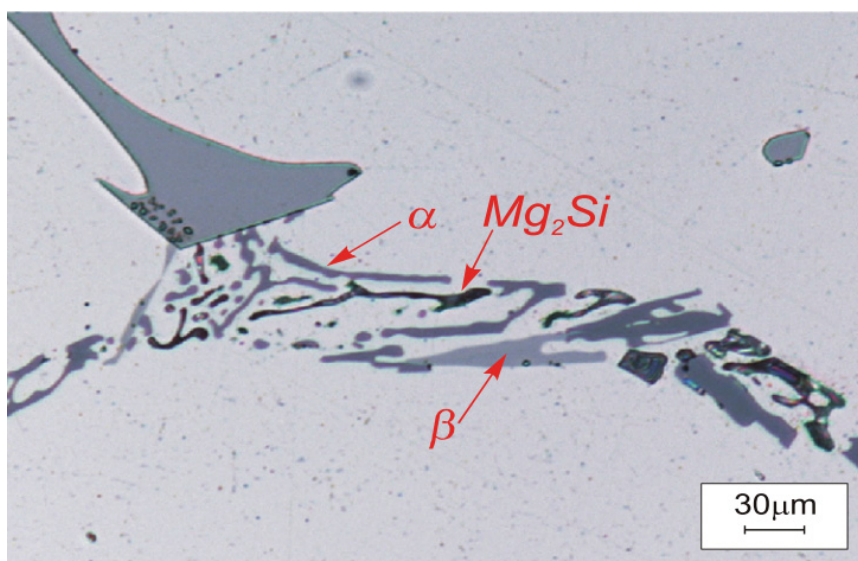


Figure 6: As-cast microstructure of AlSi1MgMn alloy [28]

However, distinguishing these two phases visually during microscopy can be difficult when they are side by side, due to their similar appearance. To be assured, the chemical composition and the crystal structure have to be determined.

During homogenization, β -Al₅FeSi can transform into globular α -Al₁₂(Fe,Mn)₃Si with a diameter of approximately 1 μ m. This process is shown in Figure 7. Through this transformation, the extrudability can be improved and the ductility of the final product is enhanced. [27], [29]–[31]

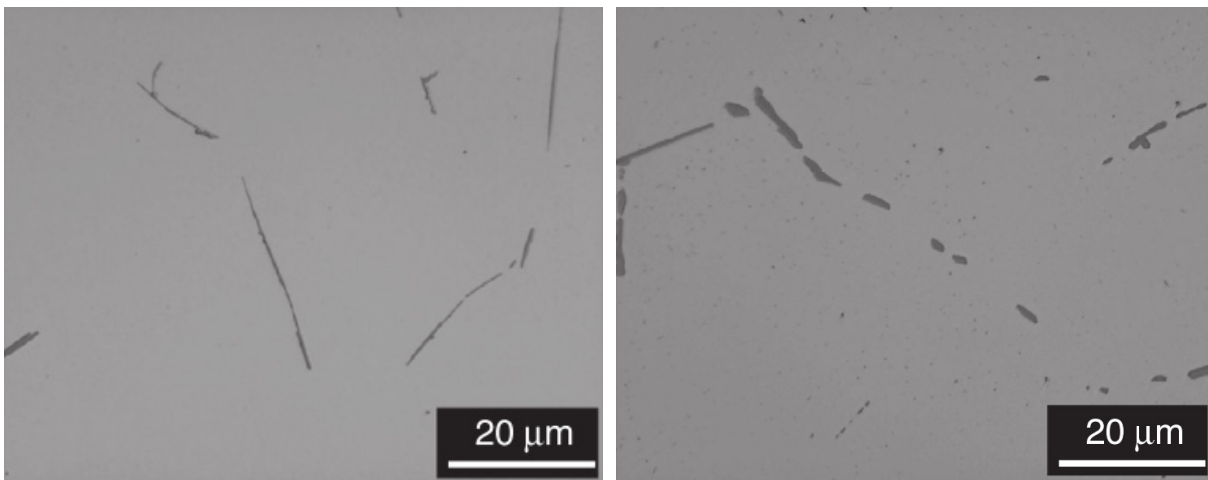


Figure 7: LOM micrographs; slightly homogenized for 20min at 540°C (left), fully homogenized for 32h at 590°C (right) [31]

Besides the already mentioned α -phases and β -phases, several other more uncommon Fe-rich phases have been observed: monoclinic β' , β^* , hexagonal α_h -Al₈Fe₂Si, rhombohedral α_R , c-centred orthorhombic α'' (q1), c-centred monoclinic α_T , monoclinic q_2 , and monoclinic α_v . [27]

3.1.4.4 Dispersoids

Dispersoids are secondary precipitates of the size of ~ 0.02 - 0.5μ m and are formed during homogenization. They are too large to contribute significantly to precipitation hardening as is the case for β'' . Nevertheless, dispersoids can have a substantial impact on the microstructure of the alloy. By impeding grain boundary movement, dispersoids can reduce grain growth and suppress recrystallization (Chapter 3.3.4.2). Additionally, an improvement in fracture toughness was observed in alloys containing dispersoids.

Dispersoids in 6061 are a variant of the phases $\alpha\text{-Al}_{12-15}(\text{Fe,Cr,Mn})_3\text{Si}_{1-2}$ or $\beta\text{-Al}_9\text{Fe}_2\text{Si}_2$ depending on the composition of the alloy. An example for their appearance is given in Figure 8. [7], [26]

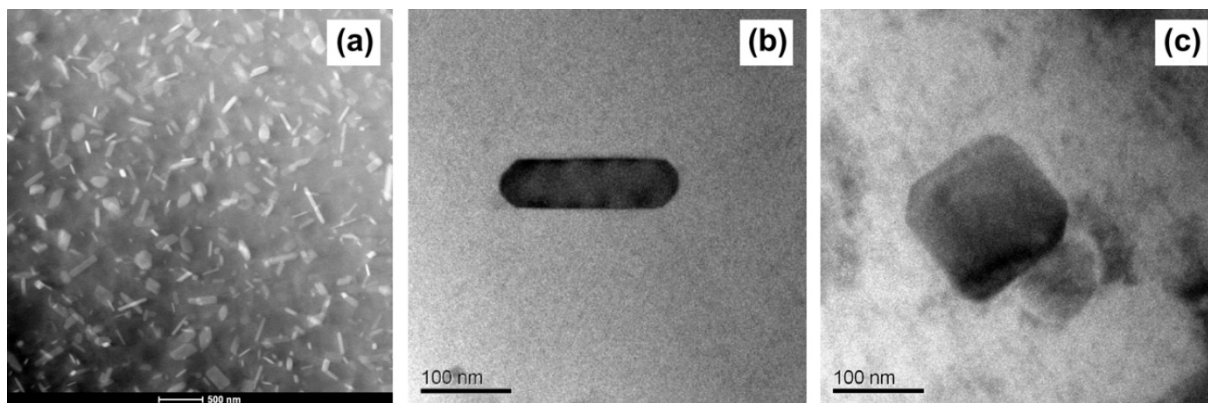


Figure 8: TEM micrographs of Mn dispersoids: (a) uniform distribution in the matrix, (b) and (c) rod and spherical shaped morphology of Mn dispersoids, respectively [24]

The size and distribution of the dispersoids strongly depend on the previous heat treatment and the alloy composition [32]. Experiments performed by Hichem et al. [33] showed that dispersoids precipitated aligned along $\langle 100 \rangle$ matrix directions. This matches the orientation of β' - Mg_2Si and related metastable phases. Apparently, β' - Mg_2Si acts as a nucleation site for dispersoids during the heating-up for homogenization. After the dissolution of Mg_2Si at homogenization temperature, only the dispersoids are left. If the temperature remains at an elevated level for an extended period, the dispersoids coarsen and lose their previous orientation [33], [34]. The orientation becomes more random as in image (a) in Figure 8. When the homogenization temperature is comparably low and the duration at this temperature is not too long, the dispersoids will be small and their number density will be relatively high [34].

Dispersoids have also proven to increase the quench sensitivity of alloys. If the quenching rate after high temperature heat treatments is too slow, coarse and non-hardening Mg-Si precipitates may nucleate at the dispersoids. This reduces the amount of Mg and Si in solid solution around the dispersoids and hence causes precipitation free zones during ageing. The resulting precipitation free zones decrease the strength and hardness of the age-hardened material. [34]

3.2 The Deformed State

Aside from the already mentioned strengthening mechanisms (solid solution strengthening in Chapter 3.1.3 and precipitation hardening in Chapter 3.1.4.1), another notable mechanism is the so-called strain hardening, also referred to as work hardening or cold working. By inducing dislocations through plastic deformation at low temperature (cold work), the hardness of the material and the stored energy is increased while the ductility is reduced.

Plastic deformation in aluminium is enabled through the diffusion of vacancies, movement along grain boundaries, and movement of dislocations along slip planes. The movement of dislocations contributes the largest part to the deformability [10]. Plastic deformation by twinning is not possible in aluminium [5]. The most densely packed planes usually act as slip planes for dislocations during deformation. In the case of aluminium those slip planes are $\{111\}$ and slip occurs along $\langle 110 \rangle$ directions [35].

Dislocations are one-dimensional crystallographic defects and occur frequently in the lattice. In an undeformed material, the dislocation density already reaches values of 10^2 - 10^3m^{-2} . Through plastic deformation, values of up to 10^8m^{-2} are achievable. New dislocations form under shear force at grain boundaries or when a moving dislocation is pinned by obstacles. Latter is called a Frank-Read-Source and is illustrated in Figure 9.

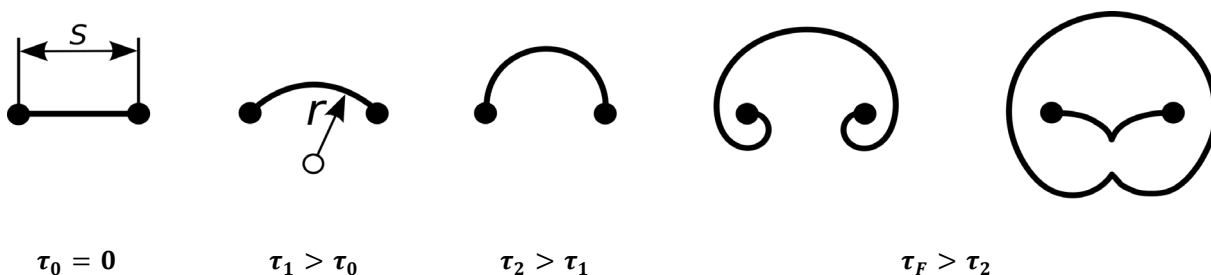


Figure 9: Pinned dislocation turns into Frank-Read-Source at $\tau = \tau_F$ [36]

When a dislocation encounters other immobile dislocations or precipitates, its movement is halted. If the shear stress increases, the dislocation will start to bulge. With further increasing stress, the dislocation then loops around the obstacle, becomes unstable and forms a new dislocation. This process can be iterated repeatedly leading to an increase in the total number of dislocations. [10], [36]

The shear stress τ_F that is necessary to create a new dislocation and to move past the obstacles can be described with the following equation:

$$\tau_F \approx \frac{Gb}{s} \quad (4)$$

In this equation G is the shear modulus, b the absolute value of the Burgers vector, and s the distance between the obstacles. With increasing dislocation density, the value of s decreases since immobile dislocations are the main obstacles. Hence, the required shear stress τ_F to continue slip increases if the dislocation density rises. The increasing numbers of dislocations constrain each other and lead to hardening of the material. [36]

3.3 Annealing after Deformation

As a result of plastic deformation of metal at low temperatures relative to its absolute melting point, the microstructure is altered, the stored energy is raised, and properties are changed. Deformed specimens exhibit an increased number of dislocations and deformed grains. Dislocations and distortion may also result from radiation or quenching, but this thesis focusses on the effects of cold work.

The dislocations and distortions lead to strain hardening with decreased ductility as described before and the grains oriented according to the direction of deformation cause anisotropic behaviour. Furthermore, properties such as corrosion resistance and electrical conductivity may also be influenced by the deformation [4].

These effects are not always desired during processing or in the final product. Workpieces may become too hard and brittle for any further processing steps. To reduce the effects of plastic deformation and to restore the properties prior to cold work, metal can be annealed at elevated temperatures. By raising the temperatures, thermally activated processes are initiated and solid state diffusion is enabled. The velocity of solid state diffusion v_d depends on the activation energy Q of the specimen and the absolute temperature T as in equation (5) [10]:

$$v_d = \frac{dn}{dt} = Ke^{-Q/RT} \quad (5)$$

In this context K is a constant, n the number of diffusion steps, and R the universal gas constant ($R=8.314\text{J/K}\cdot\text{mol}$). As a result of diffusion, the mobility of grain boundaries (M) can also be approximated with this Arrhenius type relationship [2]. The diffusion

processes and grain boundary movement are halted at absolute zero and subsequently rise with increasing temperature. When the temperature in deformed material is raised high enough, the following restoration processes as shown in Figure 10 are initiated.

- Recovery: Illustrated as dots, the dislocations in the deformed state (a) are rearranged in an energetically favourable way (b).
- Recrystallization: New crystals nucleate (c), grow, and replace the previous microstructure (d).
- Grain growth: Grain boundaries expand and devour smaller grains (e). In some circumstances a few grains may exhibit abnormal grain growth and enlarge disproportionately (f).

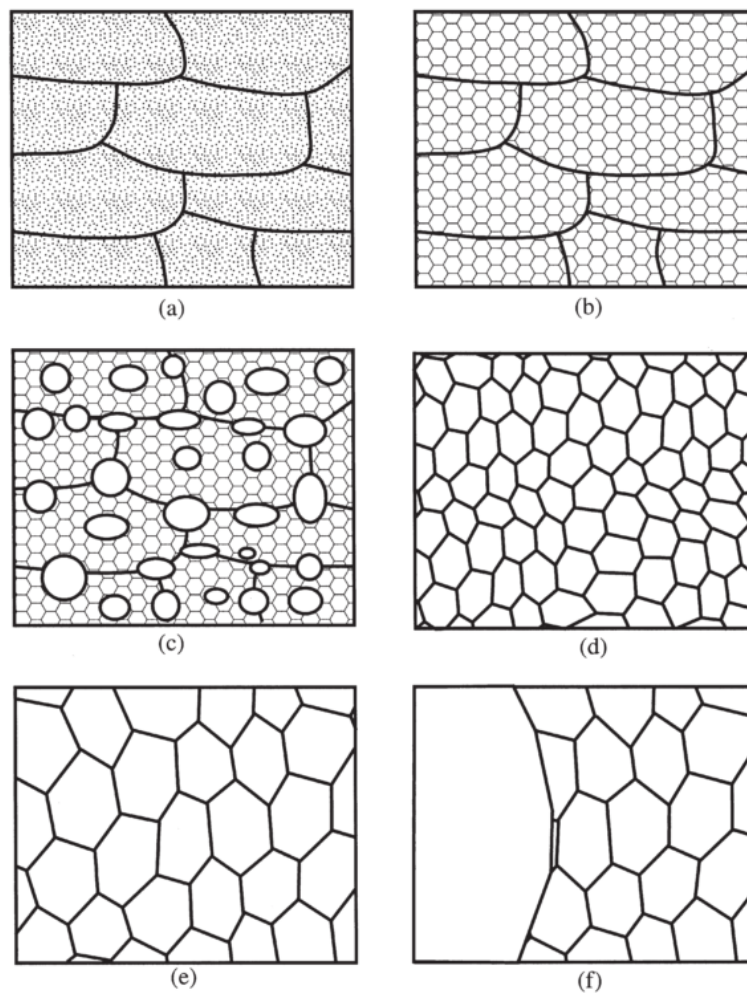


Figure 10: Schematic illustration of the main annealing processes: (a) deformed state, (b) recovered, (c) partially recrystallized, (d) fully recrystallized, (e) grain growth, and (f) abnormal grain growth [2]

The restoration sequence depends on the initial state of deformation, the annealing temperature, and the duration at annealing temperature. However, the borderlines between the single effects can be blurred and they can happen as continuous or discontinuous processes [2]. In most alloys these processes only advance at a very slow pace at ambient temperatures and are accelerated if more energy is induced. For these reasons, the mechanisms of strain hardening through plastic deformation do not apply to hot working. Hot working is performed at significantly higher temperatures at which deformation and recovery/recrystallization happen simultaneously. For this case, the hardening effects are immediately countered by recovery and recrystallization.

3.3.1 Recovery

Recovery is an annealing process where properties prior to cold work are partly regained without affecting high angle boundaries of the deformed grains. The in optical microscopy observable microstructure remains the same. Nevertheless, changes on a small scale are measurable. Strains are reduced and parts of the stored energy released. This leads to a slight decrease in strength and an increase in ductility. The main process during recovery is the rearrangement of dislocations. [10], [36]

With the help of thermally activated slip, dislocations rearrange into a lower energy configuration. If two complementary dislocations on the same plane collide, they neutralize each other. The remaining dislocations arrange by glide, climb, and cross-slip into regular formations or low angle boundaries. This way, distorted grains form a series of subgrains of lower distortion. An example for this rearrangement in a bent crystal is called polygonization and is shown in Figure 11. As recovery continues, fewer boundaries of higher misorientation form [10].

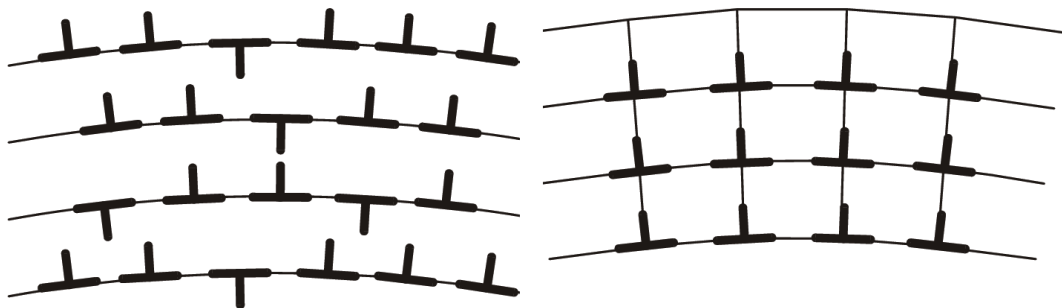


Figure 11: Arrangement of dislocations after deformation (left) and after recovery (right) - polygonization [10]

Another effect during recovery is the dissipation of excess concentrations within grains and the reduction of vacancies [10]. Interstitial atoms diffuse towards vacancies leading to a decrease of the strains. Furthermore, vacancies and precipitates accumulate at the grain boundaries in an attempt to minimize the stored energy.

3.3.2 Recrystallization

Through primary recrystallization, a completely new set of undeformed and equiaxed grains is formed. Internal strains dissolve and the stored energy is depleted. This way, the effects of strain hardening are reversed and the strength of the material is reduced significantly while ductility is increased. The conditions for the initiation of recrystallization are temperatures above a critical value as well as a certain degree of deformation.

While recovery already occurs at lower temperatures, recrystallization requires sufficiently high annealing temperatures. This required temperature is called recrystallization temperature T_R . For pure metals it is usually about 0.4-0.5 times the melting temperature T_M in Kelvin. Deformation processes at temperatures lower than T_R are defined as cold working, above T_R as hot working. T_R depends on various factors and has to be individually determined for each case of deformation. In pure aluminium, recrystallization already initiates between 80°C [4] and 150°C [37]. In the case of alloys, T_R can be significantly higher and can reach up to $0.7 \times T_M$ [4]. The higher the annealing temperatures are, the faster recrystallization occurs. Extending the annealing time leads to a lowered T_R [36].

The minimum for the required degree of deformation usually lies between 2% and 15% depending on the alloy's composition and its processing history [5]. The deformation increases the amount of stored energy and hence enhances recrystallization. A higher degree of deformation results in a greater recrystallized fraction [38] and in a lower T_R . If temperatures during deformation are elevated, it can lead to an increased T_R since recovery might already have reduced the amount of stored energy.

Nucleation points for the new grains are the regions with the highest level of stored energy. Therefore, mainly grain boundaries act as nucleation sites. A smaller initial grain size leads to a larger amount of nucleation sites, and therefore reduces T_R and accelerates recrystallization. However, the nucleation of new grains can also be observed within highly deformed grains. [2]

The nucleated grains with the radius R are still small and approximately spherical. Due to the curvature of the grain boundary with the specific energy (γ), a negative pressure (P_C) opposed to grain growth occurs in very small grains. According to Humphreys [2], this pressure can be approximated as

$$P_C = \frac{2\gamma}{R} \quad (6)$$

To overcome P_C , a driving pressure of $P_D > P_C$ is necessary. P_D results from the dislocation density ρ and is equal to the stored energy. α is a constant in the range of 0.5.

$$P = P_D - P_C = \alpha\rho Gb^2 - \frac{2\gamma}{R} \quad (7)$$

The final velocity of the grain boundaries is its mobility M multiplied with P . M can be described with a similar equation to the diffusion velocity v_d in equation (5).

$$v = MP \quad (8)$$

The newly formed grains grow by the movement of their grain boundaries with the velocity v as annealing continues. Deformed grains are consumed and replaced by new strain-free ones. When the recrystallized fraction increases, the new boundaries collide and grain growth is slowed. Overall, the recrystallization process can be described with a sigmoidal form as in Figure 12.

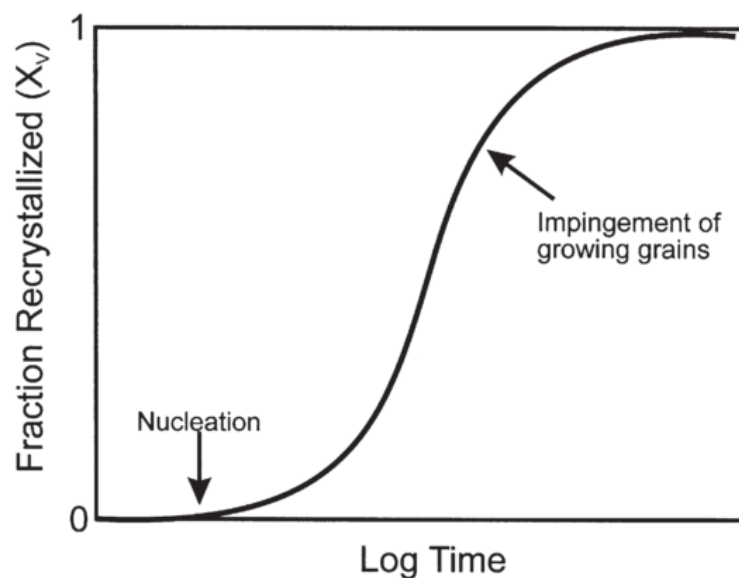


Figure 12: Typical recrystallization kinetics during isothermal annealing [2]

Figure 13 shows the grain size as a function of temperature and degree of cold work after a constant annealing time. At small amounts of deformation, the annealing temperature has a great impact on grain size, whereas the grain size remains on similar levels for higher deformation. When the annealing temperature and the degree of deformation are very high, abnormal grain growth, also referred to as secondary recrystallization, occurs.

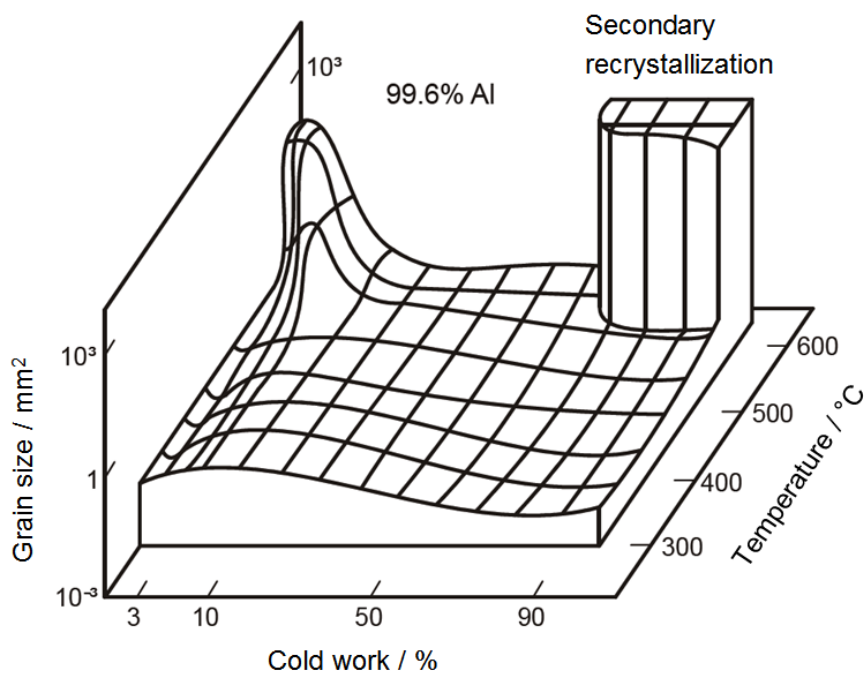


Figure 13: Recrystallization diagram for 99.6wt% aluminium [10]

Recrystallization is of special interest for aluminium since it is the only way to reduce the grain size of the material without melting it. In metals such as Fe, Sn, or Co, the grains can be refined by allotropic transformation. The higher the deformation prior to recrystallization, the smaller is the resulting grain size. By reducing the grain size, the number of grain boundaries increases and impedes dislocation movement. This strengthening mechanism is called grain boundary strengthening. The advantage of grain boundary strengthening is that, in addition to the increase in strength, the ductility of the material can be conserved. However, this mechanism is not suited for high temperature applications because the vulnerability to creep increases as well. More grain boundaries mean a higher amount of stored energy which increases the probability of recovery and lowers T_R .

The line between recovery and recrystallization is often blurred since recovery always takes part during recrystallization and both processes feed of stored energy [2].

3.3.3 Grain Growth

Even after full recrystallization, the material is not yet in an equilibrium state. A certain amount of stored energy in the form of high angle grain boundaries remains. The driving force for grain growth originates from the curvature of the single grain as described previously in the corresponding equation (6). Therefore, crystalline material tends to reduce the curvature of its grains and to minimize the boundary surface. The state of minimum energy would be a regular shape with 120° angles and plane sides that can fill space. In a two-dimensional array, this would result in a hexagonal structure. However, there is no regular polyhedron that could fulfil these criteria in a three-dimensional structure and hence grain growth is unavoidable. The grain growth kinetics can then be approximated with the parabolic growth law by Burke and Turnbull [2]:

$$\bar{R} = c_2 t^{1/n} \quad (9)$$

\bar{R} is the mean radius of the grain, c_2 a constant (influenced by the parameters γ_b and α), and n the grain growth exponent. In the case of aluminium, the grain growth exponent is equal to 4.

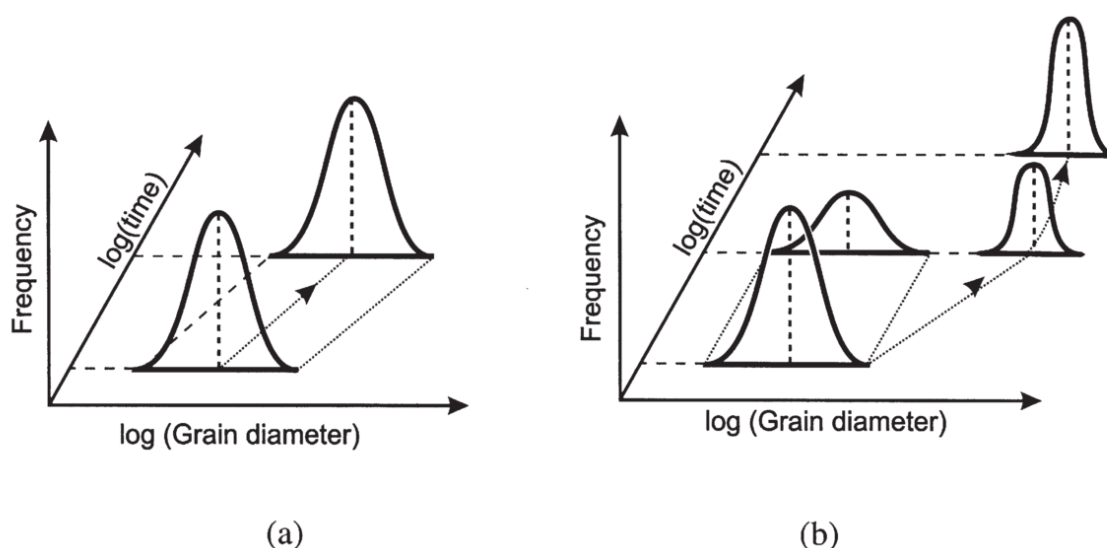


Figure 14: Schematic representation of the change in grain size distribution during (a) normal grain growth and (b) abnormal grain growth [2]

In an ideal material, abnormal grain growth cannot occur. Though under specific circumstances, individual grains can have growth advantages over the others and grow disproportionally. Second-phase particles, specimen dimensions (e.g. in thin foils), and crystal texture can promote abnormal grain growth. Especially at high temperatures and for initial high deformation, as seen in Figure 13, the continuous grain growth can give way to abnormal grain growth. A comparison of the different grain growth mechanisms over time is illustrated Figure 14.

Prior recrystallization is not a necessity for grain growth to occur. High temperatures for an extended period can be sufficient to activate grain growth.

3.3.4 Effects of Alloying Elements on Annealing

Alloying elements that are omnipresent in every industrial-grade metal have substantial influence on the annealing processes. In the form of solutes or separate phases, they retard the movement of grain boundaries and dislocations. Recovery, recrystallization, and grain growth can be slowed or even entirely suppressed. The following equations are mainly based on the book "*Recrystallization and Related Annealing Phenomena*" by Humphreys and Hatherly [2], backed up with observations described in various journal articles.

3.3.4.1 Effects of Solutes

Even marginal concentrations of solutes affect the mobility of grain boundaries significantly. Since impurities are always present in metals, it is very difficult to assess the mobility in actual pure aluminium without the influence of any solutes. Humphreys [2] described experiments where the effects of solute concentrations were investigated. At low solute concentrations, a further increased fraction of solutes has only a minor effect on the mobility. At higher solute concentrations, the mobility is inversely proportional to the concentration level.

The retarding pressure on grain boundaries induced by solutes is called solute drag P_{sol} . When considering solute drag in the equation of the velocity of the grain boundary, equation (8) is extended to

$$v = MP = M(P_D - P_C - P_{Sol}) \quad (10)$$

Experiments conducted by Huang and Humphreys [39] with different alloying elements showed that the mobility of the grain boundaries mainly depend on the solute concentration and annealing temperature. The type of solute showed only little effect.

3.3.4.2 Effects of Dispersoids on Grain Boundary Mobility

Dispersoids impede the grain boundary movement even further [22]. This effect is referred to as Zener drag (P_Z) named after Clarence Zener for his contributions to this subject. Considering the driving pressure, curvature, solute drag, and Zener drag combined [40], the grain boundary velocity results in the following equation:

$$v = MP = M(P_D - P_C - P_{Sol} - P_Z) = M(\alpha\rho Gb^2 - \frac{2\gamma}{R} - P_{Sol} - P_Z) \quad (11)$$

In the simplified case of a single non-deforming, incoherent, spherical particle, the exerted force (F_S) is described below and reaches its maximum for $\beta=45^\circ$ as shown in Figure 15.

$$F_s = 2\pi r\gamma \cos\beta \sin\beta \quad F_s(45^\circ) = \pi r\gamma \quad (12)$$

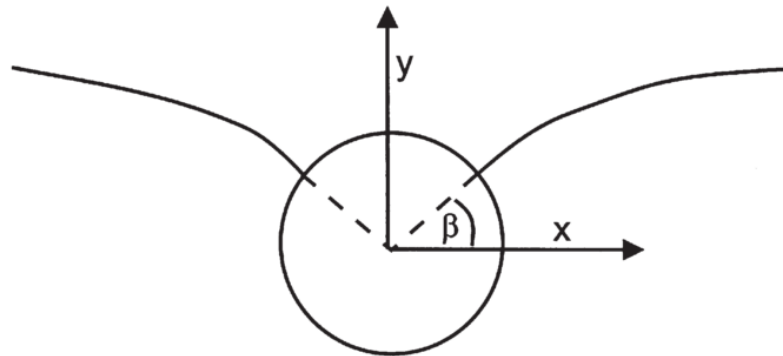


Figure 15: The interaction between a grain boundary and a spherical particle [2]

If a grain boundary intersects with a coherent particle, the required force to pass the boundary is even higher. It has been shown that the pinning effectivity of coherent particles (F_C) is twice as high as it is for incoherent particles [2].

$$F_C = 2F_s = 2\pi r\gamma \quad (13)$$

For other than spherical shapes, a correcting factor is necessary. In this case, the angle of the boundary plane towards the particle has to be considered, too. However, the shape of the particle will not be discussed any further at this point.

The total number of particles interacting with a rigid planar boundary (N_S) is the total number of particles (N_V) within distance of the radius of one particle (r) to both sides of the boundary. If the volume fraction (F_V) of the particles is given, the resulting N_S is

$$N_S = 2rN_V = \frac{3F_V}{2\pi r^2} \quad (14)$$

The resulting Zener pinning pressure of randomly distributed incoherent particles is N_S multiplied with the exerted force of each particle:

$$P_Z = N_S F_S = \frac{3F_V \gamma}{2r} \quad (15)$$

For a number of different dispersoids with the volume fractions F_{Vi} and the radii r_i , the equation is adapted as in equation (16). [41]

$$P_{Zn} = \frac{3\gamma}{2} \sum_{i=1}^n \frac{F_{Vi}}{r_i} \quad (16)$$

Deformable particles reduce the effect of Zener pinning. Considering flexible boundaries, more elaborate calculations are necessary. Nevertheless, they lead to similar results as for rigid planar boundaries. If the particle distribution is not random but forms a regular array, the equation for P_Z has to be adapted accordingly.

Pinning reveals to be most effective for cases when particle spacing is equal to the grain size. Larger and smaller particle spacing reduces the pinning pressure. [2]

The final boundary mobility during annealing treatments derived from the previous equations can be hence summarized as

$$v = MP = M\left(\alpha\rho Gb^2 - \frac{2\gamma}{R} - P_{Sol} - \frac{3F_V\gamma}{2r}\right) \quad (17)$$

3.3.4.3 Particle-Limited Grain Size

Through the pinning pressure caused by the dispersoids (P_Z), grain growth is limited. The main driving pressure for grain growth is the curvature (P_c) of the grains. When the

grain size increases, the driving pressure for grain growth diminishes and at some point $P_c = P_z$ will be reached:

$$P_c = P_z = \frac{\alpha\gamma}{R} = \frac{3F_V\gamma}{2r} \quad (18)$$

R is the radius of the grain size, γ the specific energy, α a small geometrical constant, and the last term is the Zener drag as described in the previous chapter. The resulting limiting grain diameter generated from the pinning pressure is therefore equal to

$$D_z = \frac{4\alpha r}{3F_V} \quad (19)$$

This equation is valid for $F_V < 0.05$. At higher volume fractions other effects arise. This general assumption has since been refined further. [2]

The ratio of dispersoid volume fraction to their diameter (F_V/d) also influences the stability of the grain sizes produced during recrystallization as displayed in Figure 16. In specimens with no dispersoids or large precipitates, normal grain growth is predominant. At medium dispersoid levels, grain growth only occurs to a specific extent and at temperatures above approximately 300°C abnormal grain growth takes place [42]. A further increase in dispersoid concentrations inhibits grain growth entirely.

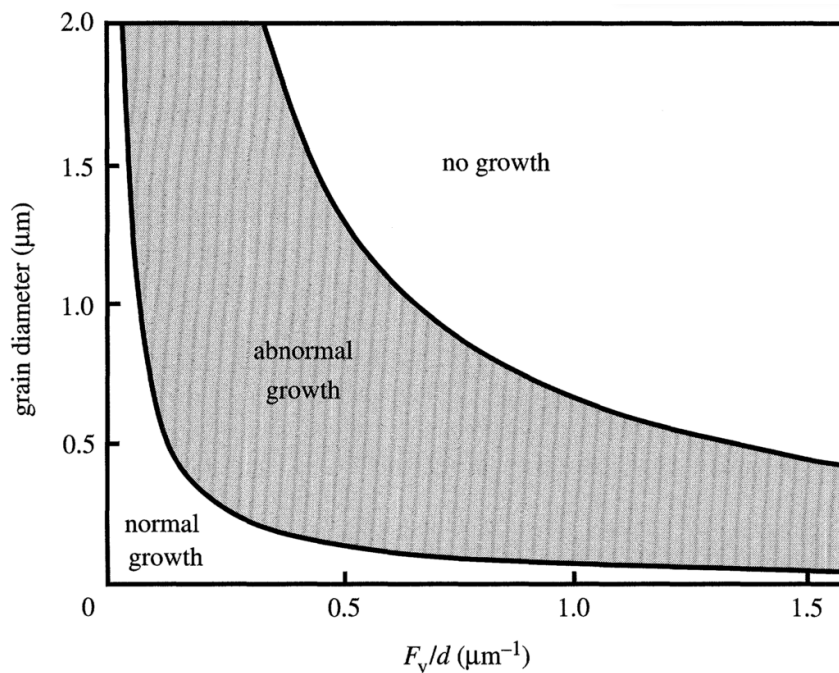


Figure 16: Regimes of normal and abnormal grain growth for particle-containing alloys [42]

3.3.4.4 Particle Stimulated Nucleation

Dispersoids (<1µm) pin grain boundaries and block grain boundary movements during recrystallization. However, for particles larger than 1µm an opposing effect can be observed. Such particles act as nucleation sites for recrystallized grains and promote recrystallization. This effect is known as particle stimulated nucleation (PSN). Through PSN, it is possible to systematically tailor grain size and recrystallization texture to the particular needs. [2], [22], [43], [44]

Particles cause a deformation zone around them where recrystallization is enhanced. Further growth of the grain around the particle may be halted when the end of the deformation zone is reached. When each large particle leads to the nucleation of one new grain, the resulting particle size is

$$D_N \approx dF_V^{1/3} \tag{20}$$

A small fraction of large particles leads to a larger grain size, whereas a greater amount of smaller particles results in small grains. If particles are too small or too close to each other, recrystallization can be prevented altogether. Small particles cause pinning effects and nearby particles block the nucleations. The corresponding diagram is shown below.

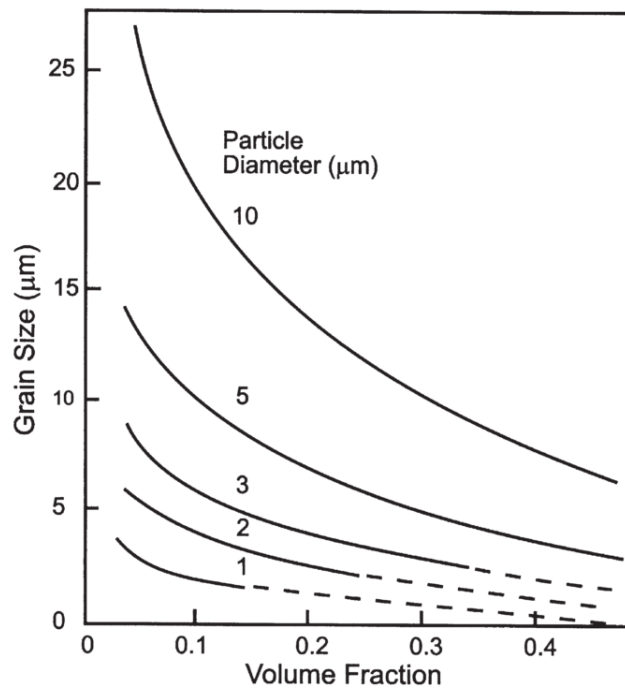


Figure 17: The predicted grain size for a PSN efficiency of unity. The dashed lines show conditions under which Zener pinning effects may prevent discontinuous recrystallization [2]

The combined effect of PSN and Zener drag on recrystallized grain size is shown in Figure 18. For particle dispersion levels of $F_V/r < A$, particle limited grain size determines the final size of the grains. On the other hand, D_N is the limiting factor for $F_V/r > A$. The minimum stable grain size lies at point A. In the case of $F_V/r > B$, the structure remains stable and recrystallization is suppressed entirely.

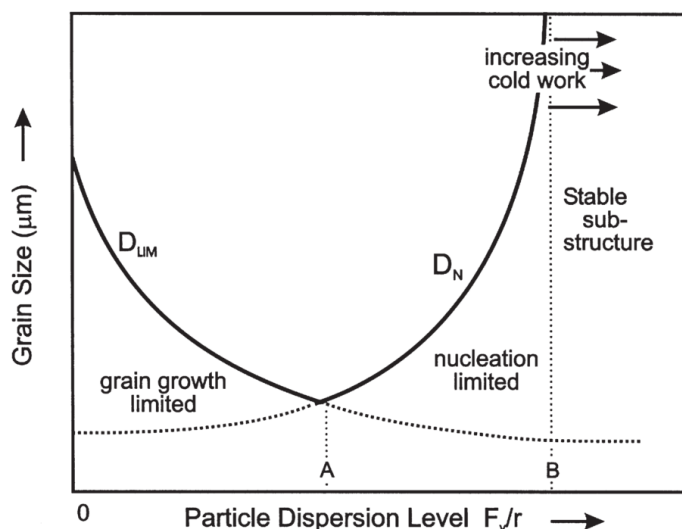


Figure 18: The effect of the particle parameters on the recrystallized grain size [2]

3.4 Dynamic Restoration

During metal working procedures such as hot rolling, extruding, or forging, deformation occurs at high temperatures above T_R . As a result, restoring effects already occur simultaneously to deformation. To distinguish the restoration processes in cold-worked metal with subsequent annealing and the restoration processes during hot working procedures, former is referred to as static recovery/recrystallization, latter as dynamic recovery/recrystallization. Dynamic restoration processes are of high technical importance as they enable high deformation with relatively low pressure. However, they are not yet understood to their full extend. [2]

3.4.1 Dynamic Recovery

A characteristic stress-strain curve for metal during hot working influenced by the effects of dynamic recovery is shown in Figure 19. At first, the level of stress rises with

increasing strain. Once ϵ_m is reached, stress will remain at a plateau even when strain is further increased. To this point, the dislocation density builds up to a critical value where recovery initiates. Increases in dislocation density are immediately compensated by dynamic recovery. Only the grains elongation proceeds and deformation bands are formed [45].

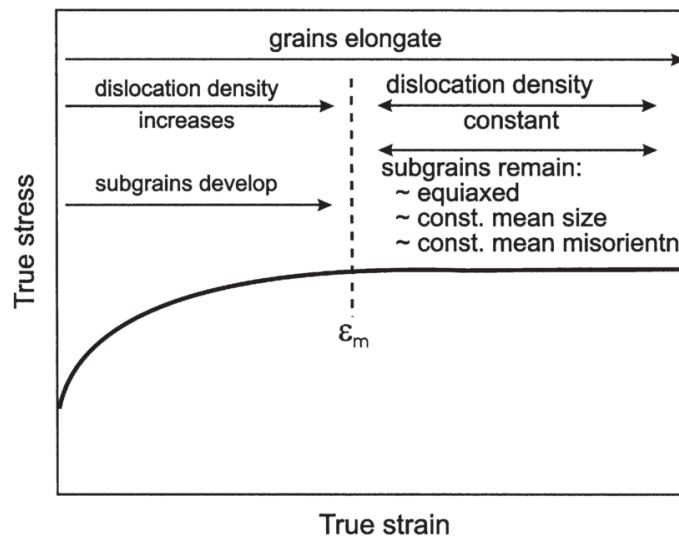


Figure 19: Summary of the microstructural changes which occur during dynamic recovery [2]

In metals of high stacking fault energy such as aluminium, dynamic recovery occurs very fast by dislocation climb and cross-slip. Hence, it is usually the only dynamic restoration process in aluminium during hot working. The amount of stored energy is already consumed by dynamic recovery before dynamic recrystallization can occur. [2]

In the process of producing fine-grained microstructures, dynamic recovery can be obstructive. High dislocation density and consequently a high amount of stored energy are required to provide as many nucleation sources as possible and sufficient driving force for recrystallization. However, dynamic recovery releases large amounts of the stored energy already during deformation. Therefore, the number of nucleation sources is reduced and coarser grains are formed. Even at ambient temperatures, dynamic recovery in deformed aluminium is extensive. An approach to suppress dynamic recovery during rolling is cryorolling. The slabs machined by cryorolling are cooled with liquid nitrogen. Hence, dynamic recovery is suppressed and a microstructure with ultrafine grains can be achieved. [46], [47]

3.4.2 Dynamic Recrystallization

In metals of low stacking fault energy (e.g. Cu, Ni, and austenitic Fe), dynamic recrystallization is more likely since recovery processes are significantly slower. There is enough time left to build up the necessary amount of stored energy. The new grains of the recrystallized microstructure nucleate along the initial high angle grain boundaries and further induced dislocations decelerate grain growth and growth halts. [2]

Figure 20 illustrates a typical stress-strain curve for dynamic recrystallization at different temperatures. The curves display a noticeable peak before levelling out. Higher temperatures require less stored energy and hence less stress before recrystallization occurs. Additionally, the curves for higher temperatures have a lower relative peak and continue more restive.

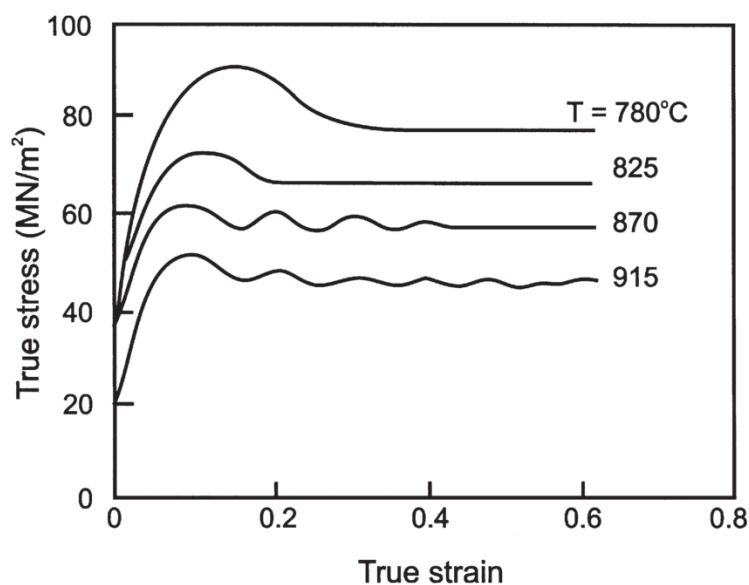


Figure 20: The effect of temperature on the stress-strain curves for 0.68wt% C steel, deformed in axisymmetric compression [2]

During deformation with dynamic recrystallization, grain size remains almost constant and is only influenced by the initial grain size to a small extent. Nevertheless, a small initial grain size can increase the kinetics of dynamic recrystallization. [2]

Usually, dynamic recrystallization does not occur in aluminium as stated before, though there has been research indicating dynamic recrystallization in high purity aluminium.

Apparently, the high grain boundary mobility in high purity aluminium enables dynamic recrystallization. Nonetheless, for 6061 this will be unlikely. Yet, there still remain unanswered questions concerning this subject and effects as dynamic recrystallization by progressive lattice rotation or geometric dynamic recrystallization have to be investigated further. [2], [48]

3.5 Measuring Recrystallization

The measurement of recrystallization in metals is a complex subject with various techniques in use. Classic microscopic evaluation with light optical microscopy (LOM) and scanning electron microscopy (SEM) is suited for gaining a general overview of the microstructure and can be easily performed. Even so, the outcome can be difficult to interpret and exact recrystallization fractions are often ambiguous. Investigations with transmission electron microscopy (TEM) offer higher resolutions and deeper insight. But the disadvantage is the limited observable area and the fact that effects occurring in the extremely thin TEM foils are not representative for larger specimens [49]. X-ray diffraction has the benefit of a three-dimensional data output but it is cumbersome and time-consuming. [2]

A different approach is to measure the progress of recrystallization indirectly through the changes of mechanical properties such as hardness or strength. An example is the measurement of the recrystallized fraction by micro-hardness testing. As hardness decreases in the process of recrystallization, it is possible to draw conclusions from the hardness measurements about the state of recrystallization. Unfortunately, the hardness also depends on the crystal orientation of the measured grains and heterogeneities can further interfere with the measurements. The general disadvantage of measuring recrystallization through mechanical properties is the variety of possibilities to interpret the correlations since numerous factors interact. [2], [50]

The most promising method for the evaluation of the recrystallized fraction is electron backscatter diffraction (EBSD) [51]. Especially for the observation of recrystallization at early stages, EBSD is well-suited [2]. For this method, an electron beam is directed towards a bulk sample at an angle of 60°-70°. Depending on the crystal structure and orientation, different patterns are generated. The diffraction patterns of the targeted crystal are then reflected towards a phosphor screen. Next, the CCD (charge-coupled device) camera captures the signal and redirects it to the attached computer system

where the patterns are processed and visualized. A schematic representation of an EBSD installation is shown in Figure 21.

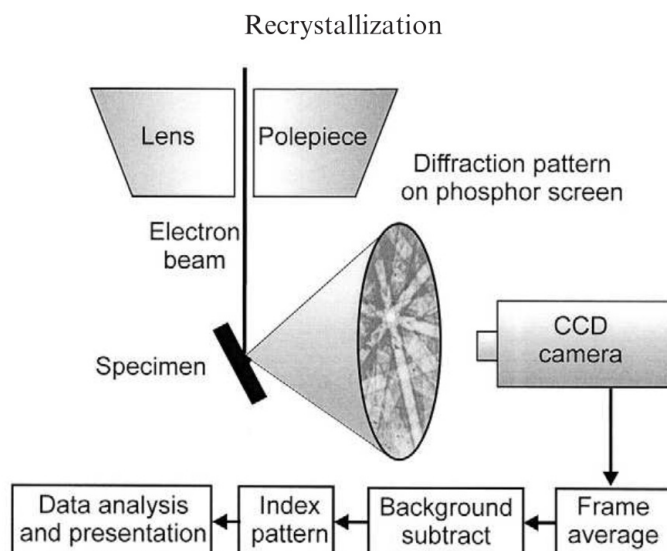


Figure 21: Schematic diagram of a typical EBSD installation [52]

Point by point, the entire surface of the sample is scanned and the final result is an orientation map giving an overview of crystal orientations and the corresponding image quality (IQ) parameters. The degree of deformation can be quantified with EBSD in two different ways: by comparing the IQ or by measuring the local misorientation [53].

For the IQ approach, the quality of the diffraction pattern of each scanned point in a sample is assessed. The IQ decreases with higher levels of deformation and increases for recrystallized grains. Therefore, it is possible to derive the recrystallized fraction from the average IQ. However, other factors can influence the IQ as well. Grain boundaries, surface topology, second phases, sample preparation, and camera settings may falsify the results. [53]

The second approach is based on the average misorientation within a sample. Deformed grains have varying orientations within the crystals, whereas already recrystallized grains exhibit steady orientations. There are different ways to calculate the local misorientation. The grain orientation spread (GOS) was chosen to define the state of recrystallization for this thesis. The GOS describes the distribution of the average deviation in orientation of each point in a grain to the average misorientation of a grain.

For each grain, one value is defined which represents its state of recrystallization. It has to be considered that careful preparation is necessary to achieve comparable results and that the GOS depends on the selected parameters defining a grain. [53]

Furthermore, a detailed grain size spread can be derived from the orientation map providing more insight into the recrystallization processes. With EBSD, smaller grains (as small as 0.2 μm) can be detected and higher accuracy can be achieved when compared with LOM [51], [54]. Measuring recrystallization kinetics with LOM is very time-consuming and highly dependent on proper etching techniques [54], [55].

4 Experimental

The experimental part of this paper was conducted at the 'Institute of Materials Science and Technology' at the 'University of Technology Vienna' in cooperation with 'Austria Metall AG' (AMAG) in Ranshofen.

At first, a pure Al-Mg-Si alloy was cast and the desired parameters were verified. The as-cast material was heat-treated in a way mimicking the industrial process and with a modified heat treatment to provoke dispersoid formation. The material was then prepared and its microstructure examined with LOM, SEM and TEM. Afterwards, the heat-treated samples were etched and a grain size analysis was performed. As a last step, compression tests followed and the deformed samples were examined with EBSD to identify the fraction of recrystallization depending on the compression parameters.

4.1 Casting

The alloy for the following research was especially casted at the foundry of 'AMAG casting'. In comparison to industrial-grade 6061, the used alloy is designated to be significantly more pure. It only contains traces of the elements Fe, Cu, Mn, Zn, and Cr. The aim was to create a model alloy free of dispersoid formation. The usual composition of 6061 is shown in Table 2.

The basis for the model alloy was aluminium with a purity of 99.9wt%. As alloying elements, Mg (92wt% Mg, rest aluminium) and pure Si were added to the melt to adjust the composition. In accordance with the object of the experiment, the final alloy should contain 0.81wt% Mg and 0.63wt% Si with a maximum of 0.05wt% Ti for grain refinement. Especially the Fe, Cr, and Mn content should be kept at a minimum (less than 0.05wt%) to avoid the formation of dispersoids. To determine the alloy composition during casting, an 'ARL 3460 OES Metals Analyzer' optical emission spectrometer was used.

A custom-made ingot mould was used for casting as can be seen in Figure 22. The external dimensions of the mould were 320x136x110mm. On the bottom side was a drilling (Figure 22) for the insertion of a thermocouple. With the aid of the thermocouple, the temperature of the mould could be monitored during the entire casting process to guarantee a controlled solidification. Ahead of casting, a boron nitride coating was applied on the surfaces of the ingot mould as a separation agent.

Experimental

Furthermore, the mould was heated up to 120°C to ensure an even solidification and a grain size distribution as in an industrial process.

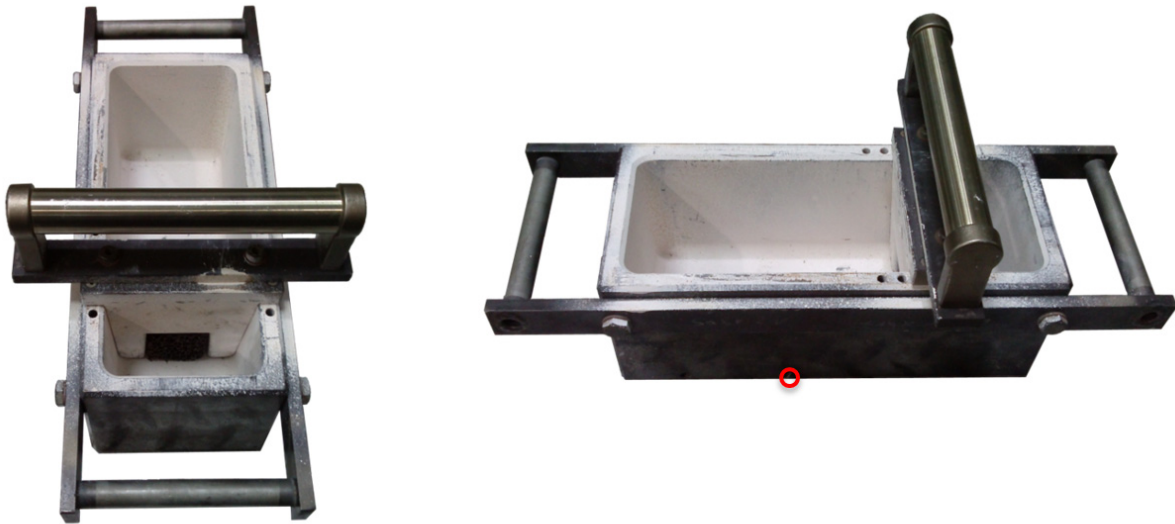


Figure 22: Custom-made ingot mould (drilling for thermocouple is marked red)



Figure 23: Separator with filter (left), ceramic filter (right)

The ingot mould was divided into two different partitions through a separator with an inserted ceramic filter as displayed in Figure 23. The molten aluminium alloy was heated up to 750°C for 45min to guarantee a homogeneous distribution of the alloying

elements and then cautiously poured into the smaller of the two partitions of the rising casting mould. Thereby, the melt flowed through the ceramic filter and ascended in the larger partition. Oxide films and other large impurities were intercepted by the ceramic filter. To avoid solidification at the filter, it had been preheated with a gas torch until it began to glow.

After solidification of the ingot, the smaller partition including the ceramic filter was cropped. The final dimensions of the ingot were approximately 190x110x110mm. For the assessment of the quality of the ingot, a slice from the centre was cut out as depicted on the left in Figure 24. The area of the slice was then divided in 15 separate squares with an edge length of 20mm. To take advantage of symmetry and to minimize the experimental efforts, only the areas along the centric axes were examined. This summed up to six squares marked on right in Figure 24 with the numbers 6, 7, 8, 9, 12, and 15.

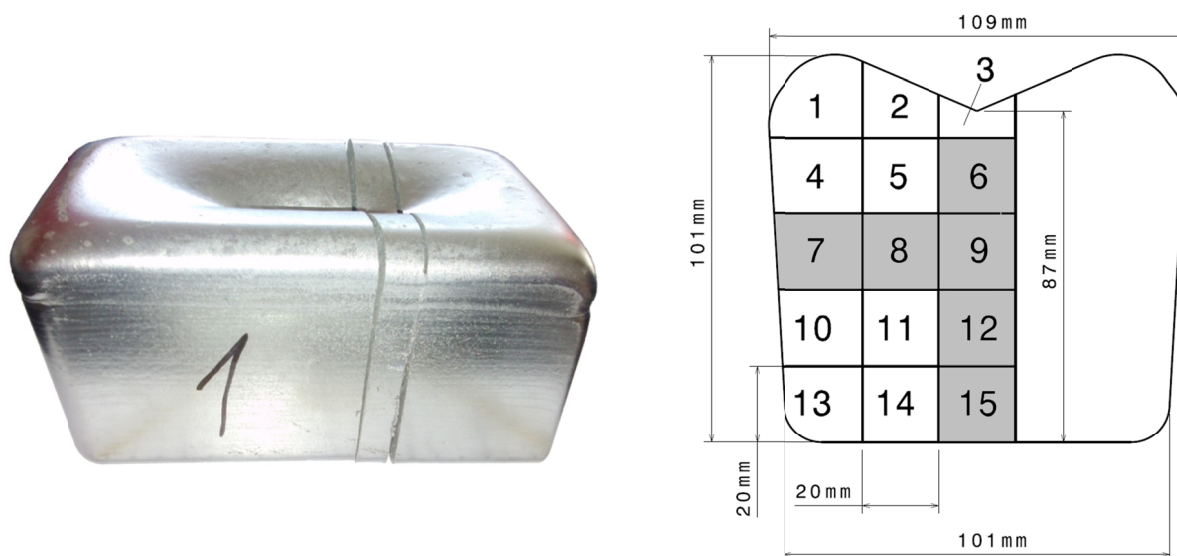


Figure 24: Cut ingot (left), examined areas of the slice (right)

The processes of the examination with LOM and SEM are further described in chapter 4.3. In addition, the quality of the ingot was assessed by 'AMAG rolling' (see appendix Chapter 12.1).

4.2 Heat Treatment

The examination of the samples 6, 7, 8, 9, 12, and 15 attested an excellent quality to the central area of the ingot (see Chapter 5.1). The boarder area was removed, leaving only

Experimental

the homogenous part as displayed on the left in Figure 25. Samples of this part were then exposed to a homogenization process in order to assess if dispersoids can form in the model alloy.

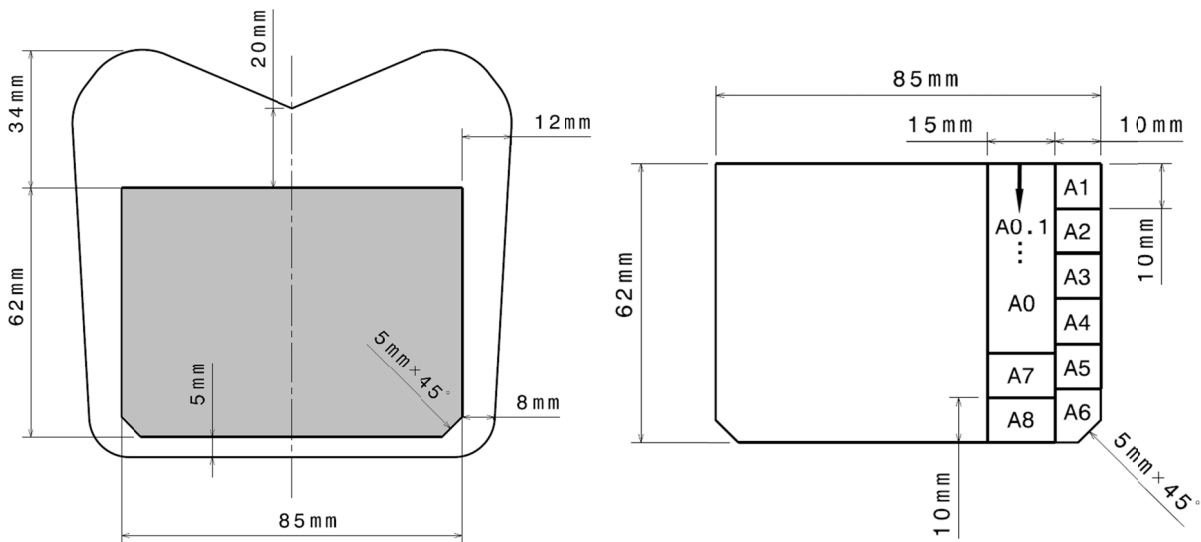


Figure 25: Homogeneous area (grey) with mapped samples used for further experiments

The samples for homogenization were cut either into cubes with a side length of 10mm (for LOM and SEM) or into 15x10x1mm slices (for TEM-examinations) with a 'Struers Accutom-5' cut-off machine and a '10S15' SiC cutting disk. The nomenclature of the samples is shown on the right in Figure 25. To measure the temperature of the samples during the heat treatment, a dummy cube of the same size and material was furnished with a thermocouple Type K (NiCr-Ni). For this purpose, thermal conductive paste and a thermocouple were inserted into a drilled hole in the centre of the dummy, which was then sealed off with an aluminium plug. That way, the samples and the dummy for measuring the temperatures had the same properties considering heat-conductivity.

Aluminium rolling slabs can be up to 9m long and 2.25m wide with a weight of almost 30t [56]. Therefore, it takes several hours for the ingot to heat up evenly across its entire body for homogenization. To simulate the slow industrial process on a small scale, a temperature profile based on an industrial process as in Figure 26 was applied. For the homogenization a 'Nabertherm RS 80/750/11' vertical tube furnace was used with Ar 4.6 as a protective gas.

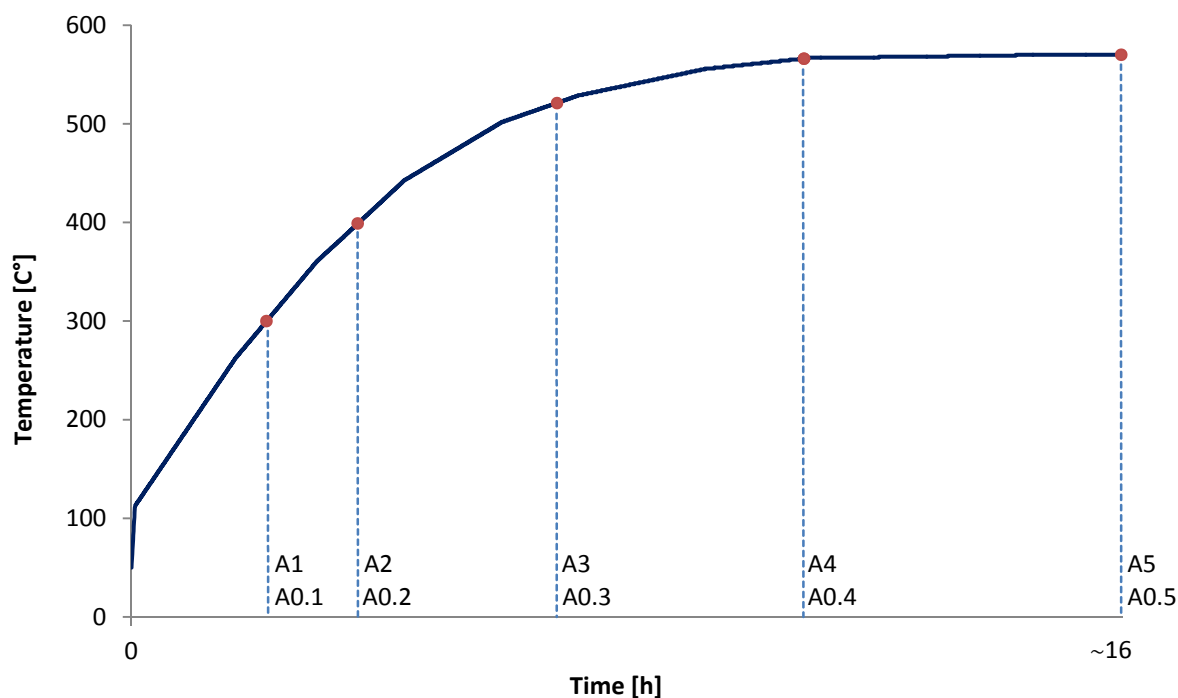


Figure 26: Target temperature profile homogenization

The samples and the dummy were hung into the vertical tube furnace, all with separate wires. At 300°C, 400°C, 520°C, 565°C, and finally at 570°C the samples were instantly quenched by cutting their wire and dropping them into cold water. The complete cycle took about 16h.

An overview of the heat treated samples is given in Table 5. The table shows the naming and respective temperature. A1-A6 were examined with LOM/SEM whereas A0.1-A0.6 were processed for TEM examinations. The origins of the samples were previously described in Figure 25.

Table 5: Description of heat-treated samples

Name	Temperature
A1, A0.1	300°C
A2, A0.2	400°C
A3, A0.3	520°C
A4, A0.4	565°C
A5, A0.5	570°C
A6, A0.6	As-cast

Samples A4 and A5 which underwent the largest part of the homogenization process showed abnormal grain growth as later described in the results in Chapter 5.2.3. Since the grain size has a significant impact on recrystallization [2], an attempt was made to suppress this abnormal grain growth.

For this purpose, a shortened version of the industrial homogenization was tested to avoid abnormal grain growth while leaving the other parameters influencing recrystallization untouched. Samples A7 and A8 were heated to 565°C in only 10min and held for 10min and 5min, respectively (see Table 6). The shape of the temperature profile was as in the previous process.

Table 6: Description of samples for the shortened homogenization

Name	Holding time at 565°C
A7	10min
A8	5min

4.3 Optical Microscopy and Scanning Electron Microscopy

For the examination of the as-cast material and the samples from the heat treatments with LOM and SEM, the cubed samples had to be embedded, ground, and polished. The embedding resin of choice was the two-component cold embedding material ‘CEM3070’. Cold embedding material was used to avoid influencing the microstructure of the heat-treated samples. Additionally, the electrical conductivity of the embedding resin ‘CEM3070’ is suitable for SEM analysis. The embedded samples were ground and polished as described in Table 7.

Table 7: Sample preparation for LOM and SEM

Step	Surface	Suspension	Lubrication	Duration [min]	Velocity [rpm]	Force [N]
Grinding	SiC 500	-	Water	3	150	15
Fine grinding	SiC 4000	-	Water	5	150	15
Polishing	MD-Mol	Diamond 3µm	Red	7	300	15
Polishing	MD-Nap	Diamond 1µm	Blue	5	150	10
Fine polishing	OP-Chem	OPS	Water, soap	2	150	10

After polishing, the samples were cleaned with ethanol and examined with a 'Zeiss Axioplan' (LOM) and a 'FEI Philips XL 30' (SEM) equipped with an energy-dispersive X-ray (EDX) analysis system. With the micrographs of SEM and LOM, the microstructure was analysed and with the help of EDX, the composition of the structures could be identified.

4.4 Grain Size Analysis

The basis for grain size analysis was the sample preparation procedure as for LOM and SEM (Chapter 4.3). After fine polishing, the samples were electrolytically etched with Barker's reagent. The reagent contained 5ml fluoroboric acid (HBF_4 , 48%) and 200ml distilled water. The etching was conducted over 45s on a 'LectroPol-5' apparatus with a flow rate of 15, a voltage of 20V, and an interface of 2cm^2 .

The micrographs for the grain size analysis were taken on a 'Zeiss Axioplan' with polarized light and a sensitive tint. Through this procedure, the grain structure became visible, could be manually mapped, and finally interpreted automatically with the grain size analysis tool of the programme 'AxioVisio'. The applied standard for the analysis was 'ASTM E 1382'.

4.5 Transmission Electron Microscopy

TEM requires a different approach to prepare the samples. First, the slices with a dimension of $15 \times 10 \times 1\text{mm}$ were ground from both sides with a 220 grit SiC paper until a thickness of about $100\text{-}150\mu\text{m}$ was reached. As a second step, disks with a diameter of 3mm were punched out of the thin slices and electropolished until a hole formed in its middle. Only the edges of the hole were thin enough to be examined with TEM. The electrolytical preparation was performed with a 'Struers TenuPol-5' apparatus. The device was cooled down to a temperature between -20°C and -8°C with liquid nitrogen and a mixture of 1/3 nitric acid plus 2/3 methanol served as electrolyte.

The examinations were performed on a 'FEI TECNAI F20' transmission electron microscope with an operation voltage between 60kV and 200 kV equipped with an EDX device. Special focus lay on detecting dispersoids and observing their behaviour depending on the heat treatment.

4.6 Compression Tests

After confirming the quality of the ingot and proving that the dispersoid formation in the model alloy was suppressed, compression tests followed. Cylindrical samples of the model alloy were deformed at elevated temperatures with varying parameters and the state of recrystallization was observed.

The deformation tests were performed on a 'DIL 805' dilatometer by 'BÄHR Thermoanalyse GmbH'. Before starting, the cylindrical samples with a length of 10mm and a diameter of 5mm were equipped with a thermocouple (Figure 27). For this purpose, the oxide layer on the samples had to be removed with abrasive paper before the wires of the thermocouple were spot-welded to it with a 'BÄHR Spot Welding Apparatus 9060'. The welding points were rather fragile and hence the wires were additionally fixated with the temperature-resistant two-component adhesive 'Thermokitt Roth'. This way, the welding joints were not damaged during deformation and the temperature curve could be continually recorded until the end. To minimize the friction between sample and compression die, and thus the bulging of the samples during deformation, a square of Mo sheet was glued to each surface of the sample (Figure 27). The glue vaporized due to the high temperatures in the course of the experimental procedure.

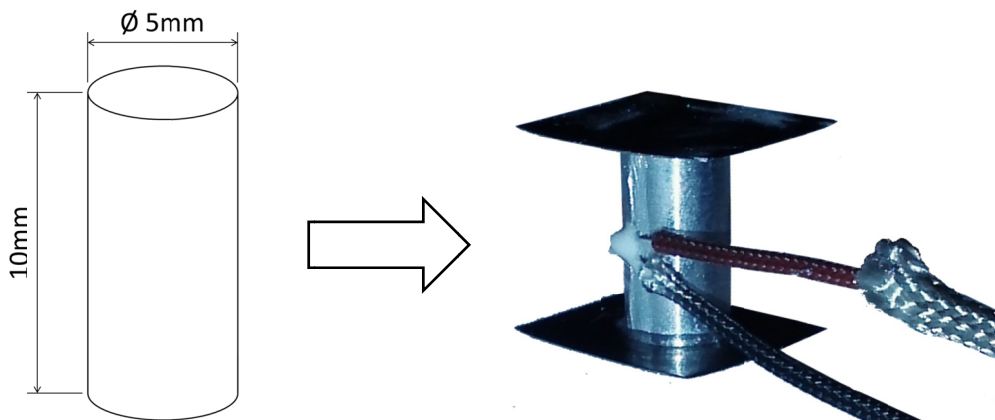


Figure 27: Sample for compression tests (left) with thermocouple and Mo sheets (right)

During the compression tests, the temperature curve, length variation, degree of deformation, and rate of deformation were recorded.

The sequences for the compression tests with the dilatometer are illustrated in Figure 28. The continuous line represents the target temperature profile modelled after the shortened homogenization process whereas the dotted area symbolizes the compression sequence.

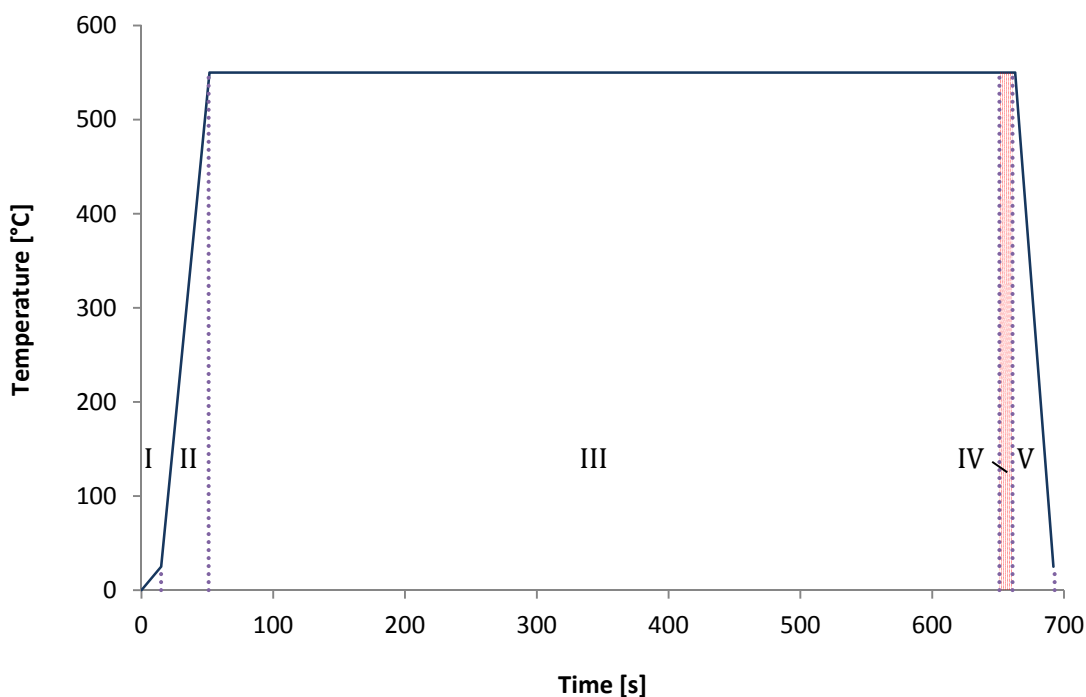


Figure 28: Temperature profile for compression tests

In Figure 28, each of the five steps of the compression test procedure is confined by dotted lines:

- I. The chamber was flooded with He as shielding gas for 15s.
- II. The temperature was linearly raised from ambient temperature to 550°C over a period of 36s.
- III. During the following 10min the temperature was held constantly at 550°C.
- IV. The sample was deformed with parameters as described in Table 8.
- V. Immediately after deformation, the sample was quenched with a rate of 17.5K/s for 30s.

Experimental

Parameters with a major influence on recrystallization are the degree of deformation (φ) and the rate of deformation ($\dot{\varphi}$). The degree of deformation is defined as

$$\varphi = \ln\left(\frac{l_0}{l}\right) \quad (21)$$

l_0 is the original length of the specimen and l the length after deformation. The rate of deformation $\dot{\varphi}$ is defined as derivative of φ with respect to time.

To assess the impact of φ and $\dot{\varphi}$ on recrystallization, the values of the parameters were varied according to Table 8. At first, sample B0/0 underwent the heat treatment without any deformation as a reference sample. As a next step, φ was varied from 0.2 to 1 while $\dot{\varphi}$ remained at 10s^{-1} . At last, $\dot{\varphi}$ was varied between 0.1s^{-1} and 10s^{-1} with constant $\varphi=1$.

Table 8: Samples for the deformation tests

Sample	Deformation φ [-]	Deformation rate $\dot{\varphi}$ [s^{-1}]
B0/0	0	0
B0.2/10	0.2	10
B0.35/10	0.35	10
B0.5/10	0.5	10
B1/0.1	1	0.1
B1/0.5	1	0.5
B1/2	1	2
B1/5	1	5
B1/10	1	10

To determine the time dependency of recrystallization and recovery, the heat treatment was modified as displayed in Figure 29. Steps I-IV remain as described in Figure 28 on the page before. However, after deformation (IV) the sequence V was inserted where the temperature was held constantly at 550°C and the quenching rate was maximized.

The holding time (sequence V) was varied between 0s and 30s while the other parameters were left untouched. Furthermore, the quenching rate in sequence VI was increased by a factor of 10 to 175K/s . The parameters of sample group C are summarized in Table 9.

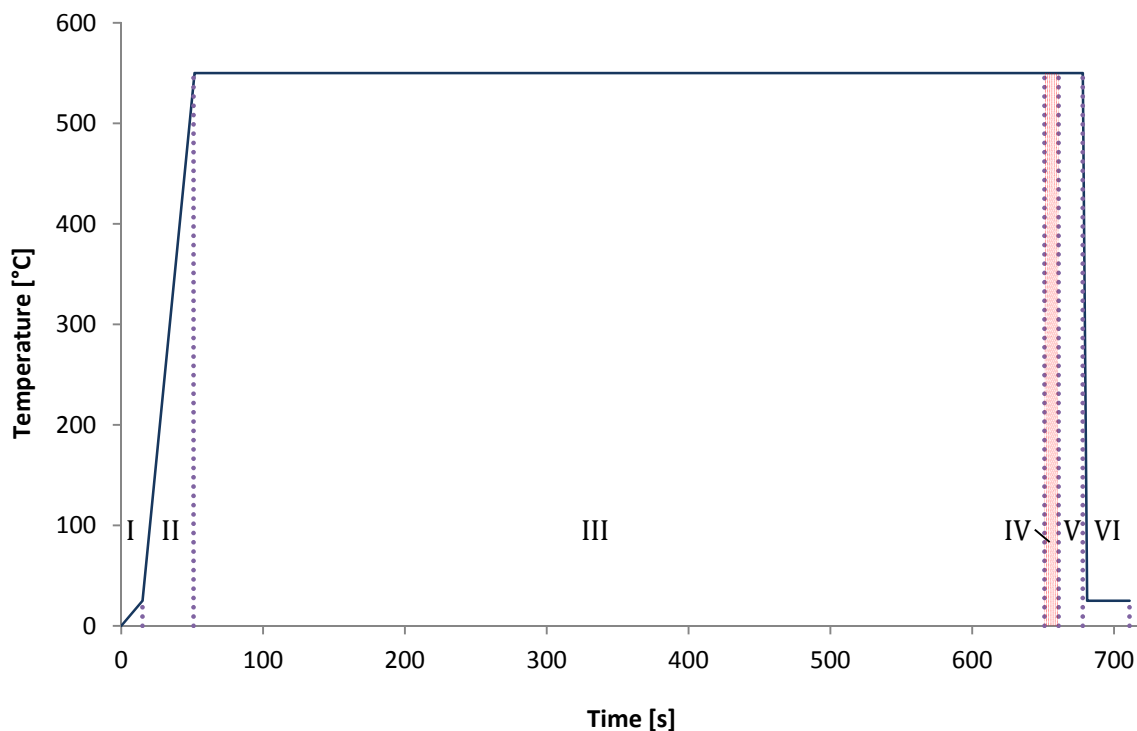


Figure 29: Temperature profile for compression tests with added holding time and increased quenching rate

Table 9: Samples with increased quenching rate varied by holding time after deformation

Sample	Deformation φ [-]	Deformation rate $\dot{\varphi}$ [s^{-1}]	Holding time [s]
C0	1	0.1	0
C2	1	0.1	2
C5	1	0.1	5
C10	1	0.1	10
C15	1	0.1	15
C20	1	0.1	20
C30	1	0.1	30

4.7 Electron Backscatter Diffraction

After the compression tests, the resulting deformed samples were prepared for EBSD examinations to analyse the state of recrystallization. As a first step, the samples were cut parallel to the direction of deformation into two parts, 0.5mm from the centre. The last 0.5mm were removed by grinding and polishing. Only the sections in the centre of the samples were considered during the examinations. Secondly, the samples were

Experimental

embedded with a 'Struers PredoPress' warm embedding press. 'PolyFast' was used as embedding material. As a last step, the samples were ground and polished according to Table 10. Polishing and fine polishing were extended compared to the preparation for LOM and SEM in order to guarantee a surface free of deformation or scratches since the EBSD examinations are very sensitive to topological defects. Between the steps, the samples including the specimen holder were cleaned with a 'Struers Lavamin'. Also, the final cleaning-step with ethanol was vital. Otherwise, the results would have been prone to error due to colloidal silica suspension residues.

Table 10: Sample preparation for EBSD

Step	Surface	Suspension	Lubrication	Duration [min]	Velocity [rpm]	Force [N]
Grinding	SiC 500	-	Water	3	300	10
Fine grinding	Largo	Diamond 9 μ m	Blue	15	150	10
Polishing	MD-Dur	Diamond 6 μ m	Blue	25	150	10
Polishing	MD-Mol	Diamond 3 μ m	Red	30	150	10
Fine polishing	OP-Chem	Colloidal silica	Water, soap	15	150	10
Cleaning	OP-Chem	Ethanol	Water, soap	3	150	10

Following the described sample preparation, the specimens were placed in an ultrasonic bath filled with ethanol, rinsed with hot water, and finally dried with a blow-dryer. If the EBSD examinations still showed residues from the colloidal silica suspension, the samples were shortly placed in hydrofluoric acid. 20-30s proved to be the ideal duration.

The EBSD examinations were conducted on a 'FEI Quanta 200 FEGSEM' equipped with a backscattered electron detector and evaluated with the 'TEAM EDS Analysis System for SEM' by 'EDAX'.

5 Results

The following chapter summarizes the results of the analysis of the samples with LOM, SEM, TEM, and EBSD. LOM and SEM were used to assess the quality of the ingot as well as to observe the primary phases and the grain size over the course of the homogenization. The TEM examinations were performed in order to monitor if dispersoids formed during the heat treatment. Finally, the EBSD examinations gave insight into the state of recrystallization after the compression tests.

5.1 Casting

As intended, the Fe content of the primary aluminium was less than 0.05wt% and the overall purity at 99.9wt% (the exact composition is displayed in Table 14 in the appendix). After adding the alloying elements, the final composition had a content of 0.80wt% Mg and 0.65wt% Si. Those values are within the expected range of the aimed contents of 0.81wt% Mg and 0.63wt% Si. The remaining aluminium content was at 98.5wt% and the other alloying elements remained at values similar to the primary material. The composition of the final alloy is listed in Table 11.

Table 11: Composition of final alloy

Alloying element	Percentage by weight
Silicon (Si)	0.652%
Iron (Fe)	0.045%
Copper (Cu)	0.000%
Manganese (Mn)	0.002%
Magnesium (Mg)	0.795%
Chromium (Cr)	0.001%
Nickel (Ni)	0.003%
Zinc (Zn)	0.002%
Titanium (Ti)	0.004%
Aluminium (Al)	bal.

Examinations with LOM showed a homogenous microstructure as in Figure 30. Further micrographs of the other areas are available in the appendix (Figure 62 to Figure 65).

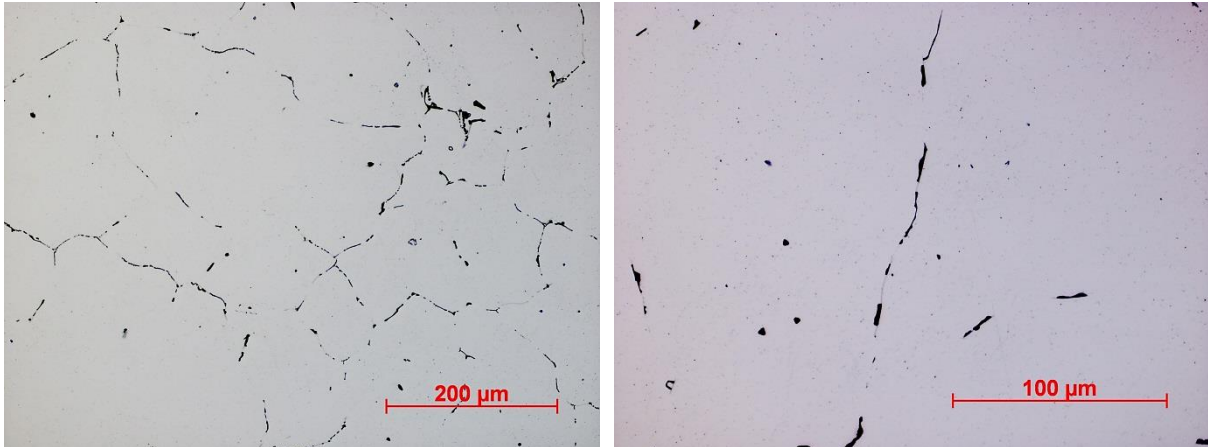


Figure 30: LOM micrographs of sample 6, 200x (left) and 500x (right) magnification

The laboratory report by ‘AMAG rolling’ (see appendix Chapter 12.1) showed isolated pores that were smaller than 50μm and oxide contaminations (Figure 31 on the right). More severe defects were only detected close to the pipe (equivalent to area 3 in Figure 24) as depicted in Figure 31 on the left. In the course of solidification, cracks with a length of up to 5mm emerged there.

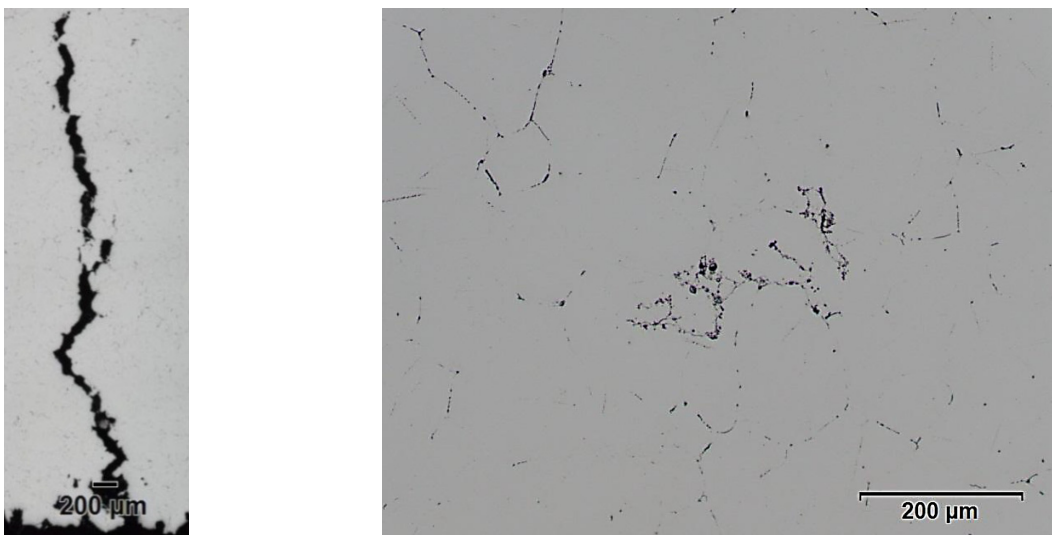


Figure 31: Solidification crack near the pipe (left), oxide contaminations (right) [57]

To minimize the effect of contaminations and defects, the boundary areas of the ingot were removed as shown in Figure 25 on page 38. Only the central area of the ingot was used in the further experiments.

5.2 Homogenization

The samples for the homogenization process were cut from the sample area previously determined as consistent. They were then heat-treated for up to 16h and quenched at certain intervals, to see if dispersoid formation occurred. In the process, the phase fractions and the grain size of the samples were collected as well.

The temperature during homogenization was monitored with a thermocouple attached to a dummy sample of equal size and material. The measured temperature followed the target temperature with only minor deviations at the beginning as seen in Figure 32. At 300°C (A1, A0.1), 400°C (A2, A0.2), 520°C (A3, A0.3), 565°C (A4, A0.4), and at 570°C (A5, A0.5) samples (one for LOM plus SEM, one for TEM) were quenched in water.

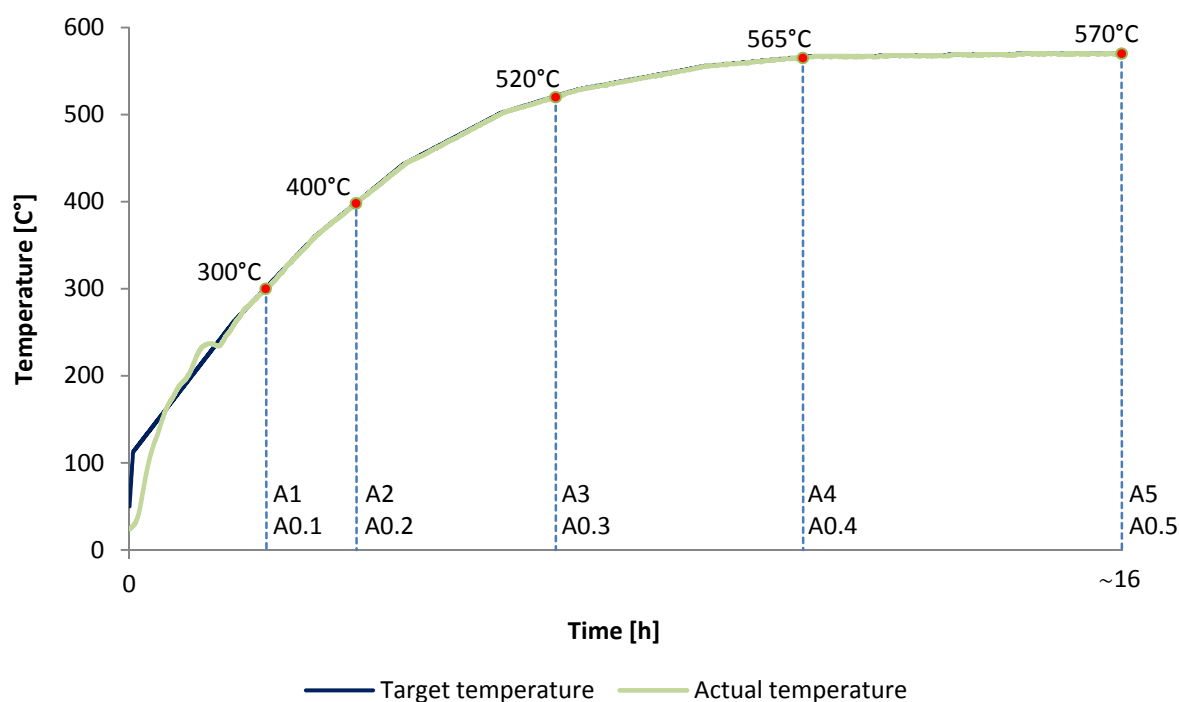


Figure 32: Temperature profile homogenization

5.2.1 Optical Microscopy and Scanning Electron Microscopy

At first, the as-cast state of the alloys microstructure was examined. The LOM micrographs (Figure 33) show two different phases embedded in the aluminium matrix: light grey and black, plate-shaped structures.

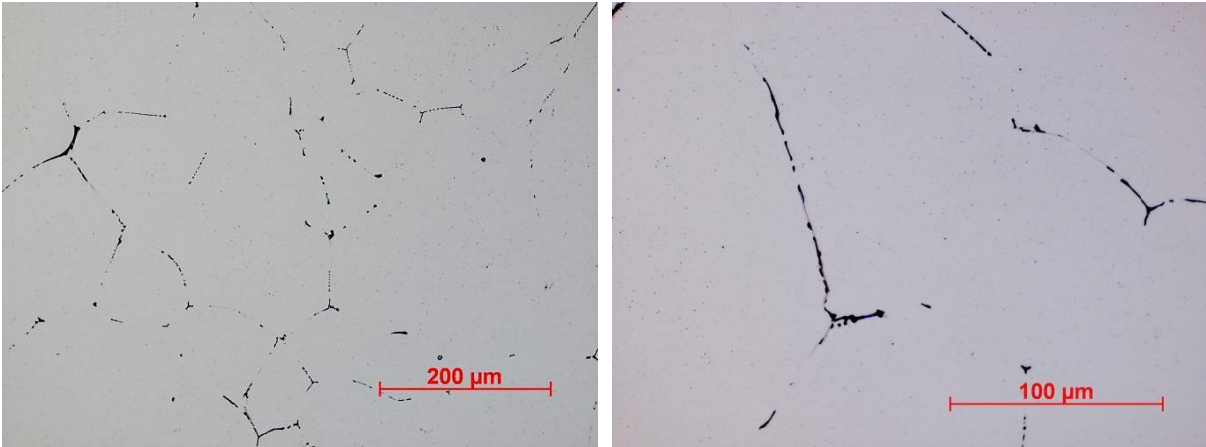


Figure 33: LOM micrographs of sample 9 (as-cast), 200x (left) and 500x (right) magnification

The composition of these phases was determined with the help of an EDX analysis. Exemplary, the surface of the as-cast sample 9 was analysed. Further images of the microstructure are attached in the appendix (pages i-ii). Every distinctive structure observed with SEM was scanned with a focused spot beam. The examined spots are indicated in Figure 34 and the following diagrams (Figure 35) show the results of the analysis.

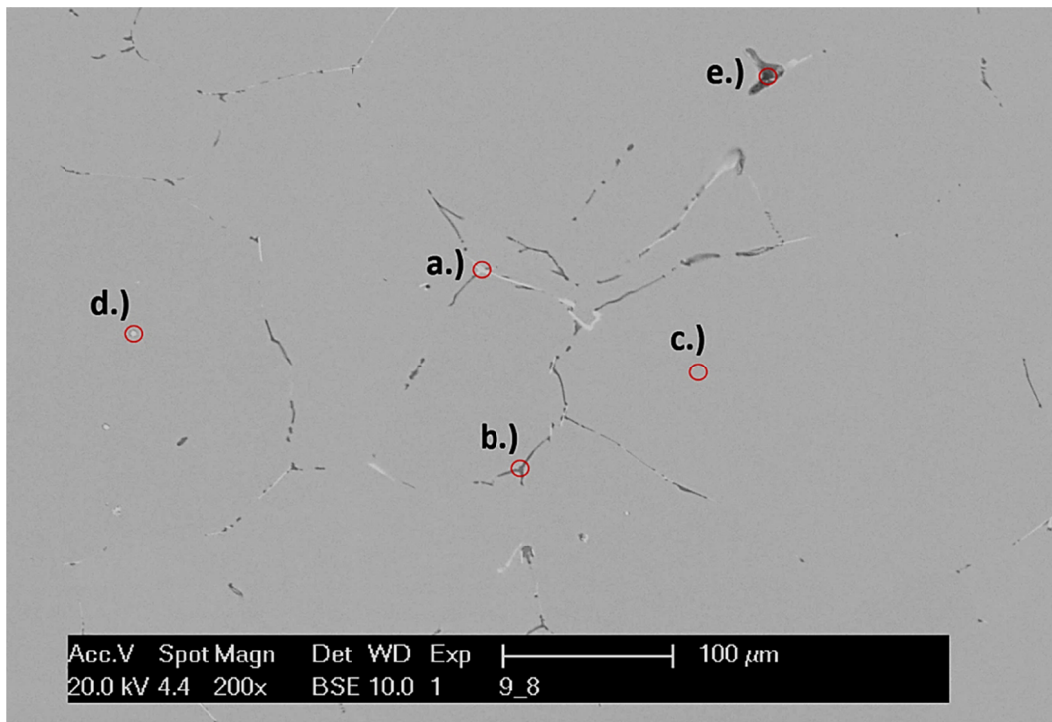


Figure 34: SEM micrograph of sample 9 (as-cast) with labelled EDX measuring points

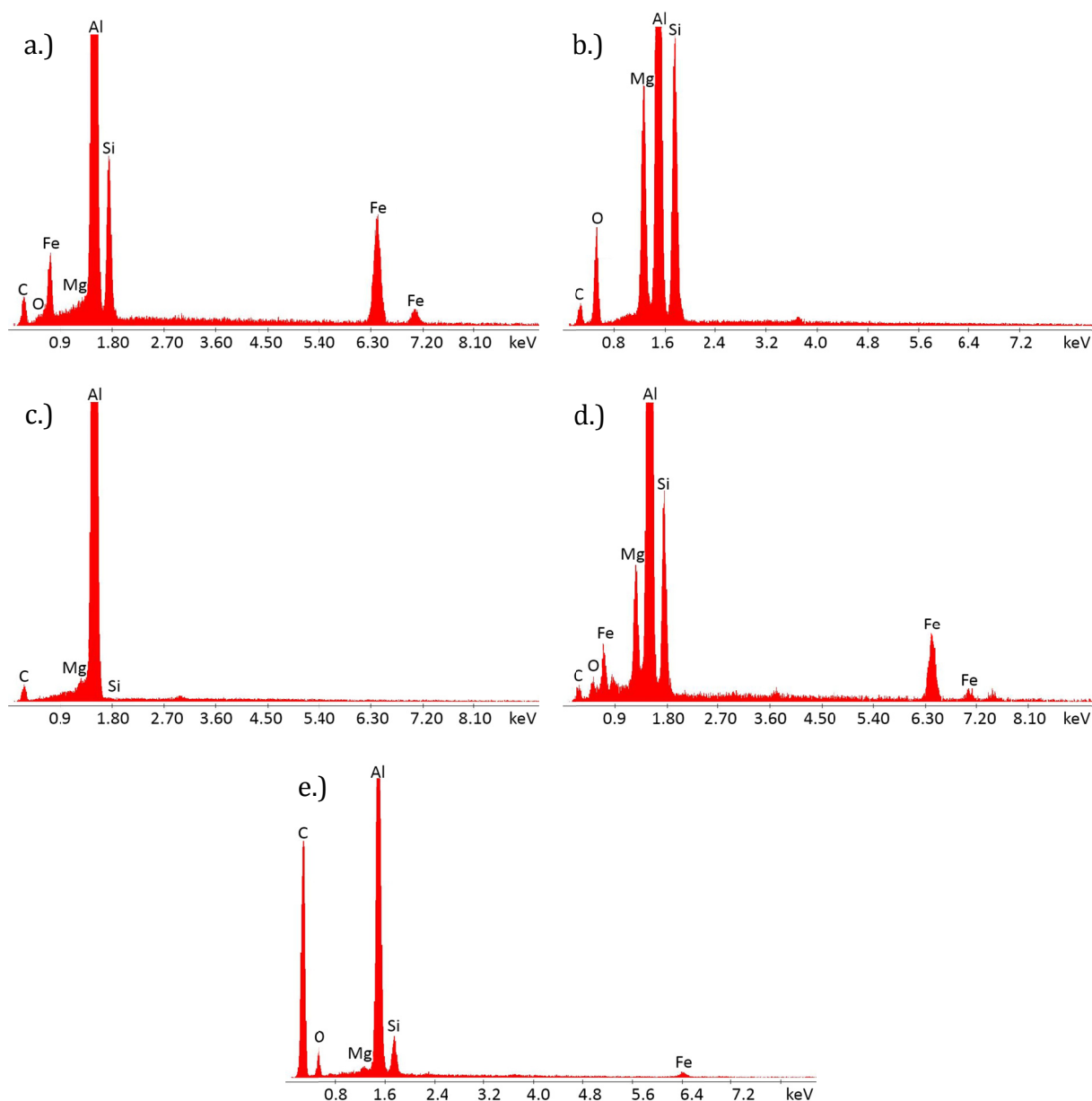


Figure 35: EDX analysis of sample 9 (as-cast); points a.)-e.) corresponding to Figure 34

- a.) Peaks at Si and Fe show that the light structures are AlFeSi phases. The straight-lined structure indicates that these are β -Al₅FeSi. There is no ‘Chinese script-like’ morphology visible suggesting the presence of any α -AlFeSi phases.
- b.) The light grey phases contain Mg and Si according to the results of the EDX analysis, forming Mg₂Si.
- c.) As a reference, this spot measures the composition of the matrix material. Only marginal traces of Mg and Si solved in the aluminium matrix were identified.

Results

- d.) Although optical similarities to the Q-phase are recognizable, the circular light grey structures are Fe-containing and appear to be the same as in a.), viewed from a different angle.
- e.) The bulky, dark areas with blurred outlines are formed of C, O, and Si. This leads to the conclusion that these structures are pores filled with residues from the grinding and polishing process.

The peaks of aluminium are not visible to their full extent in Figure 35. Otherwise, the minor amounts of the alloying elements would not be visible in the diagrams. C and O are mainly present due to slight contaminations and the formation of oxide layers. Other phases could not be identified.

Figure 37 shows the evolution of the microstructure during homogenization with LOM. Up to a temperature of 400°C (c.), no significant changes are visible. At 520°C (d.), Mg₂Si contents start to decrease. Finally at 565°C (e.), Mg₂Si completely dissolved, leaving only Fe-containing phases. SEM micrographs showing the same development are attached (Figure 67 and Figure 68).

The observations with LOM were confirmed by the calculation of the phase fractions. To determine the fractions, the different phases were distinguished by their colour and marked in SEM micrographs as depicted in Figure 36. For each temperature stage, three different micrographs were analysed and the average values calculated.

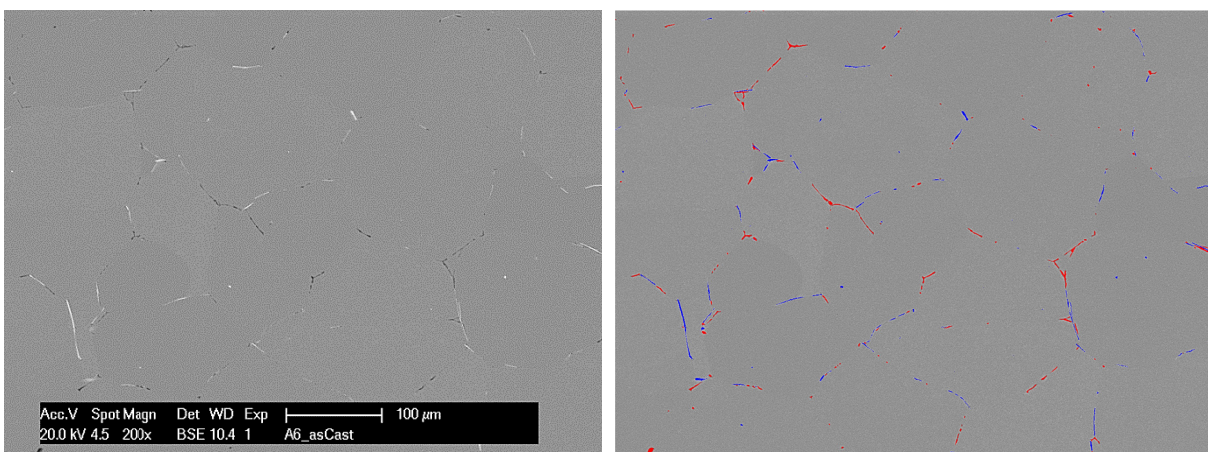


Figure 36: Phase fraction in sample A6 (as-cast) with Mg₂Si → red, AlFeSi → blue

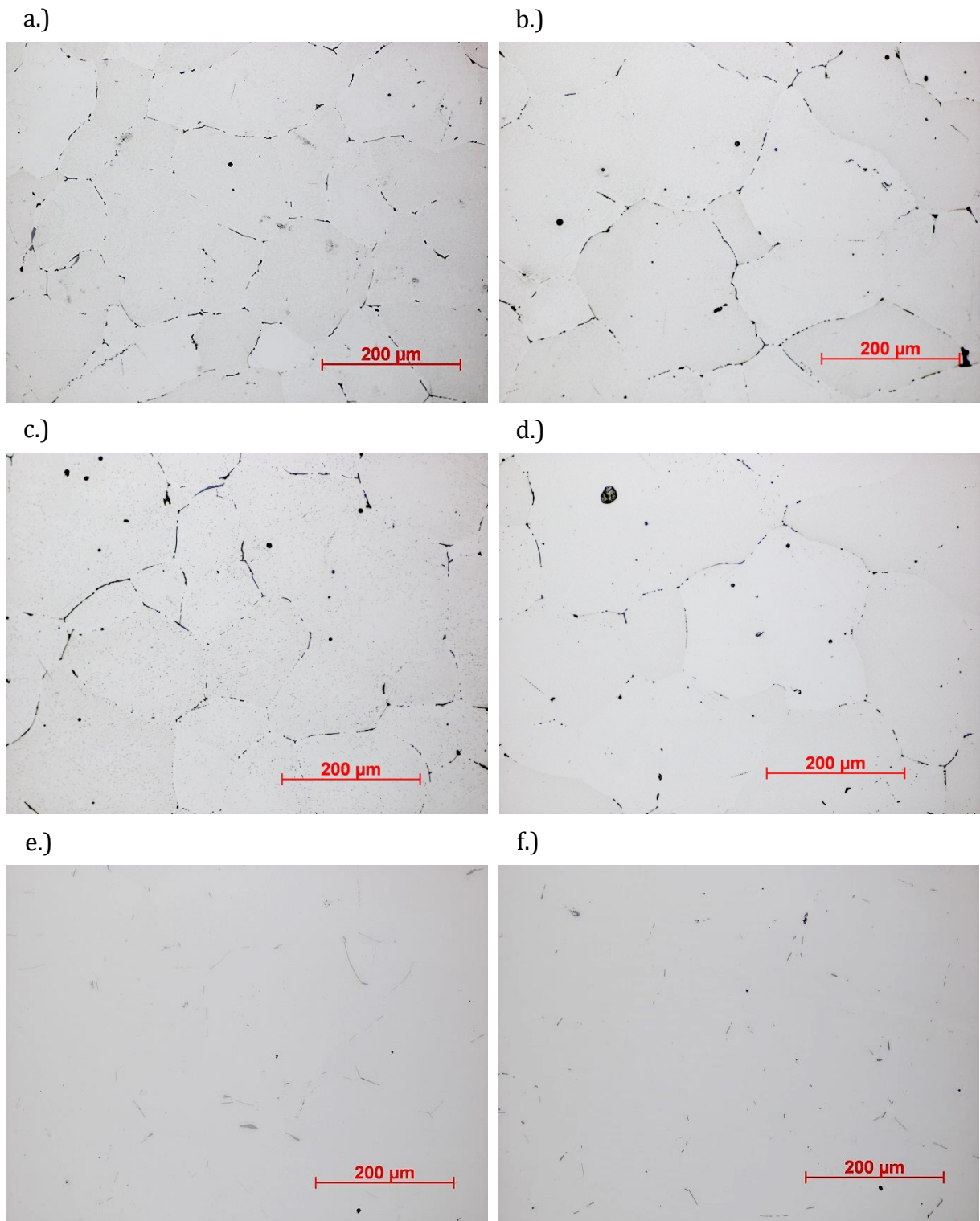


Figure 37: LOM micrographs (200x magnification) as-cast - A6 (a.), 300°C - A1 (b.), 400°C - A2 (c.), 520°C - A3 (d.), 565°C - A4 (e.), and 570°C - A5 (f.)

The ratios of the selected phase to the entire area of the micrographs form the values as shown in Figure 38. Each bar represents the mean value of three separate measurements with the corresponding standard deviation indicated.

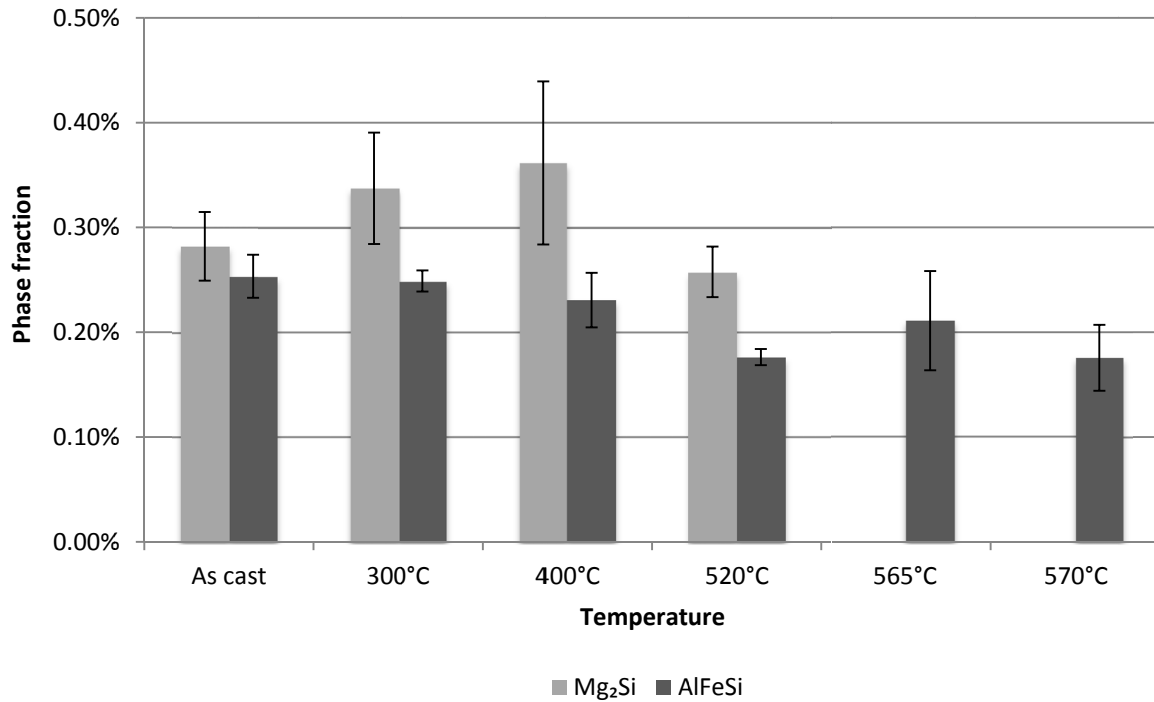


Figure 38: Phase fraction depending on duration of the heat treatment

The phase fraction of Mg₂Si ranged from 0.24% to 0.43% until 520°C before plummeting to 0% at 565°C and 570°C. AlFeSi, however, remained almost constant over the entire process, decreasing only slightly. Yet, the decrease of AlFeSi is within the fluctuation range.

5.2.2 Transmission Electron Microscopy

As a next step, the samples A0.1-A0.6 (according to Figure 25 on page 38) were further investigated with TEM. Besides generally examining the samples, special focus was placed on detecting dispersoids at the different levels of the heat treatment.

The TEM micrographs of the as-cast structure (Figure 39) showed plate-shaped structures, curled objects, and further smaller inclusions. According to the

Results

measurements (EDX measurements are shown in Figure 71 and Figure 72 in the appendix) both curls and plates consist of Si. Furthermore, one half of the circled object in Figure 39 image a.) is plate-shaped, while the other half is curled. This suggests that the curls are preparation artefacts formed where the matrix around the plates dissolved during the preparation process of the samples. Other inclusions were identified as silicon oxide and aluminium oxide.

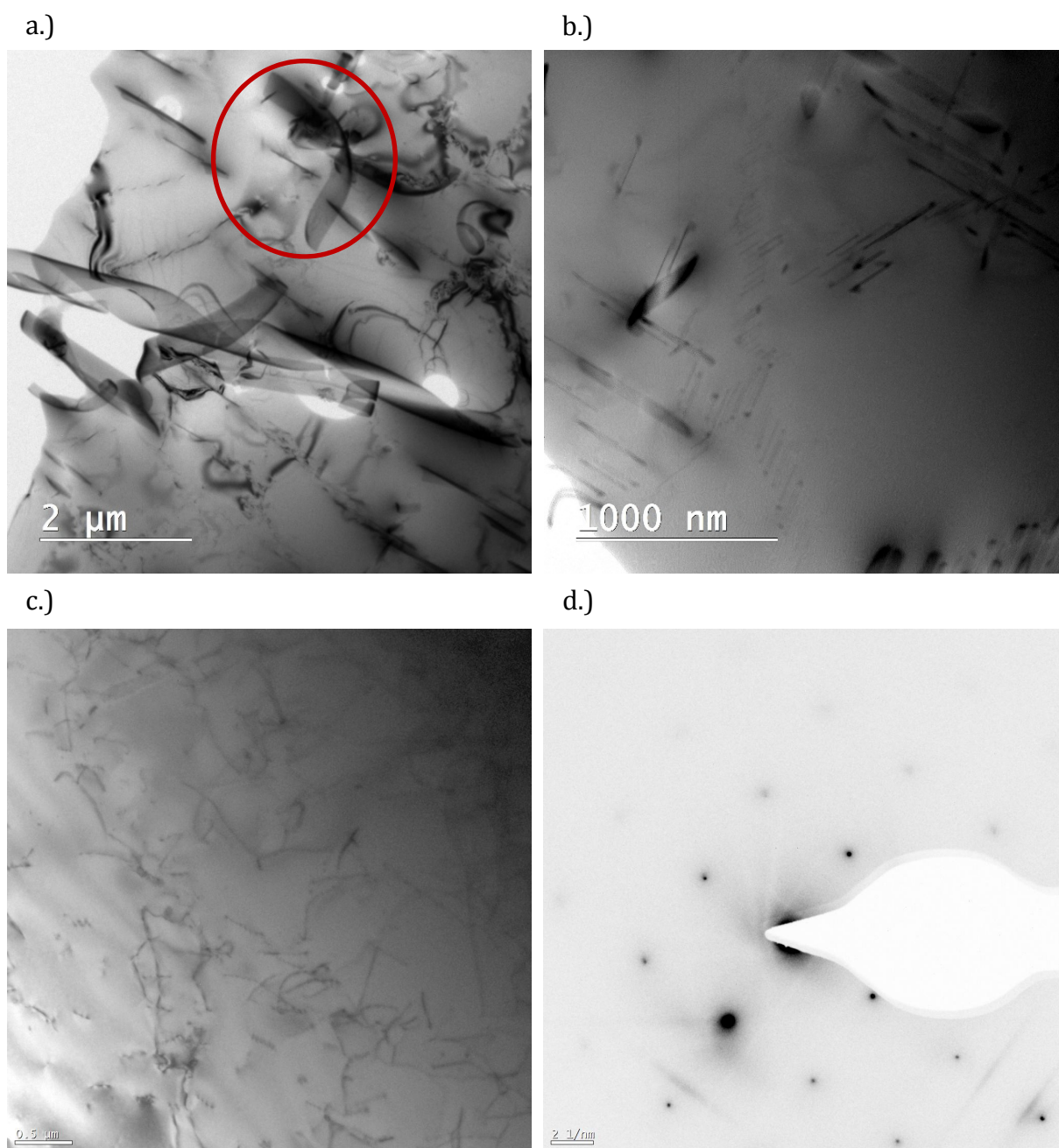


Figure 39: TEM micrographs of as-cast sample A0.6 (a.), (b.) and its matrix oriented in (100) with the corresponding SAED pattern (c.), (d.)

Results

There were no traces of Fe-containing structures or any dispersoids, even after various areas of the sample were examined. In search of Mg-Si precipitates that can act as nucleation sites for dispersoids [33], the crystal was oriented in (100) as displayed in Figure 39 c.) and d.). Nevertheless, none were visible. The crystal orientation was aligned with the help of selected area electron diffraction patterns (SAED patterns).

Sample A0.1 (quenched at 300°C) showed a lot of similarities with the untreated sample. The material contained Si plates/curls and, additionally, rods appearing to be β' -Mg₂Si were observed (left of Figure 40).

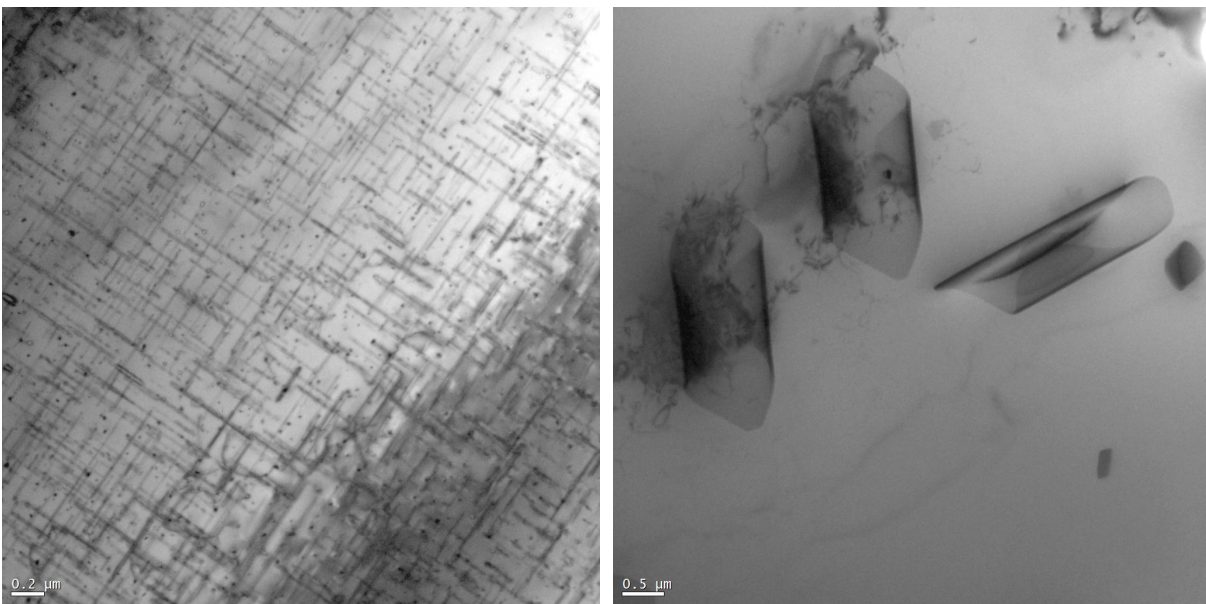


Figure 40: Sample A0.1 (300°C) with β' precipitates (left), sample A0.2 (400°C) with Si curls (right)

On the right of Figure 40, the microstructure quenched at 400°C is shown exemplary. At this point, the Si plates/curls shrank significantly from previously up to 8 μ m to only 4 μ m (comparing the first image of Figure 39 and the right one of Figure 40). Dispersoids or Mg-Si precipitates were not detected in that sample.

At 520°C (Figure 41), the Si plates completely dissolved and no Mg-Si precipitates were detectable, even when the crystal was oriented in (100). The remaining characteristics were dislocations and a few isolated oxide inclusions consisting of silicon oxide and aluminium oxide.

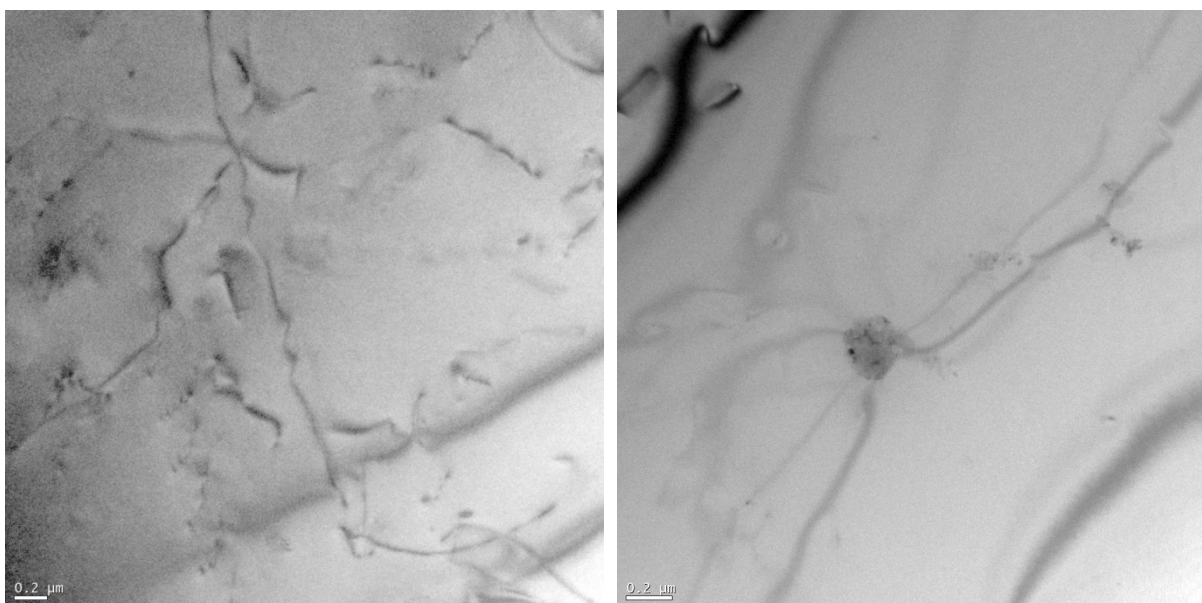


Figure 41: TEM micrographs of sample A0.3 (520°C, left) and A0.4 (565°C, right)

The samples A0.4 (565°C) and A0.5 (570°C) showed similar properties as A0.3 (520°C). Further TEM micrographs and EDX measurements at the different levels of the industrial heat treatment process are available in the appendix (Figure 71 - Figure 79 on page xvii - xxv).

The examinations have shown that the formation of dispersoids in the model alloy was successfully suppressed. Even after the entire homogenization treatment was completed, no dispersoids were detected.

5.2.3 Grain Size Analysis

The grain size is critical for the nucleation rate during recrystallization. Hence, it is necessary to compare the grain size of the model alloy with the industrial material and to keep track of grain growth during heat treatment.

For each of the samples A1-A6, at least three sectors of the surface were analysed with a magnification of 50. Each sector contained about 200 grains. Partial grains at the boundaries were excluded. As an example, Figure 42 shows the original picture (left) and the processed picture with the outline of the grain boundaries (right).

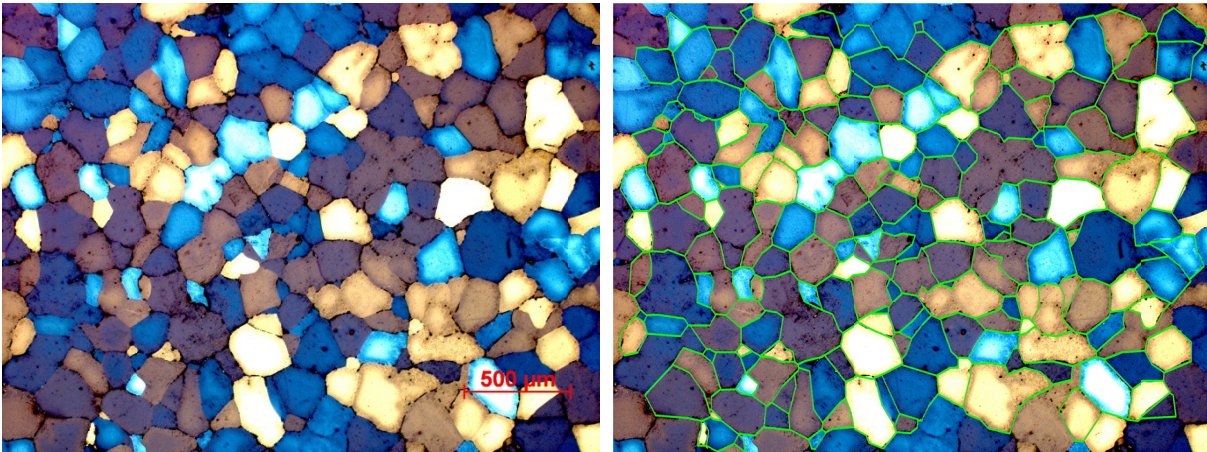


Figure 42: LOM micrograph of sample 9 (as-cast) with sketched grain boundaries; Barker's etch, 50x magnification, polarized light

The results of the grain size analysis are listed in Table 12. During the homogenization, the average grain sizes increased only marginally. Up to 520°C, the grain sizes ranged from 141μm to 153μm and are similar to the measurements of the industrial material which reached values of about 120μm. However, at 565°C (A4) and 570°C (A5) abnormal grain growth was observed. The corresponding values are highlighted red in the table below.

Table 12: Average grain sizes (values with abnormal grain growth in red)

Sample	Average grain size [μm]
As-cast - 9	147
300°C - A1	151
400°C - A2	153
520°C - A3	141
565°C - A4	155
570°C - A5	595

Figure 43 grants an overview of the stages from 300-565°C of the heat treatment where the grain size remained almost constant. Each etching was performed for 45s at 20V and the frames show an area of approximately 5.5mm².

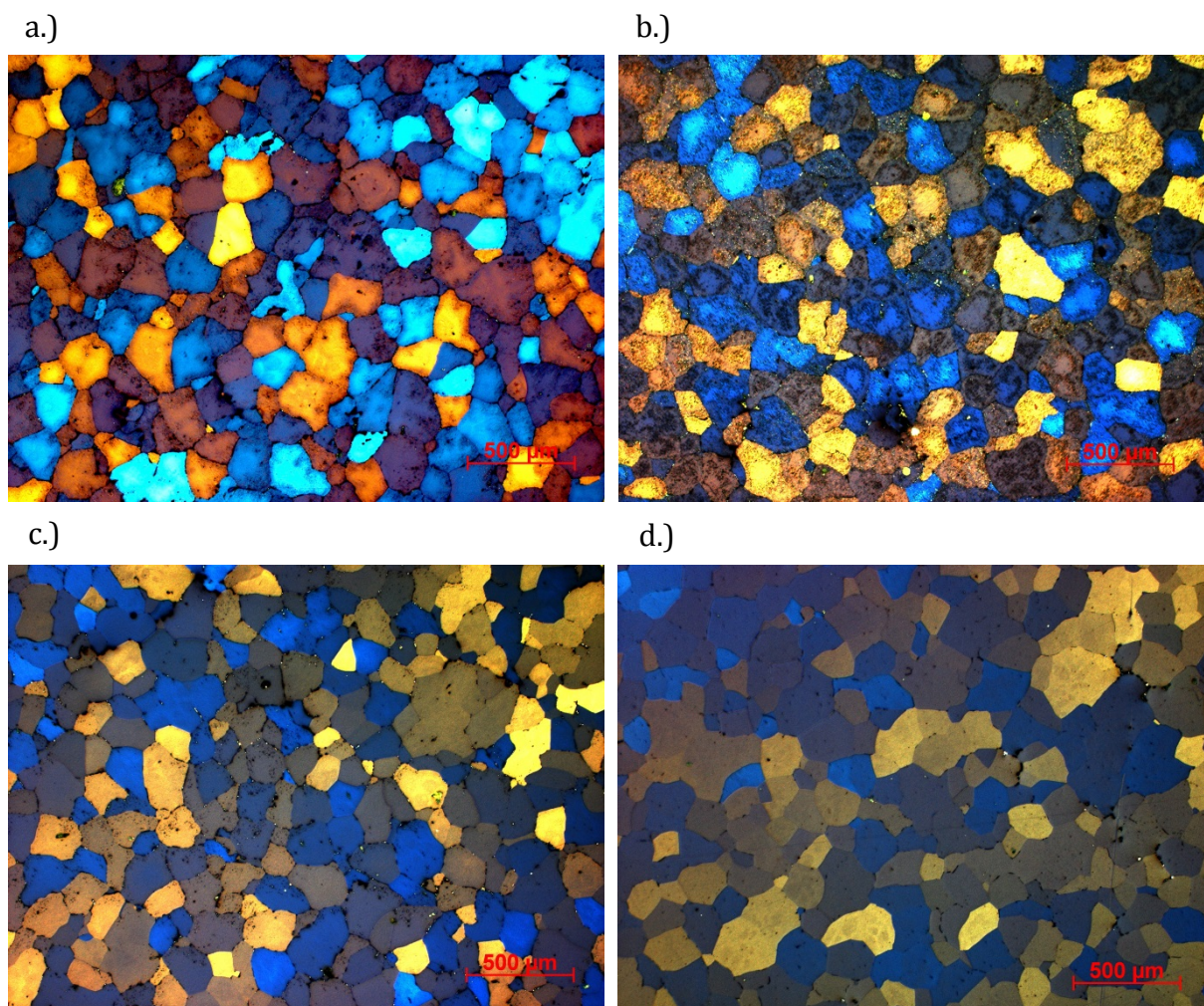


Figure 43: LOM micrographs at 300°C – A1 (a.), 400°C – A2 (b.), 520°C – A3 (c.), and 565°C – A4 (d.); Barker’s etch, 50x magnification, polarized light

The etchings showed similar grain size distribution for each sample. Interestingly, sample A4 (565°C) had areas with regular sized grains as in Figure 43 (d.). On the other hand, a single giant grain as is displayed on the left of Figure 44. Sample A5 (quenched after approximately 16h at a peak of 570°C) showed the advanced state of the abnormal grain growth. The grains reached sizes too large for the frame. Even with reduced magnification, the extent of the growth could not be captured entirely. Grains with a diameter of over 8mm were measured.

Histograms of grain size distribution for each etched specimen are attached in the appendix (Figure 69 and Figure 70 on page xv and xvi).

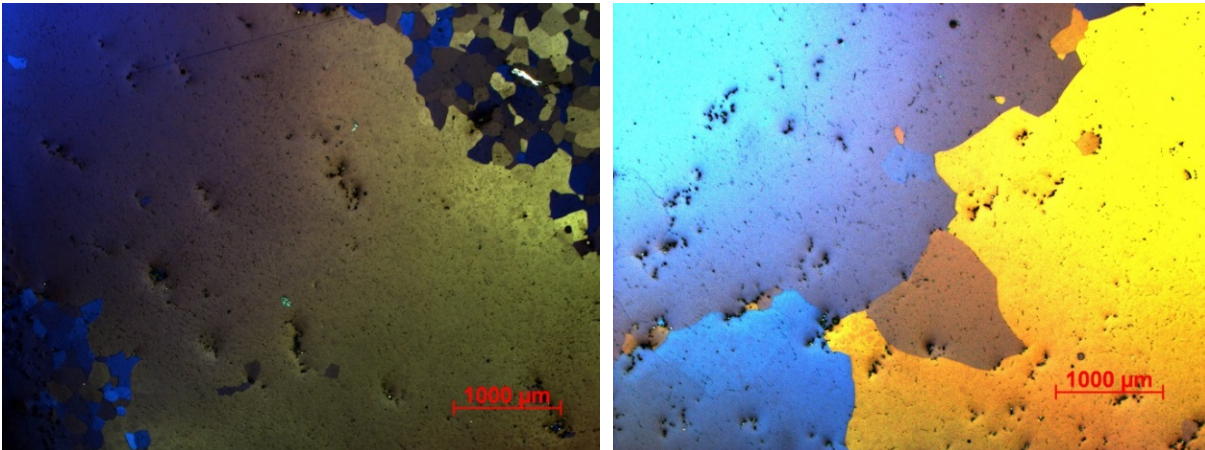


Figure 44: LOM micrographs at 565°C - A4 (left), 570°C - A5 (right); Barker's etch, 25x magnification, polarized light

5.3 Shortened Homogenization

The homogenization described in the previous chapter established that no dispersoid formation was possible in the model alloy. Unfortunately, the abnormal grain growth occurring towards the end of the homogenization presented a problem for the following compression tests. As the grain boundaries are preferable nucleation sites for recrystallization [58], abnormal grain growth reduces the number of possible nucleation sites and thus delays the rate of recrystallization. This effect would distort the results and they would not be comparable to values gathered with regular 6061 where no abnormal grain growth appears. For these reasons, a shortened version of the homogenization was designed. The aim of this version was to avoid abnormal grain growth while achieving similar phase fractions.

The temperature profile of the shortened heat treatment is shown in Figure 45. The furnace was preheated to 565°C before two specimens were inserted into it. In approximately 10min, the specimens reached 565°C. After 5min and 10min at 565°C, a sample was instantly quenched in water.

LOM micrographs of the samples which underwent the shortened heat treatment are shown in Figure 46. It takes a holding time of about 10min at a temperature of 565°C for Mg₂Si to dissolve completely. After only 5min at 565°C, significant amounts still remained.

Results

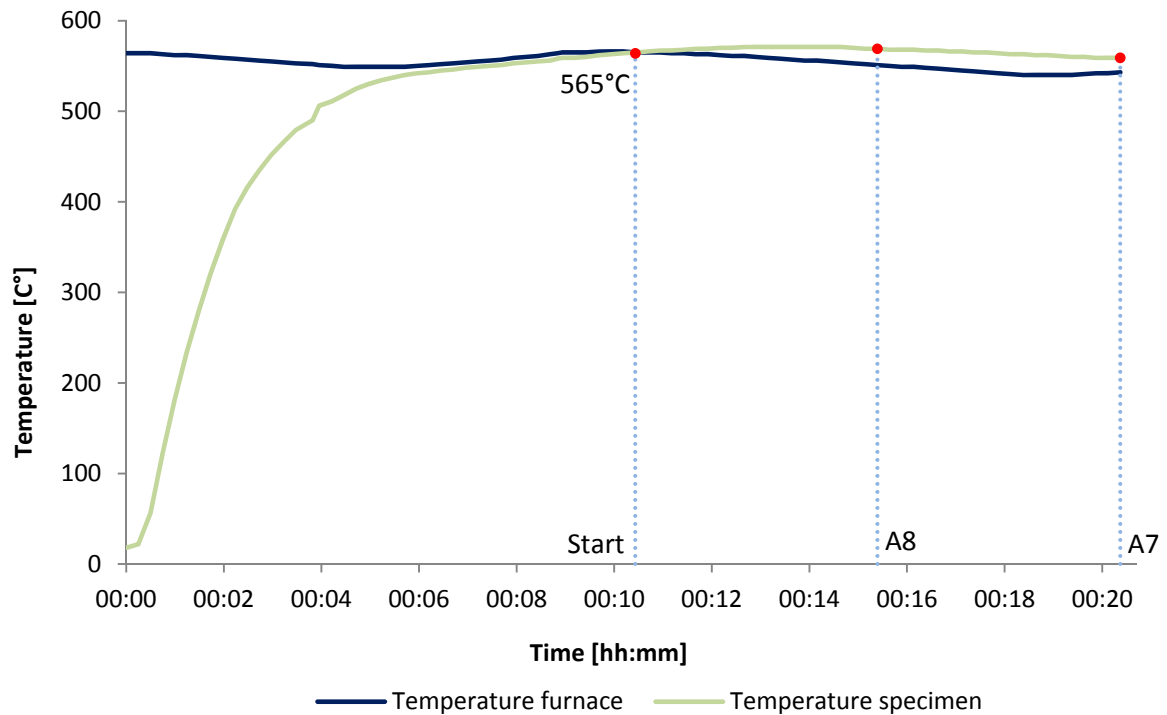


Figure 45: Temperature profile shortened homogenization

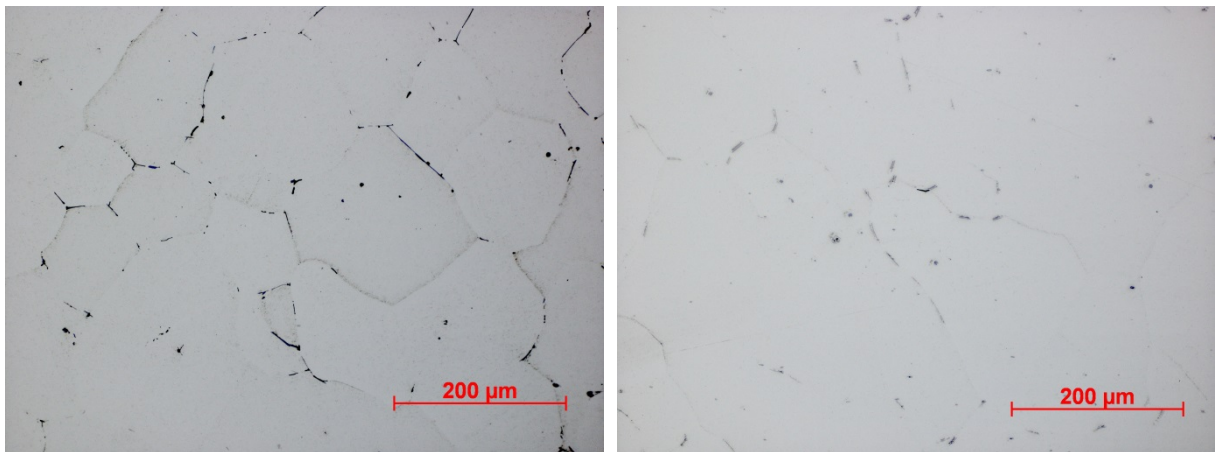


Figure 46: LOM micrographs (200x magnification) A8 - 5min at 565°C (left) and A7 - 10min at 565°C (right)

The evaluation of the phase fractions showed that during the shortened process Mg_2Si already decreased significantly within the first 5min from 0.28% to 0.13% and dropped to 0% after 10min. Again, the fraction of $AlFeSi$ only showed slight negative tendencies. The phase fractions of both homogenizations are laid out side by side in Figure 47.

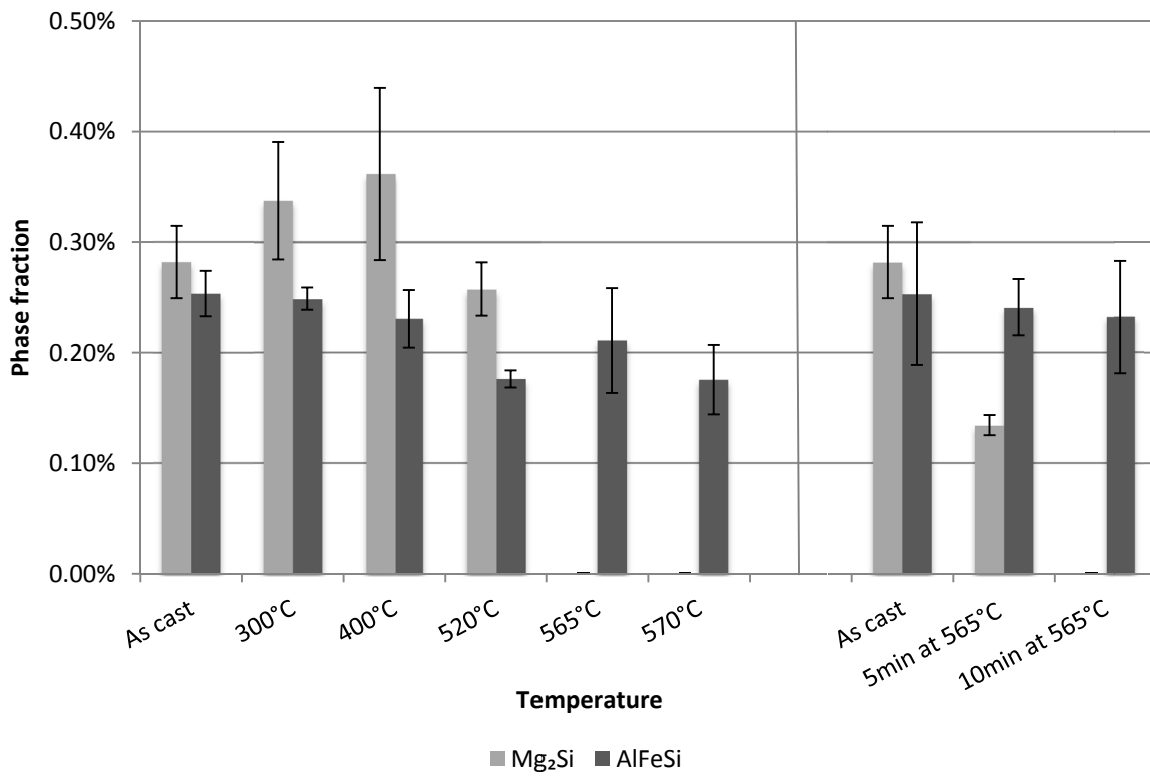


Figure 47: Phase fraction depending on heat treatment

Micrographs of the etched samples for the grain size analysis are displayed in Figure 48. In that heat treatment, grain growth was effectively limited to only a few micrometres and no abnormal grain stood out.

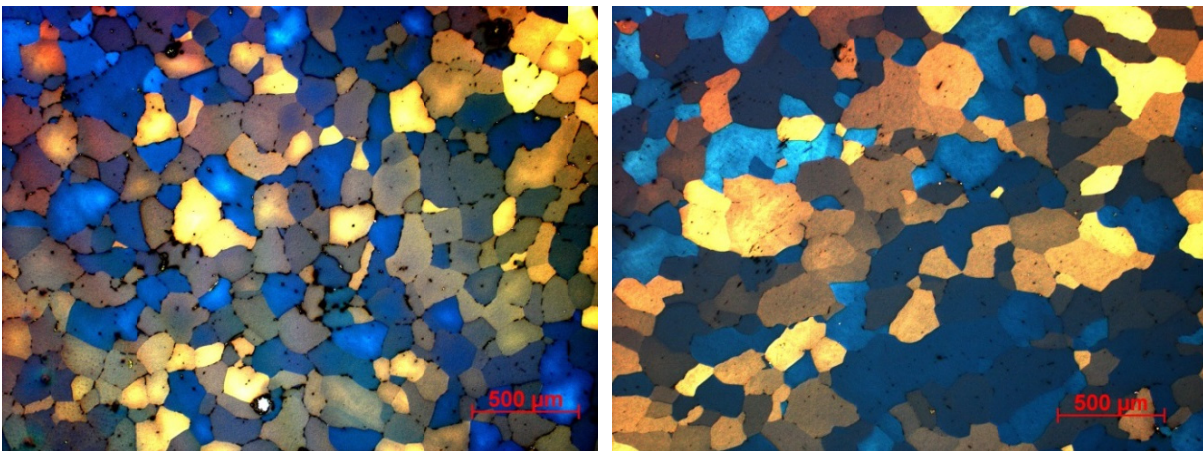


Figure 48: LOM micrographs 5min at 565°C - A8 (left), 10min at 565°C - A7 (right); Barker's etch, 50x magnification, polarized light

A summary of the average grain sizes for both heat treatments is given in Table 12. The table shows very similar values for both cases and proves that abnormal grain growth was successfully suppressed.

Table 13: Average grain sizes depending on heat treatment (values with abnormal grain growth in red)

Sample	Average grain size [μm]
As-cast - 9	147
300°C - A1	151
400°C - A2	153
520°C - A3	141
565°C - A4	155
570°C - A5	595
5 min at 565°C - A8	139
10 min at 565°C - A7	145

The shortened homogenization met all requirements for the planned compression tests: Dispersoid formation was avoided, grain sizes were similar to the one of 6061 after regular industrial homogenization, and Mg_2Si was completely dissolved.

5.4 Compression Tests

The samples for the compression tests were homogenized in a dilatometer based on the shortened homogenization at 550°C for 10min. Simulating industrial hot rolling, the samples were then compressed with varying degree of deformation, deformation rate, and holding time after deformation. The deformation triggered recrystallization that continued over the holding time until the sample was quenched rapidly. The state after quenching was then analysed with EBSD.

The temperature and the dimensions of the samples were monitored throughout the compression tests. A measured temperature profile is shown in Figure 49. The actual temperature follows the target temperature very closely until quenching. A maximum deviation of 2°C occurred during deformation. Subsequently, the temperature was lowered to less than 300°C in only 15s. At this point, however, the high quenching rate could not be sustained and a deviation from the target temperature was clearly visible.

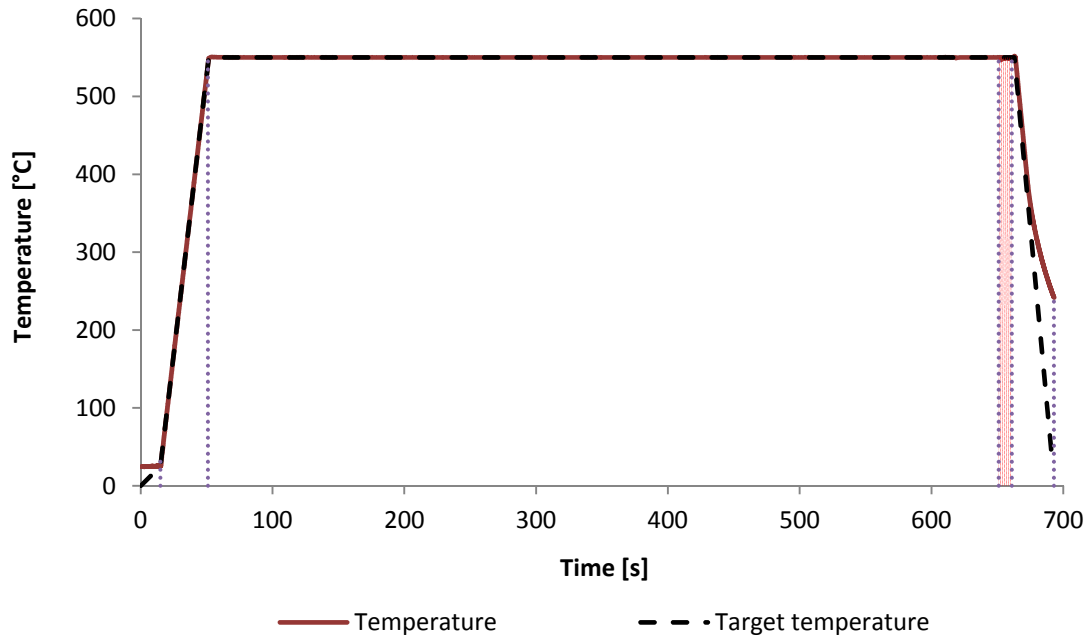


Figure 49: Temperature profile for the compression tests

Exemplary, Figure 50 shows the deformation profile of sample B1/0.1. The deformation was increased linearly to $\phi=1$ with a gradient of the deformation rate. The duration of the deformation varied from 0.02s (sample B0.2/10) to 10s (sample B1/0.1). The remaining deformation profiles are attached in the appendix (Figure 80 and Figure 81).

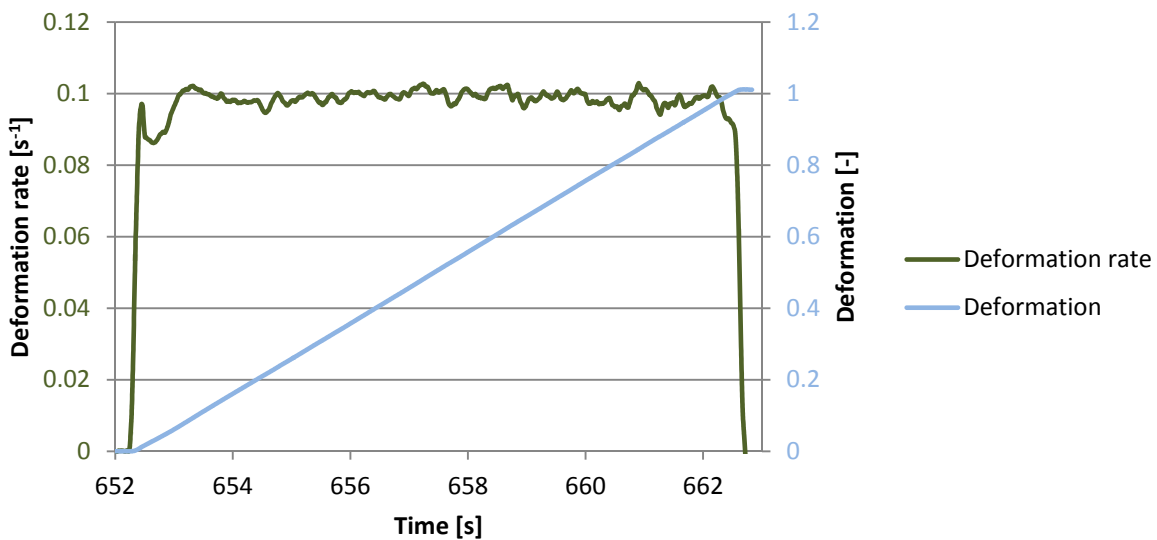


Figure 50: Deformation profile for $\phi=1$ and $\phi=0.1$ (sample B1/0.1)

Results

After deformation, the samples were examined with EBSD to evaluate the state of recrystallization. The obtained EBSD patterns offered insight on the crystal structure of the material. Together, the patterns could be assembled into an inverse pole figure (IPF) showing the orientation of the lattice in different colours. From the crystal orientation and the grain size, conclusions could be drawn regarding the state of recrystallization.

Image a.) in Figure 51 shows the crystal structure of the undeformed sample B0/0 with evenly coloured large grains. In contrast, sample B0.2/10 (b.) exhibits colour gradients within the grains indicating a slightly deformed microstructure. With increasing degree of deformation, the size of the grains decreased and the colour gradient within the grains vanished as seen in B0.5/10 (c.). This indicates already advanced recrystallization.

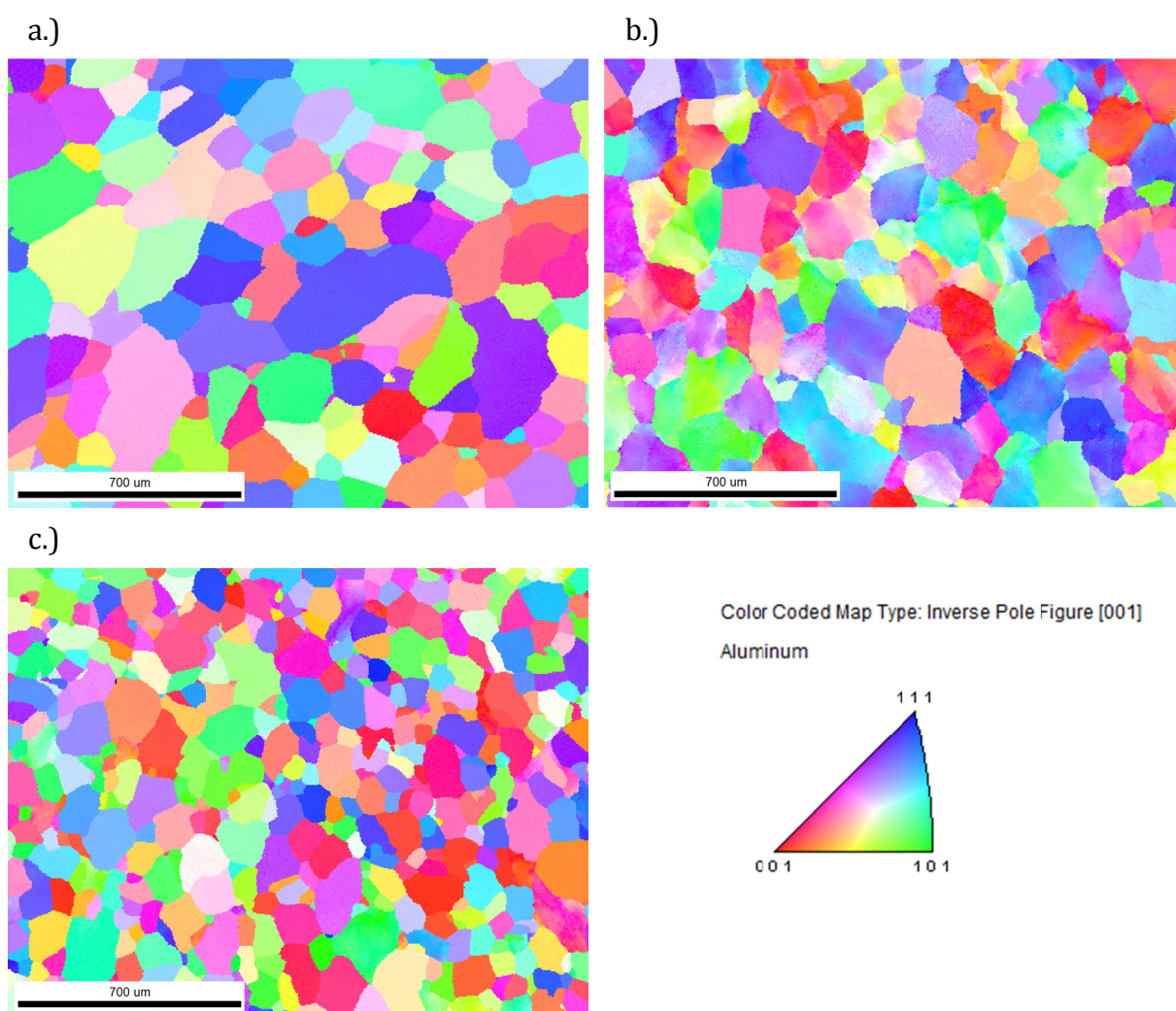


Figure 51: IPF of samples B0/0 (a.), B0.2/10 (b.), and B0.5/10 (c.)

Results

Figure 52 displays the influence of the deformation rate on the crystal structure. B1/0.1 (b.) was extensively deformed and shows multiple subgrains. When the rate of deformation increased, the grains recrystallized and the subgrains disappeared as in sample B1/5 (c.).

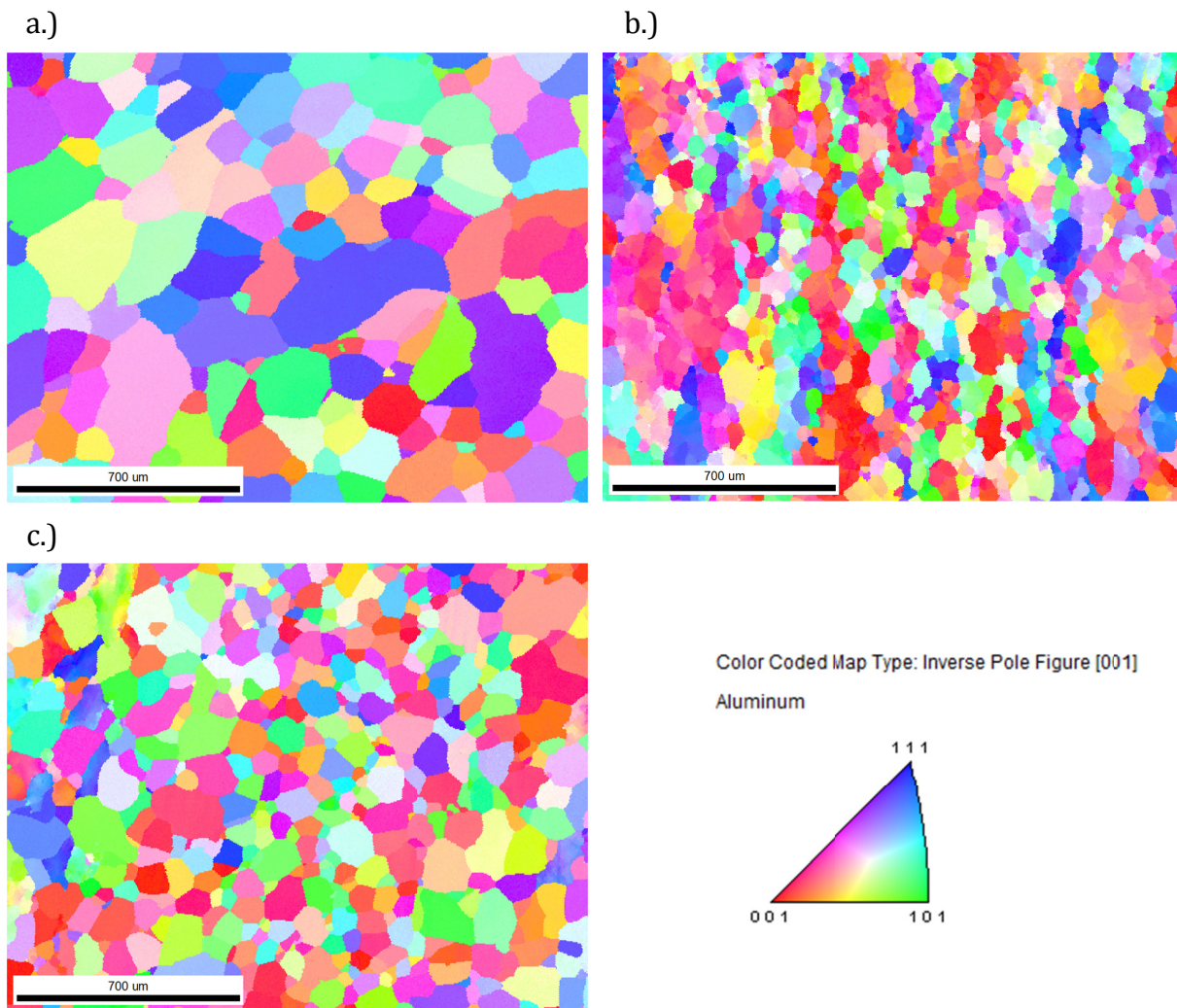


Figure 52: IPF of samples B0/0 (a.), B1/0.1 (b.), and B1/5 (c.)

However, the IPF was not sufficient as an objective indicator for the recrystallized fraction in the sample. Measuring the grain orientation spread (GOS) proved to be a more functional way to generate comparable values [59]. As a threshold, the critical angle $\theta_{cr(GOS)}=7.5^\circ$ was set to mark new grains and only grains larger than the critical diameter $d_{cr(GOS)}=1\mu\text{m}$ were considered. These parameters were defined based on previous examinations performed by Sepehrband et al. [44].

Results

Figure 53 displays the resulting GOS of the undeformed sample B0/0. The colour blue characterizes areas with a GOS smaller than 0.5° . On the other end of the scale, red areas indicate a GOS of more than 4.5° . The misorientation directly translates into the state of recrystallization or recovery. Grains with values less than 1.5° have a very low misorientation and are defined as undeformed, recovered, or recrystallized for the following assumptions analogue to a paper by Polkowski et al. [59]. Recrystallized grains are equiaxed and start small before growing. The grains that only recovered remain deformed in deformation direction. Grains with a GOS of 1.5° or more are considered deformed and unrecrystallized.

In contrast to the undeformed sample (a.), Figure 53 b.) represents a highly deformed microstructure. The outlined areas are elongated and new small grains without misorientation appear in between.

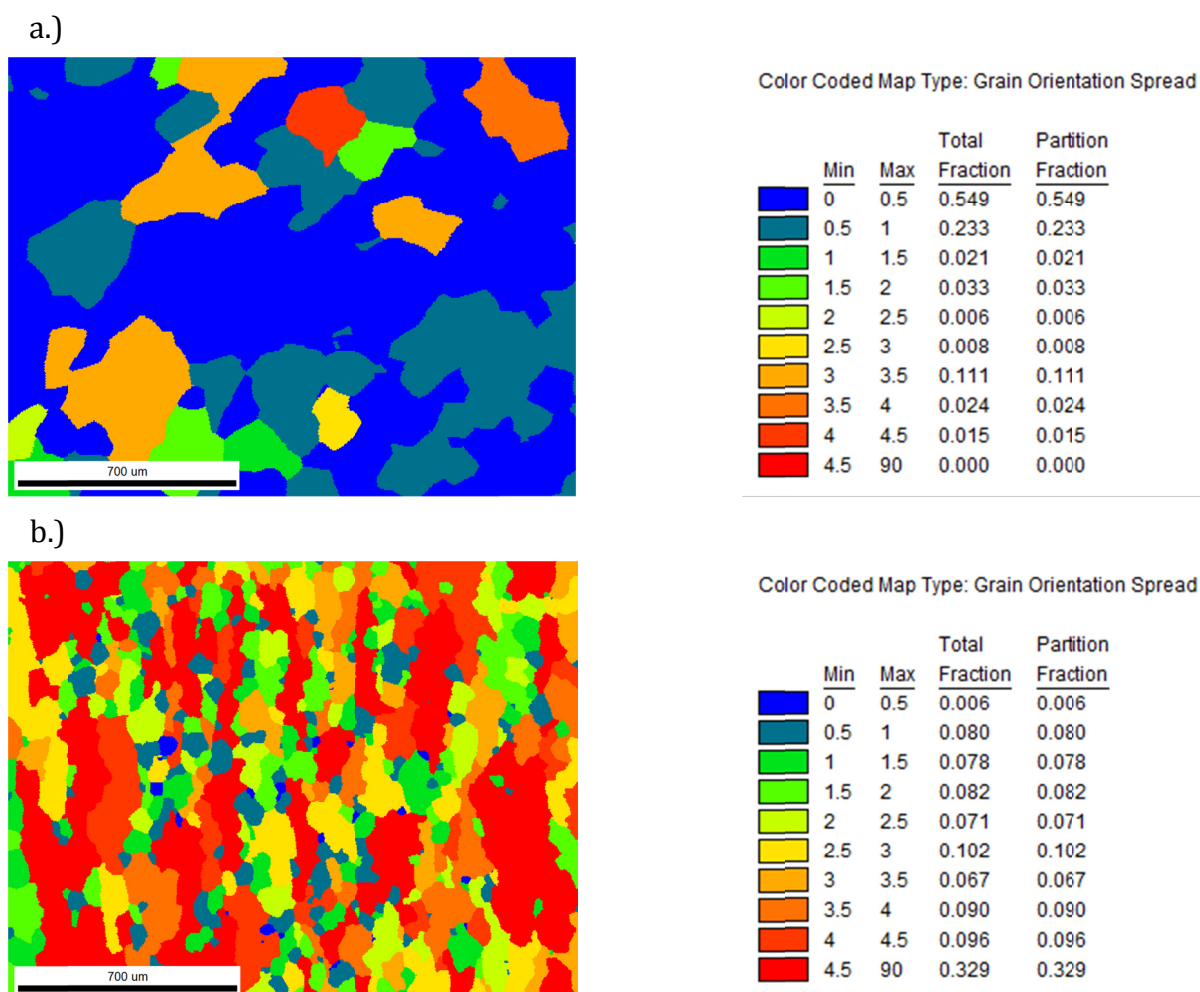


Figure 53: GOS of sample B0/0 (a.) and B1/0.1 (b.)

Results

With an increased rate of deformation, the misorientation decreases (Figure 54). Especially in the central area, where the strain reaches its peak, the grains are almost free of deformation.

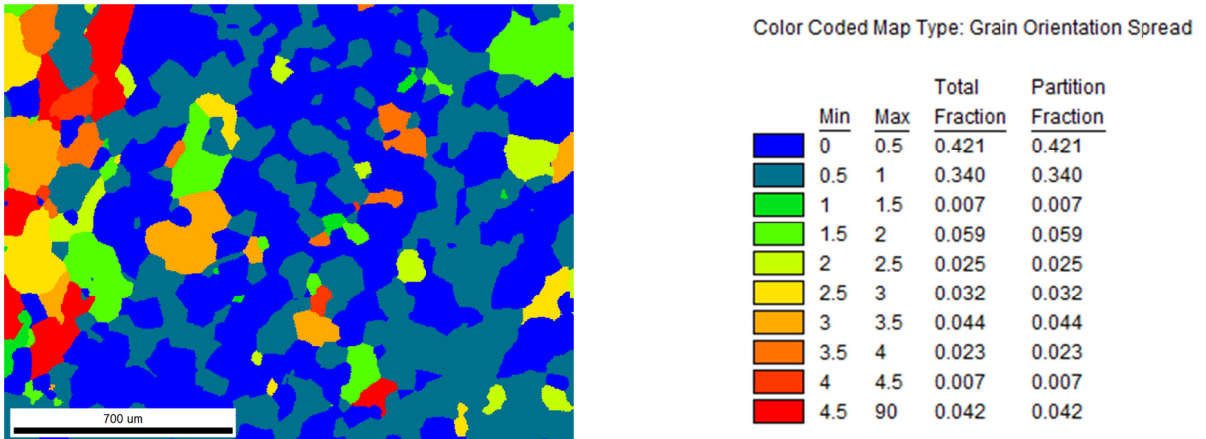


Figure 54: GOS of sample B1/5

The phenomenon of the reduced misorientation in the central area becomes even more evident in the following image of sample B1/0.5. A major part of the central area is already coloured in blue and green while the lateral borders of the image remain heavily deformed.

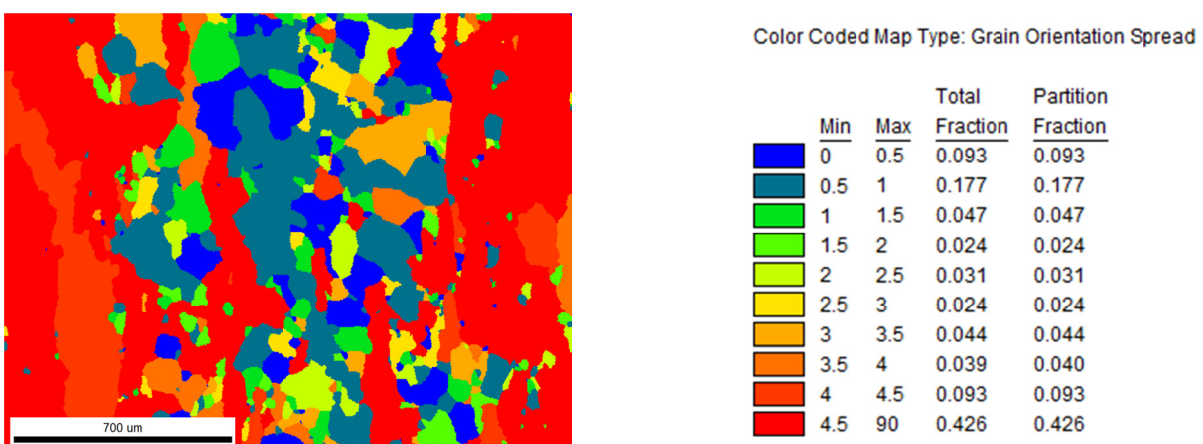


Figure 55: GOS of sample B1/0.5

Figure 56 shows the already fully recrystallized sample B0.5/10. Almost the entire surface is coloured in dark blue representing a low GOS.

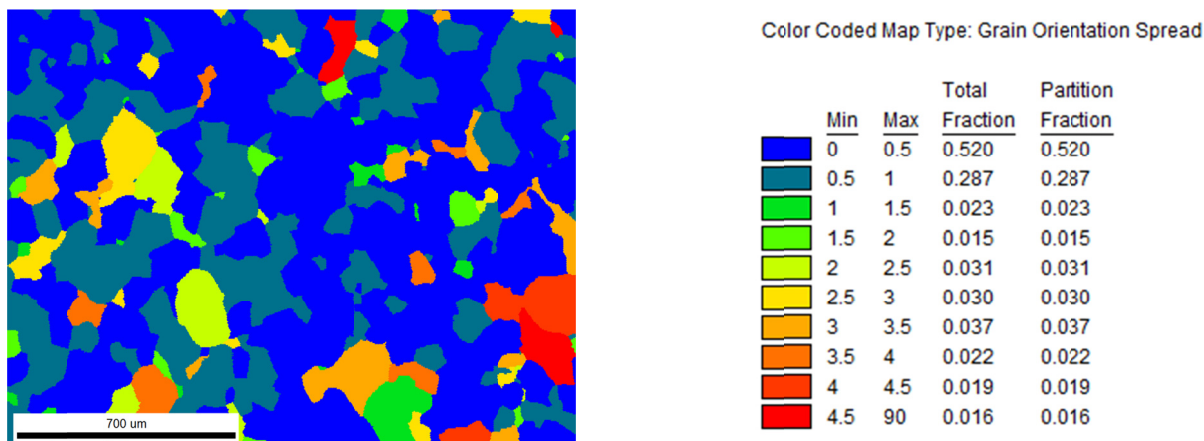


Figure 56: GOS of sample B0.5/10

Figure 57 summarizes the results of the EBSD measurements of the recrystallized fraction. The diagram on the left shows recrystallization depending on the degree of deformation with constant $\dot{\varphi}=10$. Starting at $\varphi=0.2$, the value lies at 12%. Shortly after, the recrystallized fraction rises rapidly to around 80%. This peak is very similar to the properties of sample B0/0 prior to deformation. At $\dot{\varphi}=0.35$, the sample can already be seen as fully recrystallized or recovered.

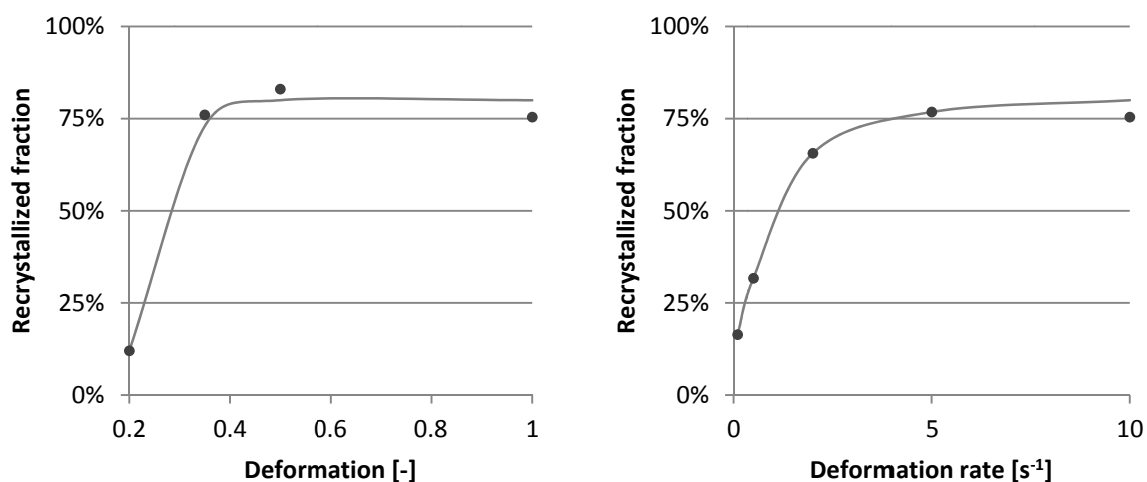


Figure 57: Misorientation depending on degree of deformation and rate of deformation

Results

The second diagram in Figure 57 displays the recrystallized fraction in relation to the deformation rate while the deformation remains at $\varphi=1$. The curve has an analogical behaviour to the one before: Initially, the fraction is 16% then rising promptly until the values settles at approximately 80% for $\dot{\varphi}=5$.

The critical angle for high angle boundaries (typically set at 10-15° [2]) and the critical grain diameter for the calculations of the grain size were defined as $\Theta_{cr(GS)}=15^\circ$ and $d_{cr(GS)}=10\mu\text{m}$. Figure 58 shows the average grains sizes after compression. A higher degree of deformation reduced the grain sizes before it levelled at about 80 μm for $\varphi=0.5$. Similar values are reached for the different deformation rates.

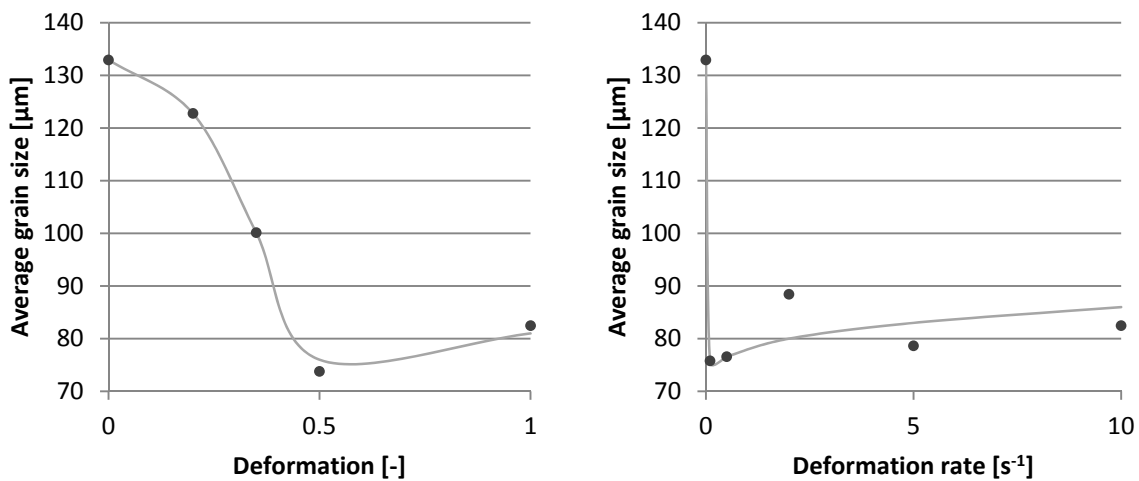


Figure 58: Average grain size depending on degree of deformation and rate of deformation

For sample group C, a holding time after deformation was inserted and the quenching rate increased. The measured temperature is shown in Figure 59.

The quenching rate was raised from 17.5K/s in group B to 175K/s in group C. As seen in Figure 61, the increased quenching rate did suppress recrystallization. On the right side is the GOS for B1/0.1 ($\varphi=1$, $\dot{\varphi}=0.1\text{s}^{-1}$) and on the left the one for C0. Sample C0 has the exact same deformation parameters as B1/0.1 aside from the increased quenching rate. The large red areas marking highly deformed grains are predominant in the left image. In the right picture with the slower quenching rate, the fraction of these red areas decreased significantly. Through recovery, the highly deformed areas turned into orange and yellow ones of medium misorientation. The small, dark blue-coloured specks

appearing in the right image are newly nucleated and dislocation-free grains. They mark the beginning of recrystallization in B1/0.1 resulting from the slower quenching rate.

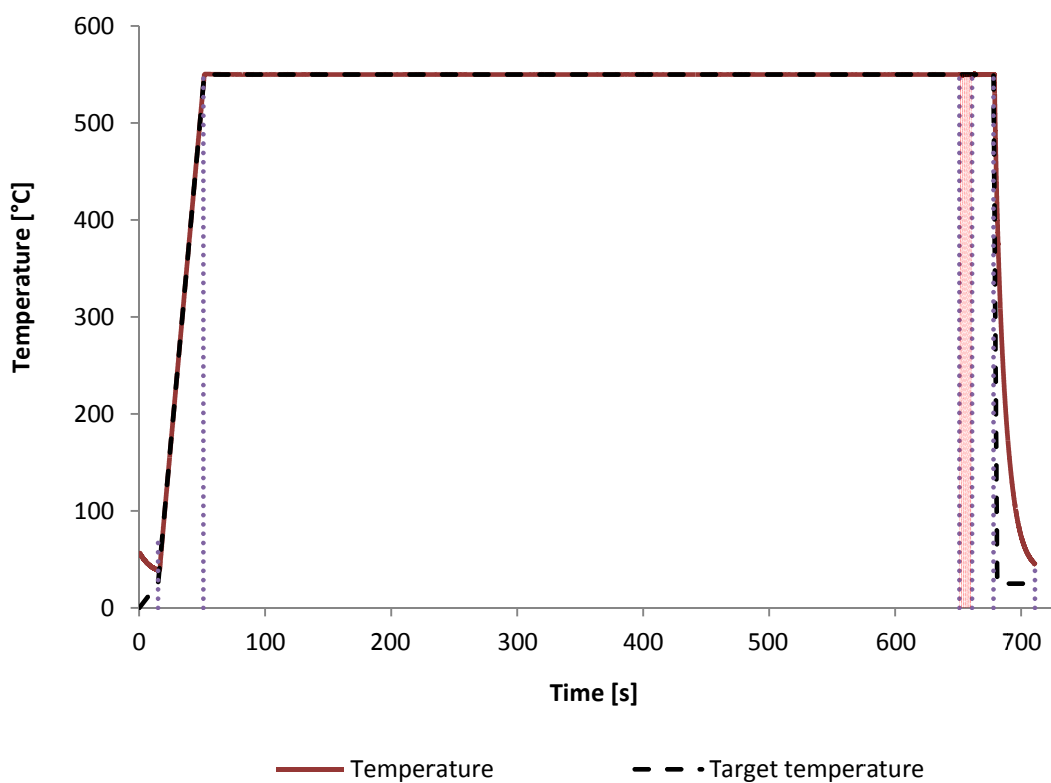


Figure 59: Temperature profile for compression tests with added holding time and increased quenching rate

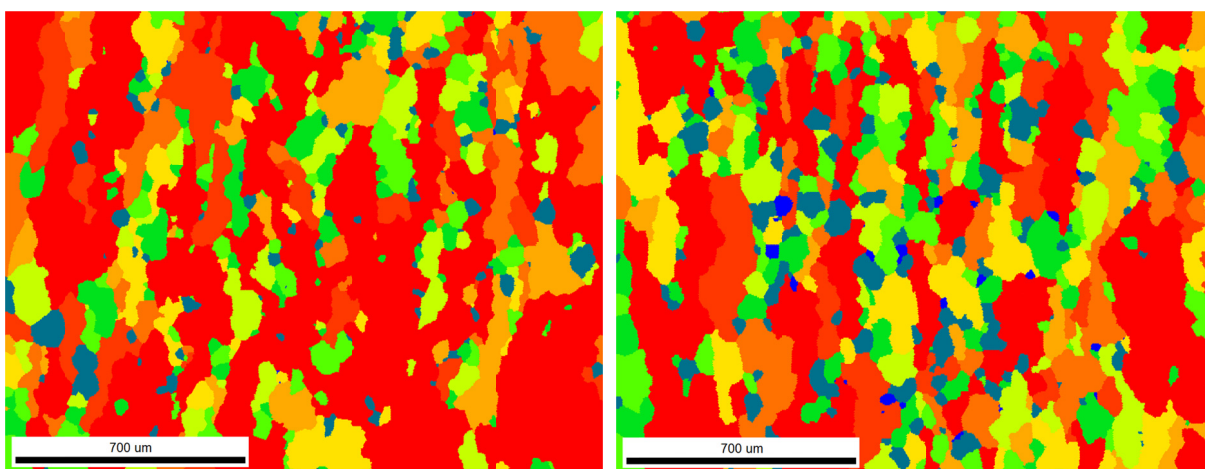
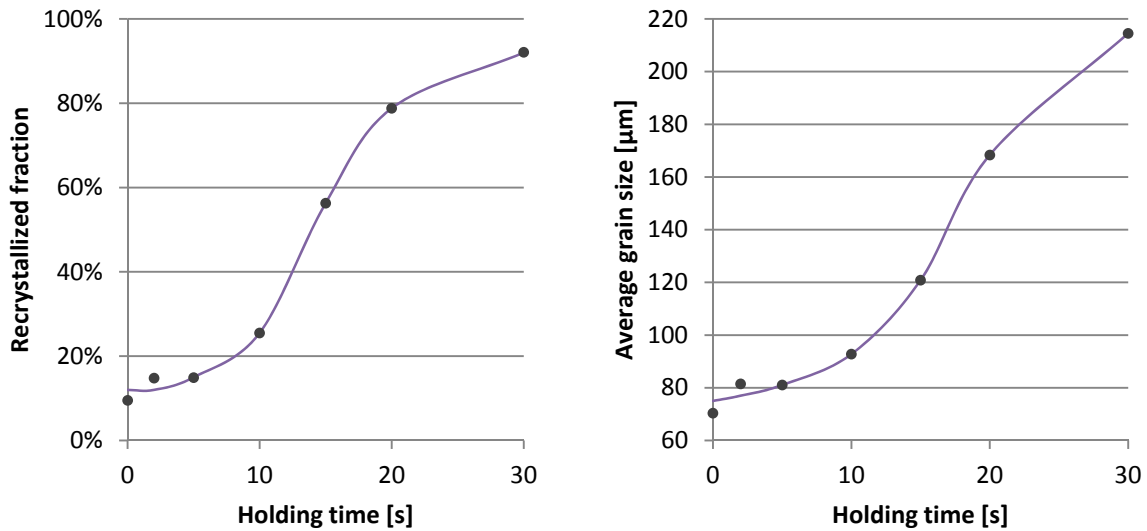


Figure 60: GOS of sample C0 (left) and B1/0.1 (right)

Results

As plotted in Figure 61, the recrystallized fraction and the average grain size equally increased when the holding time was extended. It is striking that after 20s the values of the original undeformed sample B0/0 were already reached and even surpassed.



**Figure 61: Misorientation and average grain size depending on holding time after deformation;
 $\varphi=1$, $\varphi=0.1$**

A complete selection of all IPFs, GOSs, grain maps, and histograms of grain size distribution for the sample groups B and C is available in the appendix from page xxviii to xlvlxix.

6 Discussion

The results presented in the previous chapter are further discussed in the section beneath and contextualized with pre-existing research on this topic.

6.1 Alloy Composition and Casting

Initially, it was planned that the final model alloy would have an alloying content of 0.81wt% Si and 0.63wt% Mg as a common 6061 alloy without any other accompanying elements. Although slight deviations resulted, the Mg-Si contents remained within the range of the values set by “*ÖNORM EN 573-3:2013-12-01*” [9] with an achieved alloying content of 0.80wt% Si and 0.65wt% Mg. The other alloying elements were kept at levels below 0.01wt%. The only notable impurities that also had an impact on the later microstructure were Fe with an amount of 0.045wt% and Ti acting as grain refinement even at low alloying levels.

These minor deviations can already have an impact on the grain boundary mobility as shown by Huang and Humphreys [39] but they are almost inevitable on larger scale. High-purity aluminium is very costly and contamination can occur easily. Residues on the casting equipment, the equipment itself, and contaminated alloying elements can cause impurities in the final material. However, the main focus of this work was not on solute drag, but on the effects of disperoids. The major disperoid-forming elements, Mn, Cr, and Fe, were kept at a minimum and the formation of disperoids was successfully suppressed as shown in Chapter 5.2.2. For common application, a content of 0.5wt% Fe would not have a negative influence on ductility. Above 0.5wt% Fe, AlFe-needles can form during annealing and cause brittleness [5].

The casting with the customized ingot mould with the parameters as described in Chapter 4.1 was a success since the overall quality of the ingot can be described as very satisfying. No major casting defects such as shrinkage porosity, gas porosity, or large inclusions were observed. The outer material was broadly removed as a precaution (displayed in Figure 25) leaving a centrepiece with a constant microstructure and an even grain size distribution consistent with the industrial-grade material. In the following processes and experiments, no anomalies linked to casting defects were observed. Therefore, this casting procedure can be recommended for further experiments regarding similar topics.

6.2 Microstructure

The observed and with EDX measurements confirmed primary phases occurring prior to the full homogenization in the model alloy were:

- β -Mg₂Si
- β -Al₅FeSi

Both primary phases have a plate-like appearance but β -Mg₂Si is evidently darker than β -Al₅FeSi in the micrographs with LOM and SEM. The presence of other Fe-containing phases such as variants of α -Al(Fe,Cr,Mn)Si could not be confirmed. α -Al(Fe,Cr,Mn)Si has a very distinctive 'Chinese script-like' morphology (described in [24], [28]) and did not appear in any of the micrographs. Low contents of Fe, Cr, and Mn seem to favour the formation of β -Al₅FeSi. This effect was also observed by Jeniski [26] within the examination of the role of Cr in 6061.

Another primary phase typically occurring in 6xxx alloys is the Q-phase [24]. However, there was no sign of such a phase. The absence of the Q-phase is not surprising, for the Cu contents in the model alloy are close to zero. The optical emission spectrometer showed a negligible value of less than 0.0004wt%.

Apart from Al, Mg, Si, and Fe, no other elements were identified that formed any kind of phases.

It is vital to determine the initial grain size of the specimens since the grain boundary density directly affects the recrystallization kinetics [2]. The grain size in the as-cast material measured with EBSD analysis was on average 132 μ m. The values obtained manually from the etched samples through LOM with polarized light lay between 134 μ m and 157 μ m. The average of 147 μ m is therefore slightly above the EBSD measurement. Apparently, the EBSD analysis detects and includes smaller grains better than conventional LOM techniques. Gao et al. [54] came to similar results when comparing values obtained by LOM and by EBSD analysis. According to their studies, EBSD measurements are more accurate and less dependent on preparation or the selected etching procedure.

6.3 Heat Treatment

Prior to hot rolling, aluminium slabs are usually homogenized at temperatures of around 550°C. The resulting microstructure of the model alloy exposed to such an industrial heat treatment is displayed in Figure 37 on page 53 and in the appendix from page xii to xiii.

During homogenization, the phase fraction of β -Mg₂Si increased slightly from 0.28% to 0.36% before decreasing sharply at temperatures above 500°C. At 565°C, the fraction of β -Mg₂Si reached 0%. Apparently, Mg₂Si remained in solid solution after casting and further precipitated or coarsened up to 400°C. After this point, the solubility of Mg and Si increased far enough to dissolve the entire amount of β -Mg₂Si. The content of β -Al₅FeSi decreased slightly throughout the homogenization according to the measurements. From initially 0.25%, the fraction of β -Al₅FeSi was reduced to 0.18%. It seems that β -Al₅FeSi was already precipitated completely after casting and then dissolved marginally with increasing temperatures. However, this marginal decline was within the fluctuation range.

A transformation from plate-like β -Al₅FeSi to more globular α -AlCrFeMnSi as described by Kuijpers [27], [29]–[31] and as displayed in Figure 7 was not observed during the homogenization of the model alloy. When comparing pre- and post-homogenization micrographs, no alterations of the Fe-containing phases are visible. A possible explanation is that the lack of Cr and Mn stabilizes β -Al₅FeSi as described by Jeniski et al. [26] in the case of Cr. Another reason could be that duration and temperature of the homogenization were not sufficient for the transformation to be significant. For the transformation to progress as far as in the research of Kuijpers [31], a temperature of 590°C for a duration of 32h was required.

The examinations with TEM confirmed that reducing the content of Fe, Cr, and Mn to a minimum had the desired effect of preventing the formation of dispersoids. Several areas of the samples were thoroughly scanned and not a single dispersoid was revealed with TEM. A few Si plates/curls and Mg-Si precipitates were observed at lower temperatures but were dissolved by the end of homogenization.

The grain size was almost unaffected up to 520°C and remained around 145 μ m. However, the samples quenched at 565°C and 570°C exhibited abnormal grain growth. Large grains would reduce the drive for recrystallization and falsify the results of the

deformation tests [2]. Therefore, the heat treatment had to be modified to suppress abnormal grain growth.

The occurrence of abnormal grain growth was avoided by increasing the heating rate and reducing the holding time at homogenization temperature. For the shortened heat treatment, the samples were heated up to the homogenization temperature in only 10min and the holding time was limited to 10min instead of several hours. At this point, the fraction of Mg-Si dissolved completely and the levels of β -Al₅FeSi remained similar. A holding time of 5min was not sufficient, for parts of β -Mg₂Si were still visible in LOM and SEM. Grain size analysis attested that no abnormal grain growth occurred during the shortened heat treatment. The grain sizes remained at approximately 140 μ m.

6.4 Recrystallization

The samples of group B (IPFs, GOSs, and grain maps are available in the appendix in Chapter 12.4) show a strong correlation between φ and recrystallization as well as between $\dot{\varphi}$ and recrystallization. Higher φ and $\dot{\varphi}$ result in higher recrystallization rates. For $\varphi=0.35$ and $\dot{\varphi}=5s^{-1}$, the specimens can be considered fully recrystallized. At these values, the misorientation in the grains is at the same level as it had been before deformation. The equiaxed shape and smaller grain size indicates that new grains were formed: the grains actually recrystallized and did not merely recover.

These observations are in accordance with the theoretical basics by Humphreys and Hatherly [2]. A higher degree of deformation results in a larger amount of stored energy. Therefore, the driving force for recrystallization increases. Slower rates of deformation allow a decrease in stored energy due to dynamic recovery occurring during deformation. Since the specimens were quenched immediately after deformation, however, no recrystallization at all should have been observable. Dynamic recrystallization does usually not occur in metals of high stacking fault energy such as aluminium [2], [60].

The most obvious explanation seemed to be that the quenching rate was not sufficient to cool the samples below T_R before recrystallization set in. For this reason, the quenching rate was increased in the next test group C. Furthermore, the holding time after deformation was varied to establish the relationship between recrystallization and holding time.

For the last test series, the quenching rate was accelerated from 17.5K/s in group B to 175K/s in group C. Figure 60 on page 71 shows that the recrystallization could indeed be suppressed. The nucleation sites for recrystallization, visible in sample B1/0.1 ($\varphi=1$, $\dot{\varphi}=0.1s^{-1}$), did not occur in C0 which had the exact same deformation parameters.

The recrystallization rate in the dispersoid-free material was higher than expected. In experiments by Jeniski with a 6013 alloy deformed at 440°C to a similar degree and annealed at 560°C, it took more than 10min to fully recrystallize due to present dispersoids [22]. The dispersoid-free model alloy with the parameters $\varphi=1$ and $\dot{\varphi}=0.1s^{-1}$ was fully recrystallized after merely 20s and the grains grew rapidly beyond their initial size before deformation. This difference illustrates the enormous effects of dispersoids on recrystallization.

The small specimen size was not an issue in this research. In comparison to the grain sizes, the specimens are still relatively large. Problems mostly arise when the grain sizes are in the same range as the thickness of the sample. In thin sheets or foils, growing grains may intersect with the surface and thus be restrained [2].

This work confirmed that producing a model alloy free of dispersoids formation while having similar properties to regular 6061 is possible. The tests have demonstrated the role of the Zener drag and further research can be built on these discoveries.

7 Summary and Conclusion

The results of this work are an important step to a further understanding of the influence of dispersoids on grain boundary movement and recrystallization in 6xxx series aluminium alloys. Dispersoids are non-hardening second-phase particles with a size of $\sim 0.02\text{-}0.5\mu\text{m}$. They oppose the drive for recrystallization by pinning and retarding grain boundary movement. This pinning effect is referred to as Zener drag. To be able to examine the magnitude of the Zener drag in a series of compression tests, a reference alloy without dispersoids is needed. Since dispersoids consist mainly of Fe, Cr, and Mn, the contents of these alloying elements were minimized. The final ingot contained 0.80wt% Mg, 0.65wt% Si, and 0.05wt% Fe. Other elements did not exceed 0.004wt%.

Prior to the test series, the quality of the ingot was assessed with LOM and SEM. Except for minor pores and solidification cracks near the pipe, no significant defects were observed. Next, the material underwent a standard homogenization heat treatment and TEM examinations confirmed that no dispersoids formed during processing.

The central experiments of this thesis were hot deformation tests at 550°C. The samples were initially annealed for 10min to dissolve all Mg-Si phases. The first sample group was then compressed at constant temperatures with varying φ and $\dot{\varphi}$ being quenched instantly. For the second group, a holding time after deformation was inserted to assert the time dependency of the recrystallization in this alloy. The deformed samples were finally examined with EBSD and the recrystallized fraction determined by measuring the GOS. The results showed rapid recrystallization and that raising φ , $\dot{\varphi}$, and the holding time after deformation increased the recrystallized fraction.

The rate of recrystallization was enormous in comparison to similar industrial-grade alloys. This confirmed once more the absence of dispersoids in the model alloy. Samples with high values of φ and $\dot{\varphi}$ quenched immediately with 17.5K/s managed to fully recrystallize. In order to suppress the start of recrystallization it was necessary to raise the quenching rate to 175K/s. This demonstrates the impact of the lack of dispersoids.

To calculate the exact extent of the Zener drag, further deformation tests are required in order to cover the entire φ - $\dot{\varphi}$ matrix and the time dependencies for each case. Furthermore, the tests have to be repeated for industrial-grade 6061 with the same parameters to compare the recrystallization kinetics. A further research topic would be to assess the influence of solute drag by iterating the same tests with pure aluminium.

8 Symbols and Abbreviations

b	Absolute value of the Burgers vector	AA	Artificial ageing
C	Concentration of solutes	AMAG	Austria Metall AG
d_{cr}, d	Critical diameter, diameter	bal.	Balance
D_Z, D_N, D_{Lim}	Limiting diameter	CCD	Charge-couple device
F_S	Pinning force of spherical particle	EBSD	Electron backscatter diffraction
F_C	Pinning force of coherent particle		
F_V	Volume fraction of dispersoid	EDX	Energy-dispersive X-ray
G	Shear modulus	FCC	face-centred cubic
j, n	Variables for natural numbers	GOS	Grain orientation spread
k	Scaling factor	GP-zone	Guinier-Preston zone
K, α, c_2	Constants	IPF	Inverse pole figure
l, l_0	Length, initial length	IQ	Image quality
M	Boundary mobility	L	Liquid
N_V, N_S	Total, interacting number of particles	LOM	Light optical microscopy
P	Pressure	NA	Natural ageing
P_C	Curvature pressure	PSN	Particle stimulated nucleation
P_D	Driving pressure		
P_{Sol}	Solute Drag	SAED	Selected area electron diffraction
P_Z	Zener Drag		
Q	Activation energy	SEM	Scanning electron microscopy
R	Universal Gas constant		
R, \bar{R}	Radius of grain, mean radius of grain	ssss	Supersaturated solid solution
r	Radius of particle		
s	Distance	TEM	Transmission electron microscopy
t	Time		
T_R	Recrystallization temperature	wt%	Percentage by weight
T_M	Melting temperature		
T	Temperature		
v	Velocity of dislocation or boundary		
X_V	Fraction recrystallized		
γ	Specific energy		
ε	Strain		
Θ_{cr}	Critical angle		
ρ	Dislocation density		
σ_{SS}	Contribution from the solid solution strengthening to yield strength		
τ, τ_F	Shear stress		
φ	Degree of deformation		
$\dot{\varphi}$	Rate of deformation		

9 Bibliography

- [1] L. Lodgaard and N. Ryum, "Precipitation of dispersoids containing Mn and/or Cr in Al-Mg-Si alloys," *Mater. Sci. Eng. A*, vol. 283, pp. 144–152, 2000.
- [2] F. J. Humphreys and M. Hatherly, *Recrystallization and Related Annealing Phenomena*, 2nd ed. Oxford: Elsevier, 2004.
- [3] C. Schmitz, J. Domagala, and P. Haag, *Handbook of Aluminium Recycling*. Essen: Vulkan-Verlag, 2006.
- [4] W. Callister and D. Rethwisch, *Materials Science and Engineering*, 9th ed. John Wiley & Sons, 2015.
- [5] C. Kammer, *Aluminium Taschenbuch: 1 Grundlagen und Werkstoffe*, 16th ed. Düsseldorf: Aluminium-Verlag, 2002.
- [6] DIN - Deutsches Institut für Normung, *DIN EN 573-1: Aluminium and aluminium alloys – Chemical composition and form of wrought products – Part 1: Numerical designation system*. 2005.
- [7] R. Lumley, J. Metson, H. Kvande, G. Wallace, and J. F. Grandfield, *Fundamentals of Aluminium Metallurgy*. Woodhead Publishing, 2011.
- [8] B. Arnold, *Werkstofftechnik für Wirtschaftsingenieure*, 1st ed. Springer-Verlag, 2013.
- [9] Austrian Standards Institute, *ÖNORM EN 573-3:2013-12-01: Aluminium and aluminium alloys - Chemical composition and form of wrought products - Part 3: Chemical composition and form of products*. 2013.
- [10] E. Roos and K. Maile, *Werkstoffkunde für Ingenieure*, 3rd ed. Springer-Verlag, 2008.
- [11] O. R. Myhr, Ø. Grong, and S. J. Andersen, "Modelling of the Age Hardening Behaviour of Al-Mg-Si Alloys," *Acta Mater.*, vol. 49, pp. 65–75, 2001.
- [12] J. Zander, R. Sandstro, and L. Vitos, "Modelling mechanical properties for non-hardenable aluminium alloys," *Comput. Mater. Sci.*, vol. 41, pp. 86–95, 2007.
- [13] R. Vissers, M. A. van Huis, J. Jansen, H. W. Zandbergen, C. D. Marioara, and S. J. Andersen, "The crystal structure of the β' phase in Al-Mg-Si alloys," *Acta Mater.*, vol. 55, no. 11, pp. 3815–3823, 2007.
- [14] E. Povoden-Karadeniz, P. Lang, P. Warczok, A. Falahati, W. Jun, and E. Kozeschnik, "CALPHAD modeling of metastable phases in the Al-Mg-Si system," *Calphad Comput. Coupling Phase Diagrams Thermochem.*, vol. 43, pp. 94–104, 2013.
- [15] K. Matsuda, Y. Sakaguchi, and Y. Miyata, "Precipitation sequence of various kinds of metastable phases in Al-1.0 mass% Mg-2Si-0.4 mass% Si alloy," *J. Mater. Sci.*, vol. 5, pp. 179–189, 2000.
- [16] M. A. van Huis, J. H. Chen, M. H. F. Sluiter, and H. W. Zandbergen, "Phase stability and structural features of matrix-embedded hardening precipitates in Al-Mg-Si alloys in the early stages of evolution," *Acta Mater.*, vol. 55, pp. 2183–2199, 2007.

Bibliography

- [17] G. A. Edwards, K. Stiller, G. L. Dunlop, and M. J. Couper, "The precipitation sequence in Al-Mg-Si alloys," *Acta Mater.*, vol. 46, no. 11, pp. 3893–3904, 1998.
- [18] M. H. Jacobs, "1204 Precipitation Hardening," *TALAT Lect.*, 1999.
- [19] D. J. Chakrabarti and D. E. Laughlin, "Phase relations and precipitation in Al-Mg-Si alloys with Cu additions," *Prog. Mater. Sci.*, vol. 49, no. 3–4, pp. 389–410, 2004.
- [20] C. Wolverton, "Crystal Structure and Stability of Complex Precipitate Phases in Al-Cu-Mg-(Si) and Al-Zn-Mg Alloys," *Acta Mater.*, vol. 49, pp. 3129–3142, 2001.
- [21] R. S. Yassar, D. P. Field, and H. Weiland, "The effect of cold deformation on the kinetics of the β " precipitates in an Al-Mg-Si alloy," *Metall. Mater. Trans. A*, vol. 36, no. August, pp. 2059–2065, 2005.
- [22] R. A. Jeniski, B. Tahanaboonsombut, and T. H. Sanders, "The Effect of Iron and Manganese on the Recrystallization Behavior of Hot-Rolled and Solution-Heat-Treated Aluminum Alloy 6013," *Metall. Mater. Trans. A*, vol. 27, pp. 19–27, 1996.
- [23] M. W. Zandbergen, A. Cerezo, and G. D. W. Smith, "Study of precipitation in Al-Mg-Si Alloys by atom probe tomography II. Influence of Cu additions," *Acta Mater.*, vol. 101, pp. 149–158, 2015.
- [24] Y. Han, K. Ma, L. Li, W. Chen, and H. Nagaumi, "Study on microstructure and mechanical properties of Al-Mg-Si-Cu alloy with high manganese content," *Mater. Des.*, vol. 39, pp. 418–424, 2012.
- [25] W. F. Miao and D. E. Laughlin, "Effects of Cu content and preaging on precipitation characteristics in aluminum alloy 6022," *Metall. Mater. Trans. A*, vol. 31, no. 2, pp. 361–371, 2000.
- [26] R. A. Jeniski, "Effects of Cr addition on the microstructure and mechanical behavior of 6061-T6 continuously cast and rolled redraw rod," *Mater. Sci. Eng. A*, vol. 237, no. 1, pp. 52–64, 1997.
- [27] N. C. W. Kuijpers, "Kinetics of the β -AlFeSi to α -Al(FeMn)Si transformation in Al-Mg-Si alloys," 2004.
- [28] G. Mrówka-Nowotnik, J. Sieniawski, and M. Wierzbińska, "Analysis of intermetallic particles in AlSi1MgMn aluminium alloy," *J. Achiev. Mater. Manuf. Eng.*, vol. 20, pp. 7–8, 2007.
- [29] N. C. W. Kuijpers, F. J. Vermolen, K. Vuik, and S. van der Zwaag, "A Model of the β -AlFeSi to α -Al(FeMn)Si Transformation in Al-Mg-Si Alloys," *Mater. Trans.*, vol. 44, no. 7, pp. 1448–1456, 2003.
- [30] N. C. W. Kuijpers, F. J. Vermolen, C. Vuik, P. T. G. Koenis, K. E. Nilsen, and S. van der Zwaag, "The dependence of the β -AlFeSi to α -Al(FeMn)Si transformation kinetics in Al-Mg-Si alloys on the alloying elements," *Mater. Sci. Eng. A*, vol. 394, pp. 9–19, 2005.
- [31] N. C. W. Kuijpers, W. H. Kool, P. T. G. Koenis, K. E. Nilsen, I. Todd, and S. Van der Zwaag, "Assessment of different techniques for quantification of α -Al(FeMn)Si and β -AlFeSi intermetallics in AA 6xxx alloys," *Mater. Charact.*, vol. 49, pp. 409–420, 2002.

Bibliography

- [32] K. Strobel, E. Sweet, M. Easton, J.-F. Nie, and M. Couper, "Dispersoid Phases in 6xxx Series Aluminium Alloys," *Mater. Sci. Forum*, vol. 654–656, pp. 926–929, 2010.
- [33] F. Hichem, G. D. Eddine, D. Karim, G. Rebai, and S. Fares, "Effect of Heat Treatment on the Formation and Distribution of Dispersoid Particles in AlMgSi," *Glob. J. Sci. Front. Res. Phys. Sp. Sci.*, vol. 12, no. 1, pp. 45–48, 2012.
- [34] K. Strobel, M. A. Easton, L. Sweet, M. J. Couper, and J.-F. Nie, "Relating Quench Sensitivity to Microstructure in 6000 Series Aluminium Alloys," *Mater. Trans.*, vol. 52, no. 5, pp. 914–919, 2011.
- [35] M. H. Jacobs, "Introduction to Aluminium as an Engineering Material," *TALAT*, 1999.
- [36] E. Hornbogen, G. Eggeler, and E. Werner, *Werkstoffe*, 10th ed. Springer-Verlag, 2012.
- [37] W. Weißbach, *Werkstoffkunde*, 16. Wiesbaden: Viewegs Fachbücher der Technik, 2007.
- [38] M. E. Kassner and S. C. Bergsma, "Recrystallization Behavior of Rolled Ingots of 6061 and 6069 Aluminum Alloys," *J. Mater. Eng. Perform.*, vol. 9, no. August, pp. 416–423, 2000.
- [39] Y. Huang and F. J. Humphreys, "The effect of solutes on grain boundary mobility during recrystallization and grain growth in some single-phase aluminium alloys," *Mater. Chem. Phys.*, vol. 132, no. 1, pp. 166–174, 2012.
- [40] R. Higginson and P. Bate, "Substructure Drag Effects and Recrystallization Textures in Aluminium," *Acta Mater.*, vol. 47, no. 4, pp. 1079–1090, 1999.
- [41] A. R. Eivani, S. Valipour, H. Ahmed, J. Zhou, and J. Duszczuk, "Effect of the size distribution of nanoscale dispersed particles on the Zener drag pressure," *Metall. Mater. Trans. A Phys. Metall. Mater. Sci.*, vol. 42, no. 4, pp. 1109–1116, 2011.
- [42] F. J. Humphreys, P. B. Prangnell, J. R. Bowen, A. Gholinia, C. Harris, B. Hutchinson, L. M. Brown, M. J. Stowell, J. G. Sevillano, P. J. Withers, D. Processing, and J. R. Bowen, "Developing Stable Fine-Grain Microstructures by Large Strain Deformation," *Philos. Trans. Math., Phys. Eng. Sci.*, vol. 357, no. 1756, pp. 1663–1681, 1999.
- [43] M. H. Jacobs, "Mechanical Working and Forming of Shapes," *TALAT*, 1999.
- [44] P. Sepehrband, X. Wang, H. Jin, and S. Esmaili, "Microstructural evolution during non-isothermal annealing of a precipitation-hardenable aluminum alloy: Experiment and simulation," *Acta Mater.*, vol. 94, pp. 111–123, 2015.
- [45] H. J. McQueen, X. Xia, Y. Cui, B. Li, and Q. Meng, "Solution and precipitation effects on hot workability of 6201 alloy," *Mater. Sci. Eng. A*, vol. 319–321, pp. 420–424, 2001.
- [46] S. K. Panigrahi, R. Jayaganthan, and V. Pancholi, "Effect of plastic deformation conditions on microstructural characteristics and mechanical properties of Al 6063 alloy," *Mater. Des.*, vol. 30, no. 6, pp. 1894–1901, 2009.
- [47] S. K. Panigrahi and R. Jayaganthan, "Effect of rolling temperature on microstructure and mechanical properties of 6063 Al alloy," *Mater. Sci. Eng. A*, vol. 492, pp. 300–305, 2008.

Bibliography

- [48] W. Blum, Q. Zhu, R. Merkel, and H. J. McQueen, "Geometric dynamic recrystallization in hot torsion of Al-5Mg-0.6Mn (AA5083)," *Mater. Sci. Eng. A*, vol. 205, pp. 23–30, 1996.
- [49] A. Yamamoto, M. Tsukamoto, and D. Okai, "Changes in Microstructures during Annealing after Cold-Rolling at 30% and 50% Reduction on Al-Mg-Si Alloy," *Mater. Trans.*, vol. 52, no. 5, pp. 876–881, 2011.
- [50] J. Tarasiuk, P. Gerber, and B. Bacroix, "Estimation of recrystallized volume fraction from EBSD data," *Acta Mater.*, vol. 50, pp. 1467–1477, 2002.
- [51] P. J. Hurley and F. J. Humphreys, "The application of EBSD to the study of substructural development in a cold rolled single-phase aluminium alloy," *Acta Mater.*, vol. 51, pp. 1087–1102, 2003.
- [52] F. J. Humphreys, "Grain and subgrains characterisation by electron backscatter diffraction," *J. Mater. Sci.*, vol. 36, pp. 3833–3854, 2001.
- [53] S. I. Wright, M. M. Nowell, and D. P. Field, "A Review of Strain Analysis Using EBSD," *Microsc. Microanal.*, vol. 17, pp. 316–329, 2011.
- [54] N. Gao, S. C. Wang, H. S. Ubhi, and M. J. Starink, "A comparison of grain size determination by light microscopy and EBSD analysis," *J. Mater. Sci.*, vol. 40, pp. 4971–4974, 2005.
- [55] P. L. O. Rossi and C. M. Sellars, "Quantitative metallography of recrystallization," *Acta Mater.*, vol. 45, no. 1, pp. 137–148, 1997.
- [56] Gesamtverband der Aluminiumindustrie e.V., "www.aluinfo.de." [Online]. Available: <http://www.aluinfo.de/index.php/alu-lexikon.html?lid=102>. [Accessed: 08-Dec-2015].
- [57] U. Kern, "Prüfbefund Nr: MP / 938_V0 / 15 (ROL)," Ranshofen, 2015.
- [58] R. D. Doherty, D. A. Hughes, F. J. Humphreys, J. J. Jonas, D. Juul Jensen, M. E. Kassner, W. E. King, T. R. McNelley, H. J. McQueen, and A. D. Rollett, "Current issues in recrystallization: A review," *Mater. Today*, vol. 1, pp. 14–15, 1998.
- [59] W. Polkowski, P. Józwik, and Z. Bojar, "EBSD and X-ray diffraction study on the recrystallization of cold rolled Ni3Al based intermetallic alloy," *J. Alloys Compd.*, vol. 614, no. November, pp. 226–233, 2014.
- [60] O. Engler and J. Hirsch, "Texture control by thermomechanical processing of AA6xxx Al-Mg-Si sheet alloys for automotive applications - a review," *Mater. Sci. Eng. A*, vol. 336, pp. 249–262, 2002.

10 List of Figures

Figure 1: Schematic illustration of substitutional (a) and interstitial (b) alloying atoms [12].....	5
Figure 2: Temperature profile of industrial process for hot forming aluminium	8
Figure 3: Al-Mg ₂ Si phase diagram [7]	9
Figure 4: TEM micrographs of precipitate dispersions at different stages of artificial ageing. (a) and (b) 10mins at 175°C, (c) 0.5h at 175°C, (d) 4h at 175°C, (e) 72h at 175°C, (f) 20h at 200°C [19]	11
Figure 5: SEM micrograph of alloy with 0.74wt% Mg, 0.96wt% Si, 0.50wt% Cu, and 0.22wt% Fe [26].....	12
Figure 6: As-cast microstructure of AlSi1MgMn alloy [30]	13
Figure 7: LOM micrographs; slightly homogenized for 20min at 540°C (left), fully homogenized for 32h at 590°C (right) [33]	14
Figure 8: TEM micrographs of Mn dispersoids: (a) uniform distribution in the matrix, (b) and (c) rod and spherical shaped morphology of Mn dispersoids, respectively [26]	15
Figure 9: Pinned dislocation turns into Frank-Read-Source at $\tau = \tau_F$ [38]	16
Figure 10: Schematic illustration of the main annealing processes: (a) deformed state, (b) recovered, (c) partially recrystallized, (d) fully recrystallized, (e) grain growth, and (f) abnormal grain growth [4]	18
Figure 11: Arrangement of dislocations after deformation (left) and after recovery (right) - polygonization [12]	19
Figure 12: Typical recrystallization kinetics during isothermal annealing [4]	21
Figure 13: Recrystallization diagram for 99.6wt% aluminium [12]	22
Figure 14: Schematic representation of the change in grain size distribution during (a) normal grain growth and (b) abnormal grain growth [4]	23
Figure 15: The interaction between a grain boundary and a spherical particle [4].....	25
Figure 16: Regimes of normal and abnormal grain growth for particle-containing alloys [43].....	27
Figure 17: The predicted grain size for a PSN efficiency of unity. The dashed lines show conditions under which Zener pinning effects may prevent discontinuous recrystallization [4]	28
Figure 18: The effect of the particle parameters on the recrystallized grain size [4]	29
Figure 19: Summary of the microstructural changes which occur during dynamic recovery [4].....	30
Figure 20: The effect of temperature on the stress-strain curves for 0.68wt% C steel, deformed in axisymmetric compression [4].....	31
Figure 21: Schematic diagram of a typical EBSD installation [53].....	33

List of Figures

Figure 22: Custom-made ingot mould (drilling for thermocouple is marked red).....	36
Figure 23: Separator with filter (left), ceramic filter (right).....	36
Figure 24: Cut ingot (left), examined areas of the slice (right).....	37
Figure 25: Homogeneous area (grey) with mapped samples used for further experiments.....	38
Figure 26: Target temperature profile homogenization.....	39
Figure 27: Sample for compression tests (left) with thermocouple and Mo sheets (right).....	42
Figure 28: Temperature profile for compression tests.....	43
Figure 29: Temperature profile for compression tests with added holding time and increased quenching rate.....	45
Figure 30: LOM micrographs of sample 6, 200x (left) and 500x (right) magnification....	48
Figure 31: Solidification crack near the pipe (left), oxide contaminations (right) [58]....	48
Figure 32: Temperature profile homogenization.....	49
Figure 33: LOM micrographs of sample 9 (as-cast), 200x (left) and 500x (right) magnification.....	50
Figure 34: SEM micrograph of sample 9 (as-cast) with labelled EDX measuring points.	50
Figure 35: EDX analysis of sample 9 (as-cast); points a.)-e.) corresponding to Figure 34.....	51
Figure 36: Phase fraction in sample A6 (as-cast) with $Mg_2Si \rightarrow$ red, $AlFeSi \rightarrow$ blue.....	52
Figure 37: LOM micrographs (200x magnification) as-cast – A6 (a.), 300°C – A1 (b.), 400°C – A2 (c.), 520°C – A3 (d.), 565°C – A4 (e.), and 570°C – A5 (f.).....	53
Figure 38: Phase fraction depending on duration of the heat treatment.....	54
Figure 39: TEM micrographs of as-cast sample A0.6 (a.), (b.) and its matrix oriented in (100) with the corresponding SAED pattern (c.), (d.).....	55
Figure 40: Sample A0.1 (300°C) with β' precipitates (left), sample A0.2 (400°C) with Si curls (right).....	56
Figure 41: TEM micrographs of sample A0.3 (520°C, left) and A0.4 (565°C, right).....	57
Figure 42: LOM micrograph of sample 9 (as-cast) with sketched grain boundaries; Barker's etch, 50x magnification, polarized light.....	58
Figure 43: LOM micrographs at 300°C – A1 (a.), 400°C – A2 (b.), 520°C – A3 (c.), and 565°C – A4 (d.); Barker's etch, 50x magnification, polarized light.....	59
Figure 44: LOM micrographs at 565°C – A4 (left), 570°C – A5 (right); Barker's etch, 25x magnification, polarized light.....	60
Figure 45: Temperature profile shortened homogenization.....	61
Figure 46: LOM micrographs (200x magnification) A8 - 5min at 565°C (left) and A7 - 10min at 565°C (right).....	61
Figure 47: Phase fraction depending on heat treatment.....	62

List of Figures

Figure 48: LOM micrographs 5min at 565°C – A8 (left), 10min at 565°C – A7 (right); Barker’s etch, 50x magnification, polarized light	62
Figure 49: Temperature profile for the compression tests.....	64
Figure 50: Deformation profile for $\varphi=1$ and $\dot{\varphi}=0.1$ (sample B1/0.1).....	64
Figure 51: IPF of samples B0/0 (a.), B0.2/10 (b.), and B0.5/10 (c.)	65
Figure 52: IPF of samples B0/0 (a.), B1/0.1 (b.), and B1/5 (c.)	66
Figure 53: GOS of sample B0/0 (a.) and B1/0.1 (b.)	67
Figure 54: GOS of sample B1/5.....	68
Figure 55: GOS of sample B1/0.5.....	68
Figure 56: GOS of sample B0.5/10	69
Figure 57: Misorientation depending on degree of deformation and rate of deformation	69
Figure 58: Average grain size depending on degree of deformation and rate of deformation.....	70
Figure 59: Temperature profile for compression tests with added holding time and increased quenching rate	71
Figure 60: GOS of sample C0 (left) and B1/0.1 (right).....	71
Figure 61: Misorientation and average grain size depending on holding time after deformation; $\varphi=1$, $\dot{\varphi}=0.1$	72
Figure 62: LOM micrographs of sample 7, 200x (left) and 500x (right) magnification.....	i
Figure 63: LOM micrographs of sample 8, 200x (left) and 500x (right) magnification.....	ii
Figure 64: LOM micrographs of sample 12, 200x (left) and 500x (right) magnification....	ii
Figure 65: LOM micrographs of sample 15, 200x (left) and 500x (right) magnification....	ii
Figure 66: SEM micrographs (200x magnification, as-cast) samples 6 (a.), 7 (b.), 8 (c.), 9 (d.), 12 (e.), and 15 (f.).....	xii
Figure 67: SEM micrographs (200x magnification) as-cast – A6 (a.) and at 300°C – A1 (b.), 400°C – A2 (c.), 520°C – A3 (d.), 565°C – A4 (e.), 570°C – A5 (f.).....	xiii
Figure 68: SEM micrographs (200x magnification) A8 - 5min at 565°C (left) and A7 - 10min (right) at 565°C	xiv
Figure 69: Histogram of grain size distribution for samples 9, A1, A2, and A3.....	xv
Figure 70: Histogram of grain size distribution for samples A4, A5, A7, and A8.....	xvi
Figure 71: EDX analysis of sample A0.6 (as-cast).....	xvii
Figure 72: EDX analysis of sample A0.6 (as-cast).....	xviii
Figure 73: SAED patterns of the matrix in sample A0.6 (as-cast)	xix
Figure 74: TEM micrographs of sample A0.6 (as-cast)	xx
Figure 75: TEM micrographs and EDX analysis of sample A0.1 (300°C)	xxi
Figure 76: TEM micrographs and EDX analysis of sample A0.2 (400°C)	xxii
Figure 77: TEM micrographs and EDX analysis of sample A0.3 (520°C)	xxiii
Figure 78: TEM micrographs and SAED pattern of sample A0.4 (565°C).....	xxiv

List of Figures

Figure 79: TEM micrographs, SAED pattern, and EDX analysis of sample A0.5 (570°C)	xxv
Figure 80: Deformation profile with $\dot{\phi}=10s^{-1}$ and ϕ varying from 0.2 to 1	xxvi
Figure 81: Deformation profile with $\phi=1$ and $\dot{\phi}$ varying from $0.1s^{-1}$ to $5s^{-1}$	xxvii
Figure 82: IPF of samples B0/0 (a.), B0.2/10 (b.), B0.35/10 (c.), and B0.5/10 (d.)	xxviii
Figure 83: IPF of samples B1/0.1 (a.), B1/0.5 (b.), B1/2 (c.), B1/5 (d.), and B1/10 (e.)	xxix
Figure 84: GOS of samples B0/0 (a.), B0.2/10 (b.), and B0.35/10 (c.)	xxx
Figure 85: GOS of samples B0.5/10 (a.), B1/0.1 (b.), and B1/0.5 (c.)	xxxi
Figure 86: GOS of samples B1/2 (a.), B1/5 (b.), and B1/10 (c.)	xxxii
Figure 87: Grain map of samples B0/0 (a.), B0.2/10 (b.), B0.35/10 (c.), and B0.5/10 (d.)	xxxiii
Figure 88: Grain map of samples B1/0.1 (a.), B1/0.5 (b.), B1/2 (c.), B1/5 (d.), and B1/10 (e.)	xxxiv
Figure 89: Histogram of grain size distribution for sample B0/0	xxxv
Figure 90: Histogram of grain size distribution for sample B0.2/10	xxxv
Figure 91: Histogram of grain size distribution for sample B0.35/10	xxxvi
Figure 92: Histogram of grain size distribution for sample B0.5/10	xxxvi
Figure 93: Histogram of grain size distribution for sample B1/0.1	xxxvii
Figure 94: Histogram of grain size distribution for sample B1/0.5	xxxvii
Figure 95: Histogram of grain size distribution for sample B1/2	xxxviii
Figure 96: Histogram of grain size distribution for sample B1/5	xxxviii
Figure 97: Histogram of grain size distribution for sample B1/10	xxxix
Figure 98: IPF of samples B0/0 (a.), C0 (b.), C2 (c.), and C5 (d.)	xl
Figure 99: IPF of samples C10 (a.), C15 (b.), C20 (c.), and C30 (d.)	xli
Figure 100: GOS of samples C0 (a.), C2 (b.), and C5 (c.)	xlii
Figure 101: GOS of samples C10 (a.), C15 (b.), and C20 (c.)	xliii
Figure 102: GOS of sample C30	xliv
Figure 103: Grain map of samples C0 (a.), C2 (b.), C5 (c.), and C10 (d.)	xliv
Figure 104: Grain map of samples C15 (a.), C20 (b.), and C30 (c.)	xl v
Figure 105: Histogram of grain size distribution for sample C0	xlvi
Figure 106: Histogram of grain size distribution for sample C2	xlvi
Figure 107: Histogram of grain size distribution for sample C5	xl vii
Figure 108: Histogram of grain size distribution for sample C10	xl vii
Figure 109: Histogram of grain size distribution for sample C15	xl viii
Figure 110: Histogram of grain size distribution for sample C20	xl viii
Figure 111: Histogram of grain size distribution for sample C30	xl ix

11 List of Tables

Table 1: Alloy designation system for wrought alloys [8], [9]	4
Table 2: Composition of 6061 [11]	5
Table 3: Solubility of alloying elements in aluminium solid solution [7].....	6
Table 4: Phases observed during precipitation hardening of Al-Mg-Si alloys [15]	11
Table 5: Description of heat-treated samples	39
Table 6: Description of samples for the shortened homogenization	40
Table 7: Sample preparation for LOM and SEM	40
Table 8: Samples for the deformation tests	44
Table 9: Samples with increased quenching rate varied by holding time after deformation.....	45
Table 10: Sample preparation for EBSD	46
Table 11: Composition of final alloy	47
Table 12: Average grain sizes (values with abnormal grain growth in red)	58
Table 13: Average grain sizes depending on heat treatment (values with abnormal grain growth in red)	63
Table 14: Alloy composition of raw material	i
Table 15: Values phase fraction depending on heat treatment.....	xiv

12 Appendix

12.1 Evaluation of Cast Samples

Table 14: Alloy composition of raw material

Alloying element	Percentage by weight
Silicon (Si)	0.030%
Iron (Fe)	0.037%
Copper (Cu)	< 0.001%
Manganese (Mn)	0.001%
Magnesium (Mg)	0.003%
Chromium (Cr)	0.001%
Nickel (Ni)	0.003%
Zinc (Zn)	0.001%
Titanium (Ti)	0.004%
Aluminium (Al)	bal.

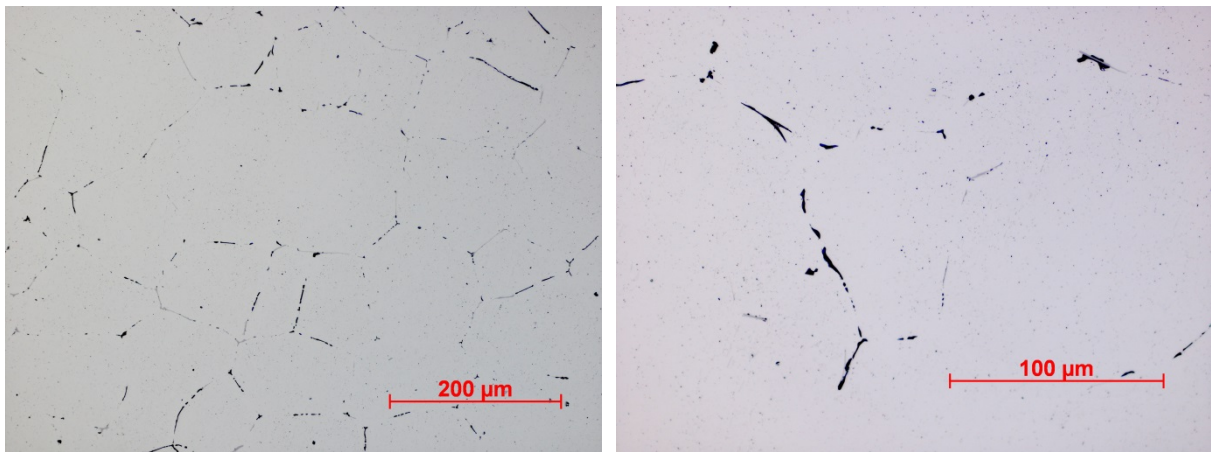


Figure 62: LOM micrographs of sample 7, 200x (left) and 500x (right) magnification

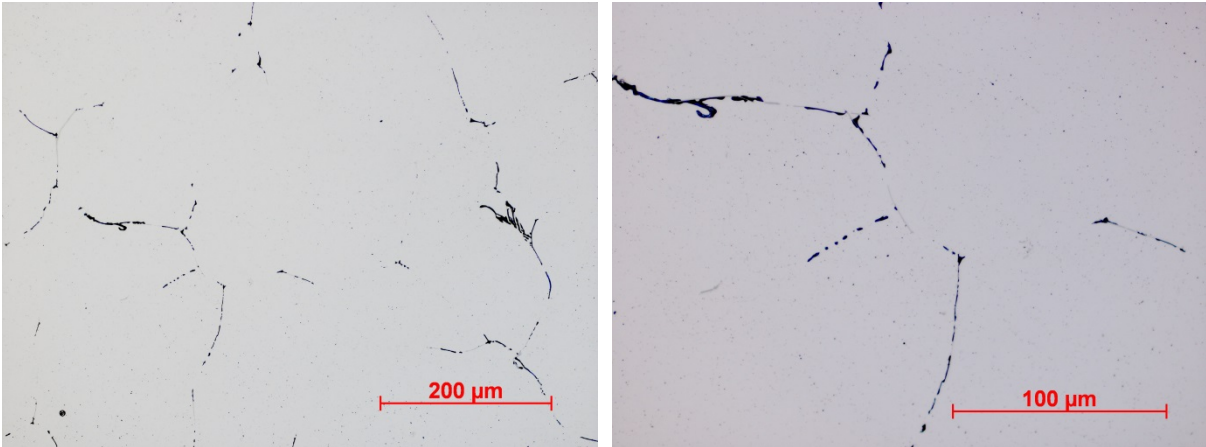


Figure 63: LOM micrographs of sample 8, 200x (left) and 500x (right) magnification

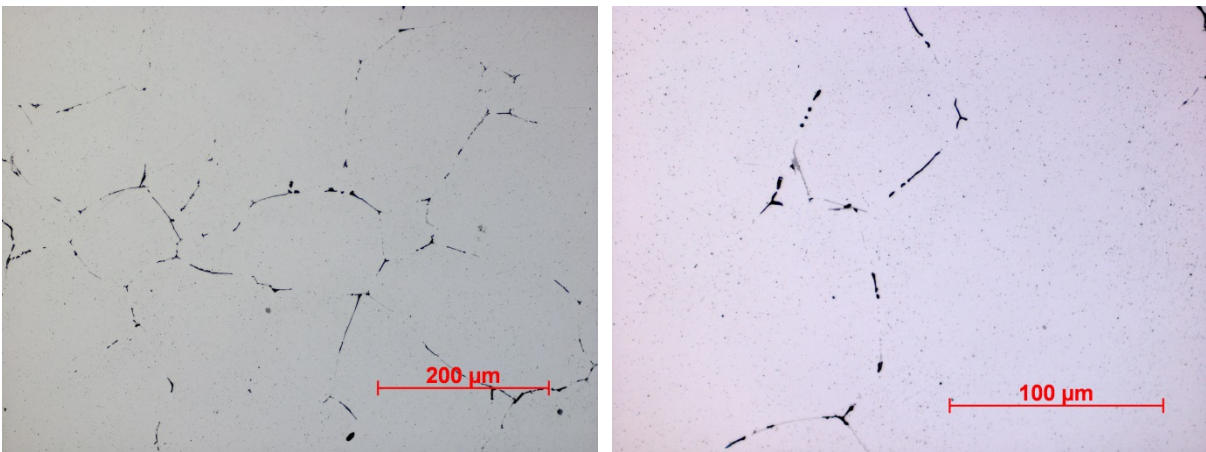


Figure 64: LOM micrographs of sample 12, 200x (left) and 500x (right) magnification

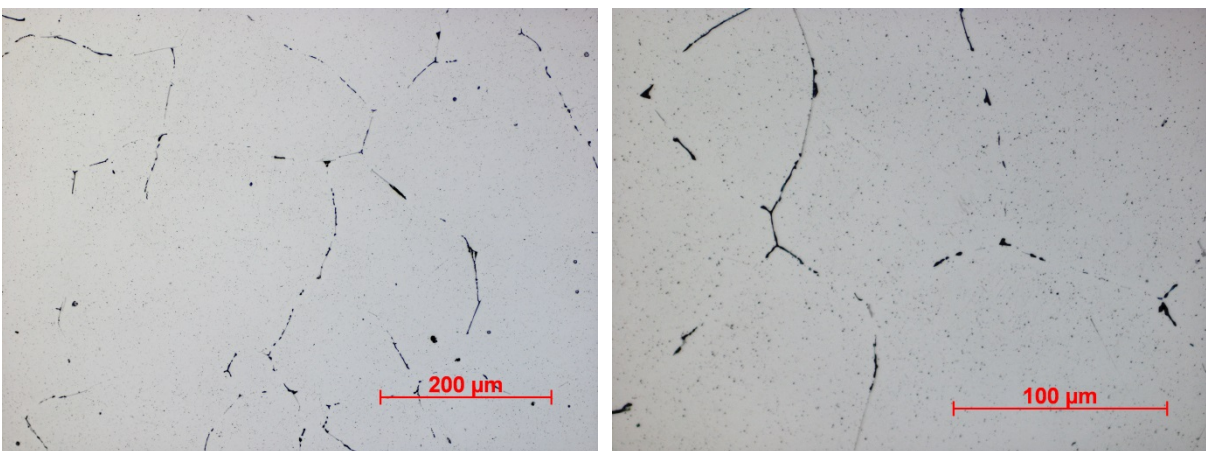


Figure 65: LOM micrographs of sample 15, 200x (left) and 500x (right) magnification

APS / Metallographie & Physik

AMAG rolling GmbH | Postfach 32 | 5282 Ranshofen | Österreich | www.amag.at

Prüfbefund Nr: MP / 938_V0 / 15 (ROL)

20-04-2015

Bezeichnung des Auftrages						
6xxx; Guss; Massel, Porosität						
Auftraggeber (Firma, Anschrift, Name)						
AMAG/Rolling, Lamprechtshausenerstr.61, 5282 Ranshofen; T PL/Ebner Thomas						
Auftragsdatum	Probeneingang	Auftrag	Kontierung	Abteilung	Tel. 07722-801-2414	Fax: 07722-809-405
01.04.2015	01.04.2015	87781	30712405	MP		E-Mail Ursula.Kern@amag.at

Aufgabenstellung

Produkt: Massel, Spezialkockille 100x100; 6xxx – AlMgSi 0,7 % Si und 0,9 % Mg
Anmerkung: Porositäten?

Prüfergebnis (Kurzfassung)

- siehe Tabelle:

Durchführung / Einzelergebnisse: (Beschreibung der Proben / Probenahme / Prüfverfahren und Normen / Messunsicherheit)

Aus der vorgelegten Probe wurden lt. Plan, 3 Bereiche entnommen und präpariert und mittels LIM analysiert. Folgende Ergebnisse liegen vor:

	Position A Abb. 2-8	Position B Abb. 9-12	Position C Abb. 13-16
Visuell:	Riss ca. 11 mm Länge im Sumpfbereich	-	-
Lichtmikroskop:	Für Legierung und Zustand liegt ein typisches unauffälliges AS-Gefüge vor		
- AS-Gefüge	Vereinzelt Oxidschlirien	Vereinzelt Oxidschlirien	Vereinzelt Oxidschlirien
- Oxide	Vereinzelt Poren <50 µm	Vereinzelt Poren <50 µm	Vereinzelt Poren <50 µm
- Porosität	-	-	-
- metallische Einschlüsse	unauffällig	unauffällig	unauffällig
- Seigerungen-Randzone			

Sachbearbeiter	Zeichnungsberechtigter	Verteiler	Anlagen:
Kern	Rachlitz	ROL/T PL/Ebner; Datei: 938_V0_15.doc	-
		Archiv: MP	Seite 1 von 9

Die Ergebnisse beziehen sich ausschließlich auf die untersuchten Gegenstände!

Im Falle der Vervielfältigung oder Veröffentlichung dieser Ausfertigung darf der Inhalt nur wort- und formgetreu und ohne Auslassung oder Zusatz wiedergegeben werden.

Firmenbuchgericht: LG Riedl | Gerichtsstand: LG Riedl | Firmenbuchnummer: FN 115998k | UID: ATU37043203

Zertifiziert nach ISO 9001 | ISO/TS 16949 | EN/AS 9100 | ISO 14001 | NADCAP | OHSAS 18001 | ISO 17025

Oberbank AG, Braunauf/Inn | Konto 201-018468 | BLZ 15040 | IBAN: AT461504000201018468 | BIC: OBKLAT2L

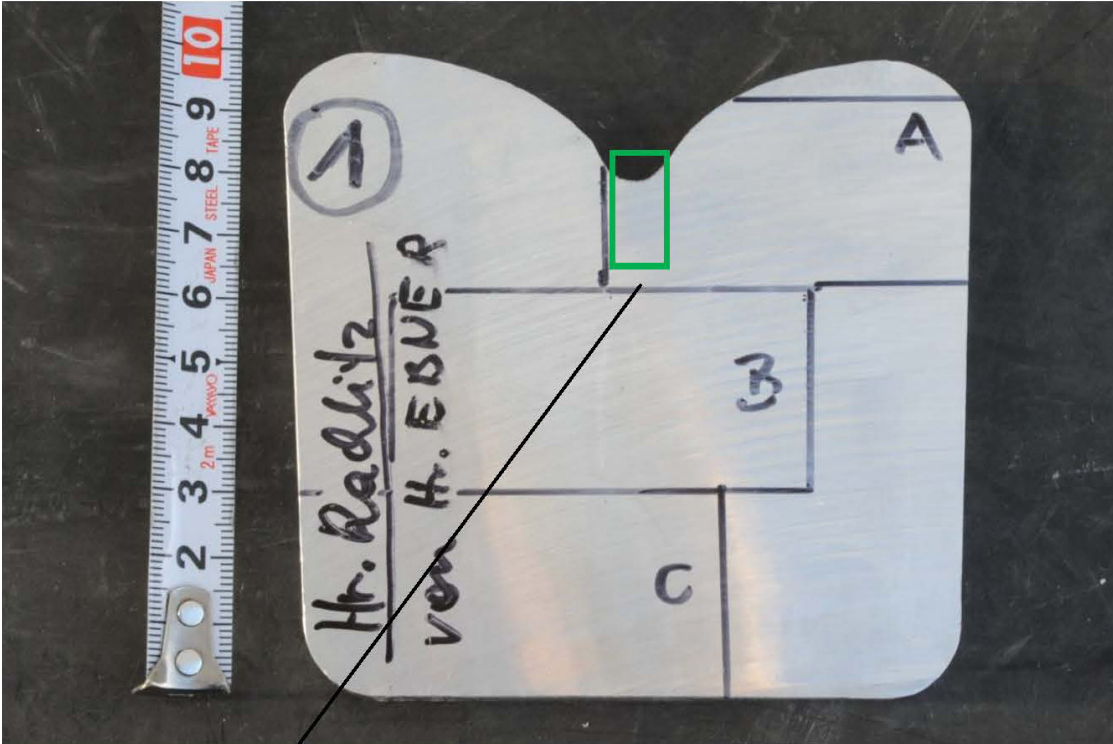


Abbildung Nr: 1.

Vorgang: P2015-04-0002
FotoNr: D1504-0031

Rissbereich



Abbildung Nr: 2.
Vorgang: P2015-04-0002
FotoNr: D1504-0482

Bildbeschreibung:

LIM/HF / Vmikr. 50x/ ungeätzt
Position A
Riss im Sumpf

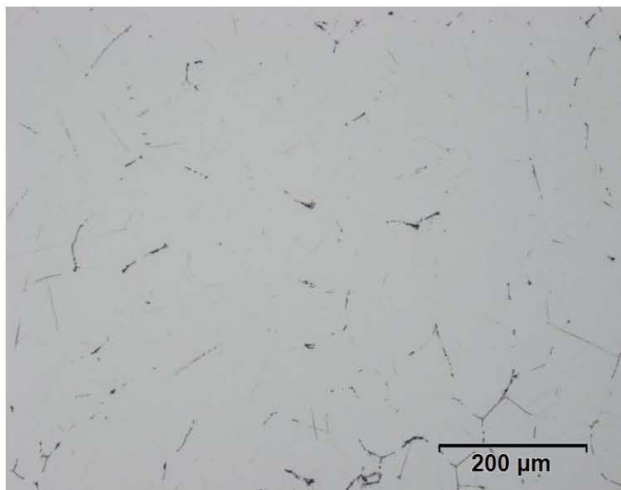


Abbildung Nr: 3.
Vorgang: P2015-04-0002
FotoNr: D1504-0483

Bildbeschreibung:

LIM/HF / Vmikr. 100x/ ungeätzt
Position A
Gefüge in Rissnähe

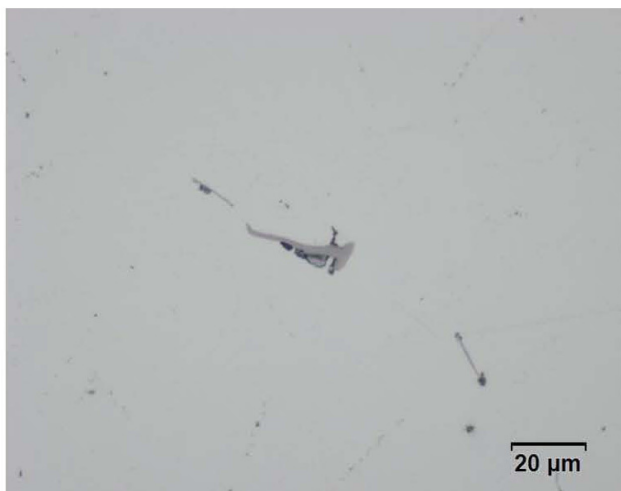


Abbildung Nr: 4.
Vorgang: P2015-04-0002
FotoNr: D1504-0484

Bildbeschreibung:

LIM/HF / Vmikr. 500x/ ungeätzt
Gefüge in Rissnähe

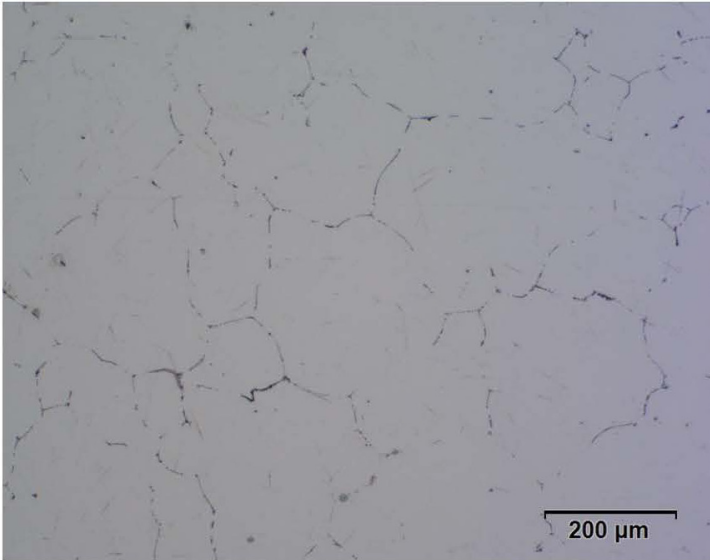


Abbildung Nr: 5.

Vorgang: P2015-04-0002
FotoNr: D1504-0480

LIM/HF/Vmikr:100x; ungeätzt
Position A

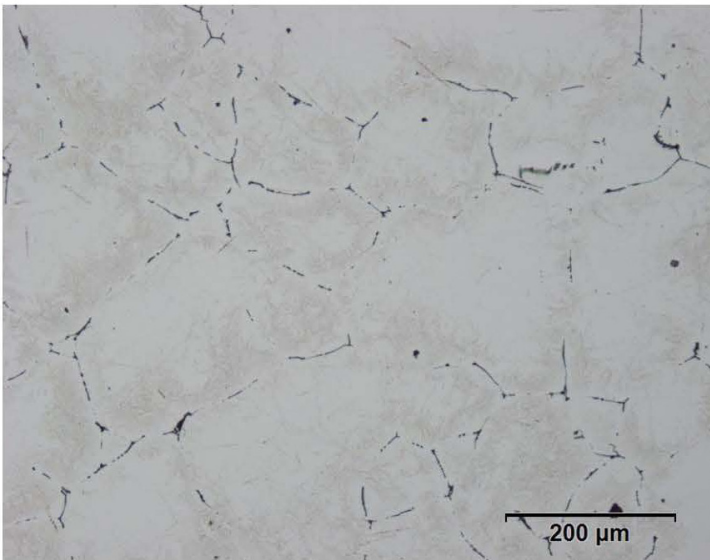


Abbildung Nr: 6.

Vorgang: P2015-04-0002
FotoNr: D1504-0485

LIM/HF / Vmikr. 100x/ 5 s Flick
Position A

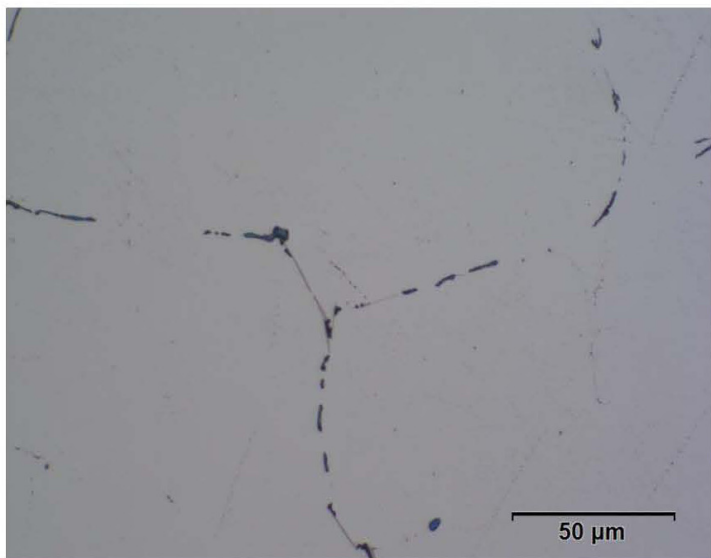


Abbildung Nr: 7.

Vorgang: P2015-04-0002
FotoNr: D1504-0481

LIM/HF/Vmikr:500x; ungeätzt
Position A

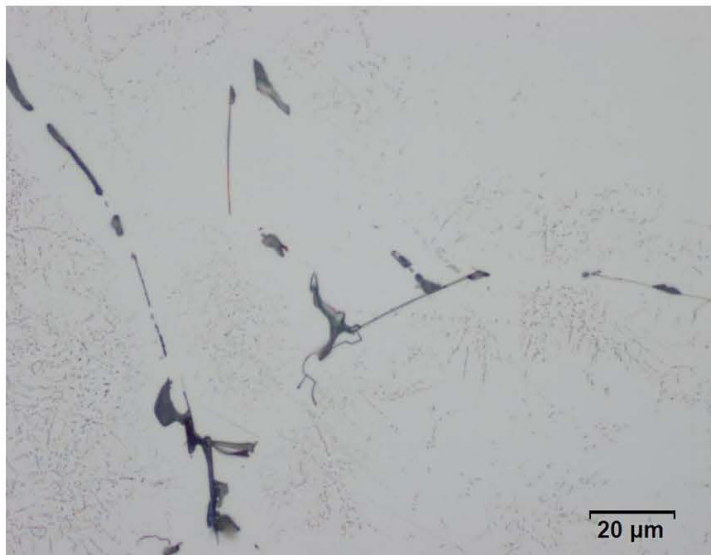


Abbildung Nr: 8.

Vorgang: P2015-04-0002
FotoNr: D1504-0486

LIM/HF / Vmikr. 500x/ 5 s Flick
Position A

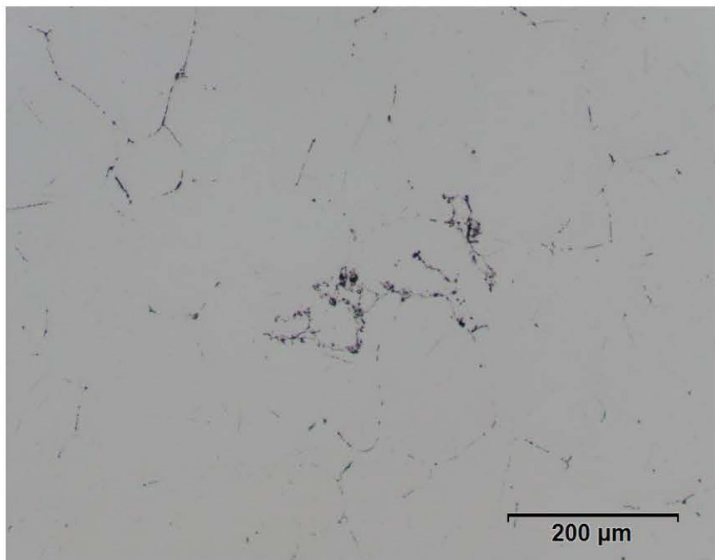


Abbildung Nr: 9.

Vorgang: P2015-04-0002
FotoNr: D1504-0750

LIM/HF/Vmikr:100x; ungeätzt
Position B
oxidische Verunreinigung

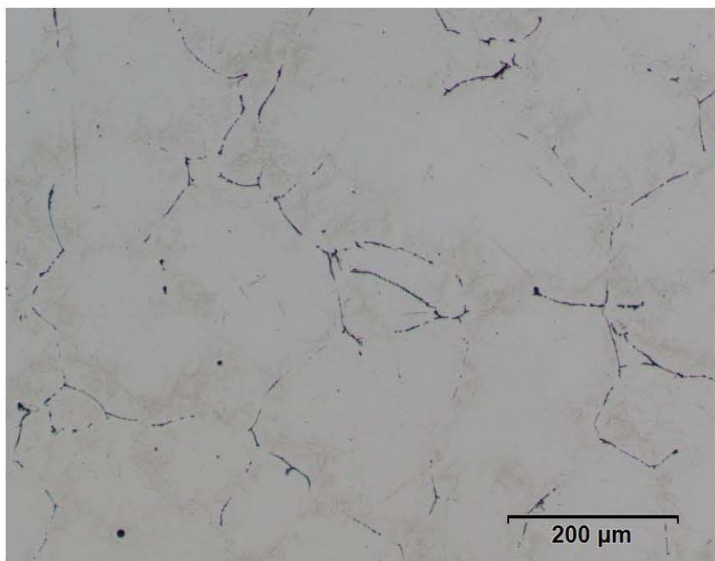


Abbildung Nr: 10.

Vorgang: P2015-04-0002
FotoNr: D1504-0753

LIM/HF/Vmikr:100x; 5s Flick
Position B

Prüfbefund: MP / 938_V0 / 15 (ROL)

Seite 7 von 9

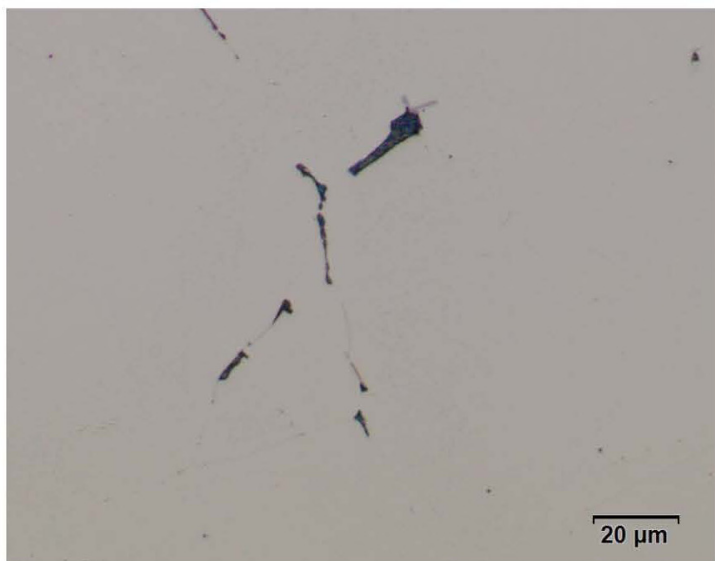


Abbildung Nr: 11.

Vorgang: P2015-04-0002
FotoNr: D1504-0752

LIM/HF/Vmikr:500x; ungeätzt
Position B

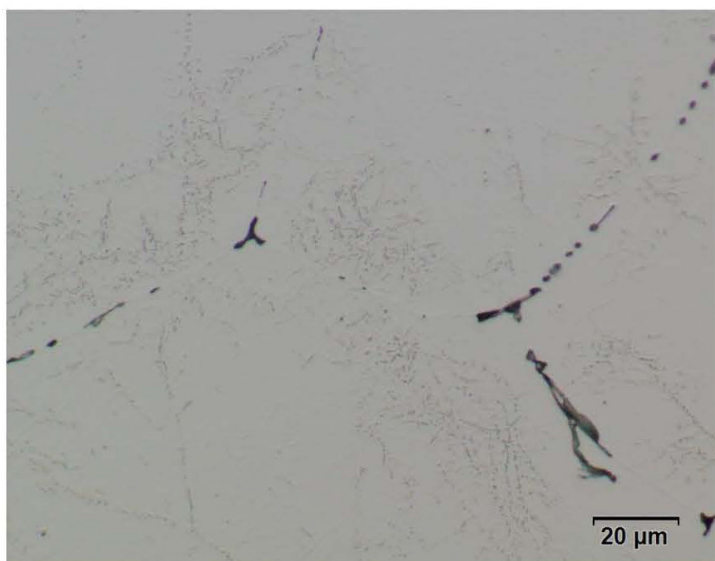


Abbildung Nr: 12.

Vorgang: P2015-04-0002
FotoNr: D1504-0756

LIM/HF/Vmikr:500x; 5s Flick
Position B

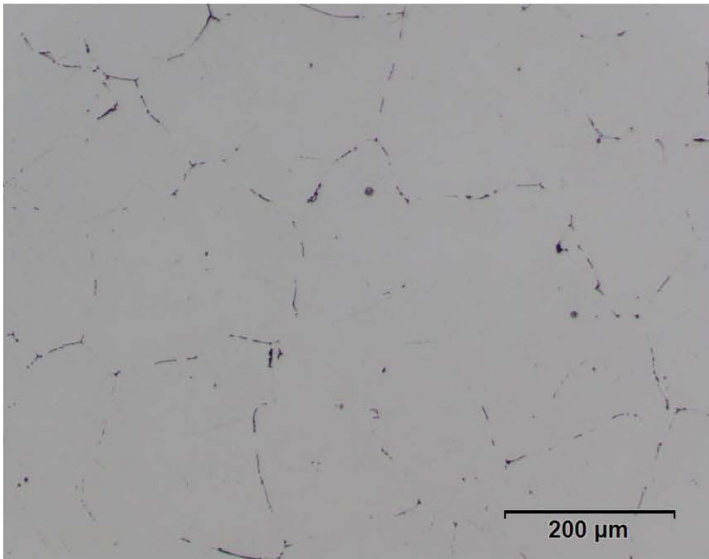


Abbildung Nr: 13.

Vorgang: P2015-04-0002
FotoNr: D1504-0758

LIM/HF/Vmikr:100x; ungeätzt
Position C

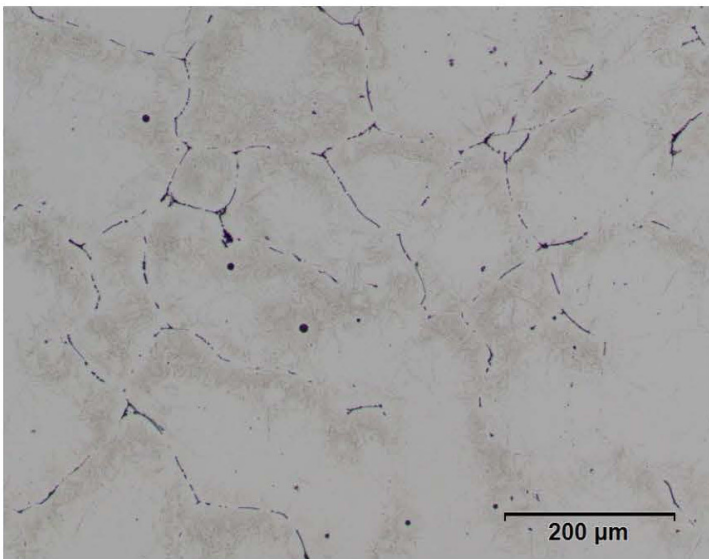


Abbildung Nr: 14.

Vorgang: P2015-04-0002
FotoNr: D1504-0760

LIM/HF/Vmikr:100x; 5s Flick
Position C

Prüfbefund: MP / 938_V0 / 15 (ROL)

Seite 9 von 9



Abbildung Nr: 15.

Vorgang: P2015-04-0002
FotoNr: D1504-0759

LIM/HF/Vmikr:500x; ungeätzt
Position C

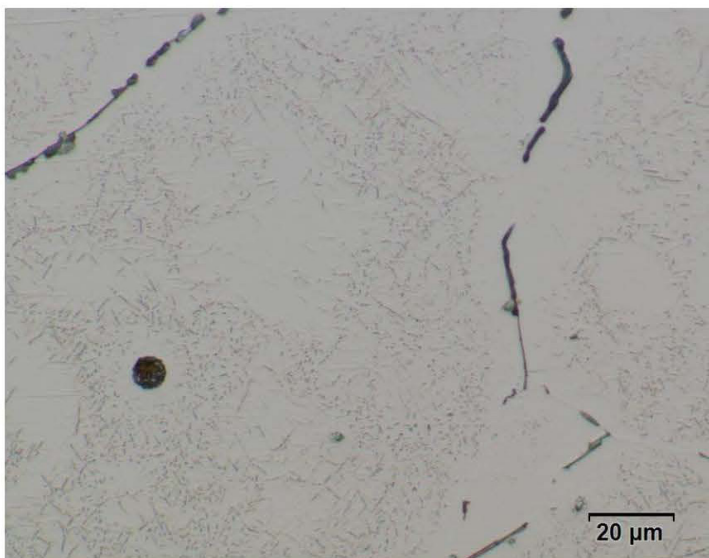


Abbildung Nr: 16.

Vorgang: P2015-04-0002
FotoNr: D1504-0761

LIM/HF/Vmikr:500x; 5s Flick
Position C

12.2 Evaluation of Heat-Treated Samples (Group A)

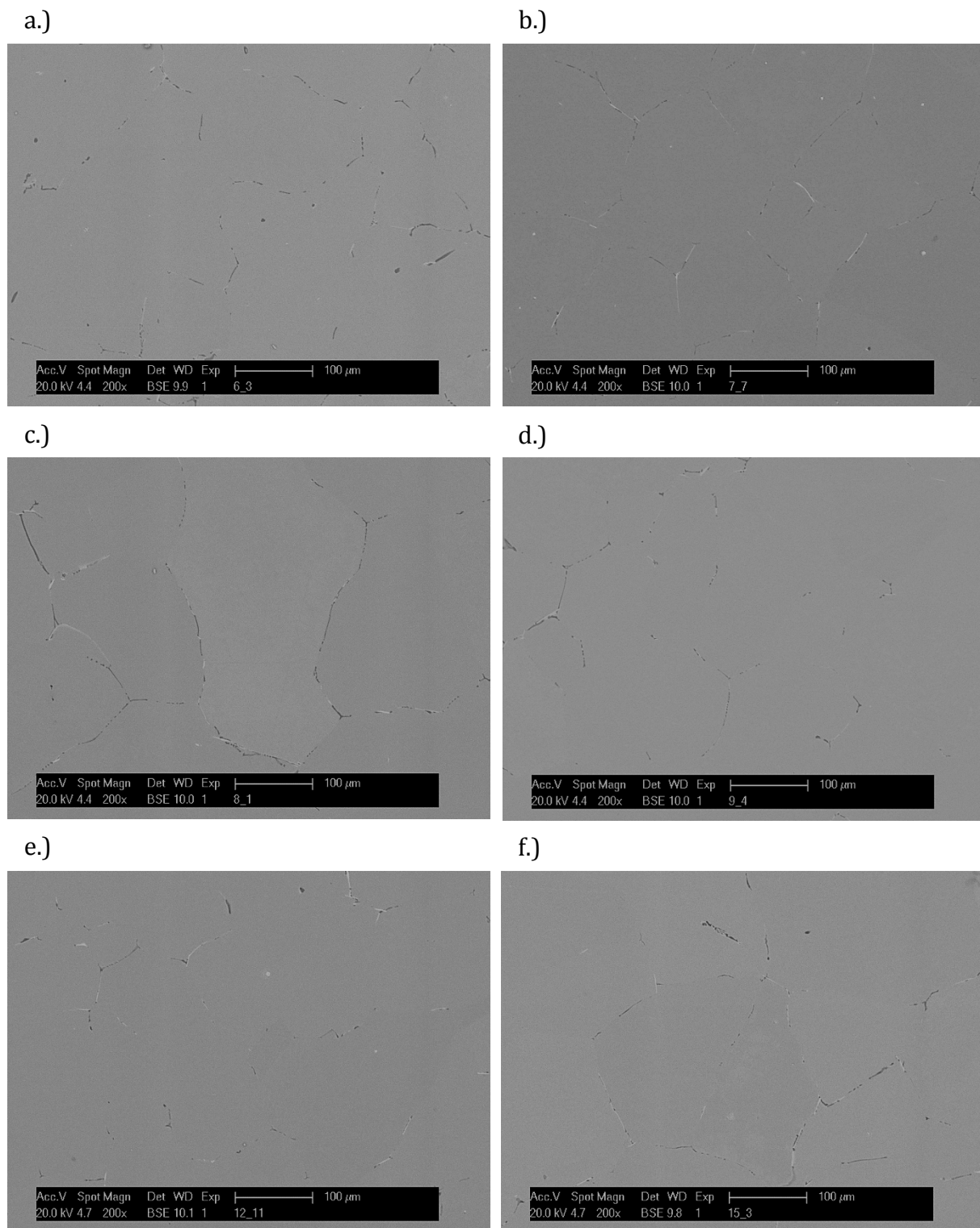


Figure 66: SEM micrographs (200x magnification, as-cast) samples 6 (a.), 7 (b.), 8 (c.), 9 (d.), 12 (e.), and 15 (f.)

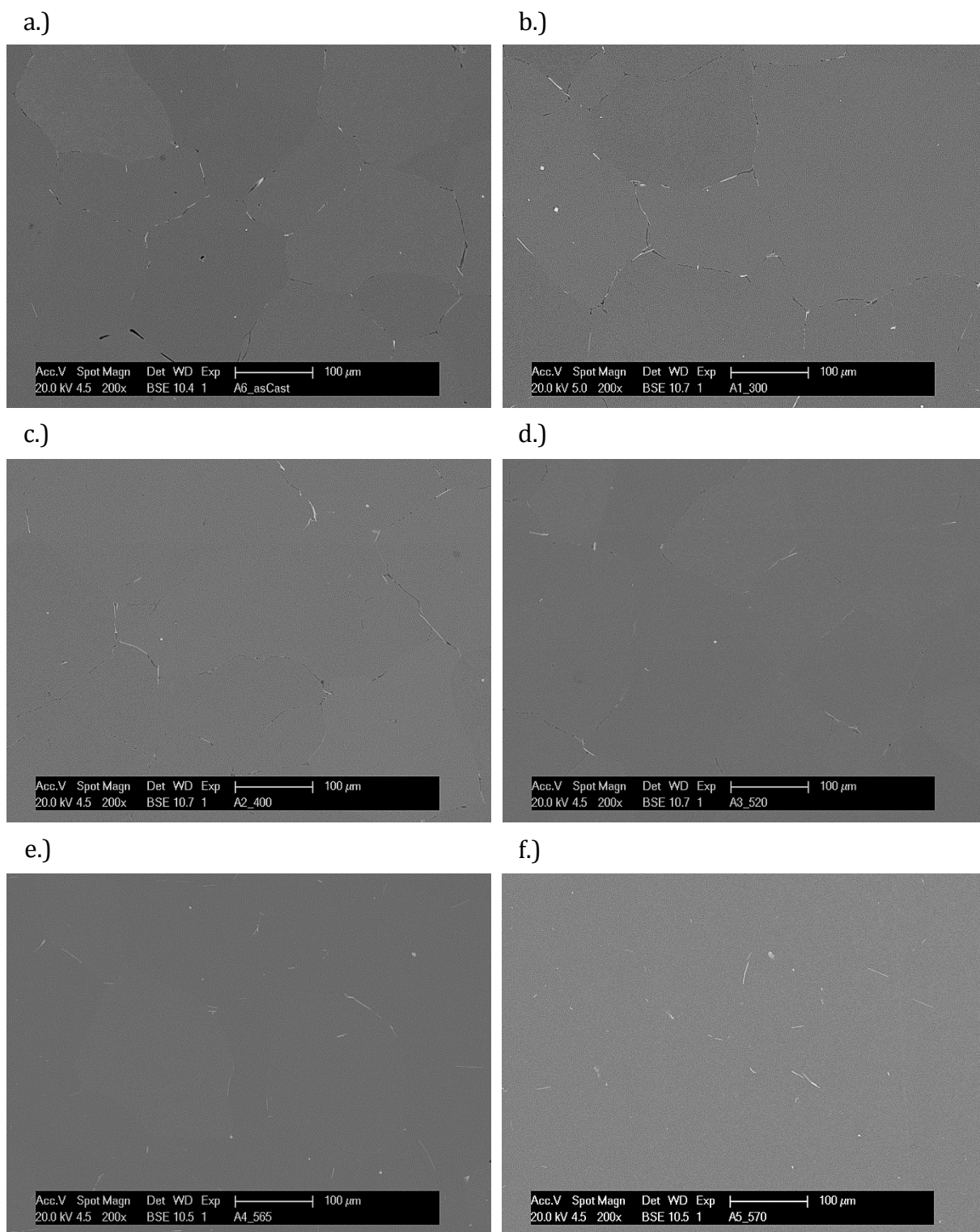


Figure 67: SEM micrographs (200x magnification) as-cast - A6 (a.) and at 300°C - A1 (b.), 400°C - A2 (c.), 520°C - A3 (d.), 565°C - A4 (e.), 570°C - A5 (f.)

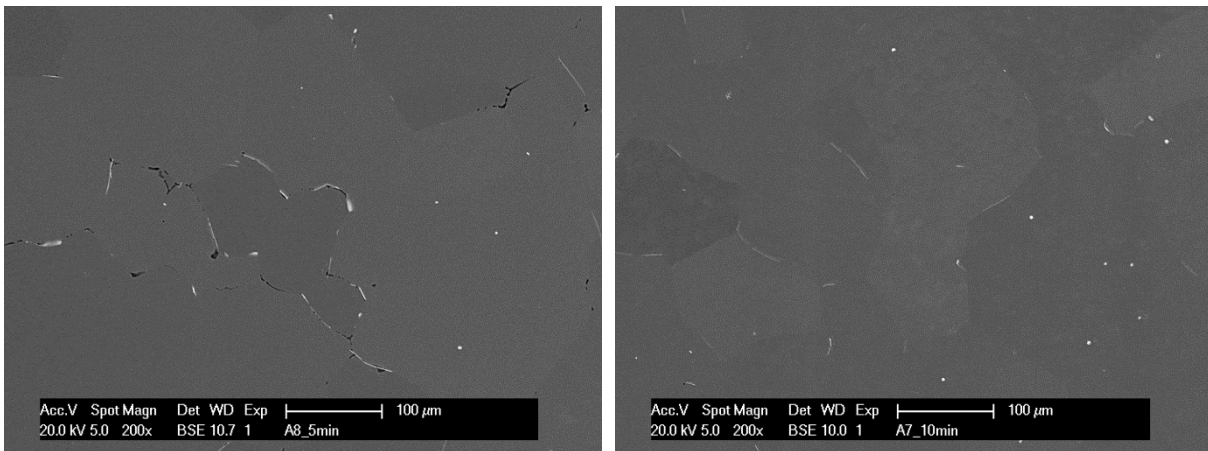


Figure 68: SEM micrographs (200x magnification) A8 - 5min at 565°C (left) and A7 - 10min (right) at 565°C

Table 15: Values phase fraction depending on heat treatment

Name	Temperature	Mg ₂ Si	AlFeSi
A6	As-cast	0.28%	0.25%
A1	300°C	0.34%	0.25%
A2	400°C	0.36%	0.23%
A3	520°C	0.26%	0.18%
A4	565°C	0.00%	0.21%
A5	570°C	0.00%	0.18%
A8	5min at 565°C	0.13%	0.24%
A7	10min at 565°C	0.00%	0.23%

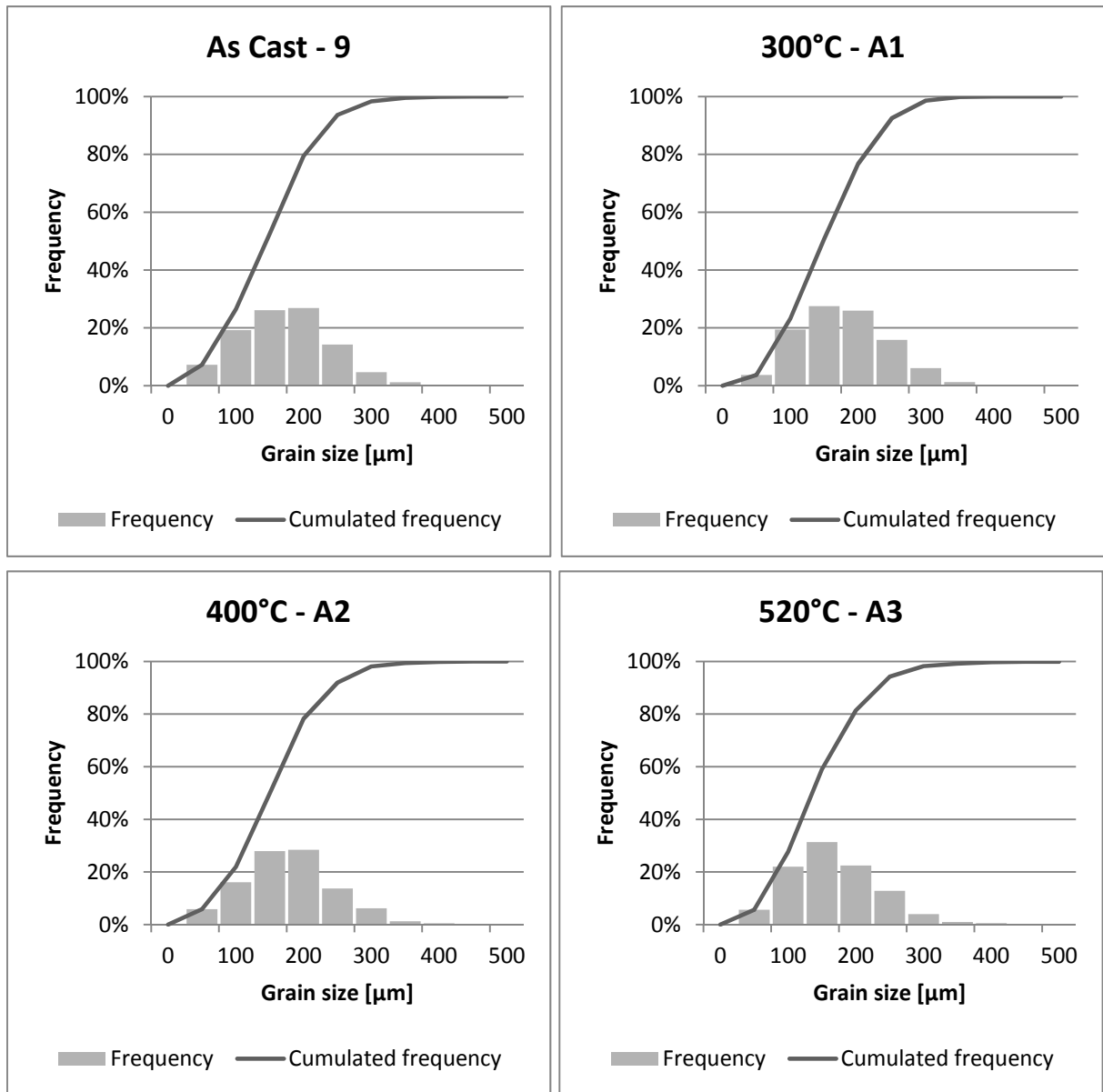


Figure 69: Histogram of grain size distribution for samples 9, A1, A2, and A3

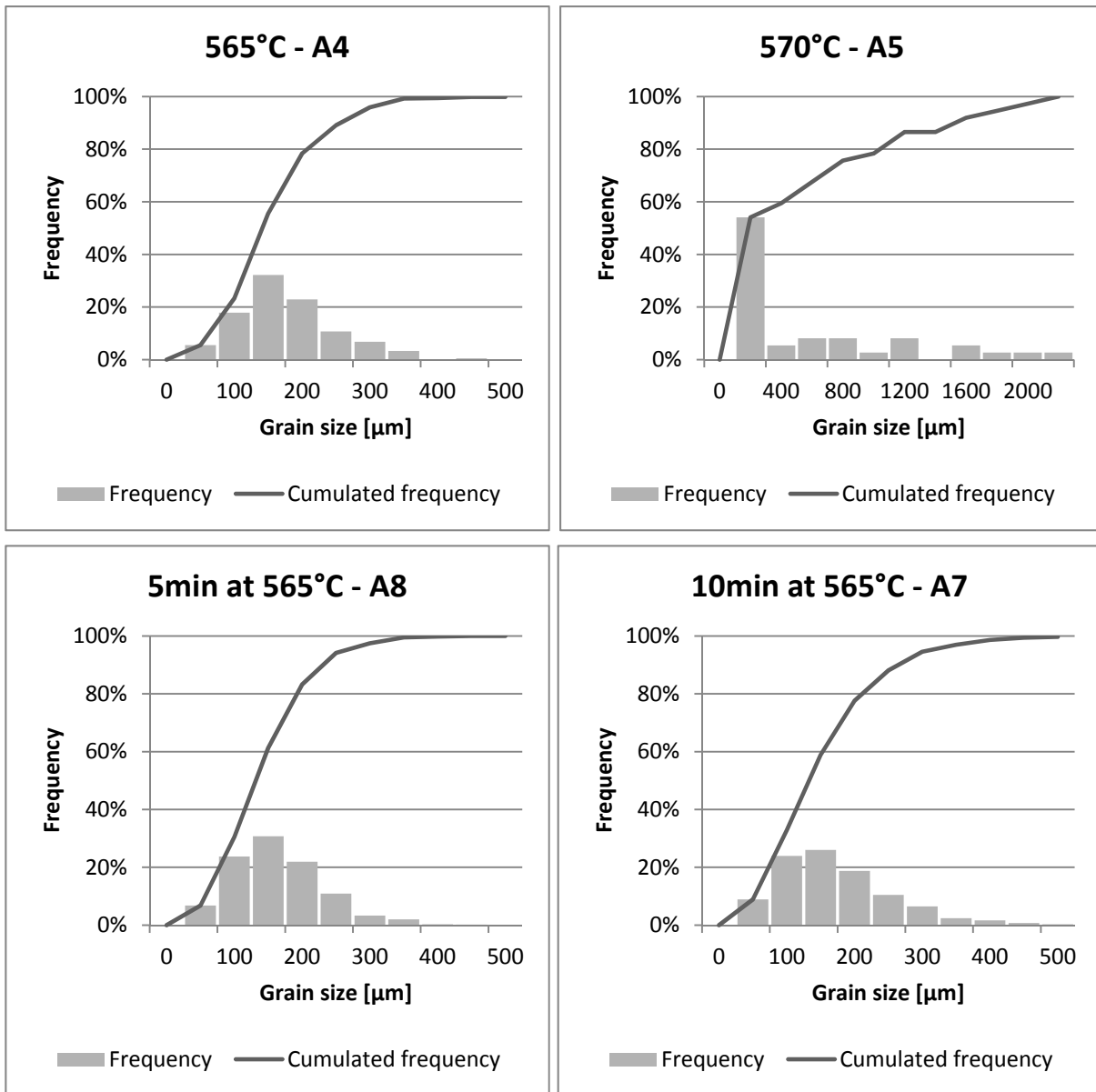


Figure 70: Histogram of grain size distribution for samples A4, A5, A7, and A8

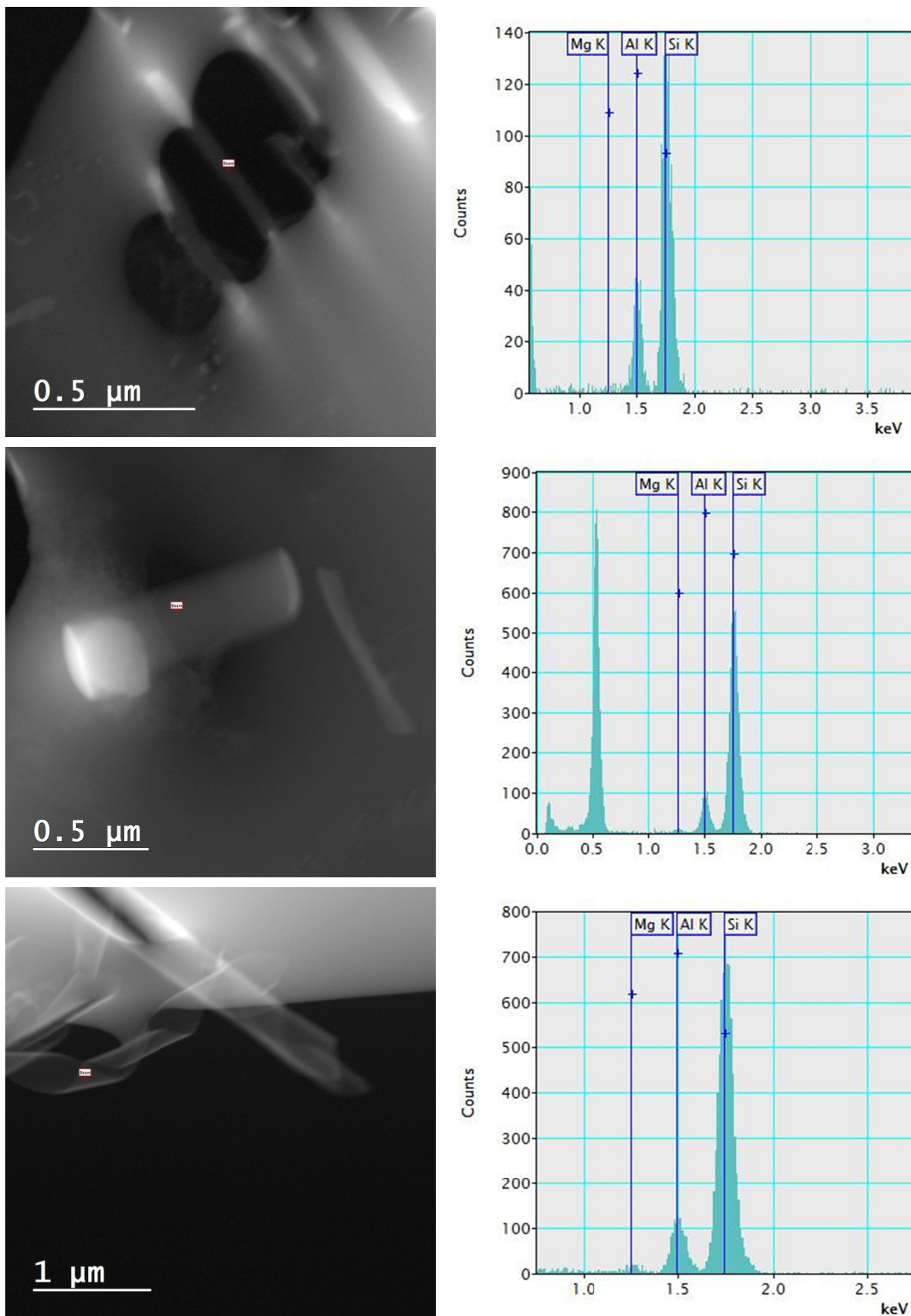


Figure 71: EDX analysis of sample A0.6 (as-cast)

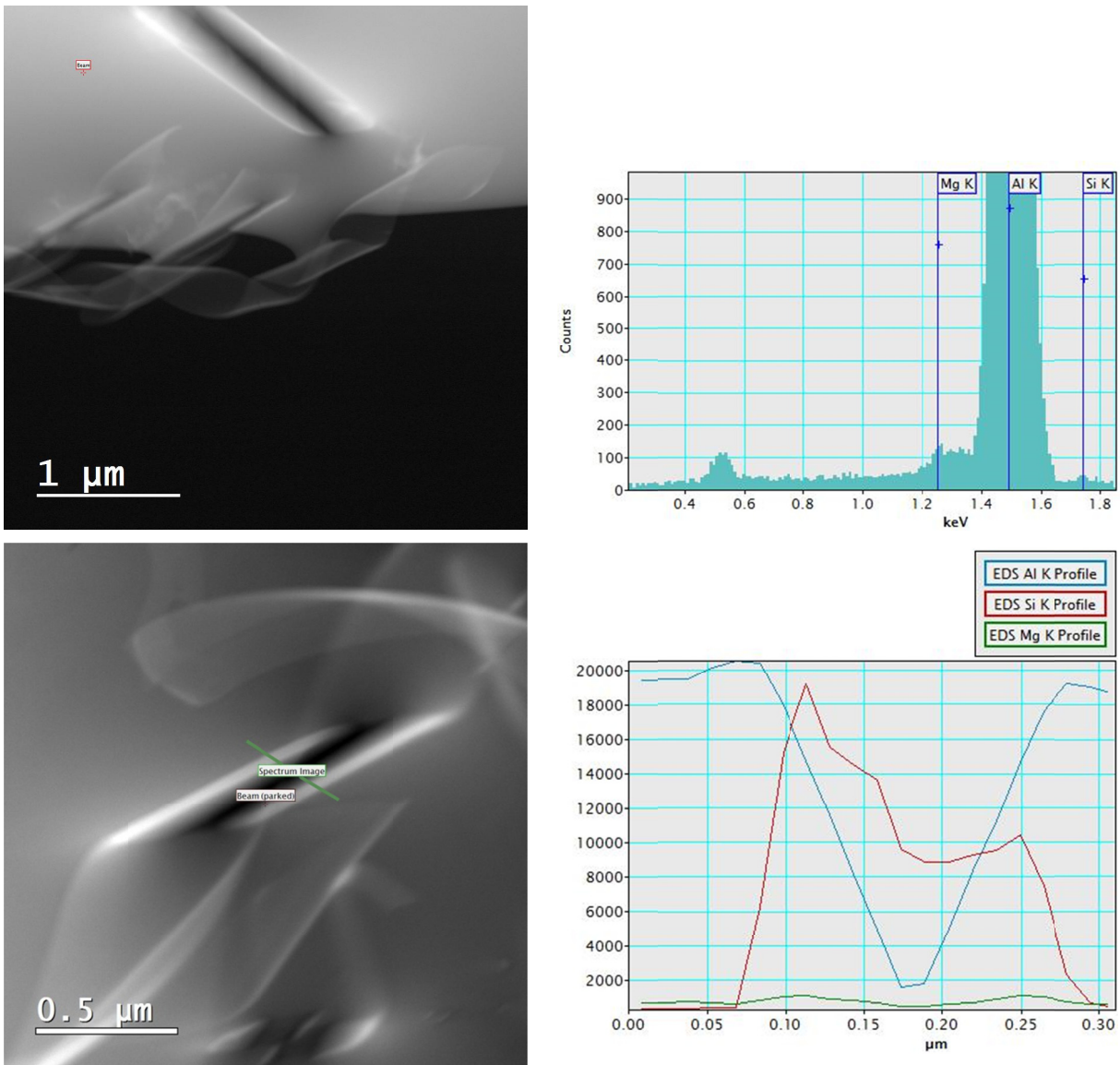


Figure 72: EDX analysis of sample A0.6 (as-cast)

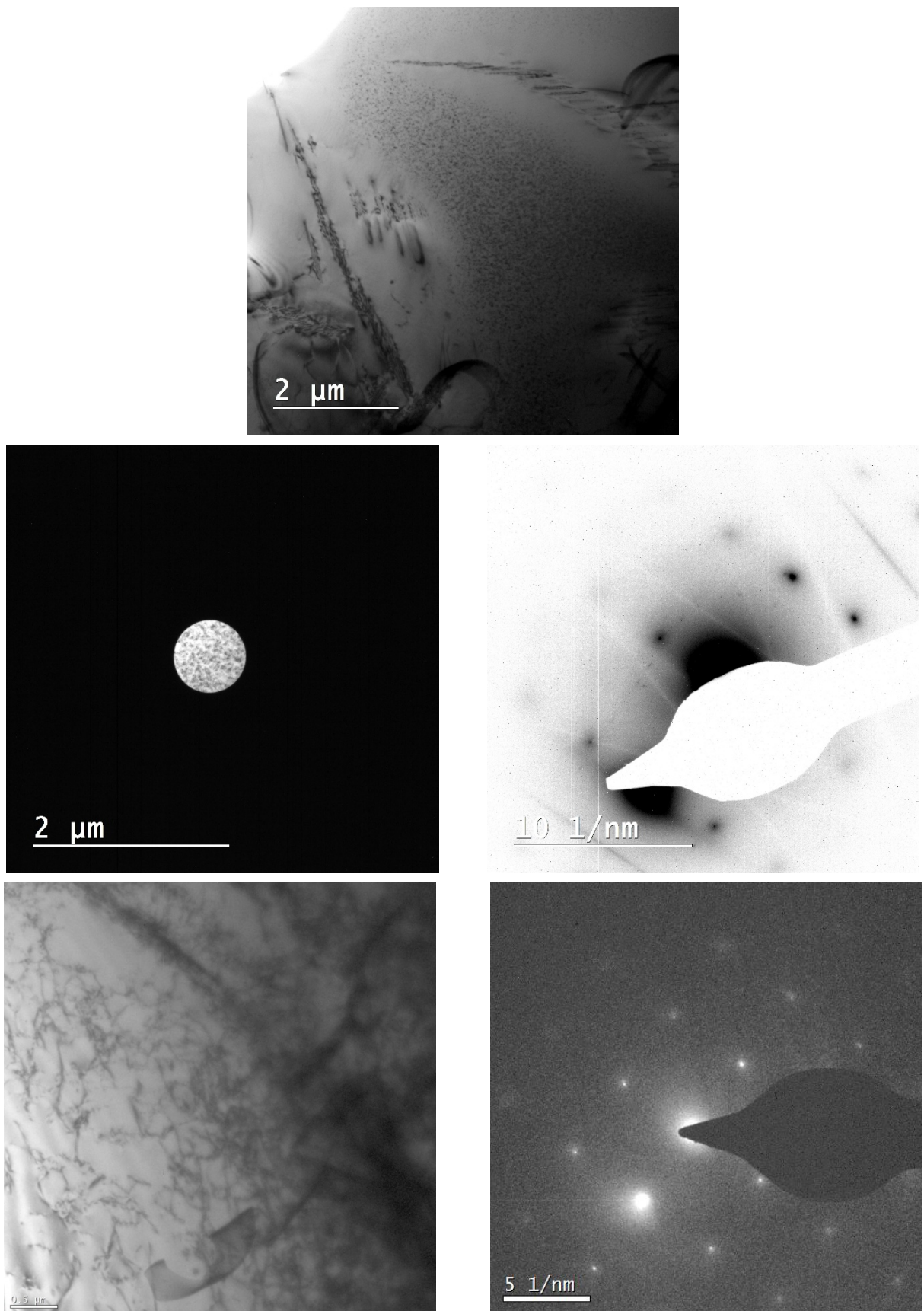


Figure 73: SAED patterns of the matrix in sample A0.6 (as-cast)

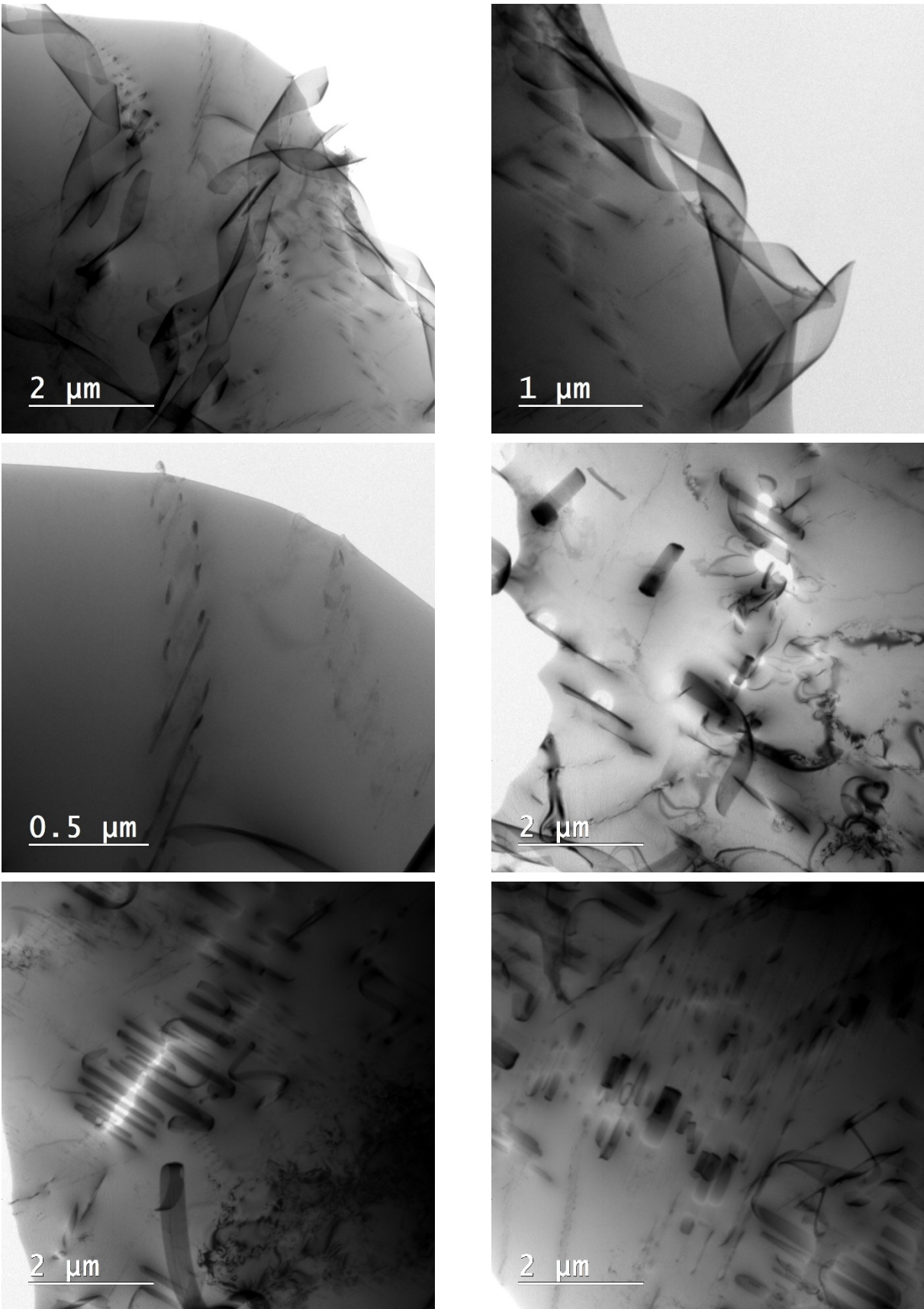


Figure 74: TEM micrographs of sample A0.6 (as-cast)

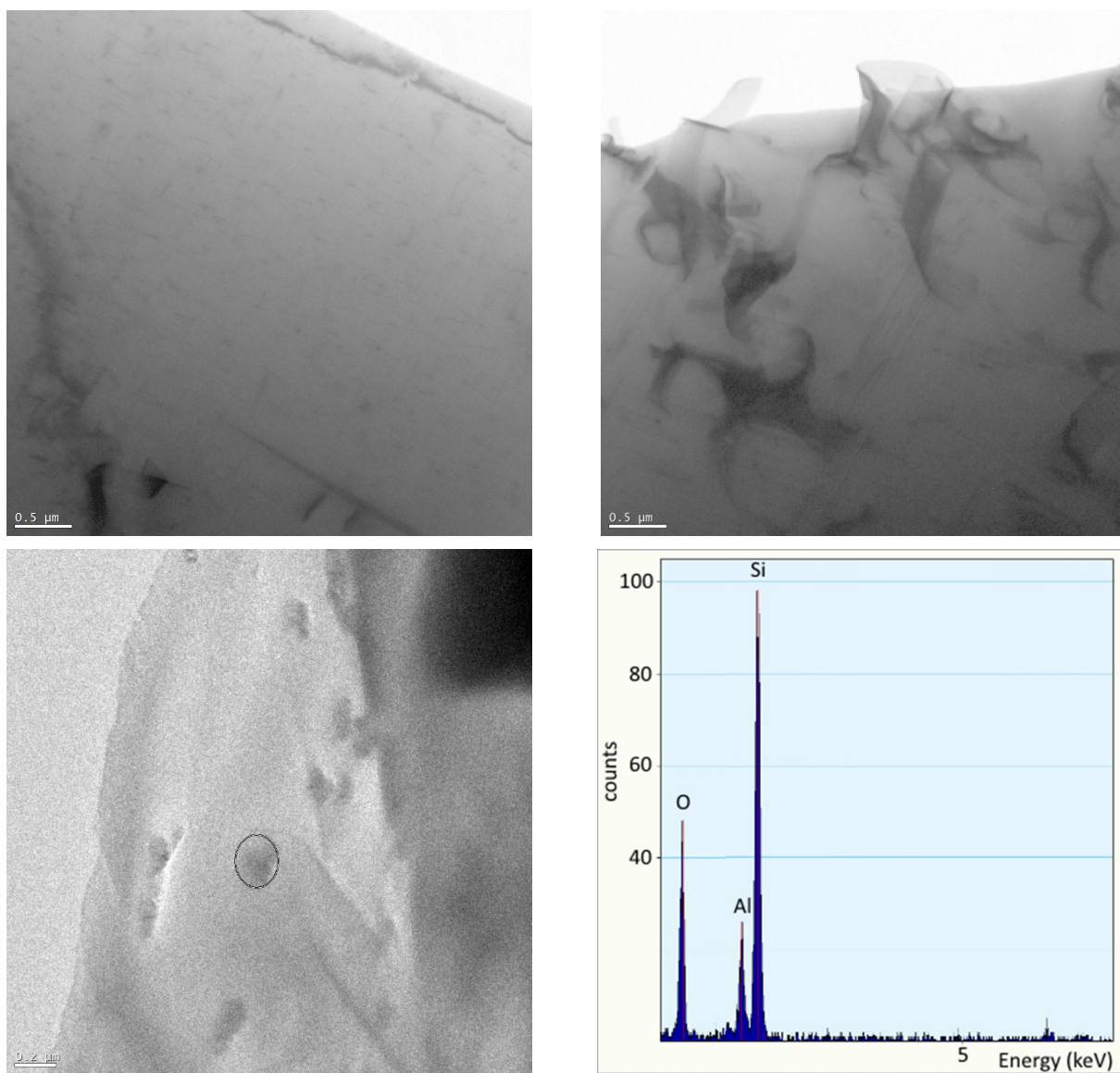


Figure 75: TEM micrographs and EDX analysis of sample A0.1 (300°C)

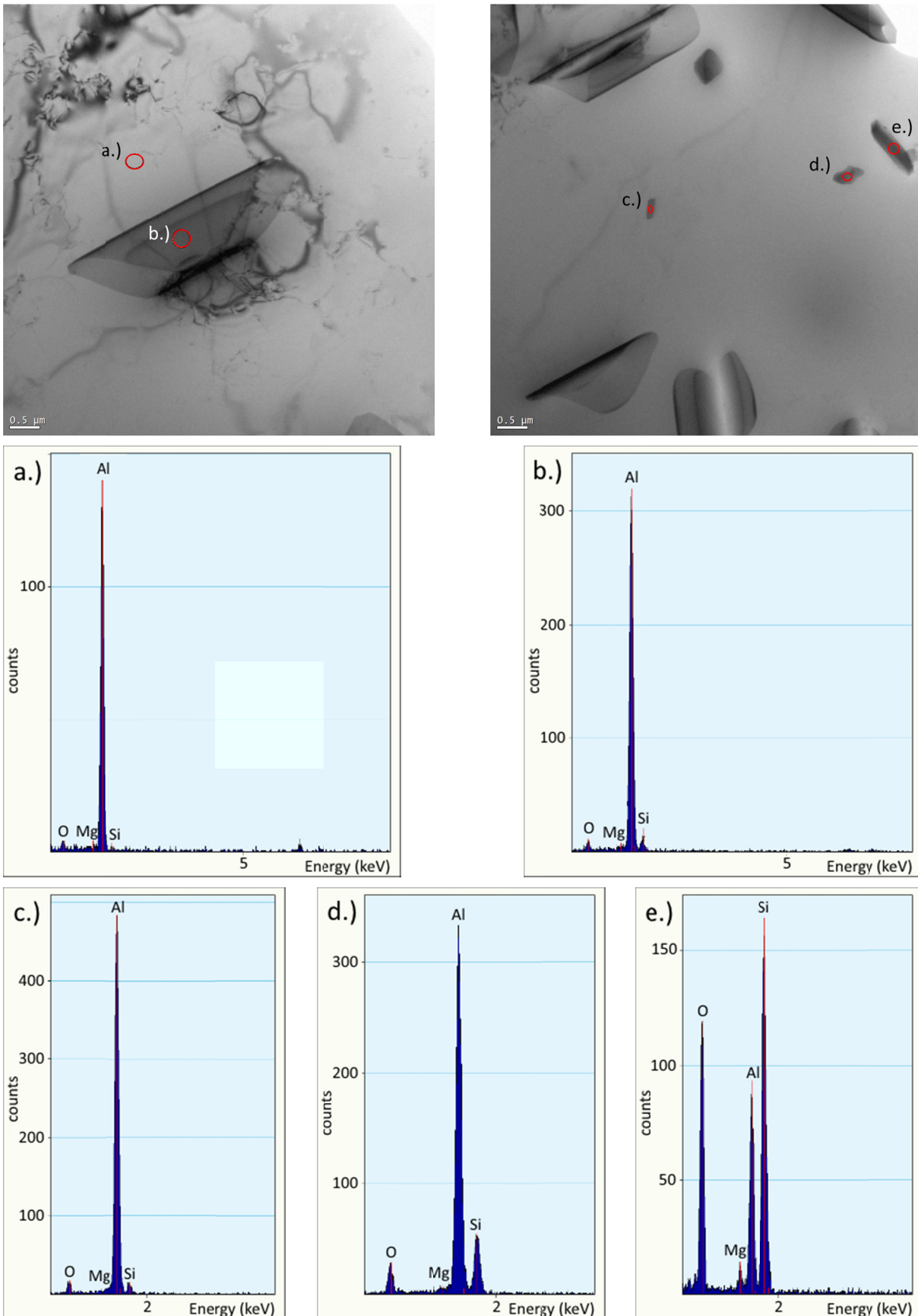


Figure 76: TEM micrographs and EDX analysis of sample A0.2 (400°C)

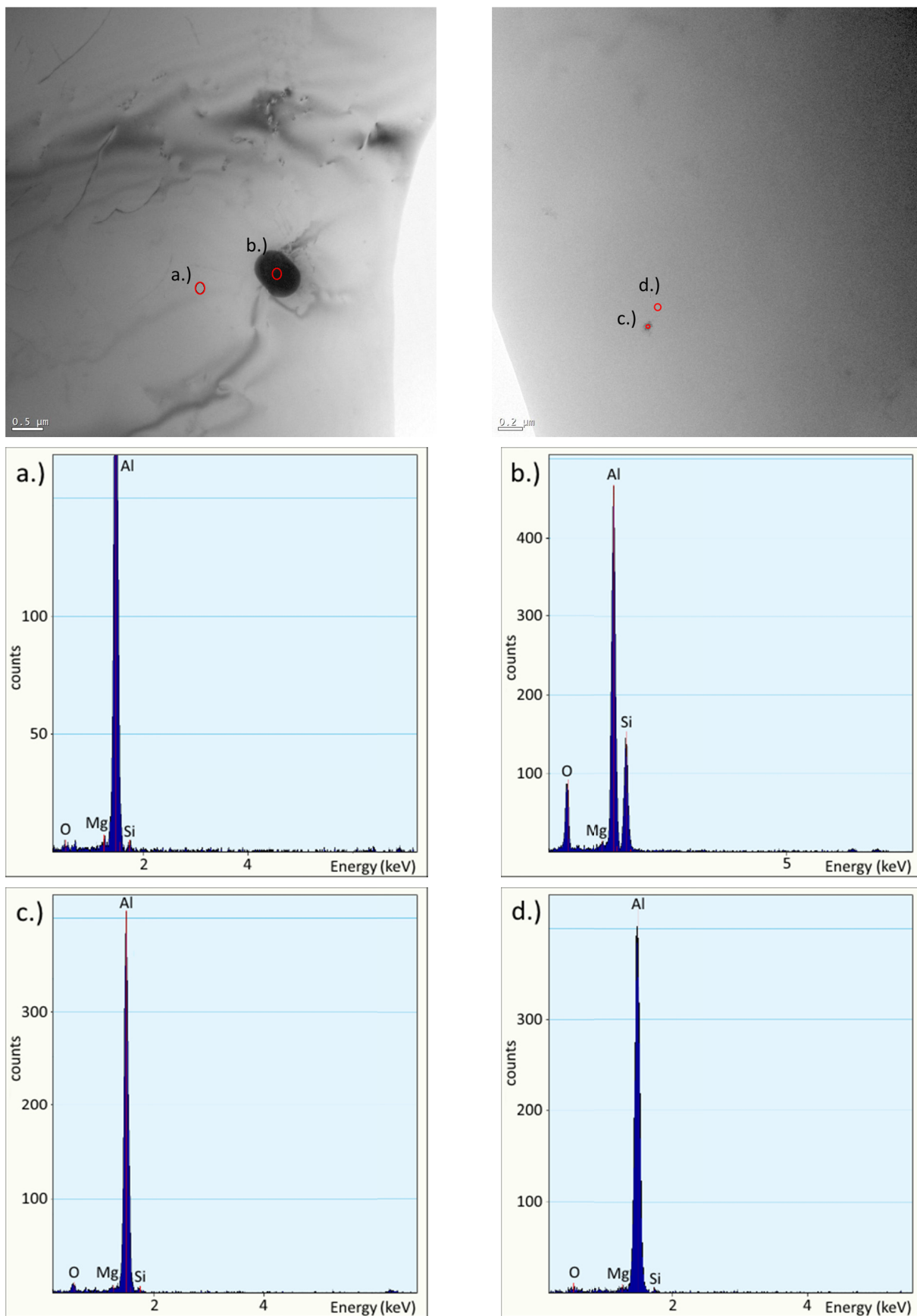


Figure 77: TEM micrographs and EDX analysis of sample A0.3 (520°C)

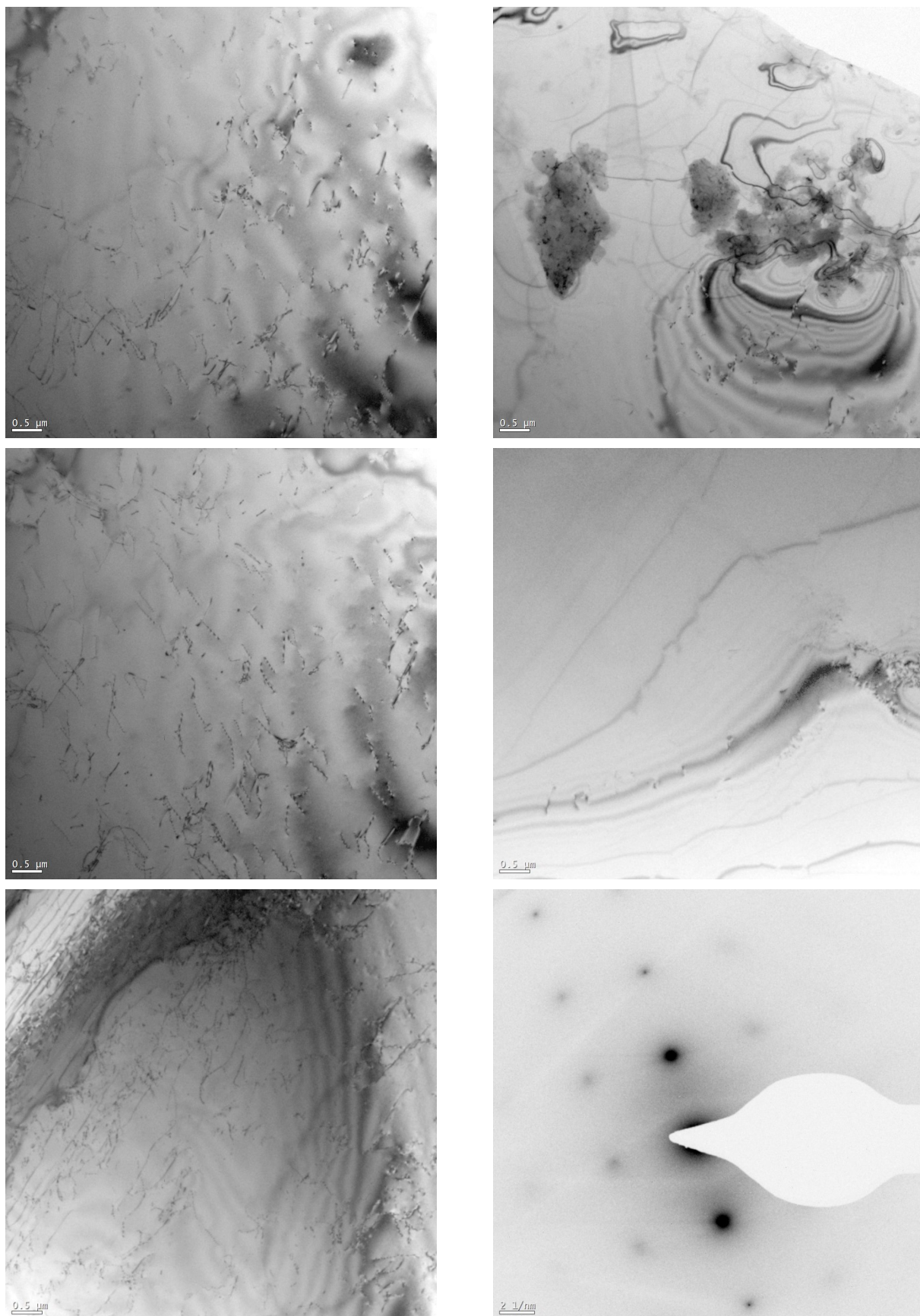


Figure 78: TEM micrographs and SAED pattern of sample A0.4 (565°C)

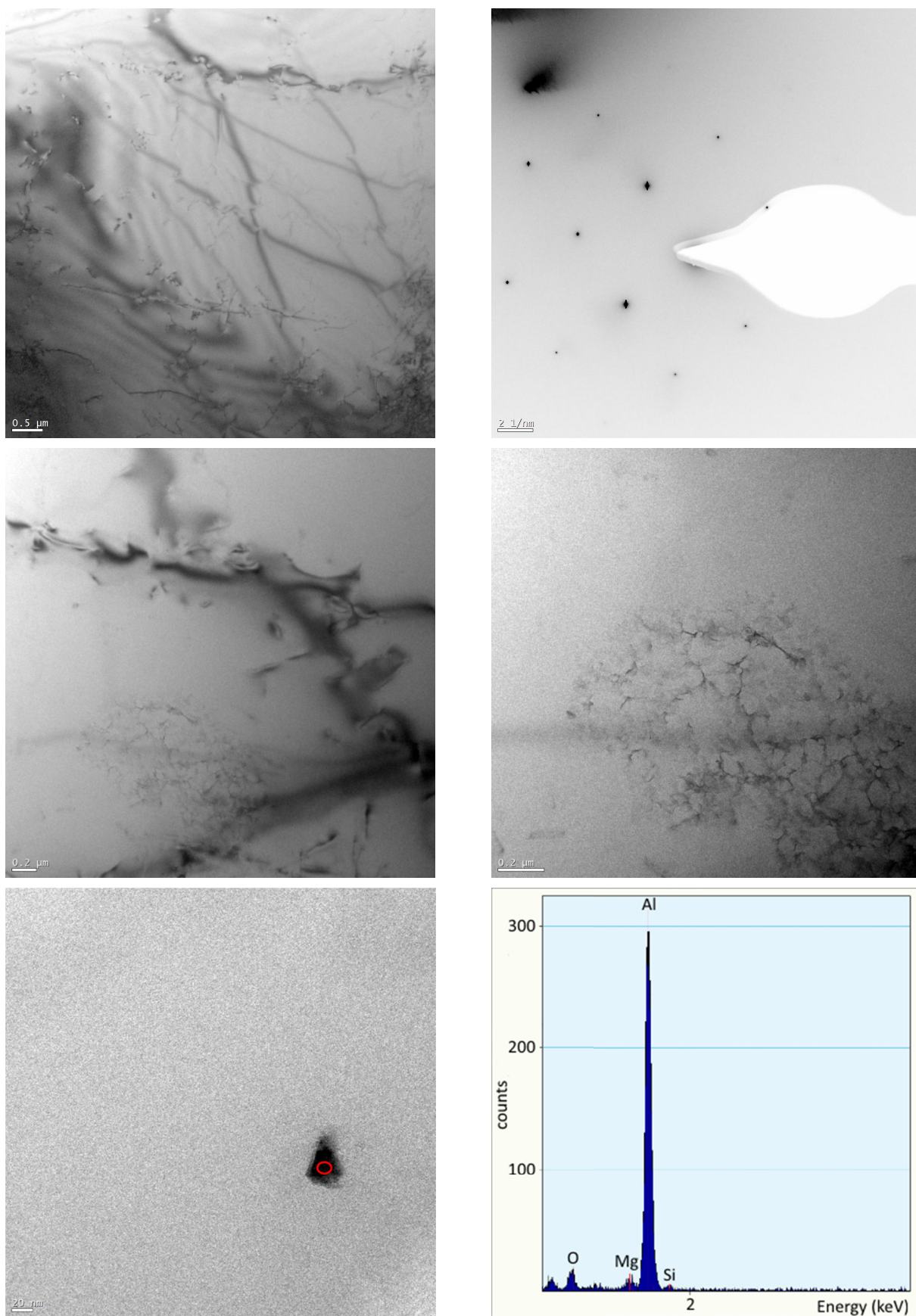


Figure 79: TEM micrographs, SAED pattern, and EDX analysis of sample A0.5 (570°C)

12.3 Deformation Profiles

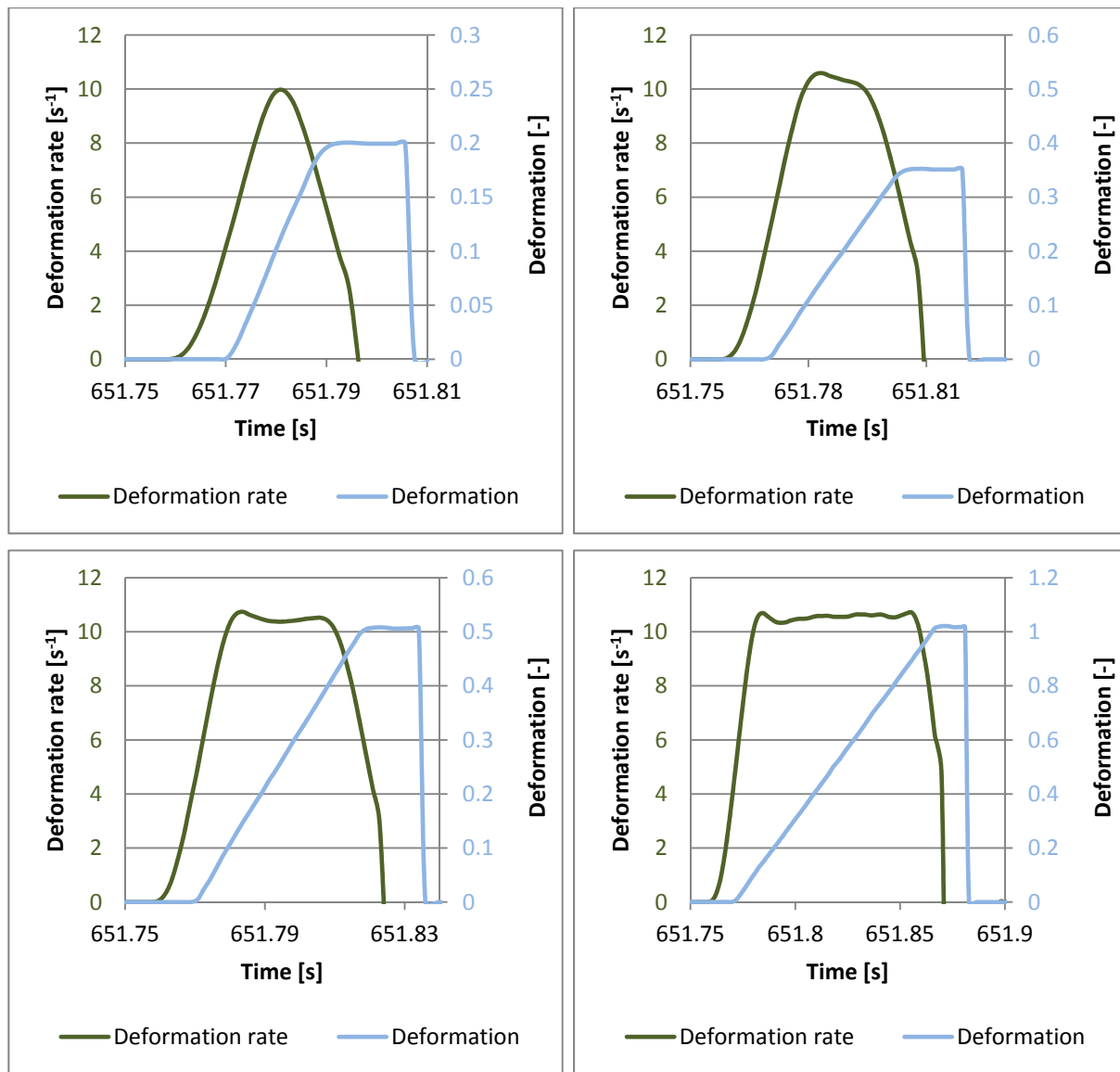


Figure 80: Deformation profile with $\dot{\phi}=10s^{-1}$ and ϕ varying from 0.2 to 1

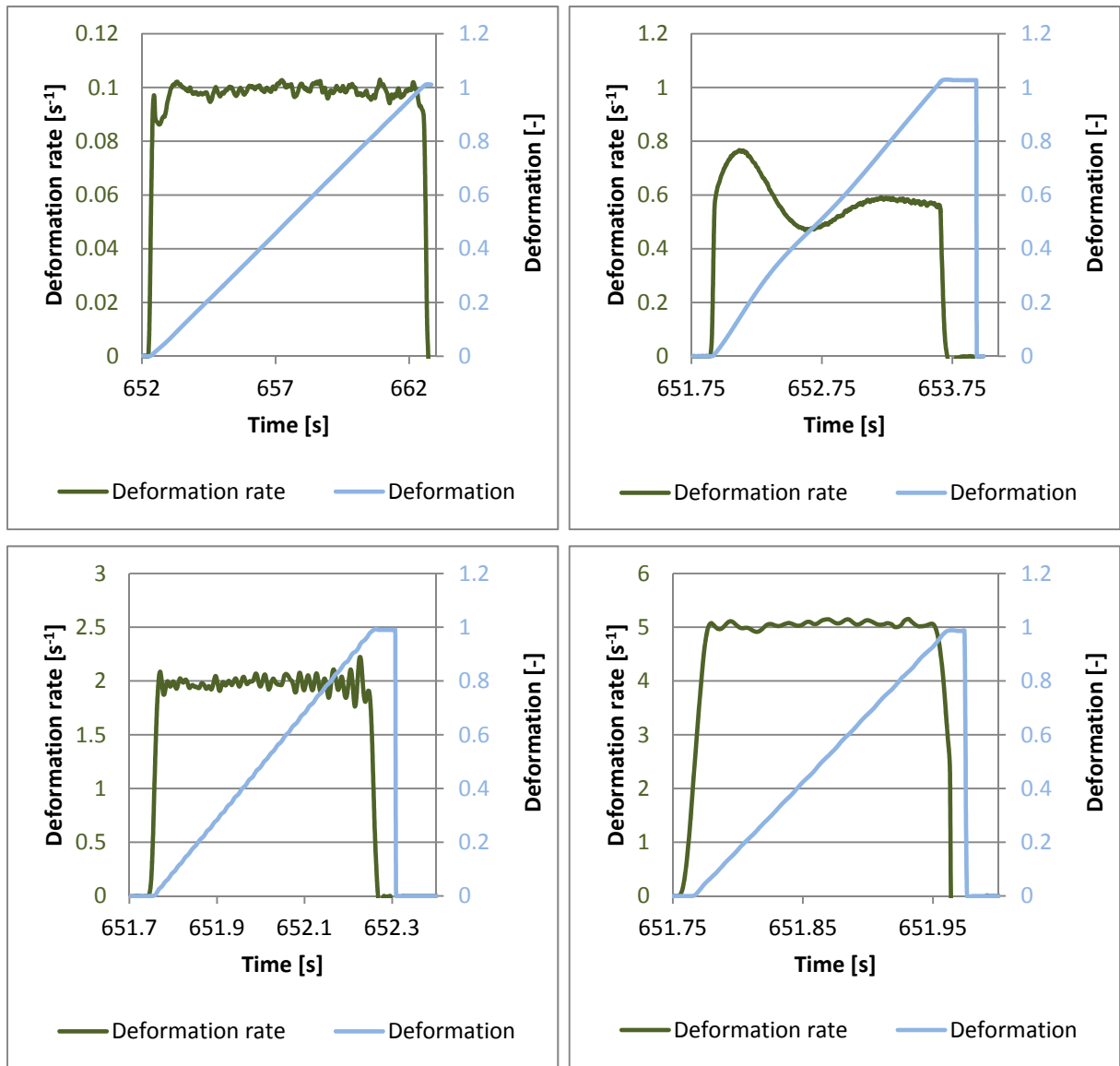
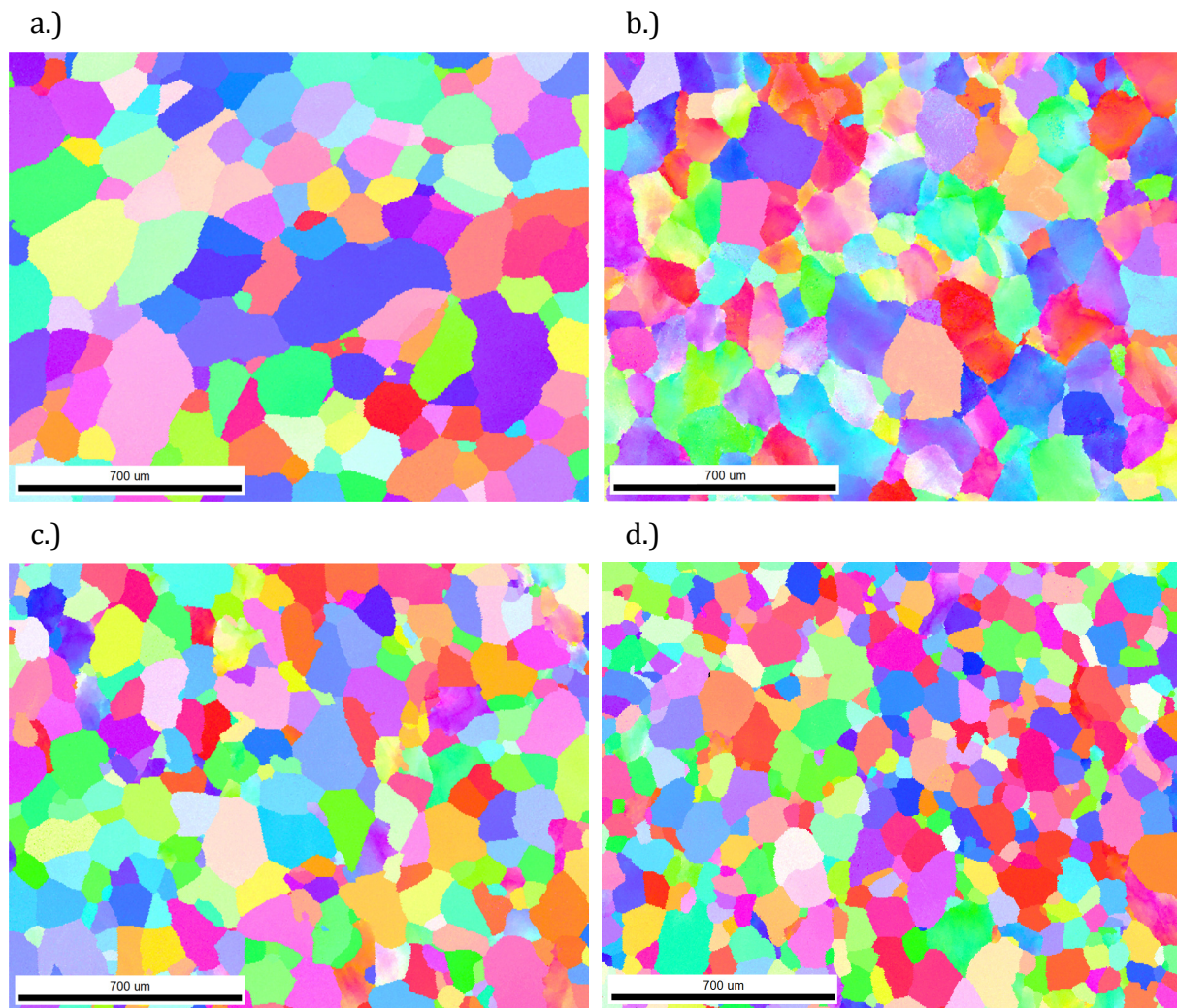


Figure 81: Deformation profile with $\varphi=1$ and $\dot{\varphi}$ varying from 0.1s^{-1} to 5s^{-1}

12.4 Evaluation of Deformed Samples (Group B)



Color Coded Map Type: Inverse Pole Figure [001]

Aluminum

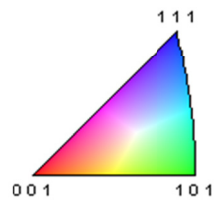


Figure 82: IPF of samples B0/0 (a.), B0.2/10 (b.), B0.35/10 (c.), and B0.5/10 (d.)

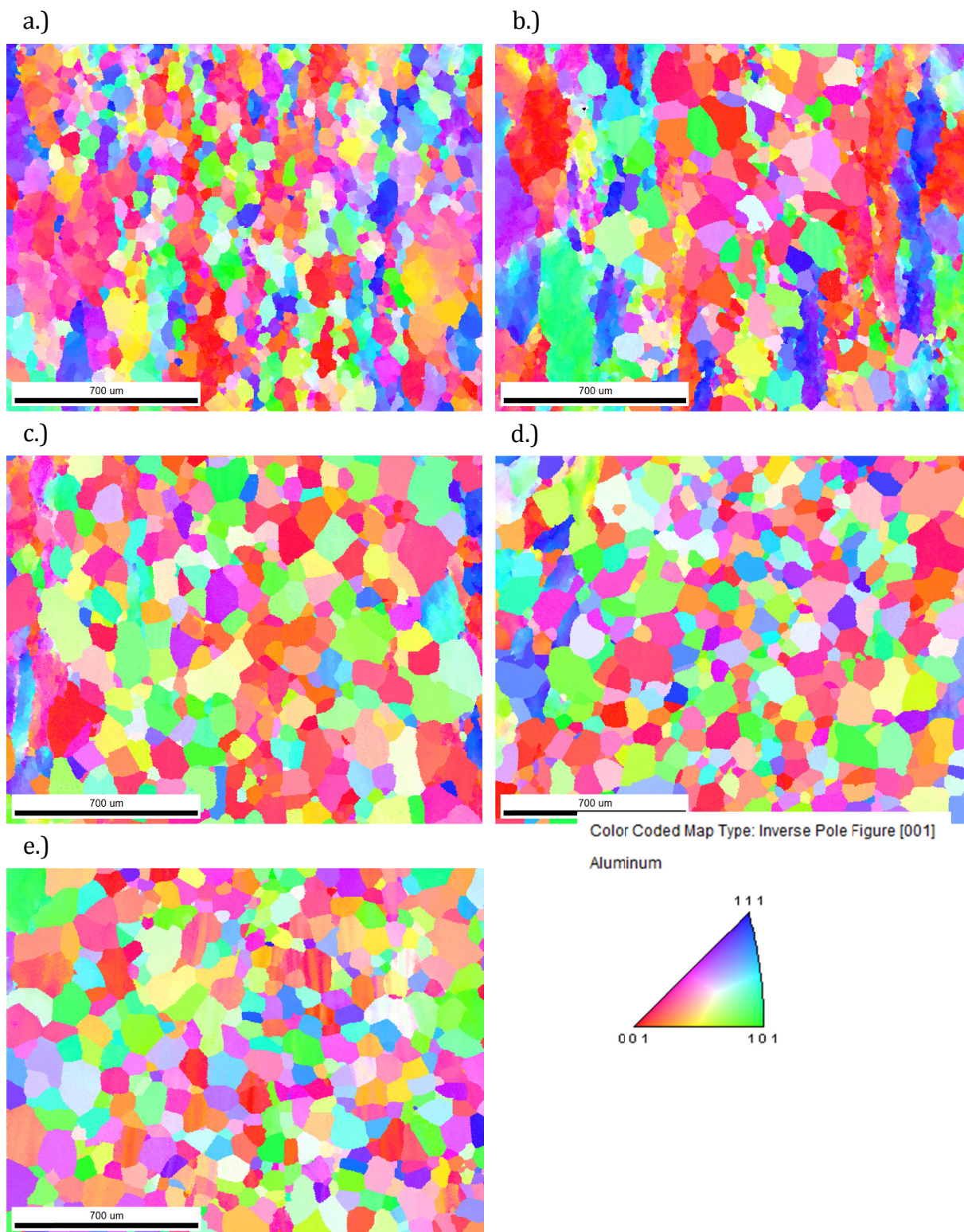
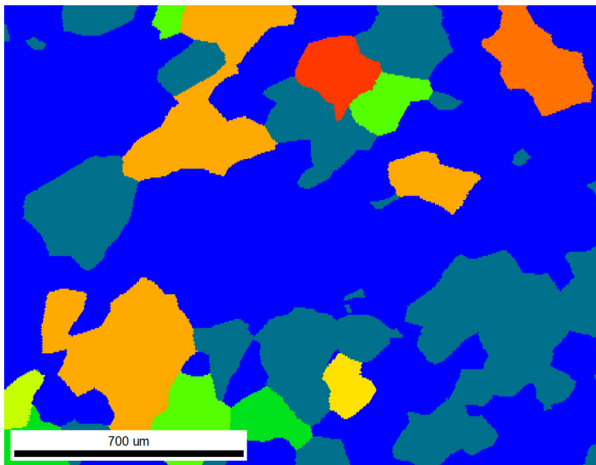


Figure 83: IPF of samples B1/0.1 (a.), B1/0.5 (b.), B1/2 (c.), B1/5 (d.), and B1/10 (e.)

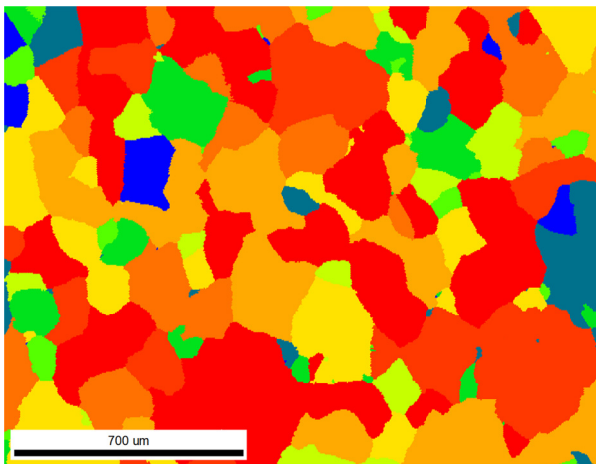
a.)



Color Coded Map Type: Grain Orientation Spread

	Min	Max	Total Fraction	Partition Fraction
	0	0.5	0.549	0.549
	0.5	1	0.233	0.233
	1	1.5	0.021	0.021
	1.5	2	0.033	0.033
	2	2.5	0.006	0.006
	2.5	3	0.008	0.008
	3	3.5	0.111	0.111
	3.5	4	0.024	0.024
	4	4.5	0.015	0.015
	4.5	90	0.000	0.000

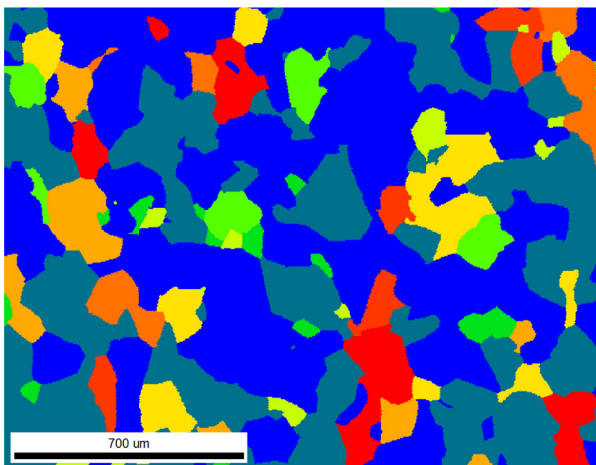
b.)



Color Coded Map Type: Grain Orientation Spread

	Min	Max	Total Fraction	Partition Fraction
	0	0.5	0.023	0.023
	0.5	1	0.042	0.042
	1	1.5	0.055	0.055
	1.5	2	0.018	0.018
	2	2.5	0.040	0.040
	2.5	3	0.123	0.123
	3	3.5	0.178	0.178
	3.5	4	0.106	0.106
	4	4.5	0.147	0.147
	4.5	90	0.267	0.267

c.)

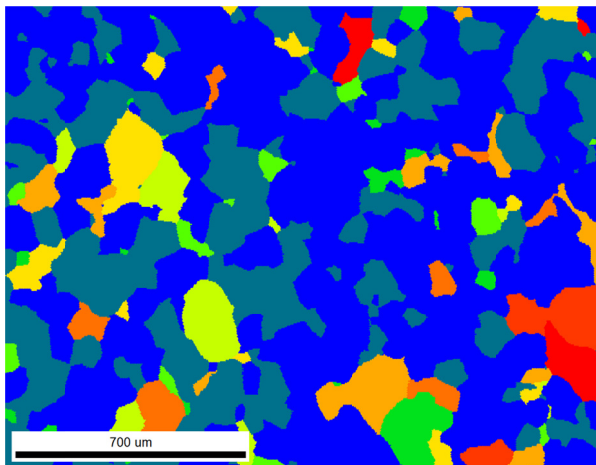


Color Coded Map Type: Grain Orientation Spread

	Min	Max	Total Fraction	Partition Fraction
	0	0.5	0.417	0.417
	0.5	1	0.327	0.327
	1	1.5	0.016	0.016
	1.5	2	0.029	0.029
	2	2.5	0.018	0.018
	2.5	3	0.055	0.055
	3	3.5	0.037	0.037
	3.5	4	0.029	0.029
	4	4.5	0.025	0.025
	4.5	90	0.046	0.046

Figure 84: GOS of samples B0/0 (a.), B0.2/10 (b.), and B0.35/10 (c.)

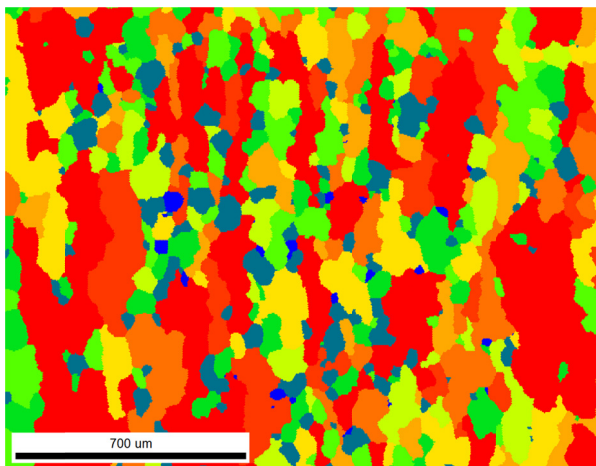
a.)



Color Coded Map Type: Grain Orientation Spread

	Min	Max	Total Fraction	Partition Fraction
	0	0.5	0.520	0.520
	0.5	1	0.287	0.287
	1	1.5	0.023	0.023
	1.5	2	0.015	0.015
	2	2.5	0.031	0.031
	2.5	3	0.030	0.030
	3	3.5	0.037	0.037
	3.5	4	0.022	0.022
	4	4.5	0.019	0.019
	4.5	90	0.016	0.016

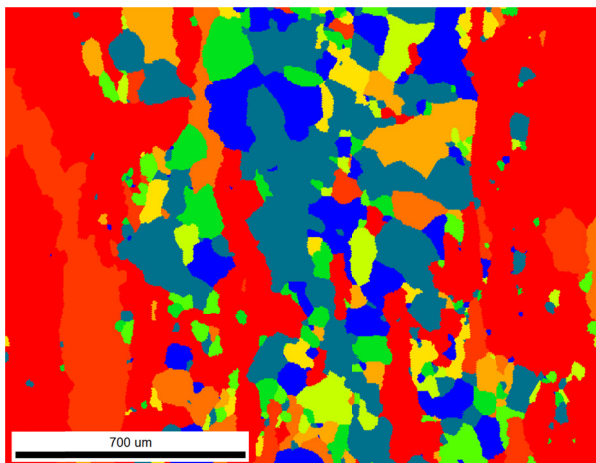
b.)



Color Coded Map Type: Grain Orientation Spread

	Min	Max	Total Fraction	Partition Fraction
	0	0.5	0.006	0.006
	0.5	1	0.080	0.080
	1	1.5	0.078	0.078
	1.5	2	0.082	0.082
	2	2.5	0.071	0.071
	2.5	3	0.102	0.102
	3	3.5	0.067	0.067
	3.5	4	0.090	0.090
	4	4.5	0.096	0.096
	4.5	90	0.329	0.329

c.)

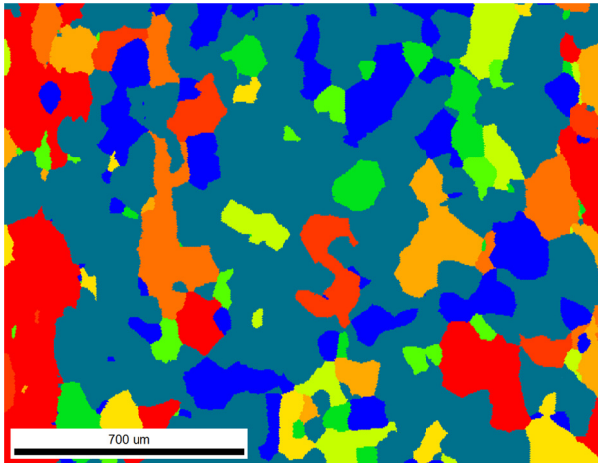


Color Coded Map Type: Grain Orientation Spread

	Min	Max	Total Fraction	Partition Fraction
	0	0.5	0.093	0.093
	0.5	1	0.177	0.177
	1	1.5	0.047	0.047
	1.5	2	0.024	0.024
	2	2.5	0.031	0.031
	2.5	3	0.024	0.024
	3	3.5	0.044	0.044
	3.5	4	0.039	0.040
	4	4.5	0.093	0.093
	4.5	90	0.426	0.426

Figure 85: GOS of samples B0.5/10 (a.), B1/0.1 (b.), and B1/0.5 (c.)

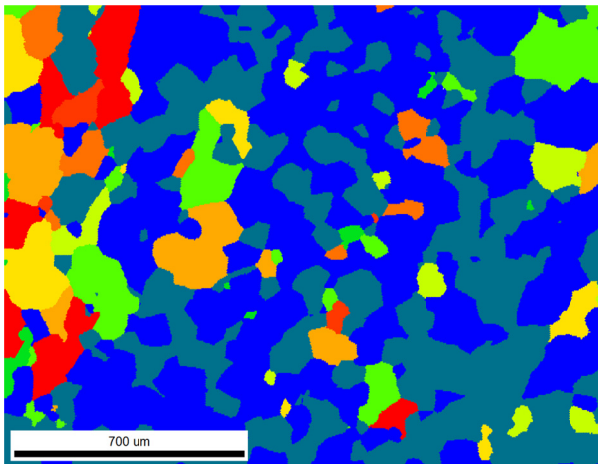
a.)



Color Coded Map Type: Grain Orientation Spread

	Min	Max	Total Fraction	Partition Fraction
	0	0.5	0.121	0.121
	0.5	1	0.496	0.496
	1	1.5	0.039	0.039
	1.5	2	0.022	0.022
	2	2.5	0.036	0.036
	2.5	3	0.029	0.029
	3	3.5	0.046	0.046
	3.5	4	0.050	0.050
	4	4.5	0.035	0.035
	4.5	90	0.126	0.126

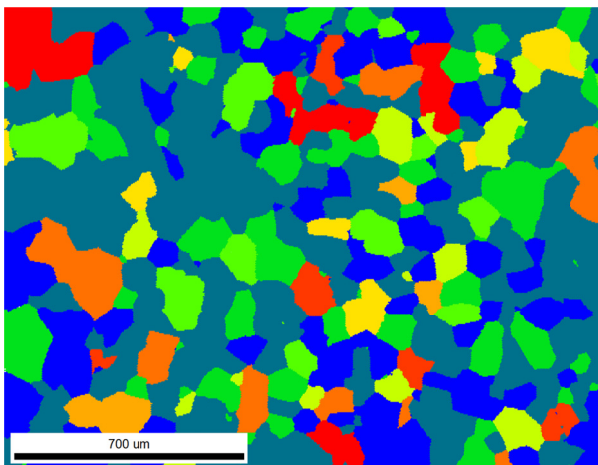
b.)



Color Coded Map Type: Grain Orientation Spread

	Min	Max	Total Fraction	Partition Fraction
	0	0.5	0.421	0.421
	0.5	1	0.340	0.340
	1	1.5	0.007	0.007
	1.5	2	0.059	0.059
	2	2.5	0.025	0.025
	2.5	3	0.032	0.032
	3	3.5	0.044	0.044
	3.5	4	0.023	0.023
	4	4.5	0.007	0.007
	4.5	90	0.042	0.042

c.)



Color Coded Map Type: Grain Orientation Spread

	Min	Max	Total Fraction	Partition Fraction
	0	0.5	0.200	0.200
	0.5	1	0.418	0.418
	1	1.5	0.136	0.136
	1.5	2	0.052	0.052
	2	2.5	0.040	0.040
	2.5	3	0.024	0.024
	3	3.5	0.017	0.017
	3.5	4	0.049	0.049
	4	4.5	0.018	0.018
	4.5	90	0.046	0.046

Figure 86: GOS of samples B1/2 (a.), B1/5 (b.), and B1/10 (c.)

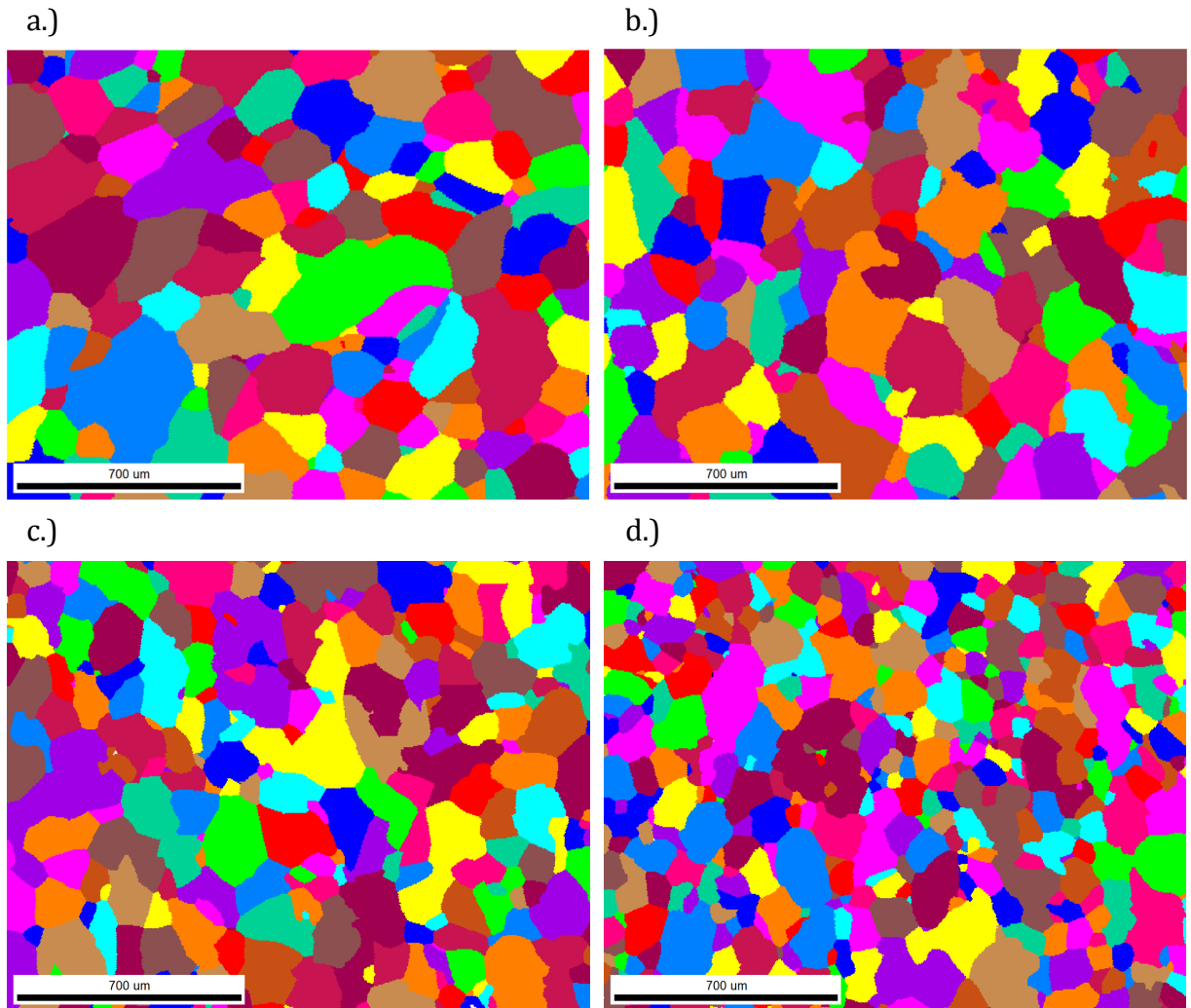


Figure 87: Grain map of samples B0/0 (a.), B0.2/10 (b.), B0.35/10 (c.), and B0.5/10 (d.)

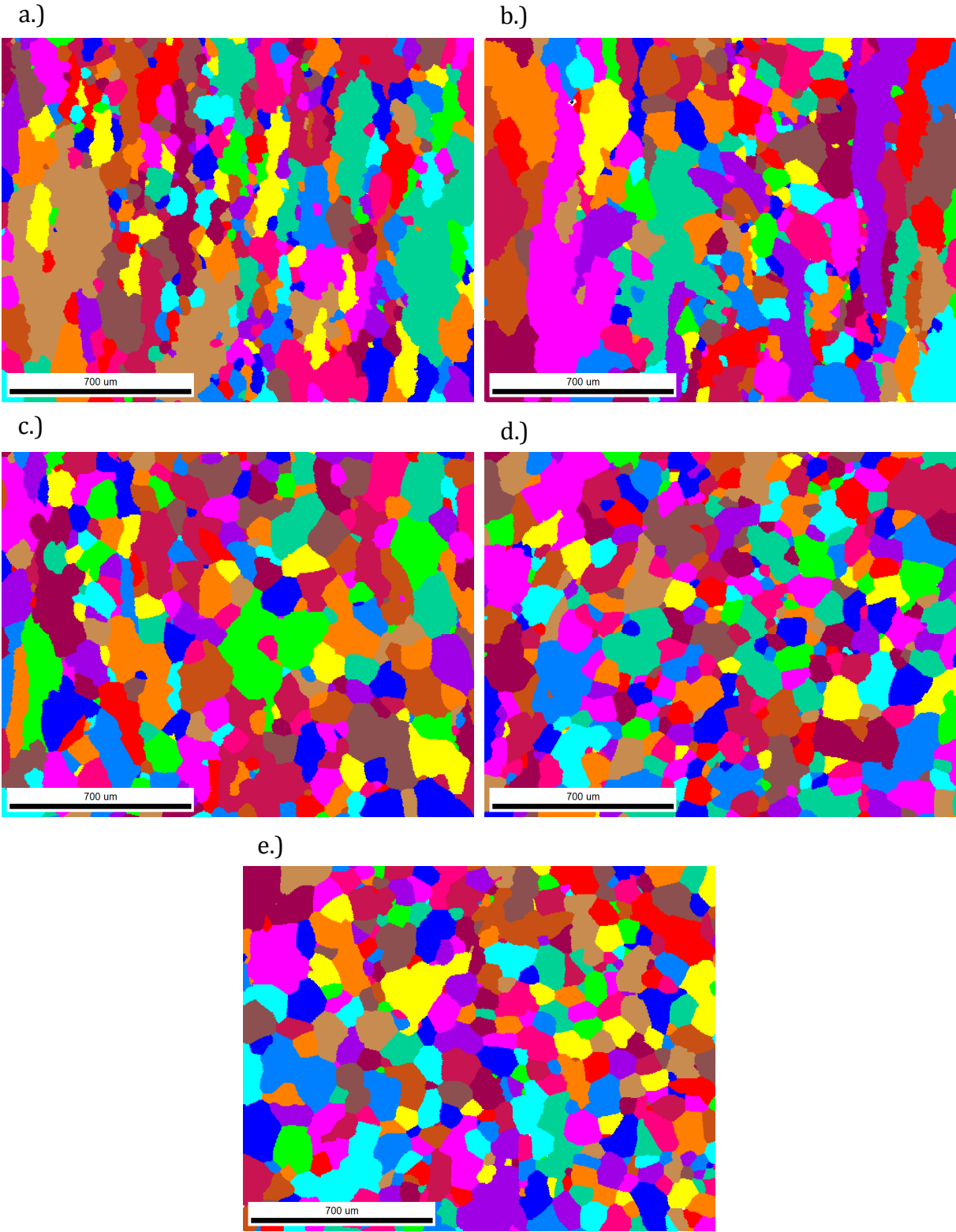


Figure 88: Grain map of samples B1/0.1 (a.), B1/0.5 (b.), B1/2 (c.), B1/5 (d.), and B1/10 (e.)

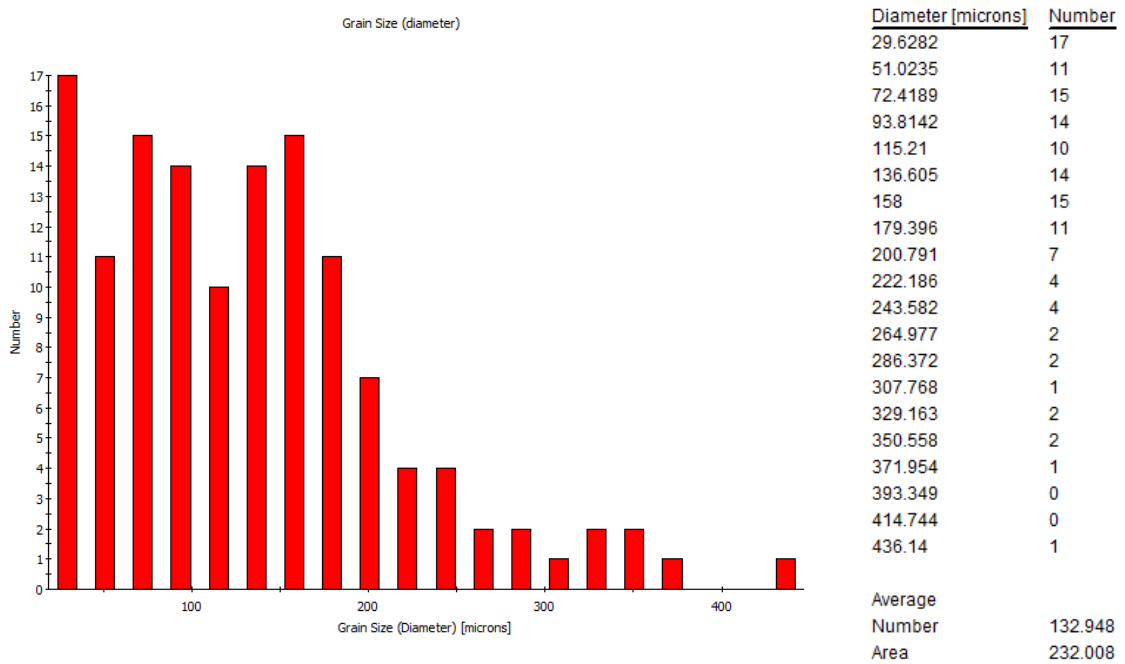


Figure 89: Histogram of grain size distribution for sample B0/0

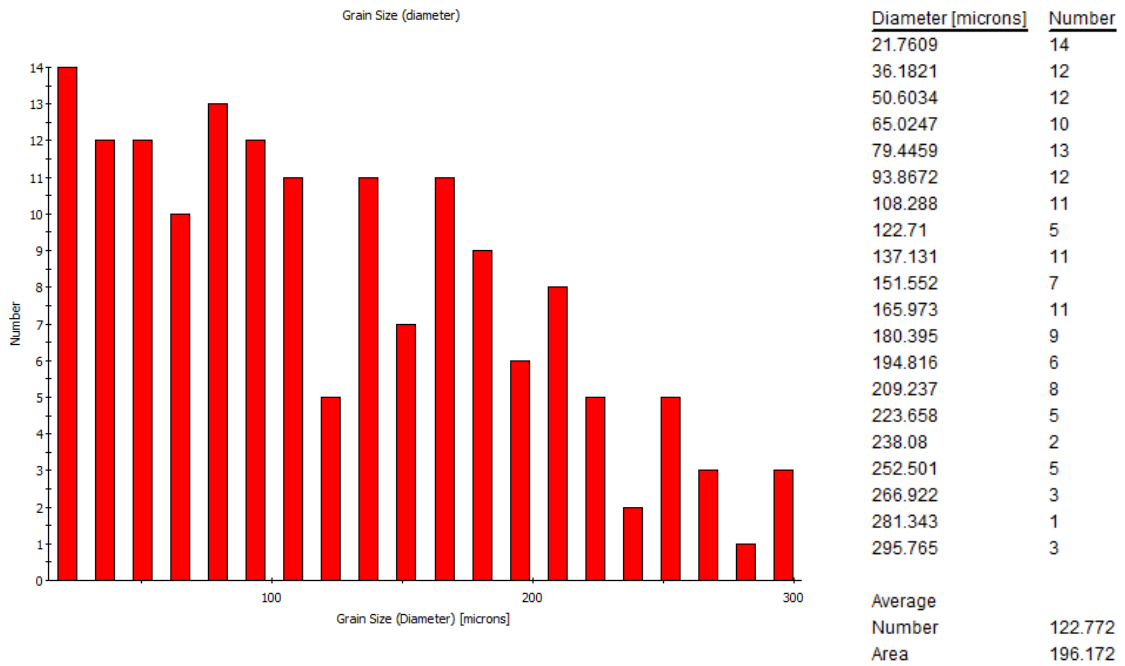


Figure 90: Histogram of grain size distribution for sample B0.2/10

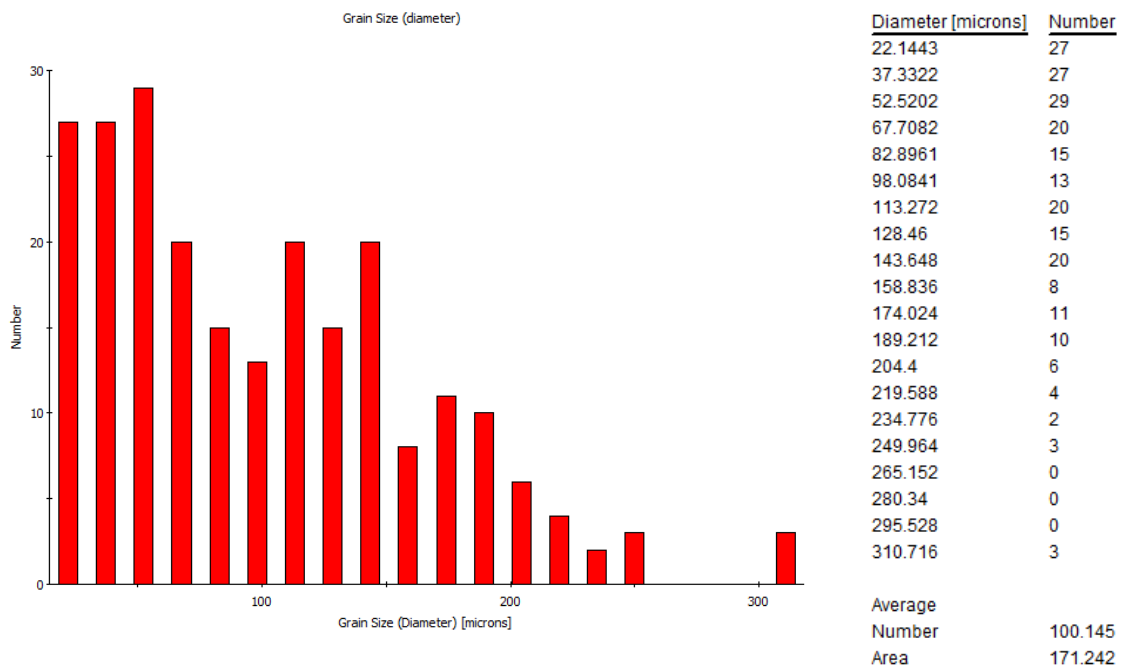


Figure 91: Histogram of grain size distribution for sample B0.35/10

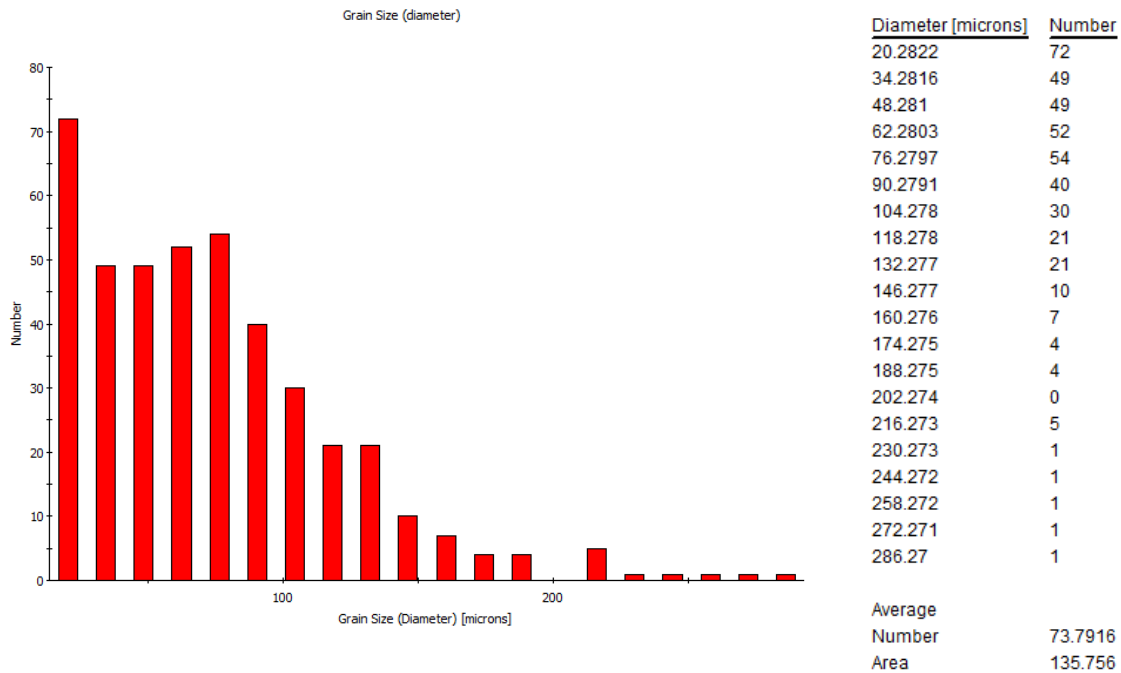


Figure 92: Histogram of grain size distribution for sample B0.5/10

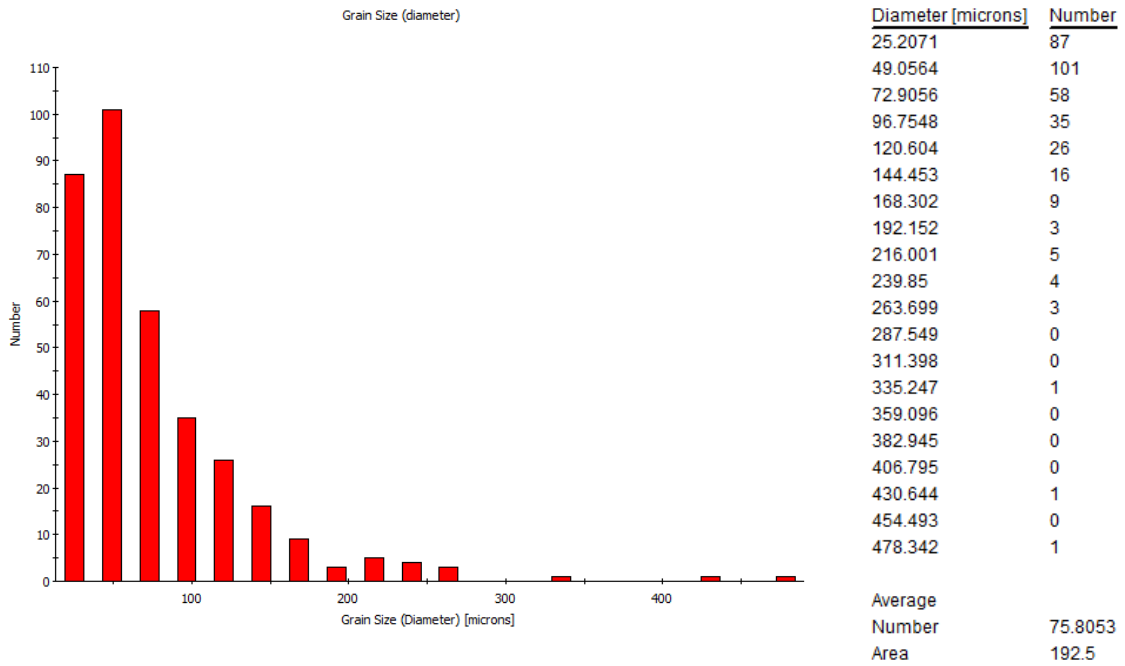


Figure 93: Histogram of grain size distribution for sample B1/0.1

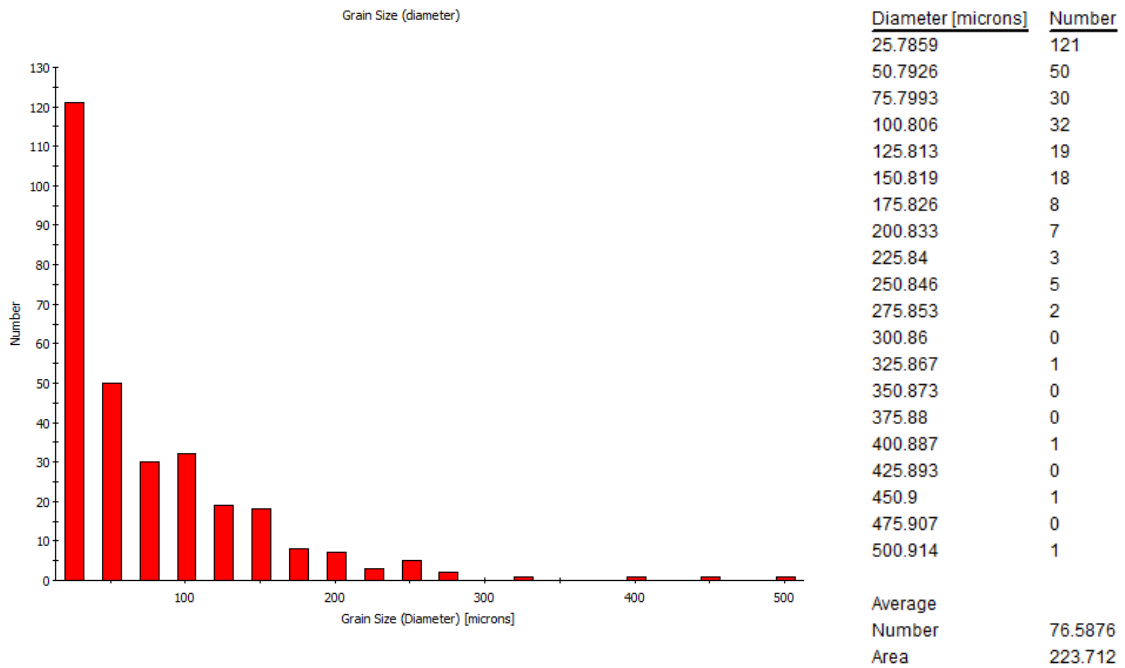


Figure 94: Histogram of grain size distribution for sample B1/0.5

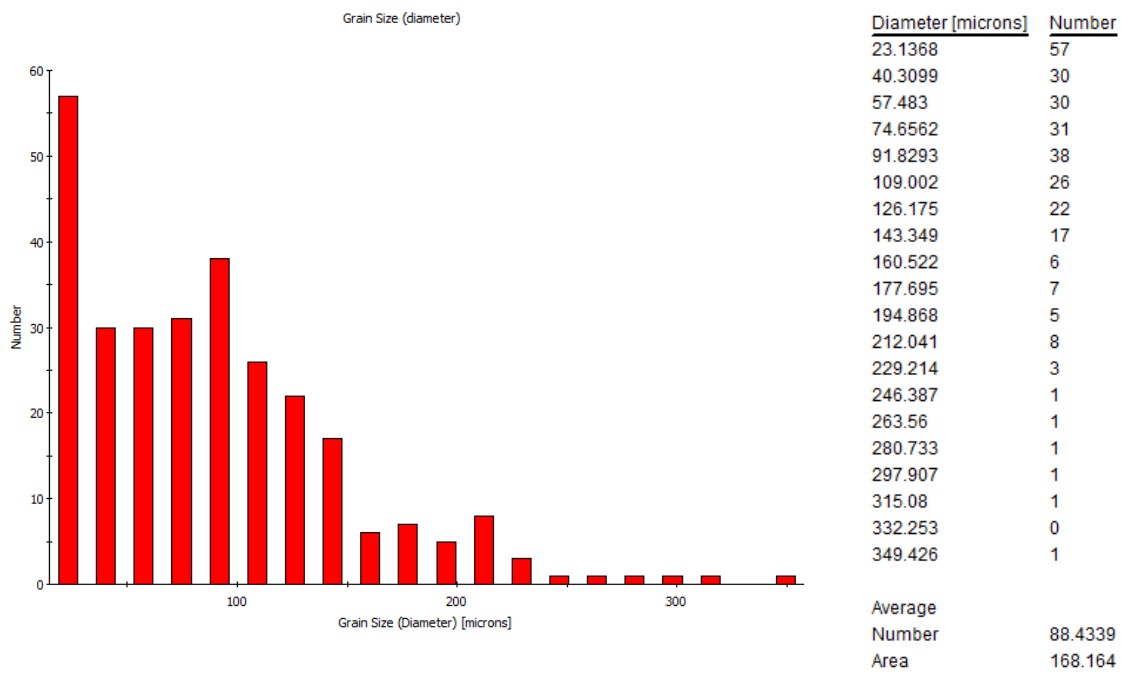


Figure 95: Histogram of grain size distribution for sample B1/2

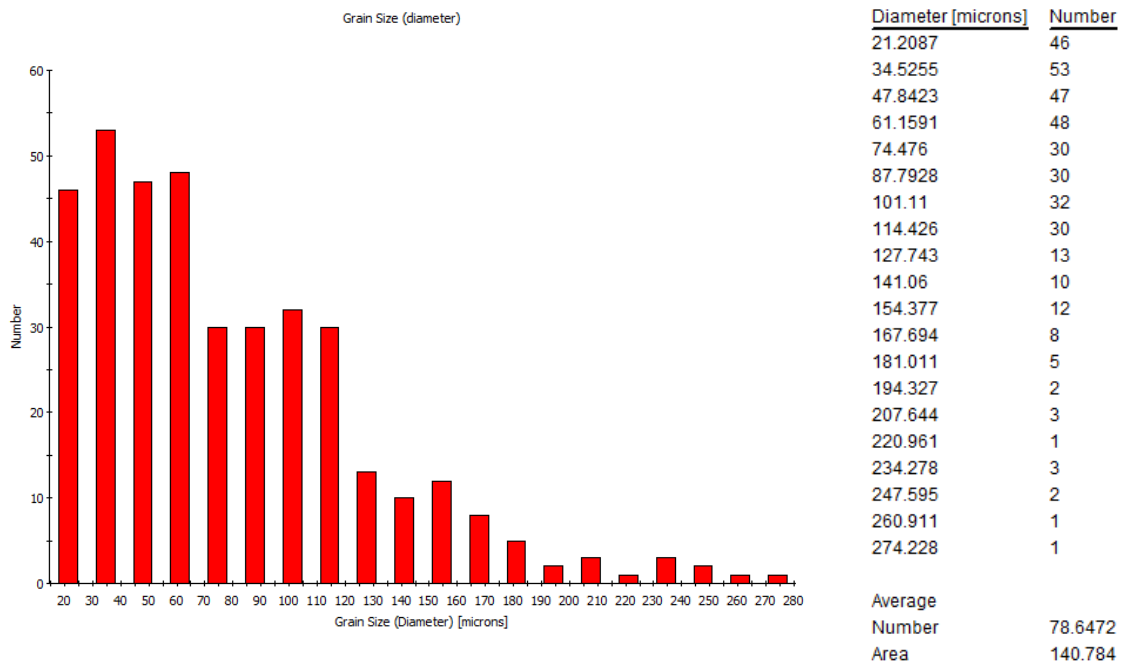


Figure 96: Histogram of grain size distribution for sample B1/5

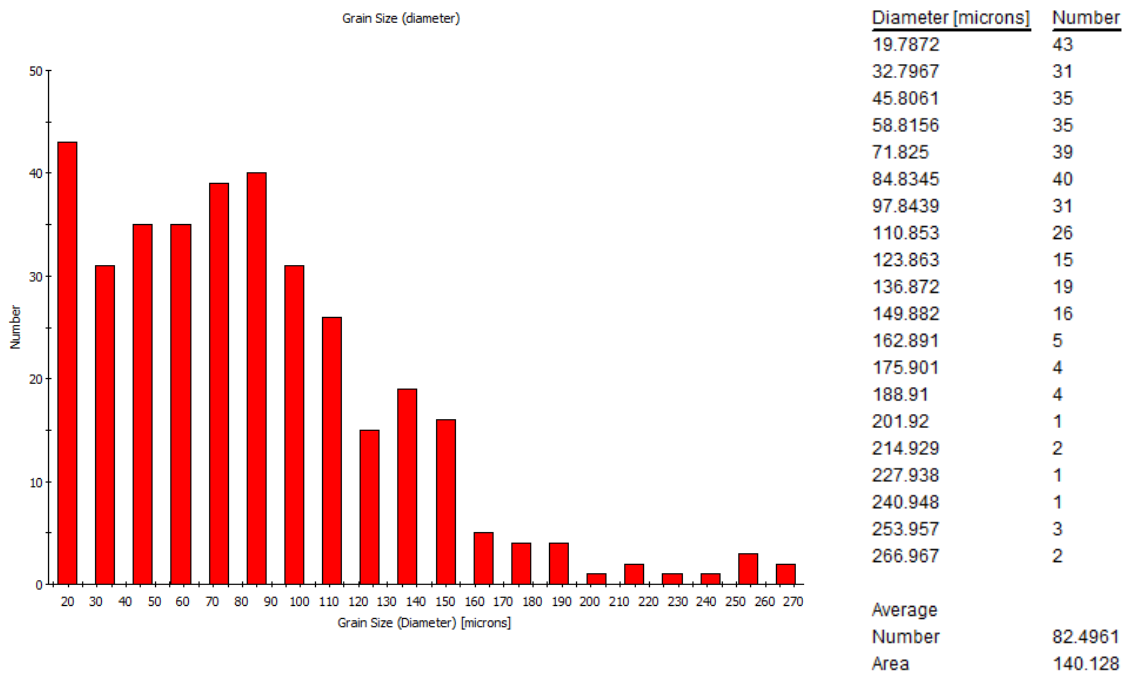
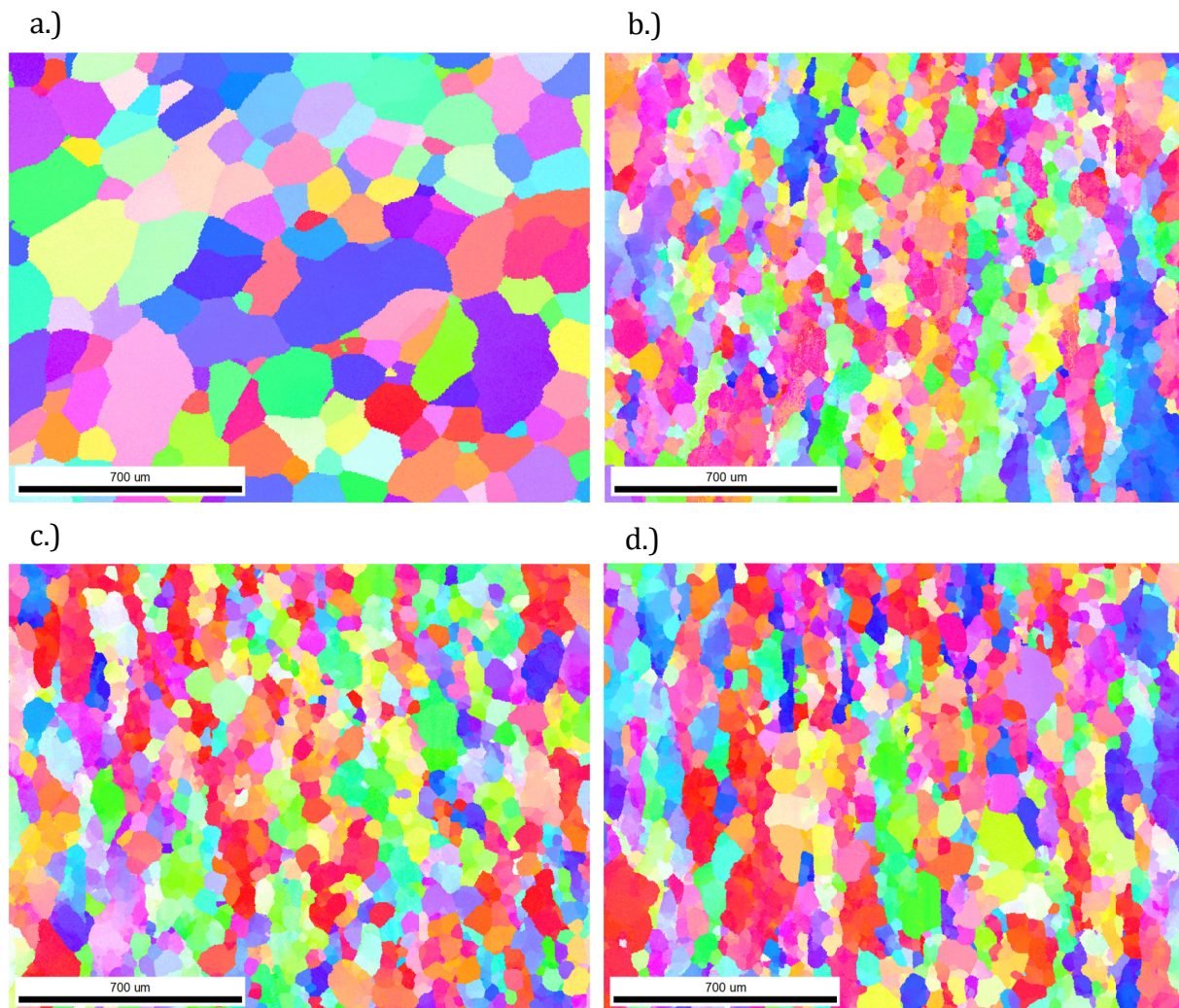


Figure 97: Histogram of grain size distribution for sample B1/10

12.5 Evaluation of Deformed Samples (Group C)



Color Coded Map Type: Inverse Pole Figure [001]

Aluminum

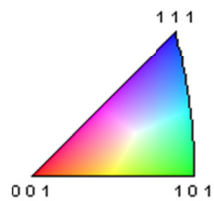
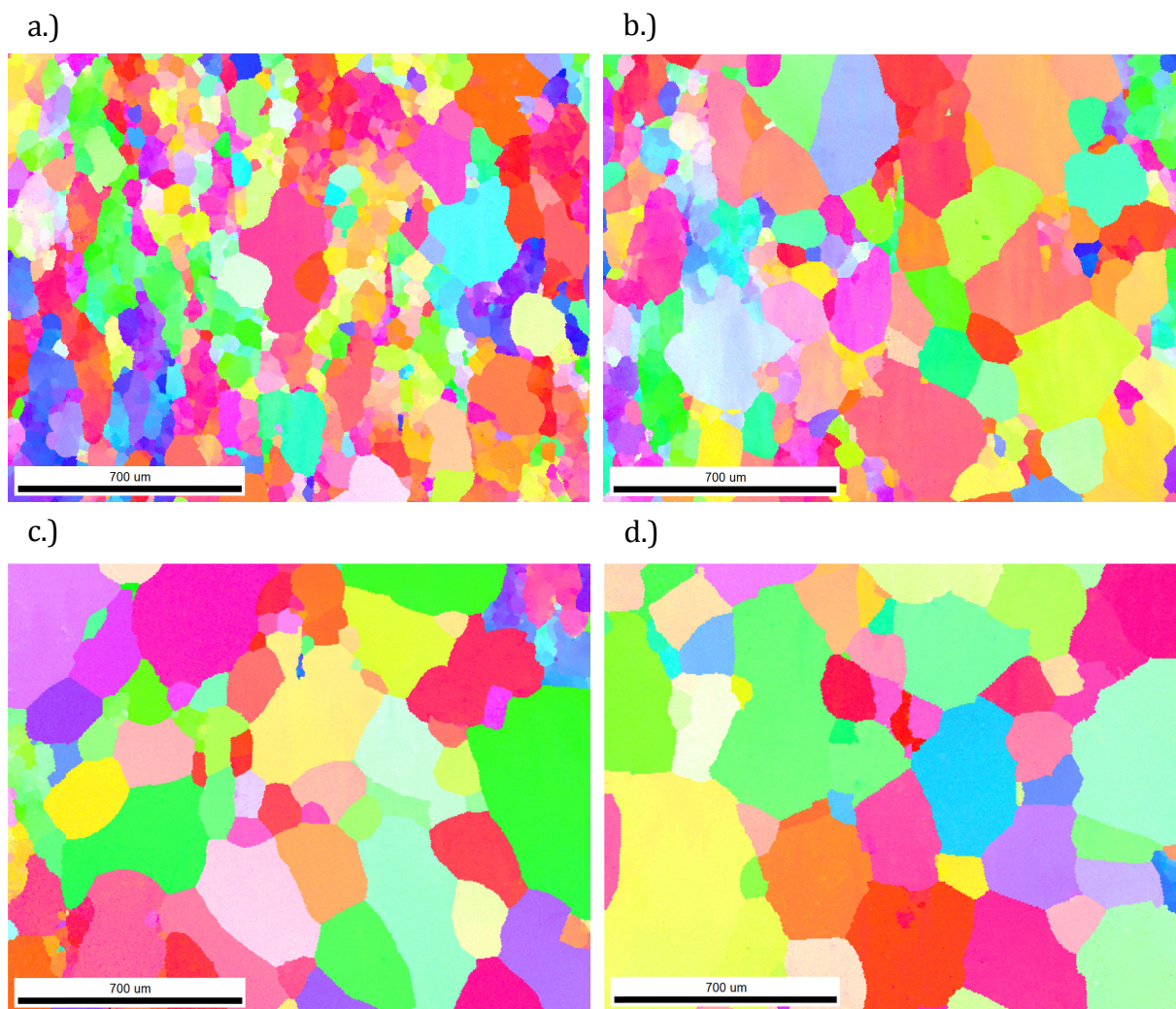


Figure 98: IPF of samples B0/0 (a.), C0 (b.), C2 (c.), and C5 (d.)



Color Coded Map Type: Inverse Pole Figure [001]

Aluminum

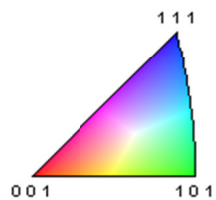
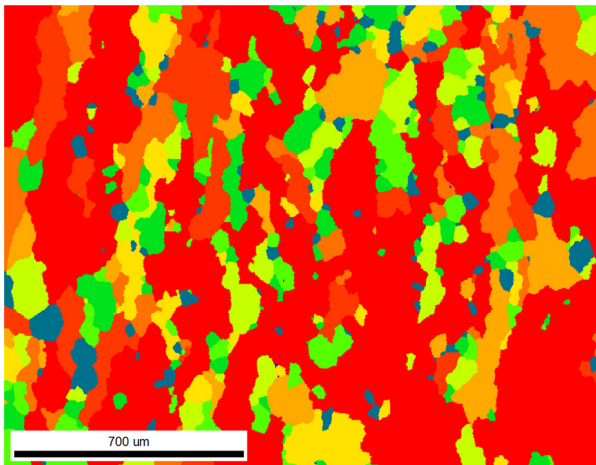


Figure 99: IPF of samples C10 (a.), C15 (b.), C20 (c.), and C30 (d.)

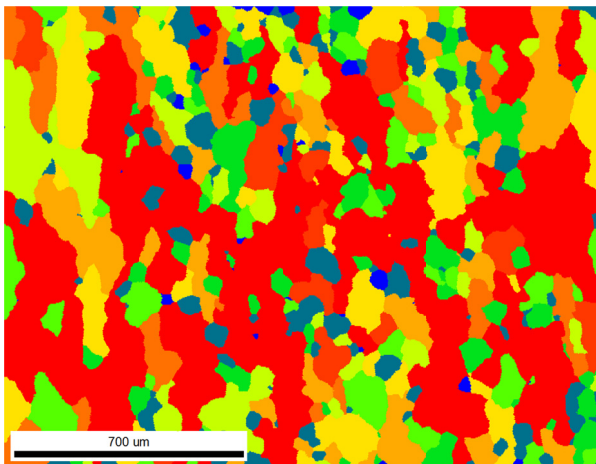
a.)



Color Coded Map Type: Grain Orientation Spread

	Min	Max	Total Fraction	Partition Fraction
	0	0.5	0.000	0.000
	0.5	1	0.037	0.037
	1	1.5	0.058	0.058
	1.5	2	0.061	0.061
	2	2.5	0.069	0.069
	2.5	3	0.053	0.053
	3	3.5	0.064	0.064
	3.5	4	0.078	0.078
	4	4.5	0.094	0.094
	4.5	90	0.482	0.482

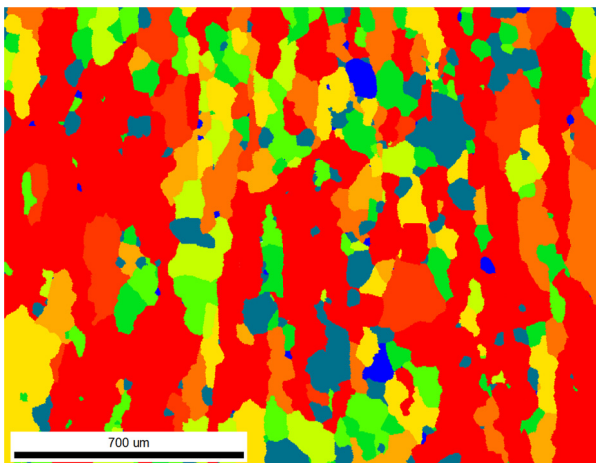
b.)



Color Coded Map Type: Grain Orientation Spread

	Min	Max	Total Fraction	Partition Fraction
	0	0.5	0.009	0.009
	0.5	1	0.074	0.074
	1	1.5	0.065	0.065
	1.5	2	0.069	0.069
	2	2.5	0.086	0.086
	2.5	3	0.105	0.105
	3	3.5	0.087	0.087
	3.5	4	0.063	0.063
	4	4.5	0.046	0.046
	4.5	90	0.394	0.394

c.)

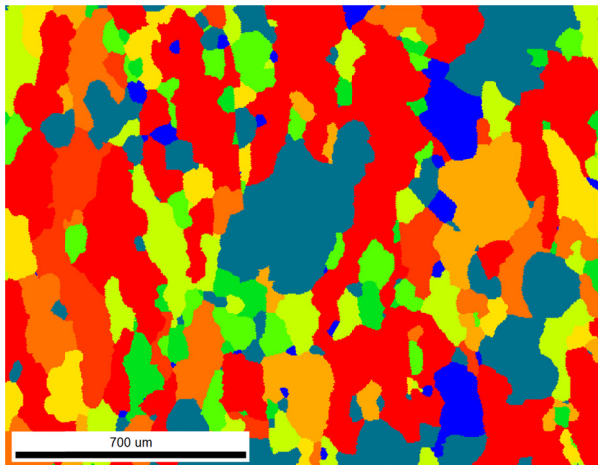


Color Coded Map Type: Grain Orientation Spread

	Min	Max	Total Fraction	Partition Fraction
	0	0.5	0.009	0.009
	0.5	1	0.077	0.077
	1	1.5	0.063	0.063
	1.5	2	0.056	0.056
	2	2.5	0.058	0.058
	2.5	3	0.088	0.088
	3	3.5	0.041	0.041
	3.5	4	0.074	0.074
	4	4.5	0.068	0.068
	4.5	90	0.464	0.464

Figure 100: GOS of samples C0 (a.), C2 (b.), and C5 (c.)

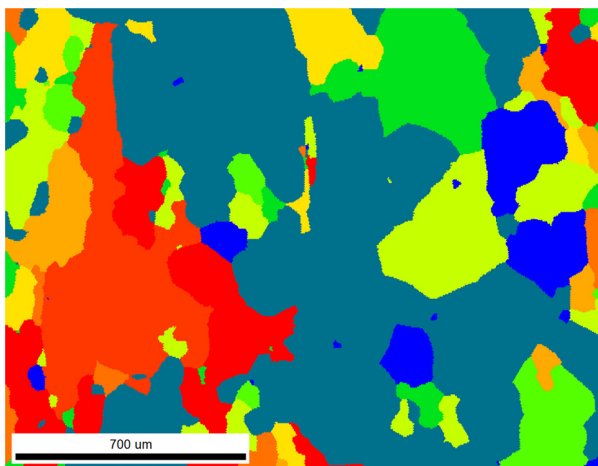
a.)



Color Coded Map Type: Grain Orientation Spread

	Min	Max	Total Fraction	Partition Fraction
	0	0.5	0.036	0.036
	0.5	1	0.185	0.185
	1	1.5	0.034	0.034
	1.5	2	0.050	0.050
	2	2.5	0.094	0.094
	2.5	3	0.051	0.051
	3	3.5	0.065	0.065
	3.5	4	0.077	0.077
	4	4.5	0.054	0.054
	4.5	90	0.355	0.355

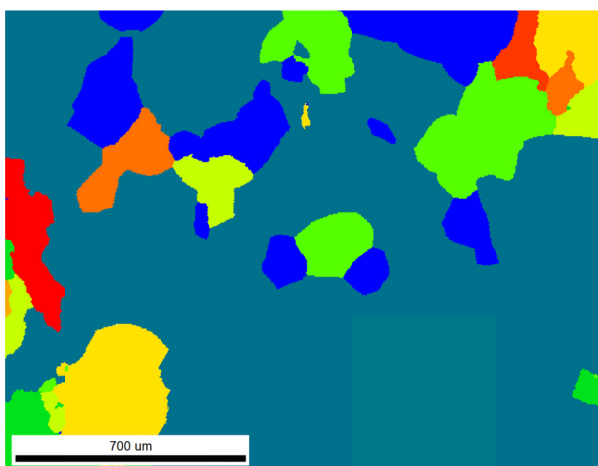
b.)



Color Coded Map Type: Grain Orientation Spread

	Min	Max	Total Fraction	Partition Fraction
	0	0.5	0.058	0.058
	0.5	1	0.432	0.432
	1	1.5	0.073	0.073
	1.5	2	0.038	0.038
	2	2.5	0.102	0.102
	2.5	3	0.043	0.043
	3	3.5	0.036	0.036
	3.5	4	0.018	0.018
	4	4.5	0.100	0.100
	4.5	90	0.101	0.101

c.)



Color Coded Map Type: Grain Orientation Spread

	Min	Max	Total Fraction	Partition Fraction
	0	0.5	0.093	0.093
	0.5	1	0.679	0.679
	1	1.5	0.016	0.016
	1.5	2	0.071	0.071
	2	2.5	0.025	0.025
	2.5	3	0.061	0.061
	3	3.5	0.001	0.001
	3.5	4	0.021	0.021
	4	4.5	0.008	0.008
	4.5	90	0.019	0.019

Figure 101: GOS of samples C10 (a.), C15 (b.), and C20 (c.)

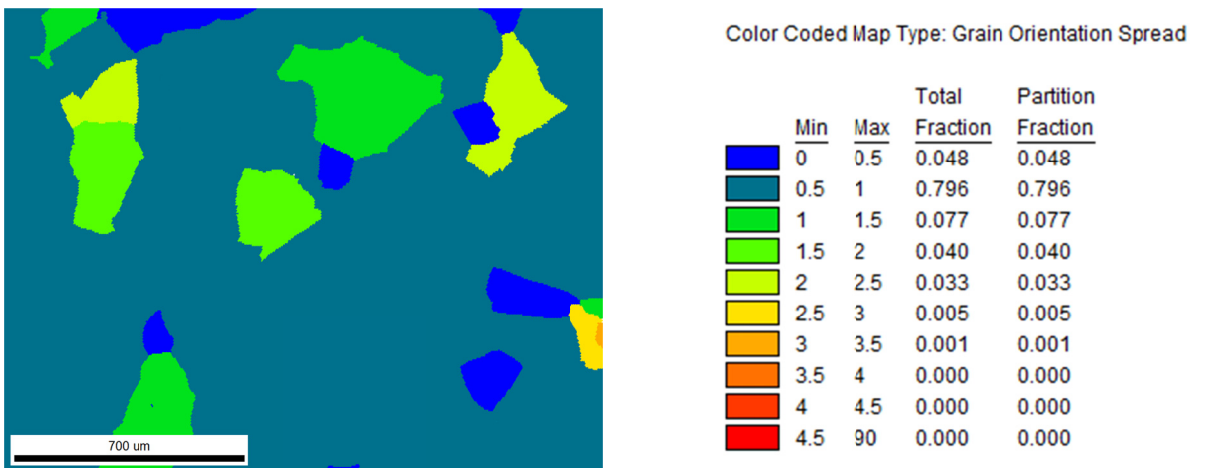


Figure 102: GOS of sample C30

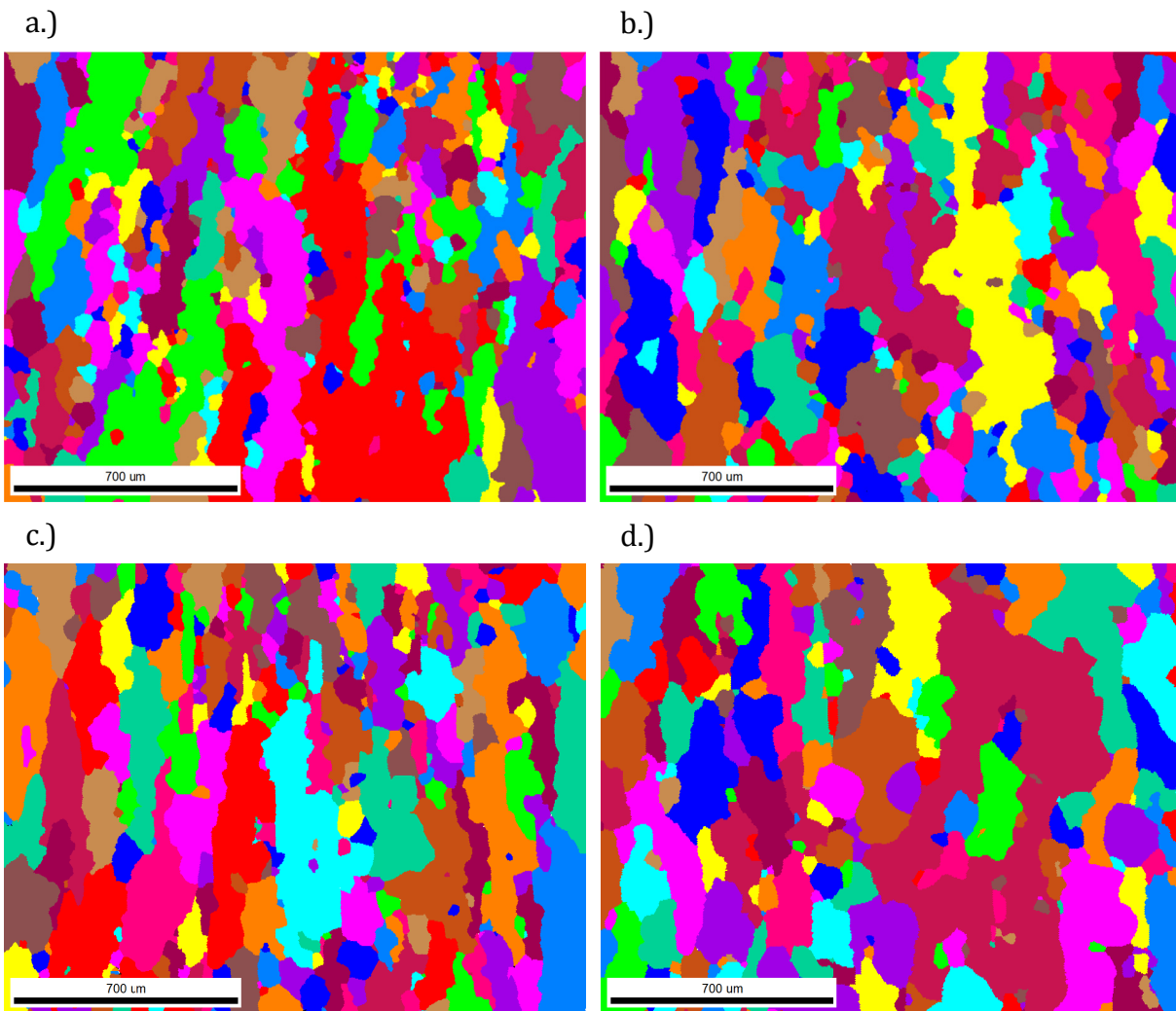


Figure 103: Grain map of samples C0 (a.), C2 (b.), C5 (c.), and C10 (d.)

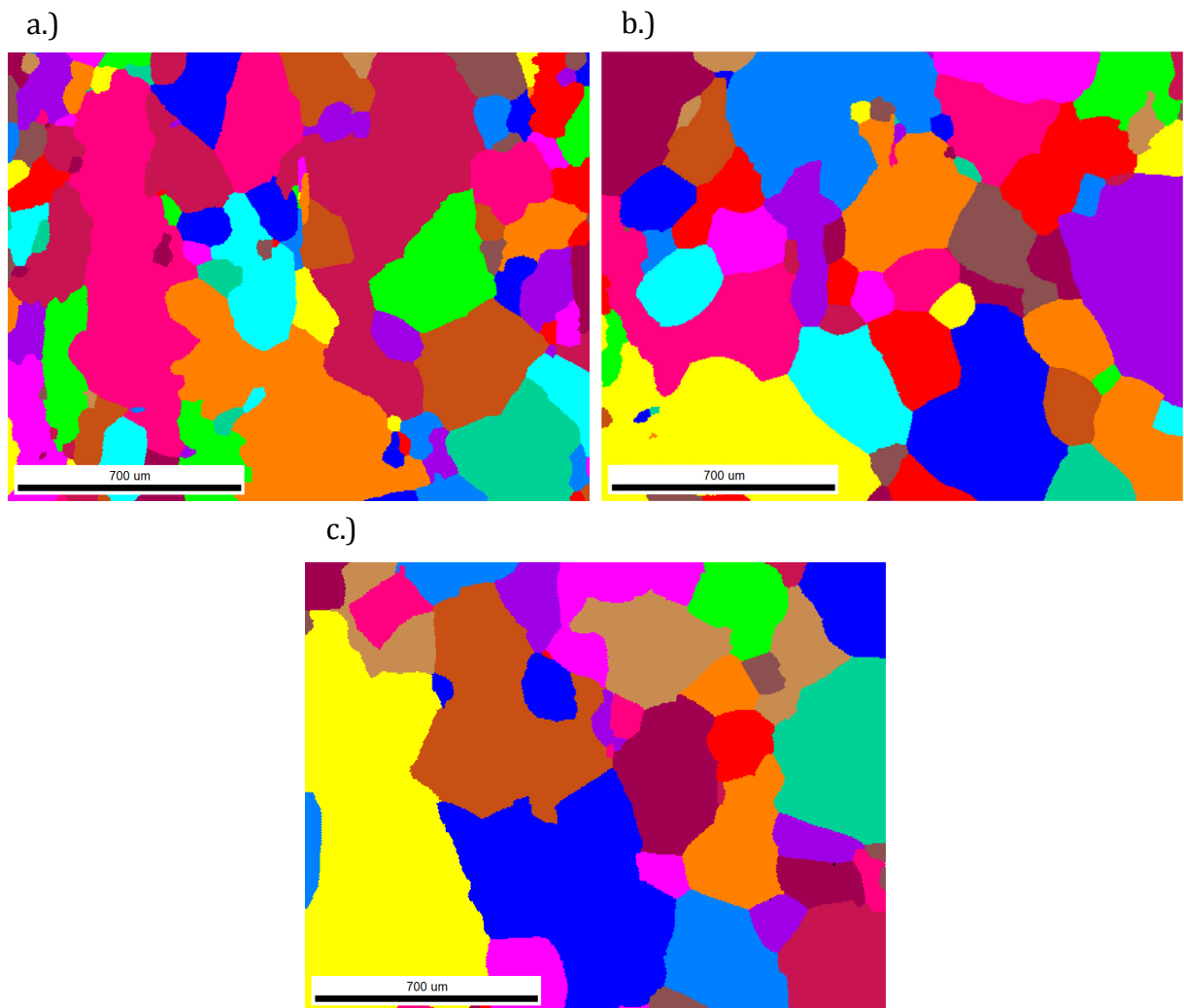


Figure 104: Grain map of samples C15 (a.), C20 (b.), and C30 (c.)

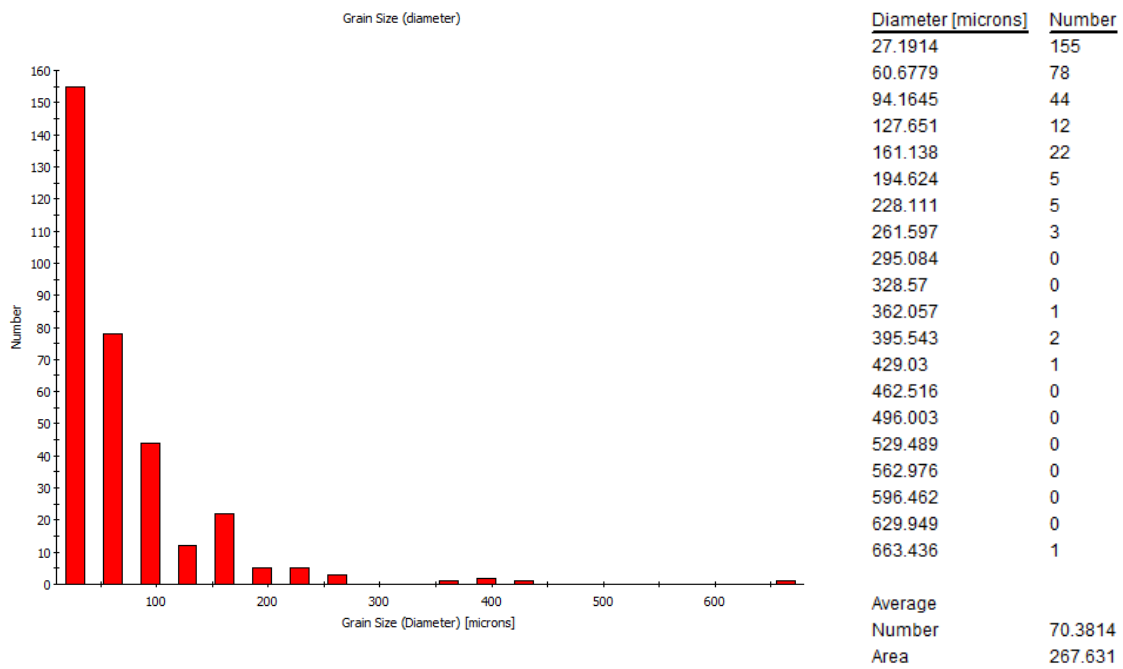


Figure 105: Histogram of grain size distribution for sample C0

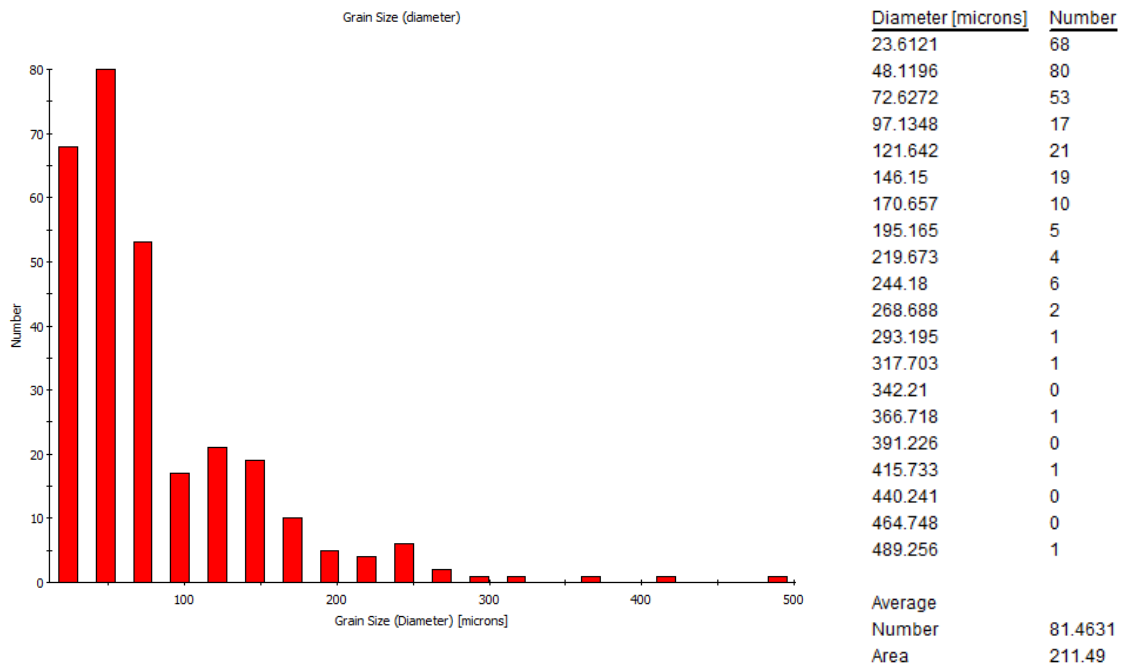


Figure 106: Histogram of grain size distribution for sample C2

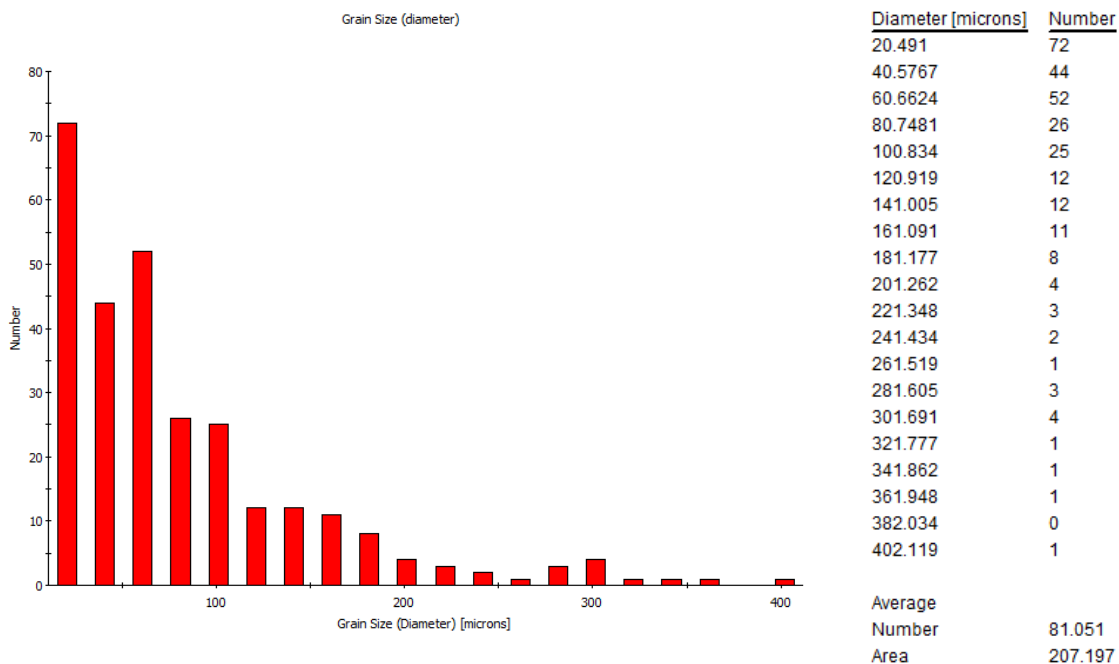


Figure 107: Histogram of grain size distribution for sample C5

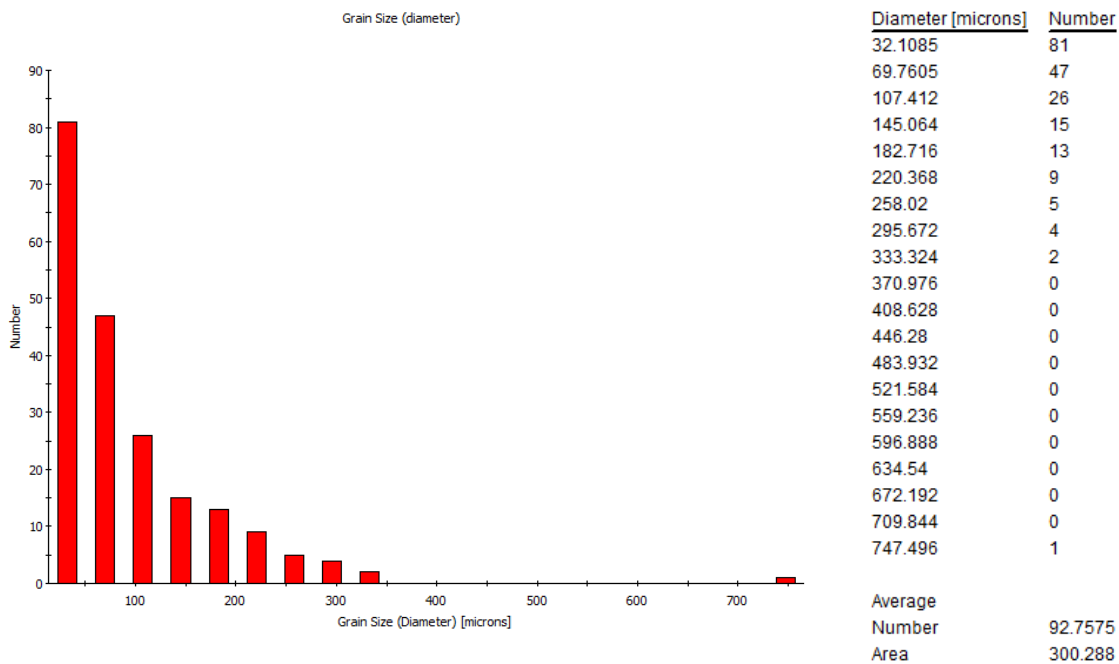


Figure 108: Histogram of grain size distribution for sample C10

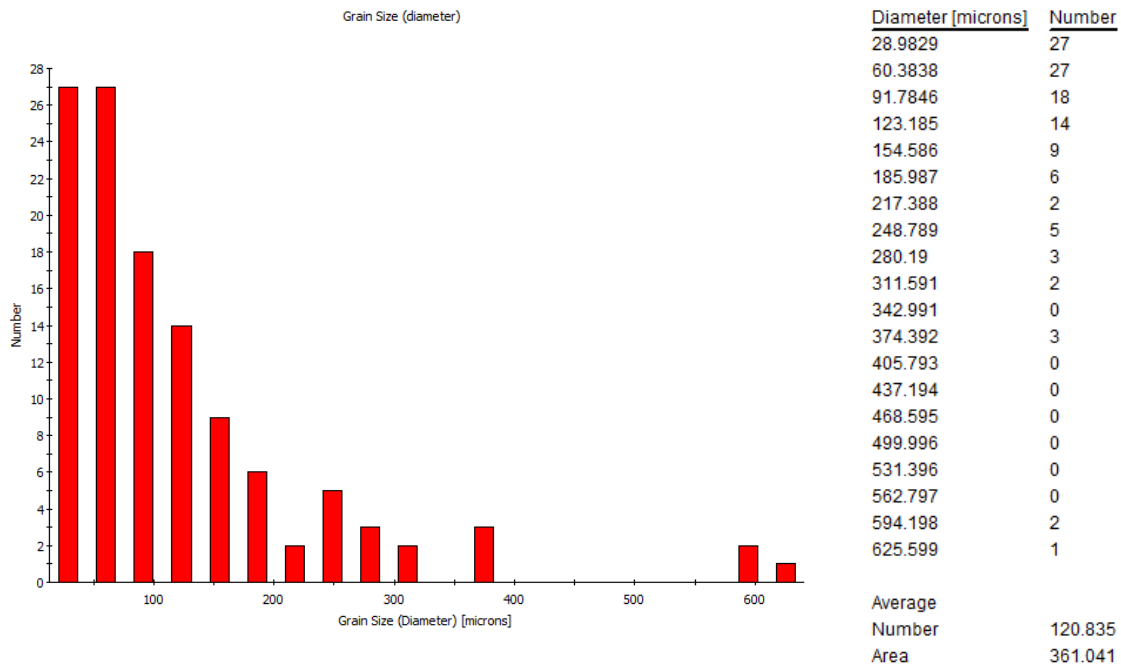


Figure 109: Histogram of grain size distribution for sample C15

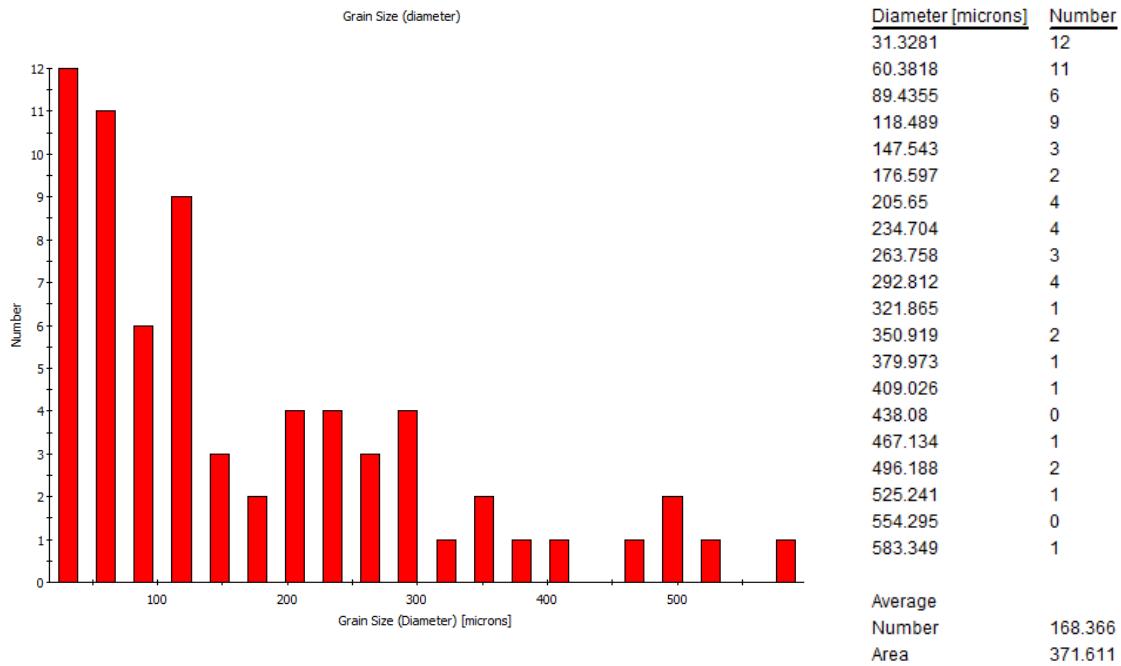


Figure 110: Histogram of grain size distribution for sample C20

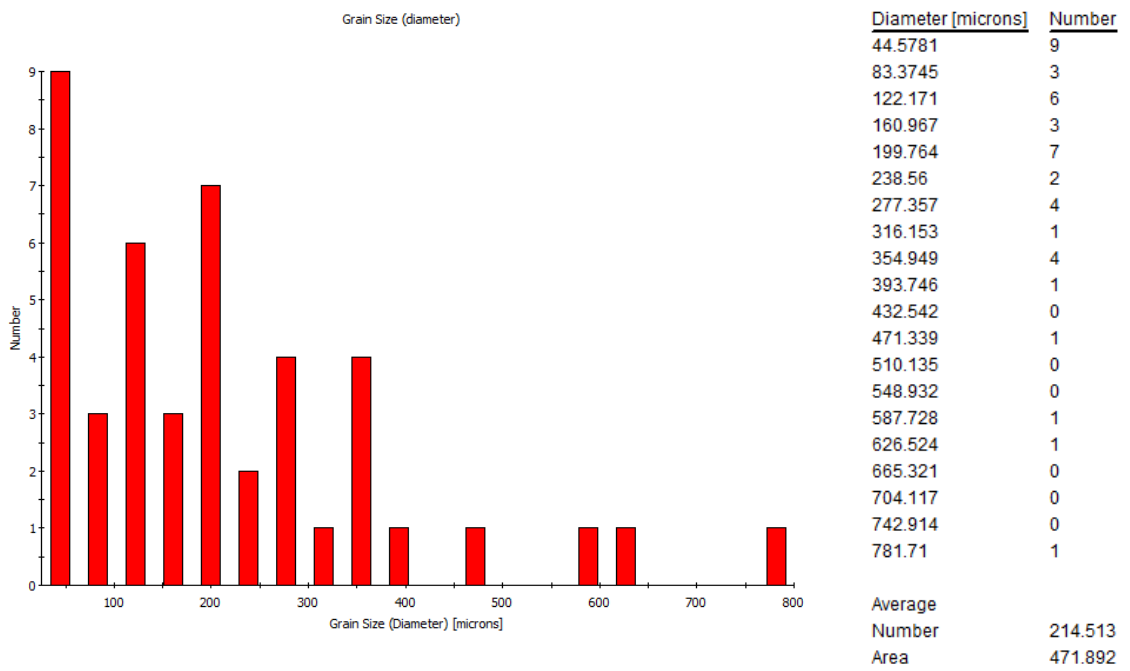


Figure 111: Histogram of grain size distribution for sample C30